USC
UNIVERSIDADE
DE SANTIAGO
DE COMPOSTELA

DEPARTAMENTO DE FÍSICA DA MATERIA
CONDENSADA

Tesis doctoral

THEORETICAL AND COMPUTATIONAL STUDY OF THERMAL AND ELECTRIC TRANSPORT PROCESSES IN NANOSTRUCTURED SYSTEMS

Jesús Carrete Montaña

D. Luis Javier Gallego del Hoyo, Catedrático del Departamento de Física de la Materia Condensada, y **D. Luis Miguel Varela Cabo**, Profesor Titular del mismo Departamento, de la Universidad de Santiago de Compostela

INFORMAN:

Que el trabajo titulado *Theoretical and computational study of thermal and electric transport processes in nanostructured systems* ha sido realizado bajo su dirección por **D. Jesús Carrete Montaña** en el Departamento de Física de la Materia Condensada de la Universidad de Santiago de Compostela, y constituye la memoria para optar al grado de Doctor en Física.

Santiago de Compostela, 30 de abril de 2012.

Prof. Luis Javier Gallego del Hoyo

Prof. Luis Miguel Varela Cabo

Summary

In the present thesis a theoretical and computational study of transport phenomena is performed for two kinds of nanostructured physical systems of very different characteristics but sharing the common feature of technological interest: semiconducting nanostructures and ionic liquids. Following this plan, it is structured in two parts, each one dealing with one of these classes of systems, even though there is a relation of thematic unity and methodological overlap between both of them. Placed before these thematic blocks, a brief chapter tries to explain the reasons for this choice of topic, as well as the global aims of this work.

Part I of this document is devoted to nanostructured semiconductor materials. The need for further miniaturisation in modern electronics together with the desire to explore the exciting possibilities offered by the nanoscale call both for methodological innovations in this field and for the generation of results with regard to promising nanostructures. Of course, given the almost infinite variety of structures which can be built from atoms of semiconductor materials, some particular instances had to be chosen. Thus, Chapter 2 addresses the thermal conductivity of indium phosphide nanowires through direct non-equilibrium molecular dynamics methods. First, some concepts about thermal conduction in the nanoscale are introduced; next, the methodological choices made for this chapter are explained and justified. Finally, numerical results for the thermal conductivity of such quasi-one-dimensional nanostructures are presented and compared with those obtained by other authors for Si nanowires. Apart from the fact that the order of magnitude of the results is certainly beneath that of bulk InP, the main conclusion is that a small enhancement in thermal conductivity happens when the diameter of the wires is reduced below a certain point. An explanation for this phenomenon is given in terms of an approximate phonon density of states, also obtained by molecular dynamics.

One of the main choices in any molecular dynamics simulation is the interaction potential, which must be judged in terms of its transferability to the situation under study. Chapter 3 contains thermal conductivity calculations

for InP, InAs and GaAs nanowires done employing the same methods as in Chapter 2 but using, in each case, two very different potentials: on one hand, the Branício-Rino potential for InP and the similarly complex Hammerschmidt potential for arsenides, in whose parameterisations their authors have taken vibrational properties into account; on the other, the Harrison potential, a very simple, biparametric and quasi-harmonic model shown by previous authors, by semi-analytic methods, to yield results an order of magnitude below those in Chapter 2. The molecular dynamics results presented in this chapter show that the Harrison potential can afford correct predictions of the qualitative trend of thermal conductivity as a function of nanowire diameter, but generally results in concrete values well below those obtained using the more sophisticated interaction potentials. In order to gain further insight into this phenomenon, the elements of the harmonic description of vibrations in solids are introduced in this chapter and the phonon densities of states associated to each potential are calculated in this formalism. The Harrison potential is shown as unable to reproduce these densities with a level of detail comparable to the other options tried. Thus, a correct choice of the interaction potential, both regarding its functional form — which must be adjusted to the underlying physics — and its parameterisation — which must include magnitudes related to thermal conductivity — is essential in molecular dynamics simulations of heat transfer in nanostructures.

Due to the limitations of molecular dynamics methods, starting with Chapter 4 thermal conduction is treated from the beginning as a phonon transmission problem. The systems chosen in this case are nanowires made from Si, the central element in electronics. For sufficiently thin nanowires, phonon scattering should be dominated by the nanowire boundary. In more macroscopic wires with rough boundaries that cause isotropic reflection of phonons, its influence translates into a phonon mean free path proportional to the diameter of the system. However, some experimental results point to values of the thermal conductivity well below those which could be expected if this result (known as Casimir's formula) held for thin wires. A theoretical study also managed to explain these experimental measurements, but seemingly did so at the expense of methodological correctness, as it made use of Fermi's golden rule outside its aprioristic domain of applicability and included boundary effects twice. In order to check the validity of Casimir's formula for very small diameters and to determine if the aforementioned experimental data can be explained exclusively in terms of boundary scat-

tering, a purely atomistic study was performed. Chapter 4 introduces the main elements behind this piece of research — the Stillinger-Weber potential, the non-equilibrium Green's function formalism and a simple form of the Boltzmann transport equation — and how they were combined in order to obtain the conductivities of thin silicon nanowires with a rough boundary. Using these tools, two scenarios were considered, shallow and deep surface disorder. The results show that Casimir's mean free path is a good approximation for shallow roughness (like that presumably present in the experimental situation) even for diameters as small as 2.22 nm but that a thermal conductivity significantly below this limit can be achieved using very deep defects, even though they might compromise other desirable properties. Therefore, a disordered boundary is not enough to explain the very low conductivities detected experimentally, and the theoretical success previously mentioned seems attributable to methodological errors. In addition to this, Chapter 4 contains some novel theoretical work and formulas that allow detailed phonon transmission probabilities across a localised defect to be calculated from knowledge of the causal t-matrix of the defect.

Chapter 5 closes the first part of this work with a study about a new kind of material: hybrid organic-inorganic superlattices built from alternated layers of a SiGe alloy and self-assembled monolayers of organic molecules (tri-tiophene, in this particular case). Research about such systems is in its infancy, but they seem to hold great promise for thermoelectric applications, *i.e.*, for the movement of heat against a thermal gradient through the use of electric power or for the generation of electricity by harnessing temperature differences. In order to have a thermoelectric material able to compete with more traditional energy conversion cycles it is necessary to achieve a high ratio between its electric and thermal conductivities, which has been so far impossible using semiconductors alone. The soft molecular interfaces in hybrid superlattices, however, could be able to scatter phonons very efficiently while maintaining a reasonable electric conductivity due to the conjugate orbitals present in the particular organic molecules chosen. In order to study such a complex system, methods from Chapter 4 are again applied to phonon transport and a similar formalism — based on the Boltzmann transport equation in the relaxation time approximation — is introduced for electrons, after briefly discussing the phenomenological description of thermoelectric conversion. A combination of *ab-initio* calculations and semiempirical interaction models is used as the input. The results obtained are promising, since even though the organic layers impede

electron transport to a certain degree, they block phonons much more dramatically, resulting in extremely low thermal conductivities, in the order of magnitude of 0.1 W/(m K) . Therefore, the dimensionless thermoelectric figure of merit (a combination of factors which determines the efficiency of a thermoelectric material) of the studied superlattices is larger than that of SiGe alone by a factor of more than two, regardless of whether ballistic or ohmic transport is assumed. Moreover, the simple addition of a phenyl group to each of the oligothiophenes in the organic layers causes a variation of more than 20% in the results, suggesting that the thermoelectric properties of these hybrid heterostructures can be tuned (and therefore optimised) using organic chemistry techniques to exploit the almost infinite flexibility of carbon-based molecules.

Part II of this thesis is devoted to the study of ionic liquids, a label applied to those substances with melting points below 100 °C that are completely dissociated into ions. Their versatility as solvents and the relative ease with which they may be separated from the products of a reaction without losses to the environment makes ionic liquids one of the cornerstones of "green chemistry". Their transport properties have been studied almost from the very discovery of this kind of substance, and remain extremely important today as ionic liquids are being considered as reaction media (which must also act as thermostatic baths) and for electrochemical applications. The study of liquid-state systems is notably complex, in part due to the absence of an ideal reference system, and very rarely can the level of predictive power often seen in solid-state theories be achieved. Instead, the results of theoretical investigations about liquids are often semi-quantitative models capable of explaining particular trends, sometimes with the help of parameters obtained from experiment. Nonetheless, even for liquids a good model must go beyond being an useful metaphor: it must be based on experimental observations and show some transferability to the study of different variables. For ionic liquids, a particularly interesting framework when judged in the light these criteria is the Bahe-Varela pseudolattice theory. Its underlying hypothesis, backed by results from X-ray scattering experiments, is the existence of a statistically regular arrangement of atoms in ionic liquids and their mixtures, as well as in concentrated solutions of conventional electrolytes. This theory has been successfully used to predict various equilibrium properties of these kinds of liquid systems.

It is a relatively well-known fact, indirectly inferred from experimental and simulation studies, that the nanostructure of ionic liquids and their mixtures with a solvent plays a crucial role in determining their properties.

However, very few works in the literature address this problem directly. Chapter 6 does so from two different points of view, as a prelude to the remainder of Part II. First, ionic and solvent cluster formation inside mixtures of 1-buthyl-3-methylimidazolium with water, methanol and ethanol is studied, reaching the conclusion that while water has a marked tendency to form big clusters — inside which water molecules experience a bulk-like environment — alcohols are only found in clusters of rather modest sizes, even at very high concentrations. Moreover, ions form a polar network that is not broken until there is a lot of solvent present in the mixture. Such breakdown occurs abruptly when the solvent is water, but passes through an intermediate regime with big ionic clusters present when the solvent is an alcohol. The second method used to study the microscopic structure of these mixtures is based on diagrams showing the conditional probability that a solvent molecule at a particular distance from a central ion has a given orientation, *i.e.*, diagrams of the angular structure of solvation layers. In those, the differences between water and alcohols can also be clearly appreciated.

In Chapter 7 a theoretical model is developed, based on the Bahe-Varela formalism, for the electric conductivity of conventional electrolyte solutions, ionic liquids and their mixtures with solvents. The central concept in this theoretical proposal is that of a cooperative rearrangement region, and electric conduction processes are explained in terms of random hops between these regions, whose probabilities are affected by the application of an electric field. Ion-ion and ion-solvent interactions are explicitly included by combining a path probability method with a Bragg-Williams-like approximation for interparticle interactions. A simple hypothesis of uncorrelated ion motion leads to the prediction that electric conductivity as a function of the volume fraction of ionic liquid has a maximum due to competition between two opposite effects, an increase in the density of charge carriers and a decrease in their mobility. When the conductivity curve is expressed in a reduced form, by dividing both the conductivity itself and the volume fraction by their values at the maximum, the theoretical model predicts an universal behaviour, *i.e.*, a corresponding-states law. Comparison with experiment shows excellent agreement between this theoretical results and the real behaviour of the systems under study. Deviations from the corresponding-states law depend on the solvent and can be qualitatively explained in terms of cluster formation, using results from Chapter 6.

Finally, the thermal conductivity of ionic liquids and their mixtures is stud-

ied in Chapter 8. Again taking the Bahe-Varela formalism as a theoretical basis, an effort is made to adapt as many elements as possible from the well-developed theory of heat transport in crystalline solids, used extensively in Part I. First, a precise definition of normal modes in the context of a liquid system is found in the literature, and these modes and their spatial distribution are studied for two pure ionic liquids. Next, an image of an ionic liquid — which, according to experimental observations, exhibits medium-range order — as a system formed by ordered domains separated by effective barriers is developed, whose approximate local translational symmetry is compatible with the existence of phonon-like vibrational modes. Those phonon-like vibrations with wavelengths longer than the characteristic width of a barrier can propagate and transport heat, while shorter-wavelength modes are essentially confined to a particular domain. Such heat transfer mechanism is known as phonon hopping and has been studied previously in different contexts, such as amorphous or polycrystalline solids. In this chapter, a general model for the thermal conductivity of ionic liquids and their mixtures based on phonon-hopping is introduced, and its predictions are studied analytically under very simple assumptions. For pure ionic liquids, this model predicts a room-temperature plateau which is observed in experimental data, while for their mixtures with a solvent it yields a parameter-free interpolation formula. The latter result is compared with experimental data for two mixtures of imidazolium-based ionic liquids with water and ethanol, showing excellent agreement for water under the assumption of bulk-like behaviour of the solvent at any concentration. For ethanol, however, the deviations of experimental results from the crude prediction of the interpolation formula highlight the need for a more detailed model of the solvent. Once again this points to the fact that the nanoscopic aggregation state of solvent particles in the mixture is crucial in determining their macroscopic properties.

This thesis ends with a brief summary of the main conclusions.

Resumen

En la presente tesis se aborda el estudio teórico-computacional de los fenómenos de transporte térmicos y eléctricos en dos tipos de sistemas nanoestructurados de muy distinta índole pero con el denominador común de su indudable interés tecnológico: diversas nanoestructuras semiconductoras y líquidos iónicos. De acuerdo con este planteamiento, la memoria está estructurada en dos partes, cada una correspondiente a un tipo de sistema, si bien existen entre ellas una relación de unidad temática y un gran solapamiento metodológico. De manera previa al desarrollo de estos dos bloques se incluye un breve capítulo que pretende explicar el porqué de la elección de este tema y los objetivos perseguidos con su estudio.

La primera parte de este trabajo está dedicada a los materiales semiconductores nanoestructurados. En sus formas más o menos masivas estos materiales, cuyas propiedades de conducción de corriente eléctrica pueden modificarse controladamente mediante temperatura, dopaje o campos eléctricos, han posibilitado la emergencia de la electrónica en general y de todas sus ramas, como la optoelectrónica. En consecuencia, juegan hoy en día un papel central en el desarrollo de las nuevas tecnologías. No obstante, el camino para su avance futuro pasa por una mayor miniaturización, lo que supone acceder a escalas donde tanto las aproximaciones teóricas para la descripción de su comportamiento como las técnicas experimentales que se han utilizado hasta ahora para su síntesis han de ser cuidadosamente revisadas. Si bien es cierto que esto abre la puerta a nuevas e interesantísimas posibilidades completamente inexistentes en escalas de longitud superiores, también lo es que representa un gran desafío para la teoría, pues muchas nanoestructuras se hallan en la incómoda tierra de nadie a donde los métodos mecano-cuánticos y atomísticos no pueden llegar con los medios computacionales existentes pero en la que las aproximaciones continuas aplicables a sistemas masivos tampoco proporcionan resultados útiles. En consecuencia, el campo se encuentra en continua efervescencia, movido fundamentalmente por la necesidad de dar una base sólida a la física experimental de semiconductores y a la nanoingeniería electrónica del mañana.

Dentro de este vasto campo, los resultados englobados en la Parte I de esta tesis suponen una contribución a la comprensión de los fenómenos de transporte en semiconductores en la nanoescala, y más en concreto de la propagación de calor y electricidad en estas nanoestructuras. Tal estudio tiene aplicaciones prácticas inmediatas, y de hecho no es en absoluto arriesgado afirmar que parte de la inversión en su avance se hace precisamente en atención a las necesidades de la nanoelectrónica. En particular, no se puede pensar en producir nanochips si no se han tenido en cuenta sus características en lo tocante a disipación de calor y la forma de aliviarla de modo que no comprometa la estructura y el funcionamiento de estos dispositivos. Los nanohilos, estructuras cuasi-unidimensionales, parecen excelentes candidatos para jugar el papel de conductores de corrientes eléctricas y térmicas en la nanoescala, y es por ello por lo que se les dedican los tres primeros capítulos de esta primera parte.

El Capítulo 2 aborda el estudio de la conductividad térmica de nanohilos de InP mediante dinámica molecular. Este conjunto de técnicas, consistentes en la integración numérica de las ecuaciones de Newton y la derivación de resultados a partir de las trayectorias clásicas obtenidas, tiene las ventajas de ser fácilmente implementable y de incluir todos los efectos anarmónicos, pero también los inconvenientes de ignorar la naturaleza cuántica de la materia y de dar una descripción poco detallada de los procesos de transporte subyacentes. El capítulo comienza con una breve introducción a estos métodos, durante la cual se comentan los principales problemas asociados al estudio de la conducción de calor en la nanoescala. A continuación se discuten razonadamente las elecciones metodológicas tomadas para el estudio: en concreto, el uso de uno de los llamados métodos directos que sitúan al sistema fuera del equilibrio, la opción por el potencial semiempírico de Branício-Rino y la aplicación de condiciones de contorno rígidas en la dirección radial a fin de garantizar la estabilidad mecánica del sistema y situar a sus átomos constituyentes en entornos más parecidos a los del sistema masivo para el cual fue parametrizado este potencial. La sección de resultados presenta los valores de la conductividad térmica obtenidos para nanohilos con diámetros de 0,83, 1,66, 2,49, 3,32, 4,15 y 4,97 nm, y una longitud de la celda de simulación suficiente para que se puedan considerar representativos de un nanohilo infinito, tras hacer algunas observaciones sobre el proceso de convergencia de la simulación. Del estudio de la dependencia de la conductividad térmica con la temperatura se desprende una tendencia generalmente decreciente entre 100 y 700 K. Los valores de esta magnitud se sitúan entre uno y dos órdenes de magnitud por debajo de

los del mismo material como sólido masivo, en concordancia con resultados de la literatura para otros semiconductores. También se presentan resultados de la dependencia de la conductividad en el diámetro del nanohilo a temperatura constante, que muestran una reducción monótona hasta diámetros muy finos, seguido de un pequeño incremento en la conductividad al reducir el diámetro hasta 1,66 nm. Mediante un estudio aproximado de las densidades de estados fonónicas de los sistemas simulados se observa que esto es compatible con hipótesis sobre efectos de confinamiento propuestas por otros autores para materiales distintos pero relacionados.

Una de las decisiones más críticas previas al uso de métodos de dinámica molecular es la elección del potencial de interacción entre partículas, que es susceptible de mostrar problemas de transferibilidad a la situación que se va a simular. La observación de que un grupo de resultados de la literatura científica predecía conductividades térmicas para nanohilos de InP un orden de magnitud menores que las obtenidas en el Capítulo 2, unida a la consciencia de la existencia de este tipo de problemas, condujo a la investigación que se resume en el Capítulo 3. En él se emplea de nuevo el método directo de no-equilibrio para calcular la conductividad térmica de nanohilos delgados de InP, pero también de InAs y GaAs, con la particularidad de que se hace utilizando dos potenciales muy diferentes para cada uno de estos materiales. Por un lado, se hacen cálculos con potenciales relativamente sofisticados cuya forma funcional comprende varios tipos de interacciones y que muestran una notable transferibilidad: el de Branício-Rino para InP y el de Hammerschmidt para ambos arseniuros. Por otro, se prueba un potencial biparamétrico muy sencillo, esencialmente armónico y que está en la base de los resultados citados: el de Harrison. Los cálculos muestran que el potencial de Harrison arroja, también cuando se usa en conjunción con los métodos de dinámica molecular escogidos para estos capítulos, resultados sustancialmente más bajos (menores en el esperado orden de magnitud) que los otros dos potenciales, más sofisticados. Sin embargo, parece que los cálculos semi-teóricos realizados con el potencial de Harrison sí son capaces de predecir tendencias cualitativas de la conductividad con el diámetro. Para indagar algo más profundamente en el motivo del desacuerdo entre diferentes potenciales, se introducen los elementos de la descripción armónica de los procesos de conducción térmica en términos de fonones y se calcula su densidad de estados para un diámetro dado. Tomando como ejemplo el caso del InP, se comprueba que la densidad de estados predicha por el potencial de Harrison difiere enormemente de la

de Branício-Rino, pese a situarse en el mismo rango general de frecuencias en virtud de proceso de ajuste de sus parámetros. Por ello, se concluye que una buena elección del potencial, tanto en lo relativo a su forma funcional — que debe ser lo suficientemente ajustada a la física subyacente — como en lo que respecta a parametrización — que tiene que prestar atención a las propiedades vibracionales del sistema bajo estudio — resulta esencial en las simulaciones del transporte térmico en nanoestructuras.

Vistas las limitaciones de los métodos de dinámica molecular, en el Capítulo 4 se aborda de lleno un planteamiento fonónico del problema de la conducción térmica. Los sistemas estudiados en este caso son nanohilos de Si, elemento clave en la electrónica. En una imagen de *scattering* de fonones, para nanohilos lo suficientemente finos la conductividad térmica debería estar dominada por el efecto del borde. Para sistemas con simetría de traslación en una dirección y un borde tal que la reflexión de los fonones es isótropa — los equivalentes gruesos de estos nanohilos — esto se traduce en un camino libre medio independiente de la frecuencia y proporcional al diámetro mediante un factor de forma de orden unidad, desarrollo conocido como la fórmula de Casimir. Sin embargo, existen resultados experimentales recientes que apuntan a una conductividad térmica en nanohilos finos con borde rugoso mucho menor que la esperable en esta aproximación. Un trabajo teórico posterior consiguió predicciones compatibles con estos experimentos, pero aparentemente al precio de incurrir en dos graves problemas metodológicos: la inclusión por duplicado del efecto del borde y el uso de la regla de oro de Fermi fuera de lo que se puede suponer *a priori* como el dominio de validez de tal aproximación perturbativa. Para comprobar la validez de la fórmula de Casimir y determinar si los datos experimentales pueden ser explicados únicamente por el efecto del borde se realizó un estudio riguroso partiendo de una descripción atomística de los nanohilos de Si. En el Capítulo 4 se introducen los elementos de este estudio: el potencial de Stillinger-Weber para describir las interacciones entre los átomos de Si, el formalismo de las funciones de Green de no-equilibrio para calcular la probabilidad de que cada fonón sea transmitido a través de un defecto espacialmente acotado, y la ecuación de transporte de Boltzmann para estados estacionarios en la aproximación del tiempo de relajación para pasar de este resultado al caso de un nanohilo infinito en régimen de transporte óhmico. Con estas herramientas se abordaron dos escenarios: defectos superficiales poco profundos, como los que presumiblemente se presentan en la situación experimental, y nanohilos con un mellado de mayor calado con-

seguido mediante la remoción de un número significativo de átomos de un segmento. Las conclusiones obtenidas son que el camino libre medio de Casimir es una buena aproximación incluso para diámetros tan pequeños como 2,22 nm, pero que se puede superar este límite mediante defectos profundos, aunque a costa de comprometer diversas otras propiedades o incluso la estabilidad estructural del sistema. De este modo, los citados resultados experimentales no se pueden explicar solamente en términos de rugosidad superficial, y el trabajo teórico que pretendía hacerlo parece más bien contener resultados no válidos debido a sus aproximaciones injustificadas. Este capítulo también contiene resultados teóricos novedosos, pues se proporcionan fórmulas explícitas para la probabilidad de transmisión detallada (modo a modo) a través de un defecto localizado, en términos de la matriz t del nanohilo en presencia de ese defecto.

La Parte I concluye con el Capítulo 5, en el que se trata un nuevo tipo de materiales nanoestructurados: las superredes híbridas orgánico-inorgánicas, consistentes en la repetición alternativa a lo largo de una dimensión de bloques de un material inorgánico y monocapas autoensambladas de moléculas orgánicas. Tales sistemas están comenzando a ser sintetizados en la actualidad y, a efectos de esta tesis, resultan prometedores de cara a sus posibles aplicaciones termoeléctricas, es decir, como materiales para la realización de trabajo eléctrico a costa del flujo de calor según un gradiente de temperatura, o bien — en sentido inverso — para la transmisión de calor de un foco frío a otro caliente mediante el uso de potencia eléctrica, todo ello sin partes móviles. Para disponer de un material termoeléctrico competitivo se debe lograr un valor aceptable de la llamada cifra de mérito, que es proporcional al cociente entre las conductividades eléctrica y térmica. Interesa, por consiguiente, dificultar el paso de fonones pero no tanto el de electrones. La idea aquí planteada para conseguirlo es usar superredes híbridas en las que la parte inorgánica consista en una aleación semiconductora (SiGe, p. ej.) y la parte orgánica en una monocapa de polímeros con buena conductividad eléctrica, pero blandos ante deformaciones. Para estudiar estos sistemas se rescatan métodos y resultados del Capítulo 4 para el estudio de fonones, y se introduce un formalismo similar — igualmente basado en la ecuación de transporte de Boltzmann en la aproximación del tiempo de relajación — para electrones, además de explicar brevemente el formalismo fenomenológico aplicable a los procesos termoeléctricos. Dada la complejidad del conjunto tratado, es necesario combinar resultados atomísticos, incluso *ab-initio*, con otros procedentes de parametrizaciones se-

miempíricas. Los resultados obtenidos resultan prometedores, pues aunque las monocapas orgánicas bloquean el paso de electrones en cierta medida, dificultan mucho más la conducción de fonones. De este modo, pese a que se observa una reducción de las magnitudes que describen el transporte eléctrico con respecto a la aleación SiGe en forma de sólido masivo, la espectacular reducción de la conductividad térmica — cuyo valor para la superred puede caer hasta el orden de magnitud de 0,1 W/(m K) — hace que la cifra de mérito termoeléctrica mejore a la del SiGe aislado en un factor $\sim 2{,}5$, tanto si se supone que el transporte es óhmico como si se usan períodos de la superred lo suficientemente cortos para suponer que el transporte térmico es balístico. Más aún, la simple adición de un grupo fenil a cada uno de los politiofenos que forman las monocapas provoca una variación del 20 % en los resultados, lo que indica que las propiedades termoeléctricas de este tipo de materiales nanoestructurados son susceptibles de ser modificadas, y en consecuencia optimizadas, utilizando toda la potencia de los métodos de la química orgánica para aprovechar la infinita flexibilidad de las moléculas basadas en el carbono.

La Parte II de la tesis aborda el estudio de un tipo diferente de sistemas nanoestructurados, los líquidos iónicos. Se clasifican bajo esta denominación aquellas sustancias cuya temperatura de fusión se encuentra por debajo de los 100 °C y que están compuestas completamente por iones, esto es, disociadas por completo. Los líquidos iónicos cuentan ya con unos cien años de historia y componen una numerosísima familia cuyas particulares propiedades — presión de vapor prácticamente nula, amplio rango de temperaturas de trabajo, etc. — y su versatilidad como disolventes les proporcionan un gran interés industrial, como alternativa a disolventes más convencionales y como piezas clave de la llamada "química verde", en la cual se intentan minimizar los residuos generados. Las propiedades de transporte de los líquidos iónicos han sido estudiadas desde el mismo instante de su descubrimiento y revisten hoy gran importancia. Así, la conductividad térmica de estos sistemas es crucial de cara a su utilización como medios de reacción — ya que una de sus funciones en ese papel será servir como baño termostático para el proceso químico —, como lubricantes, como fluidos caloportadores o como refrigerantes. Por otro lado, su conductividad eléctrica es uno de los parámetros de interés para la aplicación de estos líquidos a procesos electroquímicos (p. ej., como disolventes en electrolitos de baterías). Tales magnitudes son objeto de estudio en esta parte del trabajo, que busca establecer teorías de aplicabilidad suficientemente general. Debe tenerse presente que el estudio de sistemas en estado

líquido es notablemente complejo debido, entre otros factores, a la falta de un sistema de referencia ideal, y que por consiguiente rara vez se puede llegar a resultados que exhiban el mismo poder predictivo que teorías similares de estado sólido. En lugar de esto, a menudo el resultado de las investigaciones teóricas son modelos semicuantitativos capaces de explicar determinadas tendencias, quizás con ayuda de parámetros obtenidos de los experimentos. Sin embargo, también en estado líquido un buen modelo debe sustentar sus hipótesis en observaciones reales. Otro criterio importante para juzgar la calidad de estos desarrollos es su transferibilidad al estudio de diferentes variables. En el estudio de líquidos iónicos, un marco teórico que cumple muy bien estos dos requisitos es el formalismo pseudorreticular de Bahe-Varela. Su hipótesis subyacente, respaldada por estudios de rayos X, es la existencia de un arreglo reticular estadístico en el seno de estos líquidos, y ha sido usado para predecir diversas propiedades de equilibrio y transporte. En consecuencia, fue este el formalismo elegido para esta parte de la tesis.

Es un hecho relativamente bien conocido, o cuando menos inferido indirectamente a partir de resultados experimentales y de simulación, que la nanoestructura de los líquidos iónicos y sus mezclas con disolventes es crucial para entender sus propiedades. Son pocos en la literatura, sin embargo, los estudios que se ocupan del tema directamente. El Capítulo 6 lo hace desde dos puntos de vista, a modo de preludio al resto de la Parte II. En primer lugar, se estudia la formación de agregados de iones o de moléculas de disolvente en mezclas de tetrafluoroborato de 1-butil-3-metilimidazolio con agua, metanol y etanol. De este estudio se extrae la conclusión de que, mientras el agua tiene una gran tendencia a formar grandes agregados dentro de los cuales sus moléculas experimentan un entorno semejante al del agua pura, los alcoholes no lo hacen ni siquiera a concentraciones muy altas. Por su parte, los iones tienden a formar una red polar dentro de la mezcla que no se rompe hasta que se ha añadido mucho disolvente. Dicha ruptura es relativamente abrupta cuando el disolvente es agua, pero en el caso de los alcoholes pasa por un estadio intermedio en el que están presentes grandes agregados de iones. El segundo método de estudio de la estructura microscópica de estas mezclas son los diagramas de probabilidad de que las moléculas de disolvente adopten una orientación determinada a cada distancia de un ion central, es decir, diagramas de la estructura angular de las diversas capas de solvatación. También aquí surgen contrastes entre el agua y los alcoholes, que se relacionan con la formación de agregados.

En el Capítulo 7 se desarrolla un modelo teórico, basado en el citado formalismo pseudorreticular, para la conductividad eléctrica en líquidos iónicos y sus mezclas con disolventes, así como para disoluciones electrolíticas convencionales. El concepto central en esta propuesta teórica es el de región de reorganización cooperativa, y los procesos de conducción eléctrica se explican en términos de saltos aleatorios entre estas regiones, cuyas probabilidades se ven afectadas por la presencia de un campo eléctrico. Las interacciones ion-ion e ion-disolvente se incluyen de manera explícita combinando un método de probabilidad de camino obtenido de la bibliografía con una aproximación de tipo Bragg-Williams para las interacciones entre partículas. Admitiendo movimiento iónico no correlacionado se llega a la predicción de que la conductividad eléctrica, tratada como función de la fracción volúmica de disolvente, posee un máximo que surge de la competición entre el aumento de la concentración de portadores de carga y la disminución de su movilidad. Cuando esta curva de conductividad se expresa en términos de magnitudes reducidas, la teoría predice un comportamiento universal. La comparación con resultados experimentales para líquidos iónicos y sus mezclas y para disoluciones salinas arroja un acuerdo excelente en lo tocante a esta ley de estados correspondientes. Las desviaciones con respecto al comportamiento universal se explican, cualitativamente, recurriendo a resultados sobre formación de agregados obtenidos en el Capítulo 6.

La conductividad térmica de líquidos iónicos y sus mezclas es el tema central del Capítulo 8. Partiendo de nuevo de la teoría de Bahe-Varela, se recuperan y adaptan conceptos de la teoría de transporte en sólidos cristalinos ya usados extensivamente en la Parte I. Con base en la literatura, se precisa el sentido del concepto de modo normal en un líquido y se analizan estos modos y su extensión espacial para dos líquidos iónicos puros. A continuación se plantea una imagen del líquido iónico correspondiente a la existencia de orden de medio alcance: regiones ordenadas separadas por barreras efectivas. Esta imagen se asemeja a la situación existente en otros sistemas físicos como los sólidos policristalinos y amorfos. Este tipo de estructuras presentan el grado suficiente de orden (en forma de simetría de traslación aproximada en un entorno local) para permitir la existencia de modos vibracionales comparables a fonones. Aquellos de entre estos modos que tengan una longitud de onda mayor que la anchura característica de una barrera podrán propagarse y transmitir calor, mientras que los de longitud de onda pequeña tenderán a estar confinados en un dominio ordenado. Tal mecanismo de transferencia de

calor se conoce como *phonon hopping*. En este capítulo se desarrolla un modelo de conducción térmica basado en el mismo y, mediante algunas hipótesis adicionales que permiten un tratamiento analítico, se llega a resultados cualitativos para líquidos iónicos puros, así como a una fórmula de interpolación sin parámetros para sus mezclas con disolventes. La comparación con datos experimentales para mezclas de líquidos iónicos basados en el anillo imidazolio con agua y etanol pone de relieve la gran importancia de la nanoestructura del líquido: mientras que en mezclas con agua un tratamiento del disolvente basado en sus propiedades como sistema masivo arroja un excelente acuerdo con la experiencia, para alcoholes es claramente necesario un estudio más sofisticado como función de la concentración. Se interpreta este hecho como reflejo de la rápida aparición de agregados de agua en el seno de la mezcla y de su ausencia en el caso del alcohol.

Se cierra esta tesis con un breve capítulo en el que se resumen, de manera esquemática, las principales conclusiones.

Agradecimientos

Es frecuente escuchar que, mirando hacia atrás, el tiempo vivido siempre parece corto. Tras mi paso por la Facultad de Física, no podría estar más en desacuerdo: subjetivamente, aquel día de septiembre de 2002 en que entré en ella queda siglos atrás, y se me antoja que este documento acaso no recoja cinco años, sino toda una vida, de trabajo. Por ello, no son pocas las personas a las que en justicia debo mencionar aquí por haberme facilitado el llegar hasta este punto:

- Mis directores, que no sólo me han transmitido el "mester de investigación" sino un apoyo constante en lo científico y en lo humano.

- El Dr. Natalio Mingo, mi supervisor en el CEA de Grenoble y gran experto en el transporte térmico, por haberme aceptado bajo su tutela y por la desinteresada atención y la ayuda prestadas durante mis meses de estancia.

- Mis compañeros del Grupo de Nanomateriales y Materia Blanda, entre los que no puedo pasar sin señalar a Verónica Fuentes, mi primera compañera de despacho, a Roberto Longo, amigo y maestro en todo lo relativo a la DFT, y a Trinidad Méndez, junto a quien he tenido la oportunidad de echar a andar el trabajo de simulación de líquidos iónicos.

- El profesor Óscar Cabeza y su grupo experimental de la Universidade da Coruña, que me han permitido usar sus datos sobre líquidos iónicos.

- Los profesores J. Ferrer (Universidad de Oviedo), J. P. K. Doye (Universidad de Oxford) y R. M. Lynden-Bell (Universidad de Cambridge), con quienes he aprendido mucho durante visitas de investigación más breves.

- Todos aquellos, aparte de los ya citados, que han firmado conmigo alguna publicación, contribuyendo con sus conocimientos a mi evolución científica.

- Los equipos de desarrollo de SIESTA y GROMACS, por poner a disposición de la comunidad de investigadores estos potentes conjuntos de herramientas sin coste alguno, así como los responsables de la creación de Python y su ecosistema de bibliotecas científicas, empleadas exhaustivamente en todas las etapas del proceso que ha llevado a esta tesis.
- El personal de la USC, especialmente Minia García y Benito Doce, por su eficaz gestión, y "sir" Jan Coleman, por su asesoramiento lingüístico y su puesta en valor de la palabra *artifactually*.
- Mis amigos en España y en Francia, y entre ellos aquellos sin los cuales no hubiese podido viajar: Xesús Bendaña, Lucía González Gato y Zhao Wang.
- Ana, fuente inagotable de momentos felices, mi familia, a quienes debo todas las oportunidades que he tenido en mi vida, y también mi familia política, que ha supuesto para mí un gran apoyo en Santiago.

También deseo agradecer al Centro de Supercomputación de Galicia las numerosas horas de procesador puestas a mi disposición. Por imperativo legal, también agradezco a las distintas encarnaciones del Ministerio de Educación su financiación de mi trabajo mediante una siempre menguante beca del programa de Formación de Profesorado Universitario (FPU).

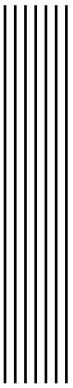

Contents

1 Motivation and purpose

> Le pregunté qué sabía de la Odisea. La práctica del griego le era penosa; tuve que repetir la pregunta.
> *Muy poco*, dijo. *Menos que el rapsoda más pobre. Ya habrán pasado mil cien años desde que la inventé.*
>
> *El Inmortal*
> Jorge Luis Borges

Since the development of quantum mechanics there has been a growing awareness [1] of the exciting possibilities offered by the control of the structure of matter at length scales $\lesssim 1\ \mu$m. However, it is commonly accepted that the emergence of the branches now known as nanoscience and nanotechnology did not take place until the 1980s, influenced by the availability of tools like the scanning tunneling microscope and the systematic study of some of the first nanostructures [2]. Some landmarks worth mentioning are the discovery in 1984 of "magic numbers" corresponding to full electron shells in alkali metal clusters [3], the identification in 1985 of the C_{60} molecule by H. W. Kroto, R. F. Curl and R. E. Smalley and its synthesis in crystalline form [4, 5] and, much more recently (in 2004), the synthesis of graphene by A. Gein and K. Novoselov [6]. Unsurprisingly, the last two contributions to science were awarded the 1996

and 2010 Nobel Prizes in Chemistry and Physics, respectively. In any case, there is little doubt that we are now in the midst of a "nanorevolution" that has put systems between the molecular and the macroscopic length scales in the focus of much of the research being done today in academy and industry alike. Those efforts are likely to deliver results applicable in fields as diverse as electronics, medicine and automotive science, to cite only three, in a short period of time.

Naturally, the opportunities offered by the varied and unfamiliar behaviour shown by nanoscopic systems come at a price: neither the highly successful macroscopic theories developed in the 19th century for bulk materials nor the very precise, but expensive, quantum-mechanical calculation techniques often employed for single molecules are applicable. Thus, this huge class of systems constitutes one of the most challenging frontiers of physics today even though, as mentioned above, it attracts a huge number of man-hours of work [7, 8]. At this stage, it is not unusual for each new concrete result to require, if not a completely new methodology, at least an ingenious combination of existing elements; indeed, to date there exist very few procedures that can be considered general.

Although a detailed understanding of the static and equilibrium properties of nanosystems is an essential first step, it is unlikely to suffice for any practical use; in fact, transport processes are at the core of some of the most promising proposed applications of nanotechnology. Perhaps the most well-known of those is nanoelectronics [9], which depends on the synthesis of nanostructures with electronic transmission properties resembling those of ordinary electronic components such as transistors, but it is not at all the only one. Sometimes, the ability to design materials with properties beyond those which can be attained from conventional bulk systems is the main driving force behind whole branches of research in nanomaterials. This is the case, for instance, with nanostructured electrolytes and electrodes for batteries and solar cells. Going beyond electric properties, thermal management [10] will be a necessary concern in nanodevices just like in everyday human-scale machines, and elements able to function as heat sinks must be developed. Another area where there are high hopes for nanoscience lies at the intersection between thermal and electric transport. The theoretical basis for the obtention of electric power from thermal gradients without the use of moving parts, *i.e.*, of thermoelectric generators, has long been known [11], but no bulk material discovered thus far does even come close to have the required properties to be competitive

with conventional systems, such as turbines, in practical applications beyond some niche uses like space probes; however, there are reasons to believe that this limitation can conceivably be overcome by means of nanostructuring.

This work intends to make a contribution to the fields of thermal and electric transport in nanostructured systems using a variety of theoretical and computational approaches. Two particular kinds of systems of technological relevance were selected: semiconductor nanostructures and ionic liquids. Regarding the former, the same properties that have led to the omnipresence of silicon and other semiconductors in technological products make them *a priori* ideal candidates for diverse nanotechnological applications, although graphene may be a viable alternative in many cases. By way of example, the exponential growth of computing power predicted by Moore's law, an important factor behind the rapid change in lifestyle experimented by the western world in the last decades, depends on industry's ability to build ever smaller integrated circuits, rapidly approaching the nanoscale. With respect to ionic liquids, these flexible solvents seem bound to become the reaction media of choice for many chemical processes [12–14], and in particular hold great promise for electrochemistry in a time when progresses in energy storage are critical to the advance of technology. Even though they are usually employed in bulk quantities, the particular nanostructure of ionic liquids is at the source of their measurable properties and must therefore also be the starting point in their study.

Following this plan, the present thesis is structured in two parts, each dealing with one of these kinds of system. Part I concerns itself with semiconductor nanowires and organic-inorganic semiconductor heterostructures. A survey of the relevant literature reveals that, regarding these materials, electronic transport is better understood than heat transport, so the work reported here is focused on thermal and thermoelectric processes. The tools employed are both classical molecular dynamics [15] and quantum non-equilibrium Green's function methods [16, 17]. As regards Part II, its purpose is to lay the groundwork for a theory of electric and thermal conduction in ionic liquids inscribed in the Bahe-Varela pseudolattice framework [18]. As it is often the case when studying liquid-state systems, the lack of a reference model from which to draw conclusions through analytic methods, comparable to the ideal gas or to the perfectly periodic crystalline solid, makes the development of a theory based purely on first principles substantially challenging so, instead of this, descriptive models with an empiric component are usually employed. Part II of this

work is no exception, and it relies on fits to and comparisons with experimental data.

The discussion of these topics aims to be self-contained to an extent; therefore, the original results are preceded in each case by a brief survey of the state of the art and a summary of the methods used. For the convenience of readers, after each chapter a list containing only those references used therein is included, in addition to the full list of references that can be found as part of the back matter.

References

1. Feynman, R. *Eng. Sci. Mag.* **23,** 22 (1960).
2. Eric Drexler, K. *Engines of Creation: The Coming Era of Nanotechnology* (Anchor Books, New York, 1986).
3. Knight, W. D., Clemenger, K., de Heer, W. A. & Saunders, W. A. *Phys. Rev. Lett.* **52,** 2141 (1984).
4. Kroto, H. W., Heath, J. R., O'Brien, S. C., Curl, R. F. & Smalley, R. E. *Nature* **318,** 162 (1985).
5. Zhang, Q. L., O'Brien, S. C., Heath, J. R., Liu, Y., Curl, R. F., Kroto, H. W. & Smalley, R. E. *J. Phys. Chem.* **90,** 525 (1986).
6. Novoselov, K. S., Geim, A. K., Morozov, S. V., Jiang, D., Zhang, Y., Dubonos, S. V., Grigorieva, I. V. & Firsov, A. A. *Science* **306,** 666 (2004).
7. Hullman, A. *The Economic Development of Nanotechnology — An Indicators Based Analysis* tech. rep. (DG Research and European Commision, 2006).
8. Ratchev, S. & Turitto, M. *Vision for Micro- and Nano-Manufacturing* tech. rep. (European Technology Platform for Micro- and Nano Manufacturing (MINAM), 2008).
9. Despotuli, A. & Andreeva, A. *Int. J. Nanosci.* **8,** 389 (2009).
10. Balandin, A. A. *IEEE Potentials* **21,** 11 (2002).
11. Nolas, G. S., Sharp, J. & Goldsmid, H. J. *Thermoelectrics* (Springer, New York, 2001).
12. Rogers, R. D. & Seddon, K. R. *Ionic Liquids: Industrial Applications for Green Chemistry* (American Chemical Society, Washington, DC, 2002).

13. Rogers, R. D. & Seddon, K. R. *Ionic Liquids as Green Solvents: Progress and Prospects* (American Chemical Society, Washington, DC, 2003).

14. Wasserscheid, P. & Welton, T. *Ionic Liquids in Synthesis* 2nd (Wiley-VCH, New York, 2008).

15. Griebel, M., Knapek, S. & Zumbusch, G. *Numerical Simulation in Molecular Dynamics: Numerics, Algorithms, Parallelization, Applications* (Springer, New York, 2007).

16. Economou, E. N. *Green's Functions in Quantum Physics* (Springer-Verlag, New York, 1990).

17. Datta, S. *Quantum Transport: Atom to Transistor* second (Cambridge University, New York, 2005).

18. Varela, L. M., García, M., Sarmiento, F., Attwood, D. & Mosquera, V. *J. Chem. Phys.* **107,** 6415 (1997).

Part I

Semiconductor nanostructures

2 Molecular dynamics predictions of the thermal conductivity of thin InP nanowires

> So many of the properties of matter, especially when in the gaseous form, can be deduced from the hypothesis that their minute parts are in rapid motion, the velocity increasing with the temperature, that the precise nature of this motion becomes a subject of rational curiosity.
>
> *Illustrations of the Dynamical Theory of Gases*
> James Clerk Maxwell

2.1. Introduction

Nanowires are quasi-one-dimensional structures whose transverse cross section seldom exceeds the thousands of square nanometers, but which can reach the centimeters in length [19]. Although some organic structures suit these requirements, and inorganic nanowires have also been found in nature, it has been only in the last few decades that the ability to create synthetic nanowires has become widespread. Accordingly, in recent years these nanostructures have attracted considerable research effort for both theoretical reasons — the desire to understand how electronic, optical, thermal and mech-

anical properties are affected by the reduction of dimensionality — and with a view to their potential technological applications of (see, *e.g.*, Refs. 20–22). Nanowires are obvious candidates for the development of miniaturised versions of devices which, in their non-nanoscale versions, show a similarly large aspect ratio. Examples of this are optical fibres and electronic interconnects. However, nanowires also show unique properties absent from their bulk counterparts, caused by the incomparably greater relevance of quantum confinement and surface effects. One of them is their notable tensile strength [23], which has stimulated research in nanowires as possible additives for structural materials. Transport properties form another important group of attributes of these quasi-one-dimensional structures which can be expected to differ from their values in the bulk.

Currently, scientific and engineering work is well underway to deliver viable nanoelectronic devices, and already two years ago there were direct methods for creating relatively complex and functional silicon-nanowire-based electronic building blocks, such as logic gates [24]. In this context, information on the thermal conductivity of semiconductor nanowires is crucial for the development of new nanoelectronic and thermoelectric devices. Extremely high thermal conductivity is essential if nanowires are to be used as heat sinks in future nanochips [25, 26], and ultralow thermal conductivity, below 1 W/(K m), in conjunction with high electric conductivity and large Seebeck coefficients, if they are to form the basis of efficient thermoelectric refrigerators and power generators [11, 27–29].

Only for a few relatively thick nanowires has thermal conductivity been determined experimentally [30–35]; and because of their relevance to the semiconductor industry, much of this work has been concerned with Si nanowires [30, 34, 35]. Over the temperature range 20 – 320 K, the thermal conductivities of Si nanowires with diameters of 22, 37, 56 and 115 nm have been reported to be about two orders of magnitude smaller than those of bulk Si and to decrease with decreasing nanowire diameter, a trend that is attributed to the concomitant increase in surface/volume ratio, which enhances the scattering of long-wavelength phonons (the dominant heat carriers) by the nanowire boundary [30]. Such possibility will be studied in detail in Chapter 4. The results of theoretical studies [36–38] and computer simulations [39–41] are in qualitative agreement with these experimental findings. For example, in the temperature range 200 – 500 K classical molecular dynamics (MD) simulations of Si nanowires with square cross sections of side 1.61 – 5.35 nm, performed

by Volz and Chen [39] using the Green-Kubo method [42] in conjunction with the Stillinger-Weber (SW) model of Si-Si interactions [43, 44], found thermal conductivities of 1 – 5 W/(m K) (one to two orders of magnitude smaller than the corresponding bulk value) that decreased with nanowire diameter. Interestingly, however, MD simulations using the "direct" method [42] with the SW potential show that for tetrahedral Si nanowires oriented along the [111] direction thermal conductivity decreases as wire diameter is reduced from 7.7 to 3.4 nm, but then increases as diameter is further reduced to 1.46 nm; this is attributed to a more subtle phonon confinement effect manifested in the fact that the excited mode of lowest frequency and longest wavelength shifts to higher frequency [41]. The thermal conductivities of Si_{34}- and Si_{46}-clathrate nanowires increase with decreasing diameter over the whole range investigated (2 – 8 nm), although only very slightly [41]; the similar but more pronounced diameter dependence of the room-temperature specific heat of thin Si [111] nanowires that is predicted by lattice dynamics theory and MD/SW simulations [45] has likewise been attributed to the combination of phonon confinement and the increase in specific free surface area [45].

In the light of the above results, Si-based nanowires seem unlikely to be very suitable for the applications mentioned earlier, although room-temperature thermal conductivities of 0.75 W/(m K) have been achieved with heavily doped Si [46]. An alternative nanowire material that has attracted considerable attention is InP. InP nanowires have been synthesised by several methods [47–52], and their energy band gaps and photoluminescence images and spectra have been determined experimentally [53, 54]. Furthermore, $p-$type doped InP nanowires function as light-emitting diodes and field effect transistors when assembled with $n-$type nanowires [55, 56], and the impurity state responsible for current flow in Zn-doped InP nanowires has been characterised [57] by first-principles calculations using PARSEC [58, 59], a real-space implementation of density functional theory and pseudopotentials. However, apparently hitherto there have been no systematic experimental or computational studies of the thermal conductivity of InP nanowires, although theoretical calculations using phonon dispersion relations based on the somewhat crude Harrison potential [60] have been performed for wires 35 – 10000 nm thick at 300 K by Mingo and Broido [61] and Mingo [62].

In the work described in this chapter the thermal conductivity of hexagonal InP nanowires was investigated by means of classical MD simulations using a potential proposed by Branício and Rino [63] that, like the SW potential for Si

[43] and the potentials developed by Vashishta and coworkers for other semiconductor materials [64–67], comprises both two-body and three-body terms. This potential has proved to be very useful for interpreting the vibrational properties and structural phase transformations of bulk InP under pressure [63, 68], but this is the first time that it has been applied to nanowires. Given the lack of systematic experimental studies of the thermal conductivity of InP nanowires, the references taken for comparison were Mingo's theoretical results [61, 62], and experimental [30, 35], theoretical [36–38] and computational [39–41] results for thin Si nanowires.

The thermal conductivity κ of a material is defined as the phenomenological coefficient which links the heat current $\vec{j}_Q$ to the temperature gradient ∇T under a particular set of constraints. In other words, for a particular choice of thermodynamic forces that includes ∇T, κ is defined by the relation

$$\vec{j}_Q = -\kappa \nabla T, \tag{2.1}$$

known as Fourier's law, when every other thermodynamic force is zero. Depending on the symmetry properties of the material, κ can be an order-2 tensor or even depend on the position. It must be noted here that throughout this work the expression "heat current" will be used to denote an energy transfer per unit time and unit area, as opposed to "heat flux", its integral over a finite surface, even though the opposite convention can also be found in the literature. The application of this terse formula to nanoscale problems is fraught with conceptual difficulties, of which at least three main sources can be identified:

What is heat? In most modern formulations of thermodynamics heat it not a central concept but rather a historical burden, as the principles on which this theory is based are introduced without making reference to it. In particular, the concept of entropy, concomitant with the notion of irreversibility, arises in the context of the second law as a consequence of the order induced by the relation of adiabatic accessibility. Under adiabatic constraints, the first law establishes that the work done by a system is equal to the variation of the internal energy, in analogy with the behaviour of a purely mechanical system. Under non-adiabatic conditions, heat is simply the term that is necessary to introduce in the equation of balance to fulfil the conservation of energy. In fact, in the well-known framework proposed by Lieb and Yngvason [69] as the culmina-

tion of the approach to the second law pioneered by Carathéodory [70] and largely developed by Buchdahl [71], Boyling [72] and others, heat is neither used nor even defined. Experimentally, there is no way to measure heat directly; instead, an energy transfer is inferred by its effects, and then classified as heat by virtue of the constraints put in place for the experiment. Unfortunately, constraints that arise very naturally in macroscopic hydrostatic systems (constant volume, for instance) have a more nebulous interpretation in the nanoscale.

Can a meaningful ∇T be defined? Clearly, temperature cannot be considered from a purely mechanical point of view. The non-mechanical quantity from which it is derived, entropy, is well-defined for equilibrium and non-equilibrium, large and small, hamiltonian and non-hamiltonian, and physical and non-physical systems alike, as long as they can be assigned a set of possible states, but only from a global perspective. The view that it can be used as a local potential from which to derive thermodynamic forces has been described as purely metaphoric [73] and depends on an approximate decoupling between state variables for different volume elements.

Can the linear regime be expected to hold? As mentioned above, Fourier's law is purely phenomenological in nature, and *a priori* expected to be most useful when $|\nabla T|$ is suitably small. However, a drop of a few kelvin over a length of 100 nm leads to a temperature gradient in the order of 10^7 K/m, enormous by macroscopic standards.

The in-depth exploration of these problems falls outside the scope of this thesis, so they will only be treated insofar as decisions had to be made in order to resolve the ambiguities that they introduce. However, it is important to stress that the theoretical foundations of non-equilibrium thermodynamics are still an area of active research, and that simulation results can only be fully justified *a posteriori*, by comparison with experiment. In practice, heat is defined as the transfer of energy not due to a change in the deformation coordinates of the participating systems (parameters of their hamiltonians in quantum descriptions) and a hypothesis of local equilibrium is introduced in order to be able to define a local temperature. How these hypotheses are implemented depends on the set of techniques available.

At room temperature, nanowires resemble a crystalline solid in that they preserve long-range order in spite of atomic movement. As a consequence, heat transfer is due both to electronic movement and to lattice vibrations, which can be described in terms of phonons. Since electrons take part in both electric and thermal transport, the relative importance of the lattice and electronic contributions to the thermal conductivity depends on the value of the electric conductivity σ. In metals, where thermal conduction is dominated by electrons, both conductivities are related by the Wiedemann-Franz law,

$$\frac{\kappa}{\sigma} = L_L T, \tag{2.2}$$

where L_L is known as the Lorenz number. In the framework of free-electron theory, L_L has a universal value of $2.44 \cdot 10^{-8}\ \frac{\mathrm{W\Omega}}{\mathrm{K^2}}$. In practice, however, there are values of L_L which afford a better fit to experimental data for each particular metal [74]. It must also be noted that the Wiedemann-Franz law can be violated in the nanoscale, either because of the important role played by fluctuations [75] or when the electron gas is close to a phase transition [76].

The case of semiconductors is more complex as both contributions to the thermal conductivity must be taken into account. A detailed study by Shanks *et al.* [77] concludes that the thermal conductivity of Si up to 1000 K can be attributed almost exclusively to phonons; likewise, Kugman and Stegmeier [78] point out that the contribution of charge carriers to the thermal conductivity of InP is negligible at least up to 800 K. However, this is not necessarily the case for nanowires. A theoretical study based on the Boltzmann transport equation [61] predicts the existence of a crossover, at a width between approximately 5 and 10 nm depending on the material, below which the electronic contribution becomes dominant. The study of this part of the total thermal conductivity is closely tied to the study of electric transport. Simple approximations like the Wiedemann-Franz law can be used to explain experimental results, but in order to achieve predictive power *ab-initio* techniques are required, which at this point are still very limited in the number of atoms they can handle. For this reason, the work contained in this chapter is limited to the study of the lattice contribution to κ.

Phonons are spin-1 bosons, and accordingly their occupation numbers follow the Bose-Einstein distribution at thermal equilibrium. Computational techniques that take into account their quantum character will be employed in later chapters. Nevertheless, when the temperature is high enough, the

internal energy of a boson gas is so large that the effects introduced by their indistinguishability become minor by virtue of the fact that there are few bosons in each quantum state, a situation known as the dilute limit. An estimate of the temperature at which this happens can be obtained from the rather crude Debye model, in which all phonons have linear dispersion relations and a frequency cutoff ω_D is introduced in order to ensure the correct number of vibrational modes. Denoting Boltzmann's constant and the reduced Plank constant by k_B and $\hbar$ respectively, it is easy to show that when $T > T_D = \hbar\omega_D/k_B$, the Debye temperature, the results of the Debye model approximate those of the classical gas of harmonic oscillators. For Si and InP, the values of T_D are 645 K and 425 K, respectively [74].

From a computational point of view, treating a system classically has some important advantages, because the available methods are less time-consuming and thus allow larger sets of atoms to be considered. However, the Debye temperatures mentioned in the previous paragraph are well above room temperature, giving the impression that such treatment would not lead to useful results. Fortunately, the vibrational modes most relevant for thermal conduction lie well below the Debye frequency and are, therefore, well populated at much lower temperatures — around 150 K for Si, according to Ref. 79. Thus, a classical simulation method was chosen to calculate the thermal conductivity of InP nanowires in the temperature range between 100 and 700 K. In particular, after a revision of the literature, an MD approach was chosen instead of a Montecarlo method, more adapted to the modelling of particle diffusion. MD methods are based on the numerical integration of Newton's equations of motion and the analysis of the resulting trajectories, and as such they require three ingredients: an intermolecular potential, an integration method and an expression of the variable under study in terms amenable to classical mechanics.

2.2. Intermolecular potential

As regards the first of these elements, there are plenty of potentials in the literature, ranging from the simplest ones (Lennard-Jones or hard spheres, for instance) to those with hundreds of parameters (such as ReaxFF [80]). The functional form of these potentials usually comes from theoretical insights about the dominant interactions in the systems they try to describe, but the precise values of their parameters are often fitted so that they afford predic-

tions for some properties of the material as close as possible to their true values. Thus, MD potentials are semiempirical. Most often, neither the system nor the properties to whose study these potentials are applied are precisely those to which its parameters were fitted, so transferability problems can arise. In particular, potentials developed for use in bulk systems are not always appropriate for studies of nanostructures with few atoms such as clusters [81, 82].

Even though the nanowires studied here comprise tens of thousands of atoms and show some bulk-like properties, in order to avoid transferability problems it is advisable to select a potential which has been parameterised taking into account some characteristics related to thermal transport. The choice for this work was the Branício-Rino potential for InP [63, 68], whose parameters were fitted to describe the lattice constants, elasticity moduli and vibrational density of states of this material, as well as its transition between the zinc-blende and halite structures. This potential contains two- and three-body contributions:

$$V = \sum_{i<j} V_{ij}^{(2)}\left(r_{ij}\right) + \sum_{i<j<k} V_{ijk}^{(3)}\left(\vec{r}_{ij}, \vec{r}_{ik}\right), \tag{2.3}$$

where i and j are indices that run over particles, $\vec{r}_{ij} = \vec{r}_i - \vec{r}_j$ is a vector between the positions of both particles and r_{ij} is its module. Their functional forms, based on the ones proposed by Vashishta *et al.* [64] for SiO_2, are

$$V_{ij}^{(2)}(r) = A_{ij}\left(\frac{\sigma_i + \sigma_j}{r}\right)^{\eta_{ij}} + \frac{Z_i Z_j}{r} e^{-\frac{r}{r_{1s}}} - \frac{\frac{1}{2}\left(\alpha_i Z_j^2 + \alpha_j Z_i^2\right)}{r^4} e^{-\frac{r}{r_{4s}}} - \frac{w_{ij}}{r^6} \tag{2.4a}$$

$$V_{ijk}^{(3)}\left(\vec{r}_{ij}, \vec{r}_{ik}\right) = B_{ijk}\, exp\left(\frac{\zeta}{r_{ij} - r_0} + \frac{\zeta}{r_{ik} - r_0}\right) \frac{\left(cos\,\theta_{ijk} - cos\,\theta_0\right)^2}{1 + C\left(cos\,\theta_{ijk} - cos\,\theta_0\right)^2}. \tag{2.4b}$$

As usual in these calculations, the two-body component is assumed to be zero when r is beyond a cutoff radius r_{cut}, and the three-body part is considered nil when either r_{ij} or r_{ik} are greater than a certain r_0. These two radii act as another pair of parameters of the potential. The following is a brief description of each term in the two equations above:

$V^{(2)}$**: First term:** steric repulsion between atoms due to overlap between their electron clouds at short distances. σ_i plays the role of a radius for the excluded volume around atom i.

Second term: Coulomb interaction between atoms in the lattice, which carry partial charges because of the polar nature of the In-P bond. It is expressed as a function of the effective atomic charges Z_i. As expected in an ionic system, there is an exponential screening of this interaction.

Third term: screened interaction between charges and induced dipoles, due to the atomic polarizabilities α.

Fourth term: attractive van der Waals interaction, in the same conventional form used in the Lennard-Jones potential.

$V^{(3)}$**: Radial part:** energy change associated to bond stretching. It is assigned a non-zero value only for P-In-P or In-P-In terns, the kinds present in a completely heterocoordinated crystal.

Angular part: θ_{ijk} is the angle between $\vec{r}_{ij}$ and $\vec{r}_{ik}$, *i.e.*, $cos\,\theta_{ijk} = \vec{r}_{ij} \cdot \vec{r}_{ik} / \left(r_{ij} r_{ik}\right)$, so this term ensures that an angle θ_0 is energetically favoured. θ_0 is set to the angle between two vertices of a tetrahedron and its centre, which makes the zinc-blende structure a minimum of the potential.

The optimal values for all the parameters where kindly provided by Prof. J. P. Rino, and are reproduced in Table 2.1.

An important point about the use of the Branício-Rino potential in this work is that three layers of fixed atoms were always placed around the nanowire. These rigid boundary conditions are needed to ensure the structural stability of the system, since unless the mobile atoms at the centre of the nanowire have a bulk-like environment, like the one for which the potential was parameterised, there is a certain probability that they escape from their finite potential well, leading to the evaporation of the nanowire surface. Fixed layers are not taken into account when computing the cross section of the nanowire. Almost all MD simulations of this kind of system make use of fixed layers [83, 84], which do not introduce significant changes in the results since these atoms do not take part in heat transport (the amplitude of any vibrational mode in these layers is always zero). A comparison between rigid and free boundary conditions, where it is also shown that this technique makes the simulation 65% faster, can be found in Ref. 39. Reasonable agreement between free and rigid boundary conditions is also in detected in Ref. 85. It is worth pointing out that the presence of the fixed layers does not prevent the

Table 2.1 Parameters of the Branício-Rino potential for InP.

$r_{1s} = 4.5$ Å	$B_{In-P-In} = 6.929 \cdot 10^{-19}$ Å	$C = 7$
$r_{4s} = 2.75$ Å	$B_{P-In-P} = 6.969 \cdot 10^{-19}$ Å	$\gamma = 1.0$ Å
$r_{cut} = 6.0$ Å	$\theta_0 = 109.47122\,^\circ$	$r_0 = 3.55$ Å

	In	P
α $\left(\text{Å}^3\right)$	0.0	2.5
σ $\left(\text{Å}\right)$	1.10	1.4412
Z $\left(\frac{e}{2\sqrt{\pi\varepsilon_0}}\right)$	1.21	−1.21

	In-In	In-P	P-P
A_{ij} (J)	$1.7573 \cdot 10^{-19}$	$1.7573 \cdot 10^{-19}$	$1.7573 \cdot 10^{-19}$
W_{ij} $\left(\text{J m}^6\right)$	0.0	$43.276 \cdot 10^{-78}$	0.0
η_{ij}	7	9	7

conservation of energy, because holonomic contraints, such as fixed positions, do not break the time-translational symmetry of the system. Furthermore, rigid boundary conditions make the simulated system resemble a common experimental setting where nanowires are covered by an amorphous coating for added stiffness [86, 87]. An approximate alternative comes from so-called potential boundary conditions [88], which emulate the effect of an infinite number of rigid outer layers. Figure 2.1 shows an InP nanowire with a diameter of $d = 4.15$ nm, comprising six layers of unconstrained atoms and three layers of fixed atoms in the radial direction.

2.3. Integration method

With respect to the method used to integrate Newton's equations

$$\frac{d\vec{r}_i}{dt} = \vec{v}_i \tag{2.5a}$$

$$\frac{d\vec{v}_i}{dt} = \vec{a}_i = -\frac{\nabla_i V}{m_i}, \tag{2.5b}$$

Figure 2.1 InP nanowire with a diameter of 4.15 nm, comprising six layers of unconstrained atoms and three layers of fixed atoms in the radial direction.

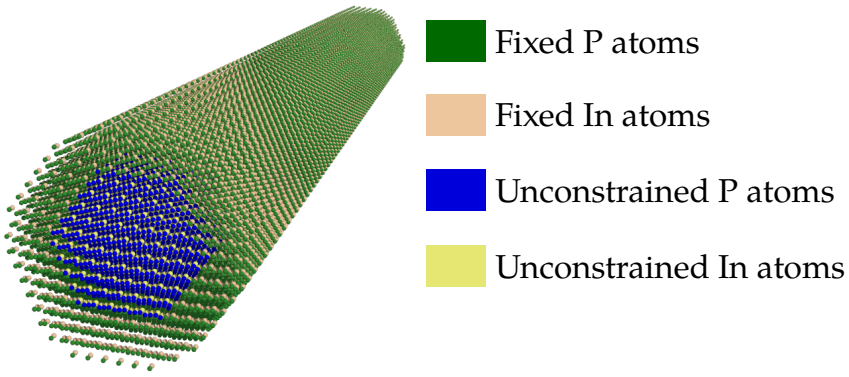

for $i \in \{1, 2 \ldots N\}$, where N is the number of atoms, a possible choice is a standard integration algorithm such as embedded fourth-order Runge-Kutta, but such methods are computationally expensive for large N, especially when the evaluation of V and its derivatives is a costly operation itself — a typical MD program can spend 80 – 90% of its CPU time in this task. Thus, methods that rely only on the first derivatives of V are preferable. Several simple numerical algorithms have been developed that meet this requirement, usually starting with truncated Taylor expansions of $\vec{r}_i$ and $\vec{v}_i$ as functions of time. One of the most popular is the velocity Verlet algorithm [89]:

$$\vec{r}_i(t + \Delta t) = \vec{r}_i(t) + \vec{v}_i(t)\,\Delta t + \frac{\vec{a}_i(t)}{2}(\Delta t)^2 \tag{2.6a}$$

$$\vec{v}_i(t + \Delta t) = \vec{v}_i(t) + \frac{\vec{a}_i(t) + \vec{a}_i(t + \Delta t)}{2}\Delta t, \tag{2.6b}$$

for a time step Δt. The velocity Verlet method is second-order, as the leading term in its global error is proportional to $(\Delta t)^2$. In spite of its great simplicity, this algorithm has a number of desirable properties, such as stability, symplecticity (conservation of volumes in phase space), conservation of linear and angular momentum and temporal reversibility. Taken together, these properties mean that the results of its use in physical simulations can be trusted as long as the potential is well-behaved and the time step small enough. An ad-

ded feature of the algorithm is that it only needs memory to store the positions, velocities and accelerations at one time step. There are symplectic integration methods of higher orders [90] for systems whose atoms get too close to divergences of the potential, but since this is not the case in a crystalline structure such as a nanowire, the velocity Verlet algorithm was considered a good choice for this work. Some tests revealed that $\Delta t = 10$ fs offered a good compromise between speed and long-term conservation of energy and heat capacity. The latter magnitude was calculated from two statistical moments of the kinetic energy E_{kin} [91] as

$$C_V = \frac{k_B}{1 + \left(\frac{2}{3N} - 1\right) \langle E_{kin} \rangle \left\langle E_{kin}^{-1} \right\rangle}. \tag{2.7}$$

2.4. Calculation of the thermal conductivity

There are three main families of methods for calculating the thermal conductivity of a system from MD simulations: equilibrium methods, non-equilibrium "direct" methods and methods based on homogeneous non-equilibrium molecular dynamics (HNEMD). Equilibrium methods make use of a Green-Kubo relation to compute thermal conductivity from the time autocorrelation function of the thermal current. If the long axis of the nanowire is taken as the z direction, the appropriate expression is

$$\kappa = \frac{V}{k_B T^2} \int_0^\infty \left\langle j_Q^{(z)}(0)\, j_Q^{(z)}(t) \right\rangle dt, \tag{2.8}$$

where V is the volume of the system. In practice, the upper limit of this integral must be substituted by a time $M\Delta t$ large enough that the autocorrelation in the integrand is close to zero at time step M. Moreover, the statistical average over the equilibrium ensemble must be replaced with a time average, leading to a completely discrete approximation to Eq. (2.8):

$$\kappa = \frac{V\Delta t}{k_B T^2} \sum_{m=1}^{M} \frac{1}{P-m} \sum_{n=1}^{\tau-m} j_Q^{(z)}\left[(m+n)\,\Delta t\right] j_Q^{(z)}(n\Delta t), \tag{2.9}$$

for a total simulated time $P\Delta t$. In order to have an MD approximation to the thermal current density, each atom in the system is conceptually assigned a part ε_i of the total energy. At equilibrium, the average thermal current per unit area towards the positive direction of the OZ axis measured at a surface

$z = z_0$ must compensate the energy loss of those particles on the negative side, so

$$\begin{aligned} j_Q^{(z)}(z_0,t) =& \frac{1}{A}\int_{z=z_0} j_Q^{(z)}\left(\vec{r},t\right)da = -\frac{d}{dt}\int_{z<z_0}\sum_i \varepsilon_i \delta(z_i - z)\,dz = \\ =& -\frac{d}{dt}\sum_i \varepsilon_i \Theta(z_i - z_0) = -\sum_i \frac{d\varepsilon_i}{dt}\Theta(z_i - z_0) - \sum_i \varepsilon_i v_i^{(z)} \delta(z_i - z_0), \end{aligned} \tag{2.10}$$

where Θ is a step function and A the cross-sectional area of the nanowire. In order to get the volume-averaged thermal current that appears in Eq. (2.9) the only operations remaining are an integration along the z direction and a division by the length L of the nanowire:

$$\begin{aligned} j_Q^{(z)}(t) =& \frac{1}{L}\int_0^L j_Q^{(z)}(z_0,t)\,dz_0 = \frac{1}{L}\int_0^L \left[-\sum_i \frac{d\varepsilon_i}{dt}\Theta(z_i - z_0) - \sum_i \varepsilon_i v_i^{(z)}\delta(z_i - z_0)\right]dz_0 = \\ =& \frac{1}{V}\sum_i \left(-z_i\frac{d\varepsilon_i}{dt} - v_i^{(z)}\varepsilon_i\right) = -\frac{1}{V}\sum_i \frac{d(z_i\varepsilon_i)}{dt}, \end{aligned} \tag{2.11}$$

and similar expressions hold for the other components of this vector. Therefore, there is an energy flux across a surface whenever either some particles cross it carrying their part of the energy with them (a process described by the second term in the right-hand side of Eq. (2.10)) or the energy of the particles at one side is modified (described by the first term). For a two-body potential, the definition of ε_i is simple: each atom is assigned its kinetic energy and half of the potential energy associated to its interactions with other atoms. However, when a three-body contribution must also be taken into account, apportioning the energy becomes a much more complicated problem whose solution is arbitrary to some extent. Two possible criteria are distributing the energy of a triplet of atoms equally among them or assigning all of it to the central atom, for instance. Fortunately, the effect of this choice on the result is minimal and falls well withing the uncertainty range of the calculated conductivities [42]. Under the first of the two criteria mentioned, the final expression of the thermal current density is

$$\vec{j}_Q = \frac{1}{V}\left[\sum_i \vec{v}_i \varepsilon_i + \frac{1}{2}\sum_{(i,j)\in \text{pairs}} \vec{r}_{ij}\left(\vec{F}_{ij}\cdot\vec{v}_i\right) + \sum_{(i,j,k)\in \text{triplets}} \vec{r}_{ij}\left(\vec{F}_{jik}\cdot\vec{v}_j\right)\right] \tag{2.12a}$$

$$\varepsilon_i = \frac{1}{2}m_i\left|\vec{v}_i\right|^2 + \frac{1}{2}\sum_{j\left|(i,j)\in \text{pairs}\right.} V_{ij}^{(2)}\left(r_{ij}\right) + \frac{1}{6}\sum_{j,k\left|(i,j,l)\in \text{triplets}\right.} V_{ijk}^{(3)}\left(\vec{r}_{ij},\vec{r}_{ik}\right). \tag{2.12b}$$

The fact that no temperature gradient needs to be applied gives equilibrium methods a certain theoretical appeal. They are also useful when studying anisotropic systems, since (2.8) can be straightforwardly generalised to any component of the conductivity tensor. However, they demand very long equilibration times and, even so, the precision they yield is quite modest ($\sim$ 20% uncertainty). On a more fundamental level, there are several possible definitions of heat current in addition to Eq. (2.11) and, as discussed in Ref. 92, each of them affords a different autocorrelation function. This is a reflection of the aforementioned problems with the concept of heat. Moreover, in order to obtain physically meaningful results, it seems necessary to filter out the high-frequency components of the autocorrelation function [92] using a somewhat arbitrary cutoff frequency.

An alternative to equilibrium methods is offered by HNEMD [93]. In this framework, a fictitious force F_e is applied to the system, chosen in such a way that the Green-Kubo relation (2.8) takes a diagonal form and κ can be shown to be proportional to $lim_{F_e\to 0}\left\langle j_Q^{(z)}\right\rangle/F_e$. Even though they are mathematically complex and require especial integration schemes [94], HNEMD methods are the best alternative available in terms of efficiency [95]. However, their generalisations to multicomponent systems and many-body potentials have only been developed recently [95, 96] and cannot be considered as proven as more traditional methods.

In the light of the shortcomings of Green-Kubo and HNEMD methods, a direct non-equilibrium approach was deemed as preferable. To keep the nanowire in a non-equilibrium steady state, two areas of the nanowire must be defined as thermostats. From that point, two routes are possible: either the temperatures of those thermostats can be kept fixed and the thermal current calculated using an expression such as Eq. (2.12), or the energy can be kept fixed and the temperature gradient calculated instead. The second option offers the advantage of being independent of any particular expression of the thermal current, so it was the one implemented in this case. Figure 2.2

Figure 2.2 Scheme of a nanowire in a steady state.

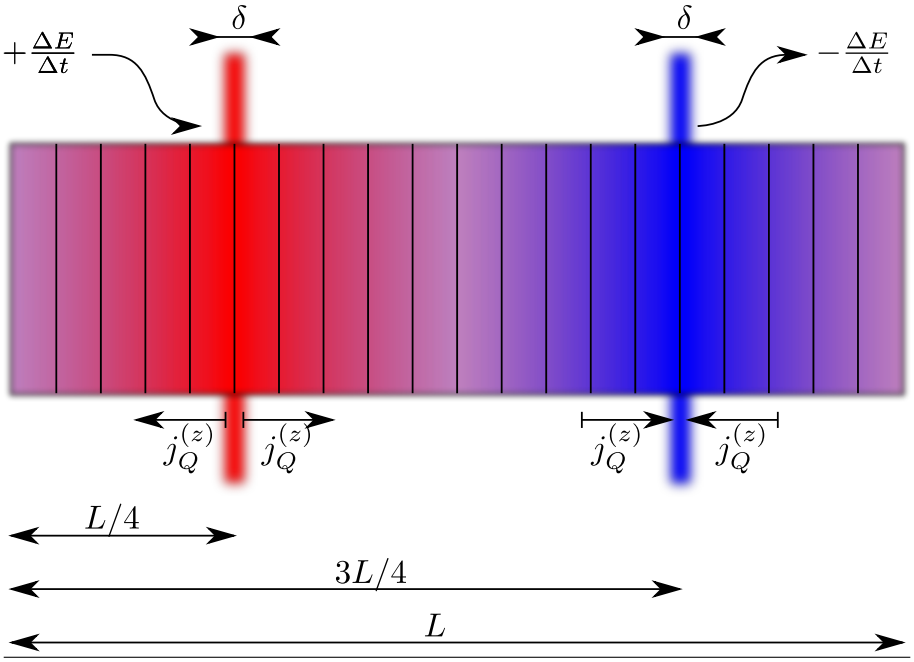

shows a schematic drawing of a nanowire in this situation. The system was divided in a number n_s of segments of equal length along its long axis, so that the I-th segment extended from $z = (I-1)\frac{L}{n_s}$ to $z = I\frac{L}{n_s}$. The temperature of each of these segments was computed using the equipartition theorem

$$T_I(n\Delta t) = \frac{1}{M}\sum_{k=n-M}^{n} \frac{\sum\limits_{\vec{r}_i(k\Delta t)\in I} m_i \left|\vec{v}_i(k\Delta t)\right|^2}{3k_B \sum\limits_{\vec{r}_i(k\Delta t)\in I} 1}, \tag{2.13}$$

which clearly implies a hypothesis of approximate local equilibrium among the atoms in each segment. It must be mentioned that a small number of studies, such as Ref. 97, apply a "quantum correction" to this temperature, based on a Debye model and the Bose-Einstein distribution. It was judged that this correction is based precisely on the application of the equipartition theorem to a quantum problem for which it is known not to hold. On the other hand, MD gives rise to completely classical velocity distributions corresponding to a thermodynamic temperature which matches the prediction of that theorem. Moreover, the Debye model is merely a rather crude approximation to reality. For these reasons, such correction was not applied here. In any case, it has

never been shown to yield better explanations of experimental data, and studies which have assessed its applicability by comparing it with fully quantum methods strongly discourage its use [98].

As depicted in Fig. 2.2, two thermostated plates were placed at $z = L/4$ and $z = 3L/4$ (hot and cold, respectively). At each time step, an amount of energy ΔE was added to the atoms inside the thermostat on the left, and the same amount was removed from those in the thermostat on the right. If, starting from equilibrium at temperature T, this procedure is repeated during enough time steps, a steady state is reached in which the average temperature of the nanowire is still T, but a constant temperature difference exists between those segments closer to the hot thermostat and those further from it. Since in such a state the heat flux along the nanowire must compensate the energy added by the hot plate (or removed by the cold plate) per unit time and area,

$$j_Q^{(z)} = \frac{\Delta E}{2A\Delta t}. \tag{2.14}$$

A factor 2 is present in the denominator of this expression because heat can flow in two directions owing to the use of periodic boundary conditions (PBC) along the OZ axis. Therefore, each segment between the plates had an equivalent outside this region, and the simulation generated twice the amount of data it would if PBC were not applied. The temperature gradient ∇T was calculated by a linear fit of the temperatures of the segments, and its stability through a long number of time steps was used as the criterion by which to determine when the system had reached the desired steady state. In the immediate neighbourhoods of the thermostats there are non-linearities in the temperature profile, so those segments were excluded from the fit. The accuracy of this approach has been favourably compared with that of Green-Kubo methods by several authors [42, 99].

Many procedures to add and remove energy from the atoms in the thermostated regions can be devised, based on the plethora of MD thermostats proposed in the physical literature. Taking into account that the precise reproduction of a Maxwell-Boltzmann distribution is not critical, a simple velocity rescaling thermostat was chosen, as usual in this kind of work [42, 100]. Let i run over the particles in a thermostat and $\vec{v}_{cm} = \sum_i m_i \vec{v}_i / \sum_i m_i$ be the velocity of its centre of mass. At each time step, the following transformation was applied:

$$\vec{v}_i' = \vec{v}_{cm} + \alpha\left(\vec{v}_i - \vec{v}_{cm}\right) \tag{2.15a}$$

$$\alpha = \sqrt{1 \pm \frac{\Delta E}{E_{kin,R}}} \tag{2.15b}$$

$$E_{kin,R} = \frac{1}{2}\sum_i m_i \left|\vec{v}_i\right|^2 - \frac{1}{2}\left(\sum_i m_i\right)\left|\vec{v}_{cm}\right|^2. \tag{2.15c}$$

In Eq. (2.15b), the positive sign refers to the hot thermostat and the negative sign to the cold plate. It is easy to check that this transformation conserves the velocity of the centre of mass and that it changes the kinetic energy by the desired amount.

To complete the description of the simulation method, it remains to specify the initial conditions. These were extracted from an equilibrium simulation with the same systems and potential, $\Delta t = 0.01$ ps and a total simulation time of 10 ns (10^6 steps), enough to stabilise the nanowires at any of the temperatures of interest using the Berendsen thermostat [101], which rescales all the velocities in a gradual fashion until the final temperature T_f is reached:

$$\vec{v}_i' = \left[1 + \frac{\Delta t}{\tau}\left(\frac{T_f}{T} - 1\right)\right]^{\frac{1}{2}} \vec{v}_i. \tag{2.16}$$

τ determines the speed at which the temperature is modified: the larger it is, the longer the simulation must be and the smaller the probability that the system explodes. A value $\tau = 1$ ps was used for this work. After reaching T_f, the nanowires were simulated without any thermostat for an additional 1 ns to eliminate any residual effect of velocity rescaling.

2.5. Characterisation of the phonon densities of states

Comparison of the phonon densities of states (DOS) between different nanowires can help analyse the effect of nanowire width on thermal conductivity. Unfortunately, *a priori* information about phonons is not directly available from MD simulations, which are based on atoms. Therefore, the DOS must be extracted from an analysis of the trajectories. Let us consider a set of N atoms with $3N$ vibrational modes, with frequencies $\{\omega_m\}_{m=1}^{3N}$, around a minimum of the potential so that for energies close to the bottom of that potential well each of the velocities can be expressed in a harmonic

form, $\vec{v}_i(t) = \Re\left\{\sum_{m=1}^{3N} \vec{A}_{i,m} e^{-j\omega_m t}\right\}$. Hence, the statistical average of its time autocorrelation function has the form

$$\begin{aligned}\left\langle \vec{v}_i(0) \cdot \vec{v}_i(t) \right\rangle &= \sum_{m=1,n=1}^{3N} \left\langle \Re\left\{\vec{A}_{i,m} e^{-j\omega_m t}\right\} \cdot \Re\left\{\vec{A}_{i,n}\right\} \right\rangle = \\ &= \frac{1}{2} \Re\left\{ \sum_{m=1}^{3N} e^{-j\omega_m t} \underbrace{\left(\sum_{n=1}^{3N} \left\langle \vec{A}_{i,m} \cdot \vec{A}_{i,n} + \vec{A}_{i,m} \cdot \vec{A}_{i,n}^{*} \right\rangle \right)}_{=:c_m} \right\},\end{aligned} \tag{2.17}$$

so its Fourier transform is proportional to $\sum_{m=1}^{3N} c_m \left[\delta(\omega - \omega_m) + \delta(\omega + \omega_m)\right]$, which is non-zero at the same positions as the phonon DOS, but is modulated by an occupancy factor. In practice, true mechano-statistical averages are not available in MD simulations, so they have to be approximated by averages over time and over particles. Moreover, MD is not a purely harmonic formalism, and anharmonic effects will introduce temperature-dependent variations in this result. Accordingly, instead of δ functions more or less broad peaks will be observed. In any case, a reasonable idea about the form of the phonon DOS can be obtained by studying the squared modulus of the Fourier transform of the normalised velocity autocorrelation function $Z(t)$, *i.e.*,

$$\left|\mathscr{F}[Z(t), \omega]\right|^2 = \left| \mathscr{F}\left[\frac{\left\langle \vec{v}_i(0) \cdot \vec{v}_i(t) \right\rangle}{\left\langle \vec{v}_i(0) \cdot \vec{v}_i(0) \right\rangle}; \omega \right] \right|^2 . \tag{2.18}$$

It is even possible to go further and calculate, by similar methods, the phonon dispersion relation $\omega\left(\vec{k}\right)$. From a theoretical point of view, this can be accomplished by taking the autocorrelation function of a projection of the velocities on the appropriate plane wave, $\vec{v}_{\vec{k}}(t) = \sum_i \vec{v}_i(t) e^{-j\vec{k}\cdot\vec{r}_i(t)}$. In practice, however, this is computationally prohibitive, especially if a fine enough k-point grid is to be sampled in order to compute group velocities or similar variables. For this reason, examples of this technique have only been found in the literature for simple pair potentials [102, 103].

2.6. Computational details

The equilibrium simulation used to generate sets of initial conditions, the non-equilibrium simulation itself and the post-processing part were implemented as Fortran 90 programs for efficiency. The most time-consuming parts

of the code, such as the evaluation of V and its derivatives, where parallelised using OpenMP, a set of directives for multiprocessing on shared-memory platforms. To this end, the systems were divided in as many segments as processors were available, so that the forces on the particles of each segment could be calculated, and their dynamic properties updated, in parallel. Since the Branício-Rino potential is short-ranged, neighbour tables were used in order to avoid the need to re-evaluate cutoffs at each time step. Analytic expressions for the forces where derived from Eqs. (2.4) and implemented:

$$
\begin{aligned}
\vec{f}_{ij} =& -\hat{r}_{ij}\frac{dV_{ij}^{(2)}}{dr_{ij}} = \hat{r}_{ij}\left\{\frac{\eta_{ij}}{r_{ij}}\left(\frac{\sigma_i+\sigma_j}{r_{ij}}\right)^{\eta_{ij}} + \left(\frac{1}{r_{ij}}+\frac{1}{r_{1s}}\right)\frac{Z_iZ_j}{r_{ij}}e^{-\frac{r_{ij}}{r_{1s}}}\right. \\
&\left. -\left(\frac{4}{r_{ij}}+\frac{1}{r_{4s}}\right)\frac{\frac{1}{2}\left(\alpha_iZ_j^2+\alpha_jZ_i^2\right)}{r_{ij}^4}e^{-\frac{r_{ij}}{r_{4s}}} - \frac{6}{r_{ij}}\frac{w_{ij}}{r_{ij}^6}\right\} \\
\vec{f}_{ijk} =& -\nabla_i V_{ijk}^{(3)} = -\vec{f}_{jki} - \vec{f}_{kij} \\
\vec{f}_{jki} =& -\nabla_j V_{ijk}^{(3)} = -\frac{AX\zeta}{\left(r_{ij}-r_0\right)^2}\hat{r}_{ij} - \frac{2A}{Yr_{ij}}\left(\hat{r}_{ij}\,cos\,\theta_{ijk} - \hat{r}_{ik}\right) \\
\vec{f}_{kij} =& -\nabla_k V_{ijk}^{(3)} = -\frac{AX\zeta}{\left(r_{ik}-r_0\right)^2}\hat{r}_{ik} - \frac{2A}{Yr_{ik}}\left(\hat{r}_{ik}\,cos\,\theta_{ijk} - \hat{r}_{ij}\right) \\
A =& B_{ijk}\,exp\left(\frac{\zeta}{r_{ij}-r_0}+\frac{\zeta}{r_{ik}-r_0}\right)\frac{X}{Y} \\
Y =& 1 + CX^2 \\
X =& cos\,\theta_{ijk} - cos\,\theta_0.
\end{aligned}
\tag{2.19}
$$

The results presented in this chapter took about 2500 h of CPU time at the Galician Supercomputing Centre (CESGA).

2.7. Results and discussion

The nanowires for this study were constructed by cutting an hexagonal prism out of zinc-blende bulk InP with the [111] crystallographic direction — the diagonal of the conventional cubic unit cell — as its axis. Alternatively, they can be thought of as built by piling layers of close-packed spheres following a periodic ABCABC… pattern, and then placing a two-atom {In,P} basis at the centre of each sphere with the In-P bond perpendicular to the corresponding layer. These three inequivalent layers are shown, for a particular diameter,

Figure 2.3 Constructive block for nanowires with six radial layers, seen from three different directions: a) [111] (long axis of the wire); b) [110]; c) [100]. Orange intersections are In atoms; violet intersections represent P.

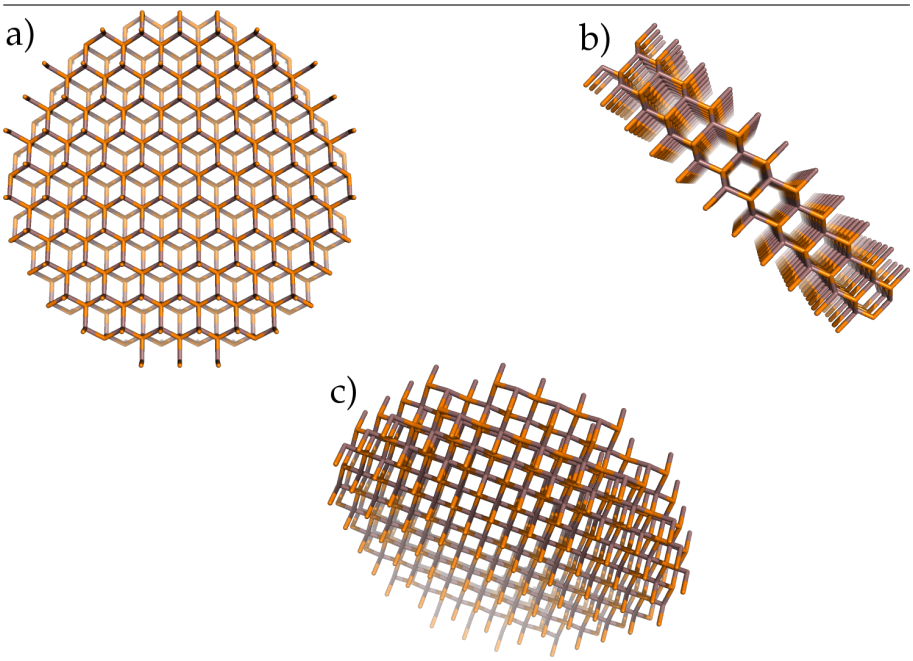

in Fig. 2.3. The equilibrium In-P distance in the bulk material is 2.54 Å, so contiguous layers are separated by 3.39 Å. On the other hand, the minimum in-layer interatomic distance equals the distance between the centres of two faces of the conventional unit cell, 4.15 Å. Hence, the radius of the smallest circumference that encloses all the atoms in a nanowire comprising n_r radial layers (excluding the fixed atoms) is $4.15\,(n_r - 1)$ Å. The cross-sectional area of the thermally conducting part of such a wire is $A = 0.447\,(n_r - 1)^2$ nm^2. Thin wires are more interesting with regard to surface effects; in addition, there is an upper bound on the diameter of a tractable nanowire owing to the quadratic dependence of the number of atoms on it. According to these criteria, nanowires with 2 to 7 radial layers of mobile atoms, and diameters 0.83, 1.66, 2.49, 3.32, 4.15 and 4.97 nm, were chosen. The case of only one mobile radial layer was excluded because it does not have a well-defined diameter. The numbers of atoms in the simulated nanowires ranged from 37950 to 94650.

The rate of energy addition and removal $\Delta E/\Delta t$ was another parameter which required a careful choice. It had to be small enough that it still made

sense to refer to the result of the calculation as the thermal conductivity at temperature T in spite of the difference in temperature (ΔT) induced between the thermostats, but not so small that ΔT was masked by fluctuations in the "instantaneous" temperature of the system. Moreover, it must be scaled proportionally to the number of mobile atoms in each thermostat if ΔT is to be roughly independent of the diameter. Based on these considerations, $\Delta E = 0.01$ eV was chosen for the thinnest nanowire, which yielded values of ΔT around 10 K. Two related parameters are the width of each thermostated plate, δ, and the number of segments around each of them which should be excluded from the linear fit. As regards the former, the results proved rather insensitive to the precise choice of δ, which was finally set to 10 nm to improve convergence by adding/removing less energy to/from each individual atom. The latter problem was solved by widening the excluded region until a point was reached where ∇T remained stable. This happened quite soon, for a width of merely 5 nm.

The value of κ derived from the simulation depends quite strongly on the length of the simulation box as long as the latter is comparable to the mean free path (MFP) or to the wavelength of phonons involved in thermal conduction. Its effect can be treated in a simplistic manner as follows [42]. Let l_∞ be the MFP of phonons in a particular state for an infinite nanowire, and l_L be the same variable for a wire of length L. If scattering by the ends of the wire is assumed to be independent from every other scattering mechanism, the total scattering probability per unit length (l_L^{-1}) can be approximated by the sum of l_∞^{-1} and $\frac{4}{L}$ (since the average distance from a random point along the nanowire to the closest thermostat is $L/4$). In elementary kinetic theory, the contribution of a vibrational mode to κ is proportional its MFP. Thus, for some constant b,

$$\frac{1}{\kappa_L} = \frac{1}{\kappa_\infty} + \frac{b}{L}. \tag{2.20}$$

In principle, this expression could be used to extrapolate the true value of the thermal conductivity, κ_∞, from a set of results (κ_L) suffering from size effects, using a simple linear fit. However, its applications in the literature have never been too successful, either because of the huge uncertainties in the extrapolated κ_∞^{-1} [99] or because it can yield unphysical, and even negative, values [104]. Some authors have obtained better results modelling the dependence of κ_L on L as linear. In any case, it seems clear that this dependence is not so simple. For the InP nanowires investigated in this work, simulation boxes comprising from

Figure 2.4 Typical steady-state temperature profile. For this figure, the nanowire was divided in 40 segments, instead of the usual 20, to show a more detailed picture of non-linear regions. Each point in the plot is the average of two segments, one to the right and one to the left of the hot thermostat, equivalent owing to the application of PBC.

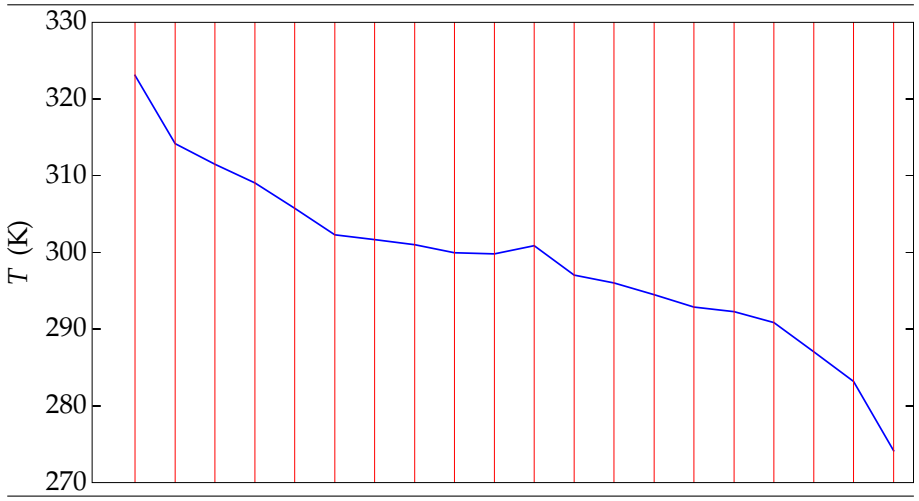

75 to 900 layers along the longitudinal axis were tried, which revealed that a fit to Eq. (2.20) is inconclusive, as it results in uncertainties of up to 400% in the ordinate at the origin. As a matter of fact, κ seems to remain constant, within the limits of computational uncertainty, if more than about 200 layers are included in the box. 225 layers were always used for the final calculations.

The Pearson deviation coefficient of temperature, as calculated using the equipartition theorem, is inversely proportional to the square root of the number of atoms used. This limits the number of segments in which the nanowire should be conceptually split. 20 segments, each one comprising between 1900 and 4700 atoms depending on the diameter, were settled on as a good compromise between a precise temperature and a sufficient number of data points for the linear fit. Figure 2.5 shows the temporal evolution of the temperature gradient thus calculated, from the instant when energy began to be moved along the nanowire at equilibrium to a point where a steady-state was reached. The criterion used to identify such point was that $\partial T/\partial z$ remained stable within a 1% for 1 ns. After this, each simulation was run for a further 1 ns; this time was divided in 10 subintervals, each of which yielded a different value of $\partial T/\partial z$. From the sample of 10 values, their mean was taken as the best estimator of the thermal gradient and their standard deviation of the sample

Figure 2.5 Representative example of the evolution with simulation time of the average temperature gradient in a nanowire. The steady-state profile for the same simulation is shown in Fig. 2.4.

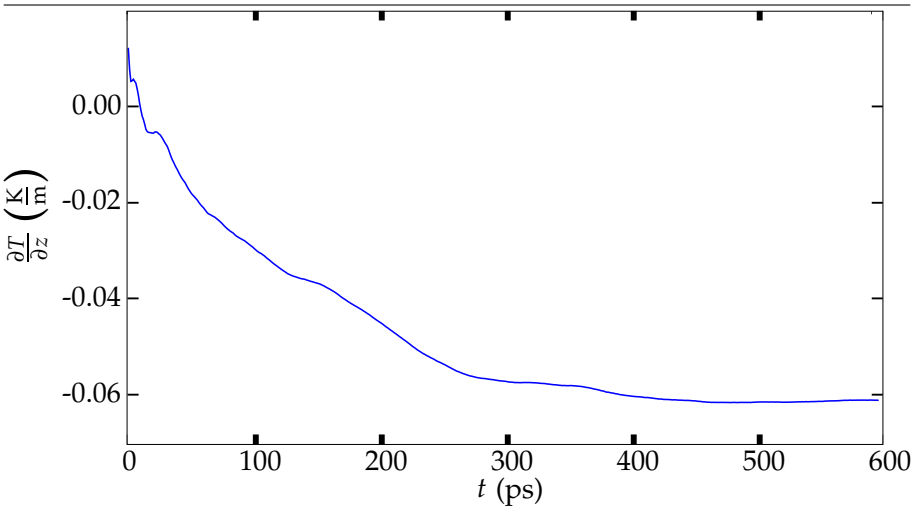

mean as the uncertainty, which was then propagated to

$$\kappa = \left| \left(\partial T / \partial z \right)^{-1} j_Q^{(z)} \right| . \tag{2.21}$$

The uncertainty $s\left(\frac{\partial T}{\partial z}\right)$ is mostly insensitive to a change in the number of temporal subintervals, but falls when the total simulation time is increased, down to a limit. Its evolution is exemplified in Fig. 2.6; the fact that it stabilises under 10%, considered a good value in the literature [42, 99], supports the choice of parameters in this work. However, this estimator of uncertainty was not considered reliable enough to attach an individual uncertainty to each result, as there are many assumptions implicit in the method whose contributions to the combined uncertainty would be difficult to ascertain.

As mentioned in previous sections, thermal conductivity calculations were performed for nanowires with diameters d between 1.66 and 4.97 nm at temperatures between 100 and 700 K. Figure 2.7 shows the results for $d = 1.66$ nm and $d = 4.15$ nm. For the smallest diameter, $\kappa(T)$ falls globally from 2.3 W/(m K) at 100 K to 1.5 W/(m K) at 700 K, but shows a local maximum of around 2.25 W/(m K) between 300 and 400 K. In contrast, the thermal conductivity of the nanowire with $d = 4.15$ nm is almost flat in the range 100 – 500 K and falls monotonically after that, from around

Figure 2.6 Time evolution of the relative uncertainty in the temperature gradient (or in κ) during the same simulation used for Figs. 2.4 and 2.5.

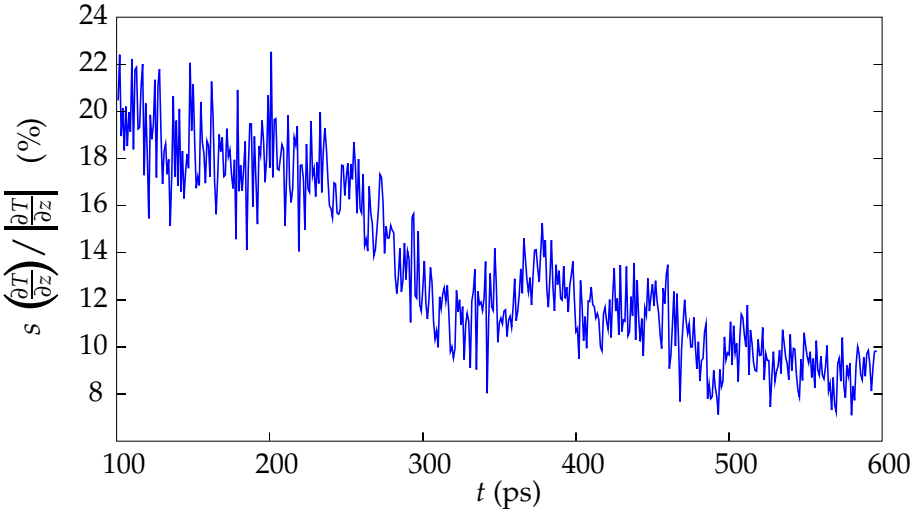

2.35 W/(m K) to about 2.0 W/(m K) at 700 K. Both curves show values similar to those calculated by Volz and Chen [39] for Si nanowires with square cross sections of comparable diameter in the temperature range 200 – 500 K. Both the results presented in this work and those by Volz and Chen are between one and two orders of magnitude lower than the thermal conductivities of the corresponding bulk materials [κ = 121 W/(m K) and 32 W/(m K) for bulk InP at 200 K and 500 K respectively [105]; κ = 241 W/(m K) and 81 W/(m K) for bulk Si at the same temperatures]. Similarly, for Si-clathrate nanowires, Ponomareva *et al.* [41] calculated a $\kappa(T)$ curve with values around 3 – 5 W/(m K) between 100 and 500 K. However, their results for tetrahedral Si nanowires with a diameter of 4.2 nm lie between 18 and 30 W/(m K) and have a maximum between 100 and 200 K, therefore showing a shape similar to the lower curve in Fig. 2.7. The discrepancy between the results by Volz and Chen and those by Ponomareva *et al.* can probably be attributed to the different crystallographic directions employed by both groups, [110] and [111] respectively.

Figure 2.8 shows the thermal conductivities obtained at 100 and 300 K as a function of nanowire diameter. In both cases, κ decreases when d is decreased from 4.97 to 2.49 nm; a behaviour which can be explained by an increase in surface to volume ratio, in a fashion qualitatively analogous to the theoretical de-

Figure 2.7 Thermal conductivity of two nanowires with different diameters as a function of temperature. Data from simulation are represented by markers; curves were obtained by cubic spline interpolation.

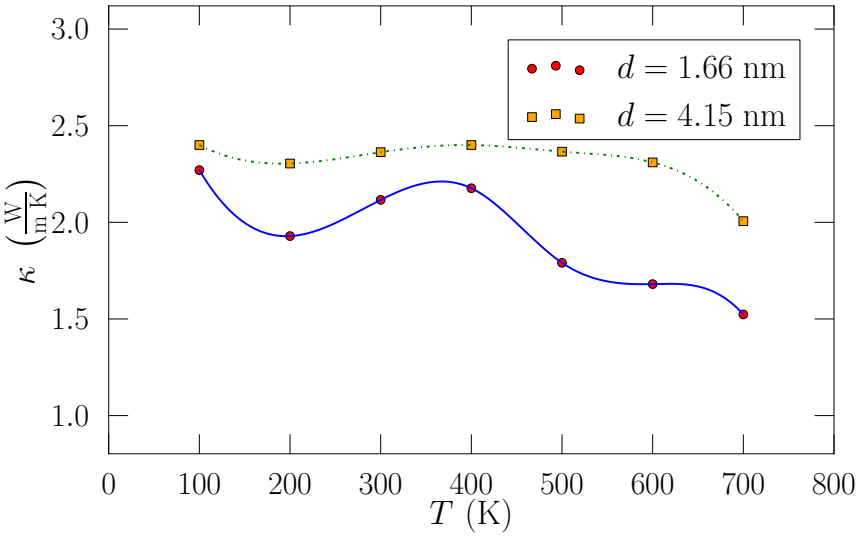

scription by Mingo [62] using complete dispersion relations and the harmonic Harrison potential [60], and in line with experimental [30, 35], theoretical [36–38] and simulation [39–41] results for Si nanowires.

Nevertheless, further reduction of the diameter down to 1.66 nm causes a small enhancement of κ, after which if falls steeply to 0.8 – 1.0 W/(m K) for $d = 0.83$ nm (the diameter of a nanowire with only two mobile layers). The presence of this local maximum in $\kappa(d)$ goes against the general trend of the curve and cannot be explained in the simple terms used in the previous paragraph. Ponomareva *et al.* [41] found that the thermal conductivity of square Si nanowires grew with decreasing diameter when $d \lesssim 3$ nm and attributed this behaviour to the same kind of confinement effects that cause their specific heat to show a similar inverse dependence on d [45]. In order to explore this hypothesis, the squared moduli of the Fourier transforms of the velocity autocorrelation functions were calculated at 100 K and 300 K for four different diameters. These are shown in Figs. 2.9 and 2.10, respectively, as functions of the linear frequency $\nu = \omega/(2\pi)$. Only the region below or around $\nu_{300\ \mathrm{K}} = k_B\,(300\ \mathrm{K})/h \simeq 6.4$ THz is represented, as phonons above that frequency do not make a significant contribution to thermal conductivity. Similar

Figure 2.8 Diameter dependence of the thermal conductivity of InP nanowires at two different temperatures. Lines are provided as guides to the eye.

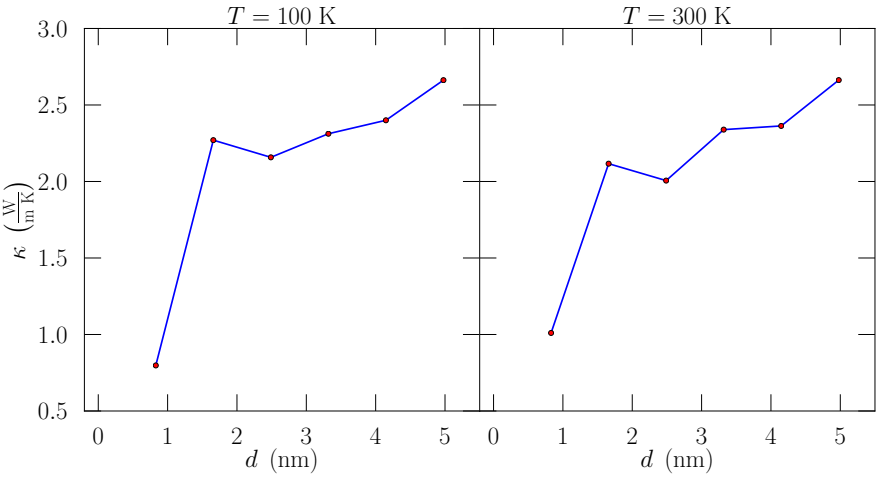

conclusions can be drawn from both figures, so this discussion will be centred on Fig. 2.9. The positions of the most important peaks in that figure are listed in Table 2.2. The very low conductivity of the thinnest nanowire can be attributed to the scarcity of vibrational modes in that frequency band. On the other hand, the aforementioned local maximum seems to be related to a shift of the two most excited modes from 2.48 and 2.62 THz to 3.16 and 3.46 THz when d is decreased from 3.32 to 1.66 nm. This "blue-shift" implies more energy carried per phonon, and is identified by some authors as the signature of confinement [41]. Such explanation should be taken as merely tentative, however, since MD is not a particularly useful tool for the description of phonons. In particular, the usage of confinement in a classical context should not be taken as necessarily equivalent to its meaning as a transport regime in quantum approaches to thermal transport, but as a reference to any modifications in the phonon spectrum due to confined boundary conditions [106, 107].

Table 2.2 Frequencies of the main peaks in Fig. 2.9. For d = 1.66, 2.49 and 3.32 nm the frequencies of the two most excited modes are shown in bold.

d (nm)	ν_{peaks}
0.83	2.37, 3.41, 3.83, 4.03, 4.15, 4.4, 4.86, 4.8 – 5.0
1.66	2.37, **3.16**, **3.46**, 3.83, 4.5 – 5.5
2.49	1.84, 2.37, 2.48, **2.72**, **2.89**, 3.25, 3.50, 3.83, 4.5 – 5.5
3.32	2.00, 2.15 – 2.30, 2.38, **2.48**, **2.62**, 3.25, 3.54, 4.5 – 5.5

Figure 2.9 Low-frequency part of the phonon spectra of four nanowires with different diameters at T = 100 K.

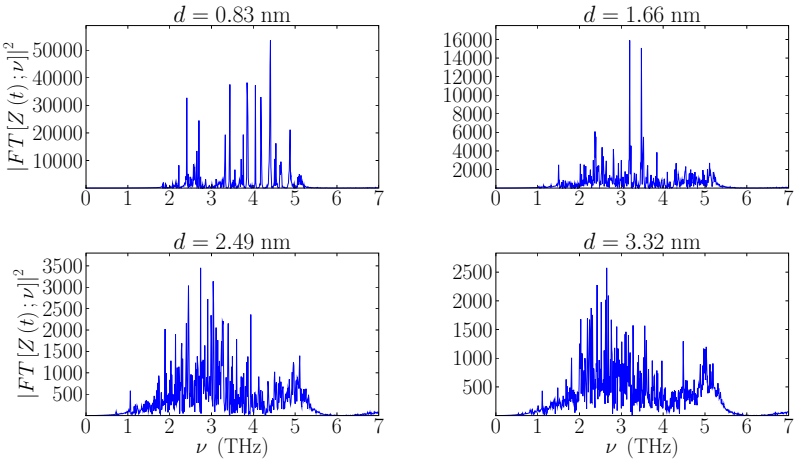

Figure 2.10 As Fig. 2.9, but for T = 300 K.

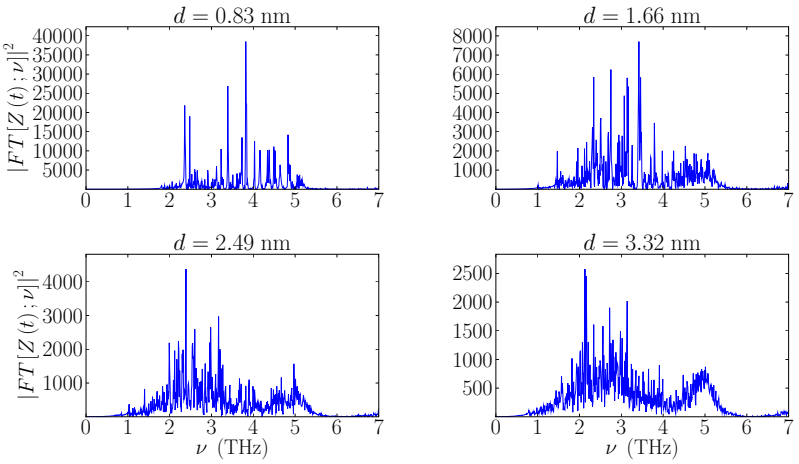

References

11. Nolas, G. S., Sharp, J. & Goldsmid, H. J. *Thermoelectrics* (Springer, New York, 2001).

19. Shi, J. & Li, J. C. M. *Nano Lett.* **9,** 1307 (2009).

20. Xia, Y., Yang, P., Sun, Y., Wu, Y., Mayers, B., Gates, B., Yin, Y., Kim, F. & Yan, H. *Adv. Mater.* **15,** 353 (2003).

21. Law, M., Goldberger, J. & Yang, P. *Annu. Rev. Mater. Res.* **34,** 83 (2004).

22. Kim, W., Wang, R. & Majumdar, A. *Nanotoday* **2,** 40 (2007).

23. Wang, G. & Li, X. *J. Appl. Phys.* **104,** 113517 (2008).

24. Kim, D. R., Lee, C. H. & Zheng, X. *Nano Lett.* **10,** 1050 (2010).

25. Zou, J. & Balandin, A. *Proc. Electrochem. Soc.* **2001-19,** 70 (2001).

26. Schelling, P. K., Shi, L. & Goodson, K. E. *Mater. Today* **8,** 30 (2005).

27. Hicks, L. D. & Dresselhaus, M. S. *Phys. Rev. B* **47,** 12727 (1993).

28. Mahan, G., Sales, B. & Sharp, J. *Phys. Today* **50,** 42 (1997).

29. Majumdar, A. *Science* **303,** *777* (2004).

30. Li, D., Wu, Y., Kim, P., Shi, L., Yang, P. & Majumdar, A. *Appl. Phys. Lett.* **83,** 2934 (2003).

31. Li, D., Wu, Y., Fan, R., Yang, P. & Majumdar, A. *Appl. Phys. Lett.* **83,** 3186 (2003).

32. Zhou, J., Jin, C., Seol, J. H., Li, X. & Shi, L. *Appl. Phys. Lett.* **87,** 133109 (2005).

33. Shi, L., Hao, Q., Yu, C., Mingo, N., Kong, X. & Wang, Z. L. *Appl. Phys. Lett.* **84,** 2638 (2004).

34. Bourgeois, O., Fournier, T. & Chaussy, J. *J. Appl. Phys.* **101,** 016104 (2007).

35. Chen, R., Hochbaum, A. I., Murphy, P., Moore, J., Yang, P. & Majumdar, A. *Phys. Rev. Lett.* **101,** 105501 (2008).

36. Mingo, N. *Phys. Rev. B* **68,** 113308 (2003).

37. Mingo, N., Yang, L., Li, D. & Majumdar, A. *Nano Lett.* **3,** 1713 (2003).

38. Chantrenne, P., Barrat, J. L., Blase, X. & Gale, J. D. *J. Appl. Phys.* **97,** 104318 (2005).

39. Volz, S. G. & Chen, G. *Appl. Phys. Lett.* **75,** 2056 (1999).

40. Chen, Y., Li, D., Lukes, J. & Majumdar, A. *J. Heat Transfer.* **127,** 1129 (1999).

41. Ponomareva, I., Srivastava, D. & Menon, M. *Nano Lett.* **7,** 1155 (2007).

42. Schelling, P. K., Phillpot, S. R. & Keblinski, P. *Phys. Rev. B* **65,** 144306 (2002).

43. Stillinger, F. H. & Weber, T. A. *Phys. Rev. B* **31,** 5262 (1985).

44. Stillinger, F. H. & Weber, T. A. *Phys. Rev. B* **33,** 1451 (1986).

45. Zhang, Y., Cao, J. X., Xiao, Y. & Yan, X. H. *J. Appl. Phys.* **102,** 104303 (2007).

46. Boukai, A. I., Bunimovich, Y., Tahir-Kheli, J., Yu, J.-K., III, W. A. G. & Heath, J. R. *Nature (London)* **451,** 168 (2008).

47. Trentler, T. J., Hickman, K. M., Goel, S. C., Viano, A. M., Gibbons, P. C. & Buhro, W. E. *Science* **270,** 1791 (1995).

48. Trentler, T. J., Goel, S. C., Hickman, K. M., Viano, A. M., Chiang, M. Y., Beatty, A. M., Gibbons, P. C. & Buhro, W. E. *J. Am. Chem. Soc.* **119,** 419 (1997).

49. Duan, X. F. & Lieber, C. M. *Adv. Mater.* **12,** 298 (2000).

50. Gudiksen, M. S. & Lieber, C. M. *J. Am. Chem. Soc.* **122,** 8801 (2000).

51. Gudiksen, M. S., Wang, J. F. & Lieber, C. M. *J. Phys. Chem. B* **105,** 4062 (2001).

52. Tang, C., Bando, Y., Liu, Z. & Golberg, D. *Chem. Phys. Lett.* **376,** 676 (2003).

53. Yu, H., Li, J., Loomis, R. A., Wang, L.-W. & Buhro, W. E. *Nature Mater.* **2,** 517 (2003).

54. Gudiksen, M. S., Wang, J. & Lieber, C. M. *J. Phys. Chem. B* **106,** 4036 (2002).

55. Huang, Y. & Lieber, C. M. *Pure Appl. Chem.* **76,** 2051 (2004).

56. Duan, X. F., Huang, Y., Cui, Y., Wang, J. & Lieber, C. M. *Nature (London)* **409,** 66 (2001).

57. Alemany, M. M. G., Huang, X., Tiago, M. L., Gallego, L. J. & Chelikowsky, J. R. *Nano Lett.* **7,** 1878 (2007).

58. Alemany, M. M. G., Jain, M., Kronik, L. & Chelikowsky, J. R. *Phys. Rev. B* **69,** 075101 (2004).

59. Alemany, M. M. G., Jain, M., Tiago, M. L., Zhou, Y., Saad, Y. & Chelikowsky, J. R. *Comput. Phys. Commun.* **177,** 339 (2007).

60. Harrison, W. A. *Electronic Structure and the Properties of Solids* (Dover, New York, 1989).

61. Mingo, N. & Broido, D. A. *Phys. Rev. Lett.* **93,** 246106 (2004).

62. Mingo, N. *Appl. Phys. Lett.* **84,** 2652 (2004).

63. Branício, P. S. & Rino, J. P. *Phys. Stat. Sol. (b)* **244,** 331 (2007).

64. Vashishta, P., Kalia, R. K., Rino, J. P. & Ebbsjö, I. *Phys. Rev. B* **41,** 12197 (1990).

65. Shimojo, F., Ebbsjö, I., Kalia, R. K., Nakano, A., Rino, J. P. & Vashishta, P. *Phys. Rev. Lett.* **84,** 3338 (2000).

66. Rino, J. P., Chatterjee, A., Ebbsjö, I., Kalia, R. K., Nakano, A., Shimojo, F. & Vashishta, P. *Phys. Rev. B* **65,** 195206 (2002).

67. Branício, P. S., Kalia, R. K., Nakano, A., Rino, J. P., Shimojo, F. & Vashishta, P. *Appl. Phys. Lett.* **82,** 1057 (2003).

68. Rino, J. P. & Branício, P. S. *Phys. Stat. Sol. (b)* **244,** 239 (2007).

69. Lieb, E. H. & Yngvason, J. *Phys. Rep.* **310,** 1 (1996).

70. Carathéodory, C. *Math. Ann* **67,** 355 (1909).

71. Buchdahl, H. A. *The Concepts of Classical Thermodynamics* (Cambridge University Press, Cambridge, 1966).

72. Boyling, J. B. *Proc. Roy. Soc. London A* **329,** 35 (1972).

73. Grandy, W. T. Jr. *Found. Phys.* **34,** 21 (2004).

74. Kittel, C. *Introduction to Solid State Physics* 8th Edition (Wiley, 2004).

75. Vavilov, M. G. & Stone, A. D. *Phys. Rev. B* **72,** 205107 (2005).

76. Tanatar, M. A., Paglione, J., Petrovic, C. & Taillefer, L. *Science* **316,** 1320 (2007).

77. Shanks, H. R., Maycock, P. D., Sidles, P. & Danielson, G. C. *Phys. Rev.* **130,** 1743 (1963).

78. Kudman, I. & Steigmeier, E. F. *Phys. Rev.* **133,** 1665 (1964).

79. Ju, Y. S. *Appl. Phys. Lett.* **87,** 153106 (2005).

80. Van Duin, A. C. T., Dasgupta, S., Lorant, F. & Goddard III, W. A. *J. Phys. Chem. A* **105,** 9396 (2001).

81. Rey, C., Gallego, L. J., García-Rodeja, J., Alonso, J. A. & Iñiguez, M. P. *Phys. Rev. B* **48,** 8253 (1993).

82. García-Rodeja, J., Rey, C., Gallego, L. J. & Alonso, J. A. *Phys. Rev. B* **49,** 8495 (1994).

83. Xiao-Kun, G. & Bing-Yang, C. *Chin. Phys.* **16,** 3777 (2007).

84. N. Yang, G. Z. & Li, B. *Nano Lett.* **8,** 276 (2007).

85. Gomes, C. J., Madrid, M., Goicochea, J. V. & Amon, C. H. *J. Heat Transfer* **128,** 1114 (2006).

86. Chen, G. Y., Stolojan, V., Cox, D. C., Giusca, C. & Silva, S. R. P. in *IEEE Conference on Emerging Technologies - Nanoelectronics* (2006), 376.

87. Yang, W., Araki, H., Kohyama, A., Thaveethavorn, S., Suzuki, H. & Noda, T. *Mater. Lett.* **58,** 3145 (2004).

88. Wang, S., Liang, X. & Ohara, T. *J. Appl. Phys.* **105,** 014316 (2009).

89. Swope, W. C., Andersen, H. C. & amd K. R. Wilson, P. H. B. *J. Chem. Phys.* **76,** 637 (1982).

90. Van Zon, R. *CHM1464: Foundations of Molecular Dynamics, course notes* Booklet avaliable online at the University of Toronto web site `http://www.chem.utoronto.ca/~rzon/simcourse/notes.html`. Retrieved on 2012-04-06. 2005.

91. Carrete, J., Varela, L. M. & Gallego, L. J. *Physica A* **27,** 6752 (2008).

92. Guajardo-Cuéllar, A., Go, D. B. & Sen, M. *J. Chem. Phys.* **132,** 104111 (2010).

93. Evans, D. J. & Morriss, G. P. *Statistical Mechanics of NonEquilibrium Liquids* 1st ed. (Academic Press, London, 1990).

94. G, G. P., Ely, J. F., McCabe, C. & Isbister, D. J. *J. Chem. Phys.* **122,** 094114 (2005).

95. Mandadapu, K. K., Jones, R. E. & Papadopoulos, P. *J. Chem. Phys.* **133,** 034122 (2010).

96. Mandadapu, K. K., Jones, R. E. & Papadopoulos, P. *J. Chem. Phys.* **130,** 204106 (2009).

97. Huang, X., Huai, X., Liang, S. & Wang, X. *J. Phys. B* **42,** 095416 (2009).

98. Turney, J. E., McGaughey, A. J. H. & Amon, C. H. *Phys. Rev. B* **79,** 224305 (2009).

99. Zhou, X. W., Aubry, S., Jones, R. E., Greenstein, A. & Schelling, P. K. *Phys. Rev. B* **79,** 115201 (2009).

100. Jund, P. & Jullien, R. *Phys. Rev. B* **59,** 13707 (1999).

101. Berendsen, H. J. C., Postma, J. P. M., van Gunsteren, W. F., Dinola, A. & Haak, J. R. *J. Chem. Phys.* **81,** 3684 (1984).

102. Papanicolaou, N. I., Lagaris, I. E. & Evangelakis, G. A. *Surf. Sci.* **337,** L819 (1995).

103. Heino, P. *Eur. Phys. J. B* **60,** 171 (2007).

104. Yoo, Y.-G., Car, R., Srolovitz, D. J. & Scandolo, S. *Phys. Rev. B* **70,** 012302 (2004).

105. Aliev, S. A., Nashelskii, A. Y. & Shalyt, S. S. *Sov. Phys. Solid State* **7,** 1287 (1965).

106. Balandin, A. & Wang, K. L. *Phys. Rev. B* **58,** 1544 (1998).

107. Adu, K. W., Gutiérrez, H. R., Kim, U. J., Sumanasekera, G. U., & Eklund, P. C. *Nano Lett.* **5,** 409 (2005).

3 Influence of the interatomic potential on MD calculations of thermal conductivity: comparison for GaAs, InAs and InP nanowires

Aunt Martha: For a gallon of elderberry wine, I take one teaspoon full of arsenic, then add half a teaspoon full of strychnine, and then just a pinch of cyanide.
Mortimer Brewster: Hmm. Should have quite a kick.

Arsenic and Old Lace
Frank Kapra

3.1. Introduction

In Chapter 2, MD simulations were used to calculate the thermal conductivity of hexagonal InP nanowires. One of the relevant conclusions was that an enhancement of κ is obtained when the diameter is reduced beyond a certain limit. However, such enhancement is small enough for its statistical significance to be questionable, given the uncertainty in the data. Therefore, it is important to assess the reliability of the diverse elements which can affect this calculation. One of the most complicated choices is the interatomic potential,

as generally none of them can be expected to give good results for every property of the system under study, and transferability can be difficult to evaluate *a priori*.

As mentioned previously, most theoretical and computational work on the thermal conductivities of nanowires has been limited to Si [36, 38, 39, 41]. In the most salient exception, predictions of the room-temperature thermal conductivities of nanowires of the zinc-blende-structured semiconductors CdTe, ZnTe, ZnSe, ZnS, InSb, InAs, GaSb, GaAs, AlSb and InP were obtained by Mingo and Broido [61] from phonon dispersion relations that were calculated atomistically using a Harrison potential [60] while fitting a parameter related to the specularity of the boundary (see also Refs. 62, 108 and 109, as well as the more precise definition of the role of specularity in Section 4.5). However, the results extrapolated from Mingo and Broido's prediction [61] are an order of magnitude smaller than those discussed in Chapter 2 and based on the Branício-Rino potential [63]. Mingo and Broido also found that for binary semiconductors of a given type (III-V or II-IV), the ratio $\kappa_{\text{bulk}}/\kappa_{\text{nano}}$ between the thermal conductivities of the bulk and of nanowires of a given diameter increased with the mass ratio r of the components, so that for GaAs ($r = 1.07$), InAs ($r = 1.53$) and InP ($r = 3.71$) $\kappa_{\text{bulk}}/\kappa_{\text{nano}}$ increased in the order GaAs $<$ InAs $<$ InP.

In the work described here the thermal conductivities of GaAs, InAs and InP nanowires at $T = 300$ K were computed by direct MD simulations of the kind described in the previous chapter, in each case obtaining results both with the classical Harrison potential [60] as parameterised by Mingo and Broido [61], and also with another, more elaborate potential. For GaAs and InAs the Abell-Tersoff potential recently parameterised by Hammerschmidt *et al.* [110] for the description of GaAs and InAs nanostructures was used, and for InP the choice was again the Branício-Rino potential [63]. The aims of these calculations were twofold: firstly, to compare the theoretical predictions of Mingo and Broido [61] with the results of MD simulations using the same Harrison potential, so as to check, in particular, whether the above-noted discrepancy between Ref. 61 and Chapter 2 was due to the use of different potentials or different methods; secondly, to investigate whether for GaAs and InAs nanowires a similar discrepancy emerged between Mingo and Broido's [61] Harrison-based theoretical results and MD results obtained with the Abell-Tersoff/Hammerschmidt potential.

3.2. Details of the MD simulations and of the model potentials

The ingredients used for MD calculations in this work are basically the same as in Chapter 2: a direct non-equilibrium method [42], hexagonal nanowires cut along the [111] direction of the zinc-blende bulk, the velocity Verlet integration algorithm [89] and rigid boundary conditions. Regarding the latter, it should be noted that the theoretical results of Mingo and Broido [61] were also obtained by imposing frozen boundary conditions on the wires.

Each nanowire occupied a large supercell with periodic boundary conditions in the z direction so as to make the wire endless. The length of this supercell, L, was chosen so as to avoid aliasing phenomena that might suppress important contributions to the thermal conductivity from long-wavelength phonons. To this end, simulations using nanowires of a fixed diameter and lengths of up to 1800 atomic layers were ran, which allowed the determination of lengths big enough to ensure that any loss of thermal conductivity resulting from the finite value of L was within the uncertainty of the simulation results: 97.2 nm for GaAs, 104.8 nm for InAs and 76.2 nm for InP. A fit of the dependence of thermal conductivity on supercell length to Eq. (2.20) was attempted as suggested by Schelling *et al.* [42], but again the results were not satisfactory. This is qualitatively in line with more recent results from the literature [99, 111–113], which call into question the linear extrapolation procedure.

To calculate the temperature gradient $\partial T/\partial z$, the nanowire was notionally divided into 20 segments, their kinetic temperatures were averaged over 10^7 time steps after the steady state had been reached, the four segments containing the thermostats were discarded (with 20 segments, each thermostat is centred at the boundary between two segments), and a linear regression of segment temperature on the distance of the segment midpoint from the hot plate was performed. The thermal conductivity at the centre of the cell (*i.e.* at the mean temperature of the two thermostats) was obtained using Eq. (2.21).

Due to their computational demands, these MD simulations were necessarily restricted to nanowires of small diameter: the unconstrained parts of the wires with 4, 5, 6 and 7 mobile layers surrounding the central row of atoms had diameters of respectively 2.57, 3.42, 4.28 and 5.13 nm (GaAs) and 2.38, 3.17, 3.97 and 4.76 nm (InAs), and those of the InP wires with 3, 4, 5 and 6 unconstrained layers around the central row had diameters of 2.49, 3.32, 4.15 and 4.97 nm respectively. The total numbers of atoms, including those of the

Table 3.1 Parameters of the Harrison potential, copied from Ref. 61.

	InP	InAs	GaAs
C_0 (eV)	47.38	42.13	42.04
C_1 (eV)	0.715	0.650	0.826

fixed layers, ranged from 18200 to 126200 for GaAs and InAs, and from 37950 to 94650 for InP.

The Harrison potential [60], which was used for GaAs, InAs and InP, computes the total potential energy of the system as the sum of quadratic terms describing the interactions between nearest-neighbour pairs and triplets,

$$V = \frac{C_0}{2r_0^2} \sum_{(i,j)}{}' \left(r_{ij} - r_0\right)^2 + \frac{C_1}{2} \sum_{(i,j,k)}{}' \left(\theta_{ijk} - \theta_0\right)^2, \tag{3.1}$$

where the primed sums run over nearest neighbours, r_0 is the equilibrium bond length, given by $\frac{3}{4}a_0$, where a_0 is the lattice constant, θ_{ijk} is the angle between the (i,j) and (j,k) bonds, and θ_0 is the equilibrium bond angle (109.471° for zinc-blende structures). Therefore, it has only two adjustable parameters, the force constants C_0 and C_1, which were obtained by Mingo and Broido [61] by computing bulk phonon dispersion relations and adjusting them to match the experimental frequencies of the zone centre longitudinal optical mode, $\omega_{LO}(\Gamma)$, and the zone edge transverse acoustic mode, $\omega_{TA}(X)$. The values so obtained were used in this work, and are reproduced in Table 3.1.

The potential proposed by Hammerschmidt *et al.* [110] for GaAs and InAs surfaces and nanostructures is a carefully parameterised Abell-Tersoff potential [114–117]. The values of its many adjustable parameters for GaAs and InAs were fitted by Hammerschmidt *et al.* [110] to a large set of reference data that included both experimental and density-functional results for structural and elastic properties of bulk Ga, As, In, GaAs and InAs, and structural and energetic properties of several reconstructed low-index GaAs and InAs surfaces, and are included in Table 3.2. This potential has the functional form

$$V = \sum_i \sum_{j \neq i} f_{ij}^{(C)}\left(r_{ij}\right)\left[V_{ij}^{(R)}\left(r_{ij}\right) - V_{ij}^{(A)}\left(r_{ij}\right)\right] \tag{3.2a}$$

$$V_{ij}^{(R)}\left(r_{ij}\right) = \frac{D_{ij}}{S_{ij}-1}\, exp\left[-\beta_{ij}\sqrt{2S_{ij}}\left(r_{ij} - R_{ij}^{(0)}\right)\right] \tag{3.2b}$$

$$V_{ij}^{(A)}\left(r_{ij}\right) = \frac{S_{ij}D_{ij}}{S_{ij}-1}\, exp\left[-\beta_{ij}\sqrt{\frac{2}{S_{ij}}}\left(r_{ij} - R_{ij}^{(0)}\right)\right] \tag{3.2c}$$

$$B_{ij}\left(r_{ij}\right) = \left\{1 + \left[\gamma_{ij}\chi_{ij}\left(r_{ij}\right)\right]^{\eta_{ij}}\right\}^{-\frac{1}{2\eta_{ij}}} \tag{3.2d}$$

$$\chi_{ij}\left(r_{ij}\right) = \sum_{k \notin \{i,j\}} f_{ik}^{(C)}\left(r_{ik}\right) g_{ik}\left(\theta_{ijk}\right) exp\left\{\left[\alpha_{ik}\left(r_{ij} - r_{ik}\right)\right]^{m_{ik}}\right\} \tag{3.2e}$$

$$g_{ik}\left(\theta_{ijk}\right) = \delta_{ik}\left[1 + \frac{c_{ik}^2}{d_{ik}^2} - \frac{c_{ik}^2}{d_{ik}^2 + \left(h_{ik} - cos\,\theta_{ijk}\right)^2}\right] \tag{3.2f}$$

$$f_{ij}^{(C)} = \begin{cases} 1, & r_{ij} - R_{ij}^{(C)} \leq -D_{ij}^{(C)} \\ \frac{1}{2}\left[1 - sin\left(\pi\frac{r_{ij} - R_{ij}^{(C)}}{2D_{ij}^{(C)}}\right)\right], & \left|r_{ij} - R_{ij}^{(C)}\right| < D_{ij}^{(C)} \\ 0, & r_{ij} - R_{ij}^{(C)} \geq D_{ij}^{(C)} \end{cases}. \tag{3.2g}$$

In all MD calculations presented here, the forces on individual atoms were obtained from the analytical derivatives of the appropriate equations for the total energy of the system.

3.3. Calculation of the phonon density of states

The method used to estimate the phonon density of states (DOS) in Chapter 2 is based on the Fourier transform of the velocity autocorrelation function and, while it has the advantage of being easy to implement as a post-processing step after MD simulations, provides imprecise results due to factors such as the influence of temperature. In this chapter, to get a more detailed picture and to be able to compare different potentials, a more direct method will be used, based on lattice dynamics. The notation introduced here will also be useful for later chapters.

It is well-known that a field defined on the nodes of a crystalline structure periodic along the *OZ* direction can — as long as it meets certain integrability criteria — be decomposed in terms of harmonic functions of a well-defined

Table 3.2 Parameters of the Hammerschmidt potential, obtained from Ref. 110.

	Ga-Ga	As-As	In-In	Ga-As	In-As
R_{ij} (Å)	2.2625	1.9018	2.6639	2.33824	2.5492
D_{ij} (eV)	1.4159	7.9717	1.5052	1.9561	1.8900
β_{ij} (Å^{-1})	0.9079	1.2165	1.1847	1.5396	1.4549
S_{ij}	1.0646	2.3439	1.2440	1.1543	1.8578
γ_{ij}	1.4401	4.8650	4.0976	0.2992	2.2113
α_{ij} (Å^{-1})	0.7469	2.5408	1.2117	−1.3824	1.1816
δ_{ij}	0.0050	0.3609	0.0109	0.0424	0.0190
c_{ij}	1.4897	0.1749	1.0853	1.7796	3.9707
d_{ij}	0.8376	0.2140	0.9465	0.6450	0.9486
h_{ij}	−0.3373	−0.1261	−0.4652	−0.4060	−0.5102
η_{ij}	1.0	1.0	1.0	1.0	1.0
m_{ij}	1.0	1.0	1.0	1.0	1.0
$R_{ij}^{(C)}$ (Å)	2.95	3.1	3.5	3.1	3.7
$D_{ij}^{(C)}$ (Å)	0.15	0.1	0.1	0.2	0.1

periodicity indicated by their wave number $k^{(z)}$. The set of all possible values of $k^{(z)}$ is called reciprocal space, and it can be generated by periodic translation of a unit cell with length $2\pi/l_z$, where l_z denotes the length of the real-space unit cell. A particularly interesting case is that where the field under study represents the displacement of each atom in the system with respect to its equilibrium position, a minimum of the potential energy which will be arbitrarily taken as $V = 0$. In a neighbourhood of this point, V admits a second-order Taylor expansion without zeroth- or first-order terms. Let each unit cell have B atoms, and $u_{I,j}^{(\mu)}$ be the displacement in the μ direction of atom $j \in \{1, \dots, B\}$ in unit cell I with position $l_z I$. The change in potential energy with respect to the minimum induced by a periodic displacement, $u_{I,j}^{(\mu)} = \Re\left\{\tilde{u}_{0,j}^{(\mu)} e^{-ik^{(z)} l_z I}\right\}$, of wave number $k^{(z)}$, is

$$V = \frac{1}{2} \sum_{\substack{I,I' \\ \mu,\mu',j,j'}} \frac{\partial^2 V}{\partial u_{I,j}^{(\mu)} \partial u_{I',j'}^{(\mu')}} u_{I,j}^{(\mu)} u_{I',j'}^{(\mu')}, \tag{3.3}$$

or, in terms of complex amplitudes,

$$
\begin{aligned}
V &= \frac{1}{4}\Re\left\{\sum_{\substack{I,I'\\ \mu,\mu',j,j'}} \frac{\partial^2 V}{\partial u_{I,j}^{(\mu)}\partial u_{I',j'}^{(\mu')}}\left\{\tilde{u}_{0,j}^{(\mu)}\tilde{u}_{0,j'}^{(\mu')}e^{-ik^{(z)}l_z[I+I']} + \tilde{u}_{0,j}^{(\mu)}\left[\tilde{u}_{0,j'}^{(\mu')}\right]^* e^{-ik^{(z)}l_z[I-I']}\right\}\right\} = \\
&= \frac{1}{4}\Re\left\{\sum_{\substack{I,I'\\ \mu,\mu',j,j'}} \tilde{u}_{0,j}^{(\mu)}\tilde{u}_{0,j'}^{(\mu')}\left\{\sum_{I,I'}\frac{\partial^2 V}{\partial u_{I,j}^{(\mu)}\partial u_{I',j'}^{(\mu')}}e^{-ik^{(z)}l_z[I+I']}\right\}\right\} + \\
&+ \frac{1}{4}\Re\left\{\sum_{\substack{I,I'\\ \mu,\mu',j,j'}} \tilde{u}_{0,j}^{(\mu)}\left[\tilde{u}_{0,j'}^{(\mu')}\right]^*\left\{\sum_{I,I'}\frac{\partial^2 V}{\partial u_{I,j}^{(\mu)}\partial u_{I',j'}^{(\mu')}}e^{-ik^{(z)}l_z[I-I']}\right\}\right\}.
\end{aligned}
\tag{3.4}
$$

Of the two terms in the right-hand side, the first one is not invariant under a translation $(I, I') \longrightarrow (I+\Delta, I'+\Delta)$, $\Delta \in \mathbb{Z}$, so it must be zero, while the second one is a sum containing the complex conjugate of each of its terms, therefore making the real-part operator unnecessary. The Hessian matrix of the potential is often called the force-constant matrix, and each of the second derivatives of the potential it comprises will be denoted by $\tilde{K}_{I,I',j,j'}^{(\mu,\mu')}$. The system's periodicity implies that force constants can only depend on I and I' through $I - I'$. Hence, the double sum between curly brackets in Eq. (3.4) can be reduced to the value of its term for $I' = 0$ times the number of unit cells in the system. If the appropriate normalisation factor is now supposed to be included in $\tilde{u}_{0,j}^{(\mu)}$ and $\tilde{u}_{0,j'}^{(\mu')}$,

$$
V = \frac{1}{2}\sum_{\mu,\mu',j,j'} \tilde{u}_{j}^{(\mu)}\left[\tilde{u}_{j'}^{(\mu')}\right]^*\left\{\sum_{I}\tilde{K}_{I,j,j'}^{(\mu,\mu')}e^{-ik^{(z)}l_z I}\right\}. \tag{3.5}
$$

Here, all the references to the central cell 0 have been omitted for brevity. This expression allows a calculation of the normal vibration modes of the infinite lattice to be performed in terms of a finite number of degrees of freedom, those of a single unit cell. Using this quadratic form of the potential in Newton's second law $m_j d^2 u_j^{(\mu)}/dt^2 = -\partial V/\partial u_j^{(\mu)}$, a set of linear differential equations is obtained, whose general solution can be expressed in terms of a basis of ex-

ponentials of the form $\tilde{u}_j^{(\mu)}(t) = \tilde{u}_j^{(\mu)}(0)\, e^{-i\omega t}$, the acceptable values of ω being those that satisfy the eigenvalue equation

$$\omega^2 \tilde{w}_j^{(\mu)}(0) = \sum_{j',\mu'} D_{j,j'}^{(\mu,\mu')} \tilde{w}_{j'}^{(\mu')}(0)\,, \tag{3.6a}$$

where

$$\tilde{w}_j^{(\mu)} \coloneqq \sqrt{m_j}\tilde{u}_j^{(\mu)} \text{ and } D_{j,j'}^{(\mu,\mu')} \coloneqq \frac{1}{\sqrt{m_j m_{j'}}} \sum_I \tilde{K}_{I,j,j'}^{(\mu,\mu')} e^{-ik^{(z)}l_z I}. \tag{3.6b}$$

The mass-weighted force constant matrix appearing in this equation is denoted by $\boldsymbol{K}$ and often called the stiffness matrix. $\boldsymbol{D}$, its Fourier transform, is known as the dynamical matrix. By construction, $\tilde{\boldsymbol{K}}$ is Hermitian at local minima, and so are $\boldsymbol{K}$ and $\boldsymbol{D}$, so all acceptable values of ω will be real. Not only does $\boldsymbol{D}$ contain information about the vibrational modes of the system, but also about their group velocities $v_g^{(z)} = \partial\omega/\partial k^{(z)}$: expressing (3.6a) in the matrix form $\boldsymbol{D}\hat{w} = \omega^2\hat{w}$ for a normalised eigenvector $\hat{w}$ and differentiating it with respect to $k^{(z)}$, it becomes

$$\frac{\partial \boldsymbol{D}}{\partial k^{(z)}}\hat{w} + \boldsymbol{D}\frac{\partial \hat{w}}{\partial k^{(z)}} = 2\omega v_g^{(z)}\hat{w} + \omega^2 \frac{\partial \hat{w}}{\partial k^{(z)}}. \tag{3.7}$$

Taking the dot product of this expression with $\hat{w}^*$ and taking into account that $\hat{w}^* \cdot \boldsymbol{D} = \omega^2\hat{w}^*$ by virtue of the Hermitian character of $\boldsymbol{D}$, finally the following expression for the group velocity is obtained

$$v_g^{(z)} = \frac{1}{2\omega}\hat{w}^* \cdot \frac{\partial \boldsymbol{D}}{\partial k^{(z)}}\hat{w}. \tag{3.8}$$

This formalism provides a straightforward algorithm for computing the phonon DOS, simply by sampling the reciprocal-space unit cell using a regular grid with M points $k_j^{(z)} = \frac{j}{M}\frac{2\pi}{l_z}$, $j \in \{0, \dots, M-1\}$, computing the allowed frequencies for each point by solving Eq. (3.6a) and using Gaussian kernel density estimation to build a continuous density from the complete set of discrete frequencies. This was the method used in this chapter. l_z was selected in such a way that, owing to the limited range of the potential, a given unit cell only interacted with its first neighbours. Therefore, Eq. (3.6b) was reduced to a sum of three terms, $\boldsymbol{D} = \boldsymbol{K}_1^\dagger e^{ik^{(z)}l_z} + \boldsymbol{K}_0 + \boldsymbol{K}_1 e^{-ik^{(z)}l_z}$. Here, $\boldsymbol{K}_0$ and $\boldsymbol{K}_1$ refer to the subblocks of $\boldsymbol{K}$ which contain the force constants corresponding to the interactions of atoms in a given unit cell among themselves and with those on

the unit cell to their right, respectively. Each force constant was numerically approximated by the symmetric finite difference between forces

$$\tilde{K}^{(\mu,\mu')}_{l,l',j,j'} = -\frac{\partial f^{(\mu)}_{l,j}}{\partial u^{(\mu')}_{l',j'}} \simeq \frac{f^{(\mu)}_{l,j}\left(\dots, u^{(\mu')}_{l',j'} - H, \dots\right) - f^{(\mu)}_{l,j}\left(\dots, u^{(\mu')}_{l',j'} + H, \dots\right)}{2H}, \tag{3.9}$$

with $H = 10^{-5}$ Å.

3.4. Results and discussion

Table 3.3 lists the thermal conductivities of GaAs, InAs and InP nanowires at 300 K as predicted by MD simulations using the Harrison potential as parameterised by Mingo and Broido [61], by MD simulations performed using an Abell-Tersoff potential parameterised by Hammerschmidt *et al.* [110] for GaAs and InAs and a Vashishta-type potential parameterised by Branício and Rino [63] for InP, and by extrapolating to the appropriate wire diameters the values obtained by Mingo and Broido [61] using Harrison-based theoretical calculations. An estimate of the uncertainty is given for each MD result in order to compare them.

The theoretical and MD Harrison-based results are of the same order of magnitude. The discrepancies between them seem likely to be due to error in extrapolating Mingo and Broido's results [61] to the wire diameters considered here, and to the adoption of different assumptions concerning boundary scattering (totally diffusive in the theoretical calculations, specular in the MD simulations). In principle, another possible source of discrepancy might be the treatment afforded to anharmonic effects: the theoretical results were obtained from the Boltzmann transport equation (BTE) in the relaxation time approximation using an anharmonic relaxation length parameterised by fitting to experimental bulk thermal conductivities, whereas in MD simulations anharmonic effects are generally introduced intrinsically, in this case through the angular term of the Harrison expression for the total energy. However, since for all three compounds the force constant C_1 is only $1 - 2\%$ of C_0 [61], anharmonic effects must have little influence on the thermal conductivities of the wires. Since the present Vashishta/Branício-Rino-based results for InP show little variation with respect to those previously commented in Chapter 2, the finding that the theoretical and MD Harrison-based results are of the same

Table 3.3 Thermal conductivities of GaAs, InAs and InP nanowires for several diameters d, as obtained by MD simulations using the Harrison and Hammerschmidt (Branício-Rino for InP) potentials. Also shown are the values obtained by extrapolation of the results obtained theoretically by Mingo and Broido [61] using the Harrison potential in conjunction with the BTE.

		Harrison (MD)	Hammerschmidt/ Branício-Rino (MD)	Harrison (theoretical)
	d (nm)		$\kappa \left(\frac{\mathrm{W}}{\mathrm{m\ K}}\right)$	
GaAs	2.38	0.87 ± 0.15	7.9 ± 1.1	0.33
	3.17	0.719 ± 0.079	9.30 ± 0.87	0.45
	3.97	0.91 ± 0.16	8.7 ± 1.2	0.58
	4.76	0.99 ± 0.11	7.88 ± 0.78	0.70
InAs	2.57	0.53 ± 0.11	4.21 ± 0.83	0.21
	3.42	0.556 ± 0.069	3.91 ± 0.50	0.29
	4.28	0.72 ± 0.14	3.79 ± 0.90	0.36
	5.13	0.71 ± 0.10	3.84 ± 0.62	0.43
InP	2.49	0.30 ± 0.11	2.11 ± 0.85	0.10
	3.32	0.39 ± 0.16	2.01 ± 0.12	0.17
	4.15	0.47 ± 0.13	2.33 ± 0.24	0.25
	4.97	0.61 ± 0.18	2.36 ± 0.69	0.33

order of magnitude shows, in particular, that the discrepancy between Mingo and Broido's results [61] and those in Chapter 2 regarding InP nanowires must be due to different potentials rather than different methods.

The MD results obtained for GaAs and InAs nanowires using the Abell-Tersoff/Hammerschmidt [110] potential are generally about an order of magnitude larger than those obtained with the Harrison/Mingo-Broido potential (Table 3.3), a difference that echoes the similar discrepancy between Harrison/Mingo-Broido-based and Vashishta/Branício-Rino-based results for InP nanowires. It may nevertheless be noted that for wires of similar diameter the thermal conductivities of Table 3.3 decrease in the order GaAs > InAs > InP whatever the method or potential used for their calculation, in spite of the bulk thermal conductivity of InP [118] (68 W/(m K)) being larger than those of GaAs [119] (45 W/(m K)) and InAs [120] (27.3 W/(m K)). The finding that the best bulk thermal conductor is not necessarily the best nanowire thermal conductor was perhaps the most salient result of Mingo and Broido's study [61]. Precise examination of whether the present results are in keeping with

Mingo and Broido's finding that $\kappa_{bulk}/\kappa_{nano}$ increased with the mass ratio r is prevented by the differences in diameter between the simulated GaAs, InAs and InP nanowires; but in all cases $\kappa_{bulk}/\kappa_{nano}$ is, in agreement with Mingo and Broido's results, much larger for InP than for GaAs or InAs, which have quite similar $\kappa_{bulk}/\kappa_{nano}$ values.

The question now arising is which of the MD predictions shown in Table 3.3 for GaAs, InAs and InP nanowires are most reliable. This is of particular technological interest because the possible use of these nanowires as heat sinks or thermoelectric devices depends on their thermal conductivities. In the absence of experimental data for nanowires with the diameters considered here, it becomes necessary to resort to a theoretical discussion about the capability of the potentials used for describing the thermal conductivities of these wires. It must be noted again that the reliability of atomistic simulations depends, in general, not only on the quality of the potential used, but also on the method employed for its parameterisation. A particular parameterisation, obtained from a specific set of reference data selected as input, might not be appropriate (or transferable) for describing situations that differ significantly from those used for its derivation (see, *e.g.*, Refs. 81 and 110).

The Harrison potential can be considered as the quadratic limit of a number of more complex two- and three- body potentials, including that by Stillinger and Weber [43], and is expected to be valid when the contributions to the total energy due to interactions between non-nearest neighbours are negligible or weakly dependent on the interatomic distances. Since it contains only two adjustable parameters, it offers a limited amount of freedom when fitting them to input properties. Moreover, it is essentially a simple two-body harmonic potential, since the main purpose of its three-body term is merely to ensure that the zinc-blende structure of the binary semiconductor is energetically favourable. In contrast, the Abell-Tersoff/Hammerschmidt and Vashishta/Branício-Rino potentials, with much larger numbers of parameters, have more elaborate two- and three-body contributions. In particular, the attractive and repulsive two-body contributions are taken into account separately, which gives a better description of the asymmetrical potential well seen by each atom. Furthermore, bulk parameters relevant to the thermal conductivity of the materials were taken into account in their parameterisation (in the Abell-Tersoff/Hammerschmidt case, which included elastic constants among the data fitted to) or validation (in the Vashishta/Branício-Rino case, which affords a good prediction of the bulk phonon density of states). The Harrison/Mingo-Broido

potential, though fitted to the experimental values of the frequencies $\omega_{LO}(\Gamma)$ and $\omega_{TA}(X)$ predicts a much less plausible phonon DOS. By way of illustration, Fig. 3.1 shows the DOS calculated using both the Branício-Rino and the Harrison potential for an InP nanowire with d = 5.13 nm, which can be compared with the DOS of bulk InP calculated *ab initio* and presented as Fig. 2 in Ref. 121 (that in turns compares very well with experimental data in Refs. [122–125]). A simple visual inspection shows that the Branício-Rino DOS has an overall shape much closer to those *ab-initio* results. Numerically, the Branício-Rino potential predicts two main peaks in the optical region of the spectrum centred at energies 39.0 and 44 meV, approximately, which agree reasonably well with the corresponding *ab-initio* peaks at 39.0 and 43.6 meV, whereas the Harrison potential puts these high-frequency maxima at 36.7 and 41.3 meV. Similar observations can be made about the acoustic part of the spectrum; in fact, the degree to which the Harrison potential underestimates the lowest-frequency peak is particularly striking: $\sim$ 3.0 meV *vs.* $\sim$ 10.3 meV (*ab-initio*) and $\sim$ 11.0 meV (Branício-Rino).

Therefore, in spite of not having been confronted with relevant experimental thermal conductivity data yet, there are reasons to believe that the results obtained in this chapter using the Abell-Tersoff/Hammerschmidt and Vashishta/Branício-Rino potentials should be more reliable than those obtained using the Harrison potential. It must be noted, however, that thermal conductivity predictions of the Harrison potential for 50 nm InAs nanowires agree quite well with experiment [126, 127]. It therefore seems possible that it is only for nanowires with diameters as small as those considered in this chapter that, presumably because of an increasing sensitivity of vibrational behaviour to many-body interactions as wire diameter decreases, it may be advisable to use more complex potentials.

Figure 3.1 Phonon DOS of the InP nanowire of diameter 5.13 nm, as obtained using the Harrison and Branício-Rino potentials.

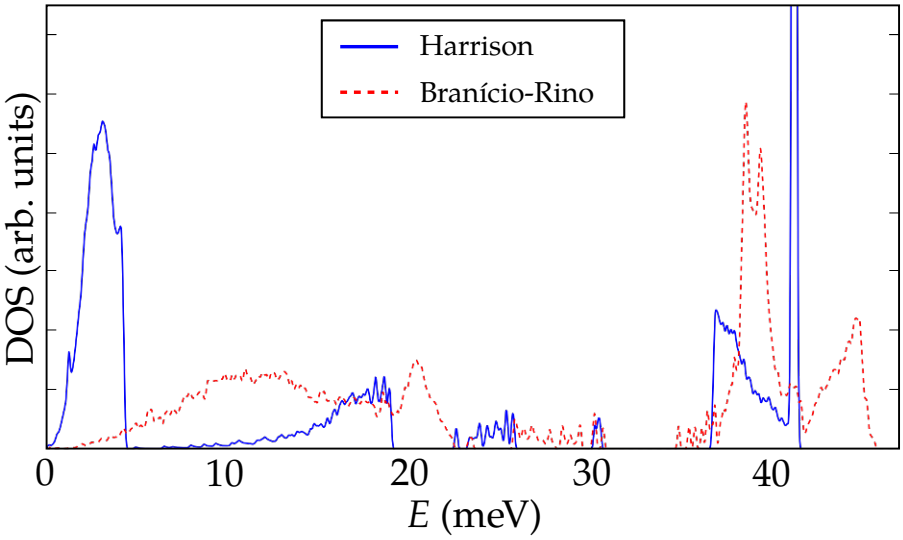

References

36. Mingo, N. *Phys. Rev. B* **68,** 113308 (2003).

38. Chantrenne, P., Barrat, J. L., Blase, X. & Gale, J. D. *J. Appl. Phys.* **97,** 104318 (2005).

39. Volz, S. G. & Chen, G. *Appl. Phys. Lett.* **75,** 2056 (1999).

41. Ponomareva, I., Srivastava, D. & Menon, M. *Nano Lett.* **7,** 1155 (2007).

42. Schelling, P. K., Phillpot, S. R. & Keblinski, P. *Phys. Rev. B* **65,** 144306 (2002).

43. Stillinger, F. H. & Weber, T. A. *Phys. Rev. B* **31,** 5262 (1985).

60. Harrison, W. A. *Electronic Structure and the Properties of Solids* (Dover, New York, 1989).

61. Mingo, N. & Broido, D. A. *Phys. Rev. Lett.* **93,** 246106 (2004).

62. Mingo, N. *Appl. Phys. Lett.* **84,** 2652 (2004).

63. Branício, P. S. & Rino, J. P. *Phys. Stat. Sol. (b)* **244,** 331 (2007).

81. Rey, C., Gallego, L. J., García-Rodeja, J., Alonso, J. A. & Iñiguez, M. P. *Phys. Rev. B* **48,** 8253 (1993).

89. Swope, W. C., Andersen, H. C. & amd K. R. Wilson, P. H. B. *J. Chem. Phys.* **76,** 637 (1982).

99. Zhou, X. W., Aubry, S., Jones, R. E., Greenstein, A. & Schelling, P. K. *Phys. Rev. B* **79,** 115201 (2009).

108. Mingo, N. *Appl. Phys. Lett.* **88,** 149902 (2006).

109. Mingo, N. *Appl. Phys. Lett.* **85,** 5986 (2004).

110. Hammerschmidt, T., Kratzer, P. & Scheffler, M. *Phys. Rev. B* **77,** 235303 (2008).

111. Thomas, J. A., Intzi, R. M. & McGaughey, A. J. H. *Phys. Rev. B* **81,** 045413 (2010).

112. Sellan, D. P., Landry, E. S., Turney, J. E., McGaughey, A. J. H. & Amon, C. H. *Phys. Rev. B* **81,** 214305 (2010).

113. Yang, X., To, A. C. & Tian, R. *Nanotechnology* **21,** 155704 (2010).

114. Tersoff, J. *Phys. Rev. Lett.* **56,** 632 (1986).

115. Tersoff, J. *Phys. Rev. B* **37,** 6991 (1988).

116. Tersoff, J. *Phys. Rev. B* **38,** 9902 (1988).

117. Tersoff, J. *Phys. Rev. B* **39,** 5566 (1989).

118. Both, W., Gottschalch, V. & Wagner, G. *Crysr. Res. Technol.* **21,** K85 (1986).

119. *Properties of Gallium Arsenide* 3rd (eds Brozel, M. R. & Stillman, G. E.) (INSPEC, London, 1996).

120. Steigmeier, E. F. & Kudman, I. *Phys. Rev.* **132,** 508 (1963).

121. Fritsch, J., Pavone, P. & Schröder, U. *Phys. Rev. B* **52,** 11326 (1995).

122. Borcherds, P. H., Alfrey, G. F., Saunderson, D. H. & Woods, A. D. B. *J. Phys. C* **8,** 2022 (1975).

123. Mooradian, A. & Wright, G. B. *Solid State Commun.* **4,** 431 (1966).

124. *Semiconductors: Physics of Group IV and III-IV Compounds* (ed Madelung, O.) (Springer-Verlag, Berlin, 1982).

125. *Semiconductors: Intrinsic Properties of Group IV Elements and III-V, II-VI, and I-VII Compounds* (ed Madelung, O.) (Springer-Verlag, Berlin, 1987).

126. Persson, A. I., Koh, Y. K., Cahill, D. G., Samuelson, L. & Linke, H. *Nano Lett.* **9,** 4484 (2009).

127. Mavrokefalos, A., Pettes, M. T., Saha, S., Zhou, F. & Shi, L. *25th International Conference on Thermoelectrics*, 234 (2006).

4 Surface roughness and thermal conductivity of Si nanowires

> For it is possible long study may increase and confirm erroneous sentences: and where men build on false grounds, the more they build, the greater is the ruin.
>
> *Leviathan*
> Thomas Hobbes

4.1. Introduction

MD provides a set of useful and easily implementable methods for thermal conductivity calculations but, as seen in Chapters 2 and 3, it also has some important shortcomings. In particular, its purely classical nature limits its applicability to relatively high temperatures, and the fact that it does not treat phonons as first-class objects makes the results from MD calculations somewhat opaque. Moreover, the results are very dependent on the choice of potential. Thus, in order to understand thermal transport in nanowires in further detail, it is desirable to use methods with their roots in more fundamental physics. That is the purpose of the work contained in this chapter.

The solution of Eq. (3.6a) for a crystalline system with one-dimensional periodicity consists not only of a set of eigenfrequencies $\left\{\omega_{\Diamond}\right\}$, but also of a basis of eigenstates $\left\{\tilde{w}_{\Diamond,j}^{(\mu)}\right\}$. This basis will be assumed to be orthogonal, something which is always possible through an appropriate choice of degenerate eigenvectors. It is straightforward to check that, in the related basis $\left\{\tilde{u}_{\Diamond,j}^{(\mu)} = \tilde{w}_{\Diamond,j}^{(\mu)}/\sqrt{m_j}\right\}$ and its periodic repetitions, the quadratic approximation to the potential energy expressed in Eq. (3.5) becomes diagonal. Hence, for each value of $k^{(z)}$ the hamiltonian of the system adopts the form of a sum of independent harmonic oscillators, which can be quantised to give

$$\boldsymbol{H}\left(k^{(z)}\right) = \sum_{\Diamond} \hbar\omega_{\Diamond}\left[\left(\boldsymbol{a}_{\Diamond}^{\dagger}\boldsymbol{a}_{\Diamond} + \frac{1}{2}\right)\right]. \tag{4.1}$$

Here, $\boldsymbol{a}_{\Diamond}^{\dagger}$ and $\boldsymbol{a}_{\Diamond}$ are the ladder operators corresponding to one of the oscillation modes, but can also be interpreted, in the second quantization formalism, as phonon creation and annihilation operators. Each phonon of frequency $\omega_{\Diamond}$ carries an energy $\hbar\omega_{\Diamond}$ and a linear momentum $\hbar k^{(z)}$ proportional to its wave number. From a statistical point of view, phonons are bosons and thus follow Bose-Einstein statistics: at equilibrium, the average occupation number of a state is

$$f_{BE}\left(T; k^{(z)}, \Diamond\right) = \frac{1}{e^{\frac{\hbar\omega_{\Diamond}\left(k^{(z)}\right)}{k_B T}} - 1}. \tag{4.2}$$

Transport theory is mainly concerned with states slightly out of equilibrium. The methods used to study them for this work will be explained briefly in the following sections.

Of particular relevance for understanding the size dependence of thermal conductivity is the role of the boundary, which becomes increasingly more important as the surface-to-volume ratio increases, and the ordered or disordered regions therein. For a sufficiently wide nanowire, scattering of phonons by a boundary surface can be approximated by the Casimir formula for bulk systems [128], which predicts a mean free path (MFP) equal to the diameter of the wire times a factor of order unity which depends on the cross-sectional shape. When this source of scattering becomes so dominant as to make any other negligible, something to be expected in very thin crystalline nanowires, it should result in a thermal conductivity proportional to the diameter. This paramet-

erisation has been shown to afford a reasonably good agreement with the available experimental and computational data in this range of widths [129]. On the other hand, experimental data for the lattice thermal conductivity of rough Si nanowires with diameters below 50 nm, reported by Hochbaum *et al.* [130] in 2008, showed values close to the amorphous limit for silicon, which could not be explained by existing theories. Martin *et al.* [131] put forward a theoretical approach which can fit the experimental results and whose key ingredients are a continuum model, the relaxation time approximation, Fermi's golden rule (from first order perturbation theory), a Gaussian approximation [132] to the power spectrum of surface roughness with an adjustable parameter and semiempirical parameterisations of the different scattering sources (phonon-phonon interactions, impurities and the boundary) [36, 133, 134]. Boundary and roughness scattering are thus treated in two different ways (the Casimir formula and perturbation theory, respectively) and then added together under an assumption of statistical independence (a procedure known as Matthiessen's rule). Since the Casimir formula, as it will be explained later in this chapter, already assumes a disordered boundary so that the probability of a phonon being scattered in a particular direction is independent of its direction of incidence, such double counting of the effect of the boundary on phonons seems unwarranted. Moreover, due to the number of adjustable parameters and unassessed approximations present in that description, it is of little predictive value.

In order to contribute to the solution of this controversy, Si was chosen as the material for the nanowires studied in this chapter, in which the results a completely atomistic calculation of boundary scattering in very thin nanowires is presented. The system under study was an hexagonal monocrystalline Si nanowire oriented along the [111] direction, structurally identical to the InAs, InP and GaAs nanowires studied previously except for the fact that all its atoms belong to the same element.

4.2. Quasi-ballistic transport

Consider two heat baths at temperatures $T + \Delta T/2$ and $T - \Delta T/2$ joined by a quasi-one-dimensional structure — such as a nanowire — of length L and cross-sectional area A. Such a setup is depicted schematically in Fig. 4.1. Each bath is large enough to be considered at equilibrium in spite of the heat flowing across the scattering region. Therefore, the occupation number of a level

Figure 4.1 Scheme of a nanowire inserted between two heat baths.

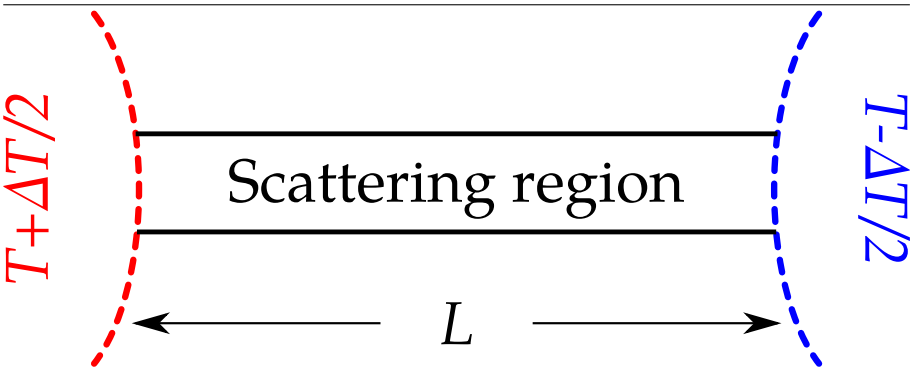

at the thermostats can be evaluated using Eq. (4.2) at the appropriate temperature. If there is a probability $p_{trans}\left(k^{(z)},\lozenge\right)$ that a phonon of wave number $k^{(z)}$ and frequency $\omega_\lozenge\left(k^{(z)}\right)$ be transferred between the two ends of the scattering region, the total heat current must be calculated as a balance between the energy transferred left-to-right and right-to-left by phonons per unit time and area

$$j_Q^{(z)} = \frac{1}{A}\sum_{\lozenge}\int_0^{\frac{\pi}{l_z}}\left[f_{BE}\left(T+\frac{\Delta T}{2};k^{(z)},\lozenge\right) - f_{BE}\left(T-\frac{\Delta T}{2};-k^{(z)},\lozenge\right)\right]\hbar\omega_\lozenge p_{trans}\left(k^{(z)},\lozenge\right)\frac{v_{g,\lozenge}^{(z)}}{L}\frac{dk^{(z)}}{2\pi/L}. \tag{4.3}$$

Provided that $\Delta T \ll T$, the difference between equilibrium distributions in the integrand can be approximated by its first-order Taylor expansion, and the whole equation rewritten as

$$j_Q^{(z)} = \frac{\Delta T}{A}\int \frac{\partial f_{BE}}{\partial T}\hbar\omega\mathscr{T}(\omega)\frac{d\omega}{2\pi}, \tag{4.4}$$

where $\mathscr{T}(\omega)$ is known as the transmission function — or simply the transmission — of the nanowire at frequency ω, and the integral over frequencies can be understood to run either from 0 to ∞, with $\mathscr{T}(\omega) = 0$ for values of ω beyond the upper edge of the vibrational spectrum (ω_U) or from 0 to that limit. From Eq. (4.3), it is clear that $0 \leq \mathscr{T}(\omega) \leq \mathscr{N}(\omega)$, where $\mathscr{N}(\omega)$ is the number of vibrational modes with frequency ω. The upper limit can only be reached if all the

transmission probabilities are 1, *i.e.*, if there is no scattering at all in the central region. Since the average temperature gradient across the nanowire is $-\Delta T/L$, a combination of Eq. (4.4) and Fourier's law (2.1) yields a thermal conductivity

$$\kappa = \frac{j_Q^{(z)}}{(\Delta T/L)} = \frac{L}{2\pi A}\int \frac{\partial f_{BE}}{\partial T} h\omega \mathscr{T}(\omega)\, d\omega. \tag{4.5}$$

In macroscopic problems, κ is independent from L. However, Eq. (4.5) implies that this is not always the case in the nanoscale. In particular, if there is no scattering, $\mathscr{T}(\omega) = \mathscr{N}(\omega)\ \forall\ \omega \in [0, \omega_U]$, and it is the thermal conductance,

$$G_T \coloneqq \frac{A j_Q^{(z)}}{\Delta T} = \frac{A}{L}\kappa, \tag{4.6}$$

instead of the thermal conductivity, that is independent of the length of the nanowire. This regime of thermal transport is known as ballistic (or, more precisely, quasi-ballistic when the transmission is not perfect) as opposed to the more usual one, referred to as ohmic due to its resemblance to Ohm's law for electric resistors. Thus, in the ballistic regime, thermal conductivity is not a especially useful concept. It is unrealistic to expect the ballistic regime to be valid for long nanowires, but Eq. (4.5) can still be useful in an ohmic setting if a suitable transmission is defined.

The problem of characterising boundary scattering in thin nanowires will be approached in two steps in the following two sections. First, a method for calculating a detailed form of the phononic transmission across a localised defect that can be treated in the ballistic regime (its length being small enough that phonons remain coherent, in quantum terms) will be presented, and then it will be used to calculate the scattering cross-section of the localised defect, which in turn can yield a transmission valid in the ohmic regime.

4.3. Transmission calculations

For a periodic system, diagonalising $\boldsymbol{D}$ is equivalent to diagonalising $\boldsymbol{K}$: their eigenvalues coincide and their eigenvectors are trivially related. If the system under consideration is of a more general nature, periodic or aperiodic, finite or infinite, the convenience of always working with a finite number of elements [using Eq. (3.6a)] has to be abandoned and the normal modes of the

system obtained by solving the general equation $\boldsymbol{K}|k\rangle = \omega^2|k\rangle$ or, in a homogeneous form,

$$\left(\omega^2\mathbf{1} - \boldsymbol{K}\right)|k\rangle = \mathbf{0}. \tag{4.7}$$

An inhomogeneous version of this equation, with a non-zero matrix in the right-hand side, can be solved using the fundamental solution (or resolvent) $\left(\omega^2\mathbf{1} - \boldsymbol{K}\right)^{-1}$. In the context of thermal transport studies, this is known as the phononic Green's function for historic reasons. There are well-known methods to calculate quasi-ballistic transmissions in the harmonic approximation using Green's functions [16], but for the work presented here a new algorithm was developed which provides more detailed information in the form of transition probabilities between the individual vibrational modes in the left and the right part of the scattering region.

Let us consider a perfectly crystalline nanowire formed by repetition of a (possibly non-primitive) unit cell of length l_z chosen so that, as in Chapter 3 and owing to the limited range of the potential, a given unit cell only interacts with its first neighbours. Its stiffness matrix will be denoted by $\mathscr{K}$, of which the only different non-zero building blocks are $\mathscr{K}_0$ and $\mathscr{K}_1$, which describe the harmonic interactions between an unit cell and itself and between an unit cell and the one to its right, respectively. For each $k^{(z)}$, the eigenvalues of the dynamical matrix are the allowed frequencies of the system squared, and the corresponding eigenvectors are the wave functions which describe the movements of each atom in the unit cell when the system is oscillating in a particular mode. Alternatively, it is possible to obtain the allowed values of $k^{(z)}$ for a given ω by solving the generalised eigenvalue problem:

$$\begin{pmatrix} \omega^2\mathbf{1} - \mathscr{K}_1 & -\mathscr{K}_1^\dagger \\ \mathbf{1} & \mathbf{0} \end{pmatrix} \vec{\tilde{c}} = \lambda \begin{pmatrix} \mathscr{K}_1 & \mathbf{0} \\ \mathbf{0} & \mathbf{1} \end{pmatrix} \vec{\tilde{c}}. \tag{4.8}$$

Obviously, the eigenvectors $\vec{\tilde{c}}$ thus obtained are defined over two unit cells. It can be easily checked that the unitary eigenvalues of the problem are $e^{ik^{(z)}l_z}$ and that the first half of each $\vec{\tilde{c}}$ is the corresponding $\vec{\tilde{w}}$, an eigenvector of the dynamical matrix. In the remainder of this section, $\left\{\left|k_\lozenge^{(z)}\right\rangle\right\}$ will denote the set of normal modes of the perfect system for a particular ω, as defined over the whole nanowire, with wave numbers $\left\{k_\lozenge^{(z)}\right\}$. Although the system is infinite, for normalisation purposes a very large number N_z of unit cells will be considered,

keeping in mind that the final expressions will be valid in the limit $N_z \longrightarrow \infty$; therefore, $\left\langle k_{\diamondsuit}^{(z)} \middle| k_{\clubsuit}^{(z)} \right\rangle = N_z \delta_{\diamondsuit\clubsuit}$. This implies that $\left[\vec{\varpi}_{\diamondsuit}(I)\right]^{*} \cdot \vec{\varpi}_{\clubsuit}(I) = \delta_{\diamondsuit\clubsuit}$, if $\vec{\varpi}_{\diamondsuit}(I)$ is the restriction of $\left|k_{\diamondsuit}^{(z)}\right\rangle$ to the I-th unit cell. For notational brevity, $\vec{\varpi}_{\diamondsuit}(0)$ will be simply denoted as $\vec{b}_{\diamondsuit}$.

In $k^{(z)}$-space, the Green's function of this perfect nanowire can be expressed as [16]:

$$\boldsymbol{g}^{+}\left(\omega, k^{(z)}\right) = \frac{1}{N_z} \sum_{\diamondsuit} \frac{\left|k_{\diamondsuit}^{(z)}\right\rangle \left\langle k_{\diamondsuit}^{(z)}\right|}{\omega^2 - \omega_{\diamondsuit}^2 + i\eta}, \tag{4.9}$$

for $\eta \longrightarrow 0^{+}$. Strictly speaking, this is the causal Green's function. The anti-causal Green's function $\boldsymbol{g}^{-}$ would be obtained if $\eta \longrightarrow 0^{-}$ was taken instead.

A defect can be introduced in the nanowire by replacing the unit cell $I = 0$ of the perfect system with a different set of atoms. This operation breaks the translational symmetry of the system, which becomes aperiodic. If the stiffness matrix of the defective nanowire is represented by $\boldsymbol{K}$, the impurity operator, $\boldsymbol{V}$, is defined as

$$\boldsymbol{V} := \boldsymbol{K} - \mathscr{K}, \tag{4.10}$$

and the t-matrix which connects both situations, as

$$\boldsymbol{t}^{+} = \boldsymbol{V}\left(\mathbf{1} - \boldsymbol{g}^{+}\boldsymbol{V}\right)^{-1} = \left(\mathbf{1} - \boldsymbol{V}\boldsymbol{g}^{+}\right)^{-1}\boldsymbol{V}. \tag{4.11}$$

Provided that l_z is large enough, the real-space representations of these two operators are nonzero only over the unit cell $I = 0$, that is, if $\boldsymbol{t}^{+}(I, I')$ is the submatrix of $\boldsymbol{t}^{+}$ connecting cells I and I', only $\boldsymbol{t}^{+}(0,0)$ is non-zero, and the same applies to $\boldsymbol{V}$.

The normal modes of the system containing the defect, at each frequency ω, will be denoted by $\left\{\left|q_{\diamondsuit}\right\rangle\right\}$, and their restrictions to the central unit cell ($I = 0$) by $\left\{\vec{e}_{\diamondsuit}\right\}$. They are related to $\left\{\left|k_{\diamondsuit}\right\rangle\right\}$, since Eq. (4.7) for the defective nanowire can be recast in the inhomogeneous form

$$\left(\omega^2\mathbf{1} - \mathscr{K}\right)\left|q\right\rangle = \boldsymbol{V}\left|q\right\rangle \tag{4.12}$$

and solved using its fundamental solution, which is precisely $\boldsymbol{g}^{+}$. This process leads to the Lippmann-Schwinger equation

$$\left|q_{\diamondsuit}\right\rangle = \left|k_{\diamondsuit}\right\rangle + \boldsymbol{g}^{+}\boldsymbol{t}^{+}\left|k_{\diamondsuit}\right\rangle \tag{4.13a}$$

$$\vec{\tilde{e}}_{\diamondsuit} = \vec{\tilde{w}}_{\diamondsuit} + \boldsymbol{g}^{+}(I,0)\,\boldsymbol{t}^{+}(0,0)\,\vec{\tilde{w}}_{\diamondsuit}. \tag{4.13b}$$

Phonons can be scattered by the impurity. A phonon travelling from the left part of the system, which acts as the left lead, can either be transmitted to the right lead or reflected. The probability amplitude of each process is measured by the amplitude transmission and reflection coefficients, $\left\{t_{\clubsuit\diamondsuit}\right\}$ and $\left\{r_{\clubsuit\diamondsuit}\right\}$. $r_{\clubsuit\diamondsuit}$ is the probability amplitude that a phonon of mode $\diamondsuit$ coming from the left be reflected as a phonon of mode $\clubsuit$ propagating to the left in the left lead. Likewise, $t_{\clubsuit\diamondsuit}$ denotes the probability amplitude of it being transmitted as a phonon of mode $\clubsuit$ propagating towards the right in the right lead. In terms of eigenstates, this means that very far into the leads the following expansions apply:

$$I \longrightarrow -\infty \qquad \Rightarrow \qquad \vec{\tilde{e}}_{\diamondsuit}(I) = \vec{\tilde{w}}_{\diamondsuit} + \sum_{\clubsuit\,(\text{left})} r_{\clubsuit\diamondsuit}\vec{\tilde{w}}_{\clubsuit}(I) \tag{4.14a}$$

$$I \longrightarrow \infty \qquad \Rightarrow \qquad \vec{\tilde{e}}_{\diamondsuit}(I) = \sum_{\clubsuit\,(\text{right})} t_{\clubsuit\diamondsuit}\vec{\tilde{w}}_{\clubsuit}(I)\,. \tag{4.14b}$$

A plane wave with amplitude a and frequency ω carries an amount of energy per unit time proportional to $\omega^2\left|a\right|^2\frac{d\omega}{dk^{(z)}}$ through a surface perpendicular to its wave vector. Thus, the energy transmission and reflection coefficients between modes can be trivially obtained from $\left\{t_{\clubsuit\diamondsuit}\right\}$ and $\left\{r_{\clubsuit\diamondsuit}\right\}$:

$$R_{\clubsuit\diamondsuit} = \left|r_{\clubsuit\diamondsuit}\right|^2\left|\frac{v_{g,\clubsuit}}{v_{g,\diamondsuit}}\right|^2 \tag{4.15a}$$

$$T_{\clubsuit\diamondsuit} = \left|t_{\clubsuit\diamondsuit}\right|^2\left|\frac{v_{g,\clubsuit}}{v_{g,\diamondsuit}}\right|^2. \tag{4.15b}$$

Comparing Eqs. (4.13b) and (4.14a), the following expression is obtained, valid for $I \longrightarrow -\infty$:

$$\sum_{\clubsuit\,(\text{left})} r_{\clubsuit\diamondsuit}\vec{\tilde{w}}_{\clubsuit}(I) = \sum_{\clubsuit\,(\text{left})} r_{\clubsuit\diamondsuit}\vec{\tilde{b}}_{\clubsuit}e^{-ik_{\clubsuit}^{(z)}l_z I} = \boldsymbol{g}^{+}(I,0)\,\boldsymbol{t}^{+}(0,0)\,\vec{\tilde{b}}_{\diamondsuit}. \tag{4.16}$$

The limit $\lim_{I\longrightarrow-\infty} g(I,0)$ can be obtained in an efficient fashion using the decimation method, which will be briefly described in a later section so, in principle,

this system of linear equations could be solved in order to yield the amplitude reflection coefficients. This is numerically impossible, however, because of the complex exponentials on the left-hand side. When $|I|$ is very large, they are infinitely sensitive to small variations in $k_{\clubsuit}^{(z)}$, so any approximations to their numerical values are meaningless in practice. A better approach is thus to study analytically the asymptotic behaviour of the Green's function. The first step to achieve this is to obtain an expression for this operator in real space from the Fourier transform in Eq. (4.9):

$$g^{+}(-I,0)=\frac{l_z}{2\pi}\int_{-\frac{\pi}{l_z}}^{\frac{\pi}{l_z}}\frac{e^{ik^{(z)}l_zI}}{\omega^2-\omega_{\diamondsuit}^2\left(k^{(z)}\right)+i\eta}dk^{(z)}. \tag{4.17}$$

Next, the fact can be used that $\left[\omega^2-\omega_{\diamondsuit}^2\left(k^{(z)}\right)+i\eta\right]^{-1}$ is the Laplace transform, evaluated at point η, of the function $exp\left\{i\left[\omega^2-\omega_{\diamondsuit}^2\left(k^{(z)}\right)-\pi/2\right]\right\}$, so in the limit $\eta\longrightarrow 0^{+}$

$$g^{+}(-I,0)=\frac{-il_z}{2\pi}\sum_{\diamondsuit}F_{\diamondsuit},\ \text{with}\ F_{\diamondsuit}:=\int_{-\frac{\pi}{l_z}}^{\frac{\pi}{l_z}}\int_{0}^{\infty}e^{i\left\{\left[\omega^2-\omega_{\diamondsuit}^2\left(k^{(z)}\right)\right]+k^{(z)}l_zI\right\}}dtdk^{(z)}. \tag{4.18}$$

Due to the quickly oscillating nature of the integrand, only the stationary points of the exponent $E_{\diamondsuit}(k,t)$ contribute to each $F_{\diamondsuit}$ in the limit $|I|\longrightarrow\infty$. Differentiating $E_{\diamondsuit}$ with respect to $k^{(z)}$ and t and imposing the condition that both derivatives are zero, the following relations are found for the coordinates $k_{\diamondsuit,st}^{(z)}$ and $t_{\diamondsuit,st}$ of those points: $\omega=\omega_{\diamondsuit}\left(k_{\diamondsuit,st}^{(z)}\right)$ and $l_zI=-2\omega_{\diamondsuit}\left(k_{\diamondsuit,st}^{(z)}\right)v_{g,\diamondsuit}\left(k_{\diamondsuit,st}^{(z)}\right)t_{\diamondsuit,st}$. The first of them implies that the stationary point obeys the dispersion relation. The second relation determines the value of $t_{\diamondsuit,st}$ for that point. Continuing with the argument that only the stationary points contribute to the integral, the following second-order Taylor expansion of the exponent is valid:

$$e^{E_{\diamondsuit}\left(k^{(z)},t\right)}=e^{ik_{\diamondsuit}^{(z)}l_zI}e^{-i\left\{\frac{1}{2}\left.\frac{d^2\omega_{\diamondsuit}^2}{dk^{(z)^2}}\right|_{k^{(z)}=k_{\diamondsuit}^{(z)}}\left(k^{(z)}-k_{\diamondsuit}^{(z)}\right)^2t_{\diamondsuit,st}+2\omega v_{g,\diamondsuit}\left(k_{\diamondsuit,st}^{(z)}\right)\left(k^{(z)}-k_{\diamondsuit,st}^{(z)}\right)\left(t-t_{\diamondsuit,st}\right)\right\}}. \tag{4.19}$$

Moreover, the limits of integration can be extended, without altering the result, to $k^{(z)},t\in(-\infty,\infty)$. A Dirac δ function then results from integration in t, and

the result is simply

$$F_{\diamondsuit} = \frac{\pi e^{ik_{\diamondsuit}^{(z)} l_z I}}{l_z \omega \left| v_{g,\diamondsuit}(\omega) \right|}, \tag{4.20}$$

which can be substituted into (4.18) and (4.16) to give

$$I \longrightarrow \infty \Rightarrow -\boldsymbol{t}^{+}(0,0)\,\vec{\tilde{b}}_{\diamondsuit} i \sum_{\clubsuit} \frac{e^{ik_{\diamondsuit}^{(z)} l_z I}}{2\omega \left| v_{\clubsuit}(\omega) \right|} = \sum_{\clubsuit\,(\text{left})} \vec{\tilde{b}}_{\clubsuit} e^{ik_{\diamondsuit}^{(z)} l_z I} r_{\clubsuit\diamondsuit}. \tag{4.21}$$

Taking the dot product of this expression by the conjugate of a left-propagating mode $\heartsuit$:

$$I \longrightarrow \infty \Rightarrow -\vec{\tilde{b}}^{*}_{\heartsuit} \cdot \boldsymbol{t}^{+}(0,0)\,\vec{\tilde{b}}_{\diamondsuit} i \sum_{\clubsuit} \frac{e^{ik_{\diamondsuit}^{(z)} l_z I}}{2\omega \left| v_{\clubsuit}(\omega) \right|} = \sum_{\clubsuit\,(\text{left})} \vec{\tilde{b}}^{*}_{\heartsuit} \cdot \vec{\tilde{b}}_{\clubsuit} e^{ik_{\diamondsuit}^{(z)} l_z I} r_{\clubsuit\diamondsuit}. \tag{4.22}$$

Now, for any two different modes $\heartsuit$ and $\clubsuit$, both propagating to the left, either $k_{\heartsuit}^{(z)} \neq k_{\clubsuit}^{(z)}$, in which case the two exponentials are linearly independent, or $\vec{\tilde{b}}^{*}_{\heartsuit} \cdot \vec{\tilde{b}}_{\clubsuit} = 0$. In any case,

$$r_{\heartsuit\diamondsuit} = \frac{i}{2\omega \left| v_{g,\heartsuit} \right|} \vec{\tilde{b}}^{*}_{\heartsuit} \cdot \boldsymbol{t}^{+}(0,0)\,\vec{\tilde{b}}_{\diamondsuit}. \tag{4.23}$$

Finally, group velocities can be obtained using Eq. (3.8); taking everything into account, an expression for the energy reflection coefficients, based on Eq. (4.15a) , can be formulated:

$$R_{\clubsuit\diamondsuit} = \frac{\left| \vec{\tilde{b}}^{*}_{\clubsuit} \cdot \boldsymbol{t}^{+}(0,0)\,\vec{\tilde{b}}_{\diamondsuit} \right|^2}{\left| \vec{\tilde{b}}^{*}_{\clubsuit} \cdot \frac{\partial \boldsymbol{D}}{\partial k^{(z)}} \vec{\tilde{b}}_{\clubsuit} \right| \left| \vec{\tilde{b}}^{*}_{\diamondsuit} \cdot \frac{\partial \boldsymbol{D}}{\partial k^{(z)}} \vec{\tilde{b}}_{\diamondsuit} \right|}, \tag{4.24}$$

where $\diamondsuit$ is right-propagating and $\clubsuit$ left-propagating. Perfect [111] nanowires have left-right inversion symmetry, so for each left-propagating mode $\clubsuit$ there is a right-propagating mode with the same frequency, opposite wave number and conjugate eigenvector. Therefore, Eq. (4.24) can be rewritten, more conveniently, in terms of two right-propagating modes $\diamondsuit$ and $\clubsuit$:

$$R_{\clubsuit\diamondsuit} = \frac{\left| \vec{\tilde{b}}_{\clubsuit} \cdot \boldsymbol{t}^{+}(0,0)\,\vec{\tilde{b}}_{\diamondsuit} \right|^2}{\left| \vec{\tilde{b}}^{*}_{\clubsuit} \cdot \frac{\partial \boldsymbol{D}}{\partial k^{(z)}} \vec{\tilde{b}}_{\clubsuit} \right| \left| \vec{\tilde{b}}^{*}_{\diamondsuit} \cdot \frac{\partial \boldsymbol{D}}{\partial k^{(z)}} \vec{\tilde{b}}_{\diamondsuit} \right|}. \tag{4.25}$$

Arguments identical to the ones presented lead to the following equations for the energy transmission coefficients:

$$T_{\clubsuit\diamondsuit} = \frac{\left|\vec{\tilde{b}}^{*}_{\clubsuit} \cdot \boldsymbol{t}^{+}(0,0)\,\vec{\tilde{b}}_{\diamondsuit}\right|^{2}}{\left|\vec{\tilde{b}}^{*}_{\clubsuit} \cdot \frac{\partial \boldsymbol{D}}{\partial k^{(z)}}\vec{\tilde{b}}_{\clubsuit}\right|\left|\vec{\tilde{b}}^{*}_{\diamondsuit} \cdot \frac{\partial \boldsymbol{D}}{\partial k^{(z)}}\vec{\tilde{b}}_{\diamondsuit}\right|}. \tag{4.26}$$

Here, $\diamondsuit$ and $\clubsuit$ must not only be right-propagating, but also different. $T_{\diamondsuit\diamondsuit}$ can be obtained from the conservation of energy:

$$T_{\diamondsuit\diamondsuit} = 1 - \sum_{\clubsuit} R_{\clubsuit\diamondsuit} - \sum_{\heartsuit\neq\diamondsuit} T_{\heartsuit\diamondsuit} \tag{4.27}$$

since the energy carried by a phonon must be either reflected or transmitted in the scattering region.

The total transmission at a given frequency, $\mathscr{T}(\omega)$, can be recovered as the sum of all the detailed transmission coefficients, $\mathscr{T}(\omega) = \sum_{\diamondsuit,\clubsuit} T_{\diamondsuit\clubsuit}$. As an intermediate step, the probability that the energy of a phonon of mode $\diamondsuit$ coming from the left be transmitted, either by a phonon of the same mode or by one of a different mode, is equal to the sum $T_{\diamondsuit} = \sum_{\clubsuit} T_{\diamondsuit\clubsuit}$. A more common way to express the same idea is in terms of the total scattering cross section of the defect for phonons of mode $\diamondsuit$, *i.e.*, the flux of phonons scattered by the defect per unit incoming current [135]:

$$\sigma_{\diamondsuit}(\omega) = \frac{2\pi\Omega}{\left|\vec{\tilde{b}}^{*}_{\diamondsuit} \cdot \frac{\partial \boldsymbol{D}}{\partial k}\vec{\tilde{b}}^{*}_{\diamondsuit}\right|} \sum_{\clubsuit} \left|\vec{\tilde{b}}^{*}_{\clubsuit} \cdot \boldsymbol{t}^{+}(0,0)\,\vec{\tilde{b}}_{\diamondsuit}\right|^{2}, \tag{4.28}$$

where Ω is the volume used to normalise the eigenvectors $\left\{\vec{\tilde{b}}_{\diamondsuit}\right\}$. When $\left|\boldsymbol{g}^{+}\boldsymbol{V}\right| \ll 1$ in a suitable norm, $\boldsymbol{t}^{+} \simeq \boldsymbol{V}$ is a very useful approximation to Eq. (4.11) that avoids having to find the inverse of any operator. When this is introduced in Eq. (4.28), it becomes a version of Fermi's golden rule for calculating transition probabilities between pairs of quantum states [136]. In this context, it is also an instance of the Born approximation to $\boldsymbol{t}^{+}$. Regardless of its convenience, it must be borne in mind that the domain of validity of this approximation is limited.

4.4. Infinite rough nanowires: the ohmic regime

The method developed in the previous section allows the transmission probabilities across a localised defect in an otherwise perfect nanowire (or, equivalently, the cross section of the defect) to be calculated. However, the nanowires with which this chapter concerns itself have defects distributed all along their surface. To overcome this limitation, it will be assumed that coupling between different defective segments is completely incoherent, that is, phases are not important since they are randomised by anharmonic effects. In practical terms, this means that interactions of a phonon with different defects can be treated as independent stochastic events, and their probabilities (as opposed to their complex probability amplitudes) combined. Therefore, the transit of a phonon through an infinite nanowire with a homogeneous distribution of defects in its surface is a stationary Poisson random process. The fundamental parameter in such a process is the average number of collisions per unit time or per unit length. The inverse of the latter is called the MFP (Λ); the inverse of the former is known as the relaxation time (τ). By the definition of scattering cross section, $\sigma_\Diamond$,

$$\frac{1}{\Lambda_\Diamond} = \rho_d \sigma_\Diamond, \tag{4.29}$$

where ρ_d is the density of defects. Clearly, the ratio $\Lambda_\Diamond/\tau_\Diamond$ must be equal to $v_{g,\Diamond}$, so both descriptions are trivially equivalent.

For a long nanowire, the situation depicted in Fig. 4.1 is not realistic. Instead, a linear temperature field $T(z)$ must be assumed to be defined along the nanowire, with a local distribution of phonons over states close to the equilibrium Bose-Einstein distribution,

$$f\left(z;k^{(z)},\Diamond\right) = f_{BE}\left(T(z);k^{(z)},\Diamond\right) + f_1\left(z;k^{(z)},\Diamond\right), \text{ with } \left|f_1\right| \ll \left|f_{BE}\right|. \tag{4.30}$$

In a steady state, $\partial f\left(z;k^{(z)},\Diamond\right)/\partial t = 0$. This partial derivative has two contributions which must, accordingly, cancel each other. The first is a ballistic term that measures the changes in the distribution due to phonons flowing in and out the volume around z from the adjacent regions. By arguments completely analogous to those that led to Eq. (4.4), this term is found to have the expres-

sion

$$\left(\frac{\partial f\left(z;k^{(z)},\lozenge\right)}{\partial t}\right)_{\text{ballistic}} = -\frac{\partial f\left(z;k^{(z)},\lozenge\right)}{\partial z}v_{g,\lozenge}^{(z)} \simeq -\frac{\partial f_{BE}\left(T;k^{(z)},\lozenge\right)}{\partial T}\frac{\partial T}{\partial z}v_{g,\lozenge}^{(z)}. \quad (4.31)$$

The second term comes from scattering processes which add or remove phonons from the same volume. These processes have been assumed to be stochastic, Poisson-type and stationary, so the form of this term, which tends to re-establish thermal equilibrium, must be a product of the rate at which scattering processes are happening, $\tau_{\lozenge}^{-1}$, and the deviation from equilibrium f_1:

$$\left(\frac{\partial f\left(z;k^{(z)},\lozenge\right)}{\partial t}\right)_{\text{scattering}} = -\frac{f_1\left(z;k^{(z)},\lozenge\right)}{\tau_{\lozenge}}. \quad (4.32)$$

This heuristic course of reasoning thus leads to a simple form of the Boltzmann transport equation (BTE) in the relaxation time approximation [137]:

$$\frac{\partial f_{BE}\left(T;k^{(z)},\lozenge\right)}{\partial T}\frac{\partial T}{\partial z}v_{g,\lozenge}^{(z)} = -\frac{f_1\left(z;k^{(z)},\lozenge\right)}{\tau_{\lozenge}}. \quad (4.33)$$

At equilibrium, there can be no net thermal transport and, as a consequence, the net heat current can be computed using only f_1. Taking its value from Eq. (4.33), combining the contributions of all normal modes, and dividing by the cross-sectional area,

$$j_Q^{(z)} = \frac{1}{A}\sum_{\lozenge}\int\left(-\frac{\partial T}{\partial z}\right)\hbar\omega\frac{\partial f_{BE}}{\partial T}\tau_{\lozenge}v_{g,\lozenge}^{(z)}\frac{d\omega}{2\pi} \quad (4.34)$$

is obtained, which affords a thermal conductivity

$$\kappa = \frac{1}{2\pi A}\int\hbar\omega\frac{\partial f_{BE}}{\partial T}\left(\sum_{\lozenge}\tau_{\lozenge}v_{g,\lozenge}^{(z)}\right)d\omega. \quad (4.35)$$

This equation can be cast in the form of Eq. (4.5) if the transmission is identified, in the ohmic regime, with $\mathscr{T}(\omega) = \frac{1}{L}\sum_{\lozenge}\tau_{\lozenge}v_{\lozenge}^{(z)}$. It should be noted that, as expected, the value of κ afforded by Eq. (4.35) does not depend on L.

4.5. The Casimir mean free path

In 1938, H. Casimir theoretically derived the MFP for particle-like carriers in thin wires under diffuse boundary conditions [128]. The Casimir formula is valid under the assumption that phonons behave like classical point-like particles bouncing off the walls of a translationally-symmetric wire with rough boundaries in such a way that after each collision phonons are isotropically re-emitted at random and lose any memory of their incident direction. In this setup, the length of the wire and the wavelengths of phonons do not enter the problem; therefore, the phonon MFP must be proportional to d, the only length scale left. In fact, it can be proven by simple geometrical arguments that

$$\Lambda_{\text{Casimir}} = \frac{3\pi}{4} \langle D \rangle , \tag{4.36}$$

where $\langle D \rangle$ is the average distance from a random point inside the wire to a random point at its boundary with the same value of z, understood as a double average over the cross-sectional area and over the corresponding boundary curve. When a constant-z slice of the nanowire is a regular polygon, whose sides are segments of straight lines, Λ_{Casimir} is particularly easy to calculate semi-numerically. In that case, the average distance from a point to the whole boundary is equal to its average distance to a particular side of the polygon, due to rotational symmetry. Thus, the integral over the boundary can be performed analytically as a simple integral over a segment. The Casimir MFP for regular polygons of up to 20 sides is shown in Fig. 4.2. It can be seen that Λ_{Casimir} converges rapidly to d as the number of sides is increased; indeed, $\Lambda_{\text{Casimir}} = d$ is the analytic result for a cylindrical nanowire. Of particular interest for this work is the case of an hexagonal prism, for which the Casimir MFP is $0.907d$.

This approach was extended by Ziman [137] to consider the effect of partly specular surfaces, yielding a correction factor $\frac{1+p}{1-p}$, where p is the coefficient of specularity, ranging from 0 for diffusive scattering to 1 for mirror-like reflection. Work by Dingle [137, 138] showed that when some intrinsic bulk scattering mechanism acts together with boundary scattering, the exact solution of the BTE yields nearly the same conductivity as if one used an effective MFP given by Mathiessen's approximated rule, $\Lambda^{-1} \simeq \Lambda^{-1}_{\text{intrinsic}} + \Lambda^{-1}_{\text{Casimir}}$. For thin wires the boundary term dominates, and thus Casimir's diffuse boundary MFP determines a lower bound for the thermal conductivity. However Casimir's deduction neglects factors such as the atomistic structure of the

Figure 4.2 Casimir MFP for nanowires of regular polygonal cross-section (3 to 20 sides) as a fraction of their outer diameter. The solid line is provided only as a guide to the eye.

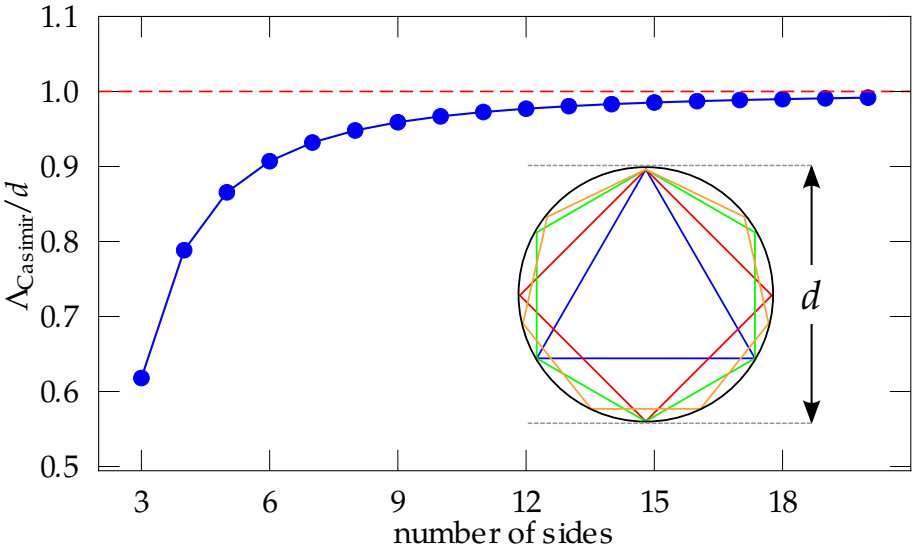

boundary and the wave nature of phonons, which could come into play for very small diameters. It is therefore desirable to check its validity using atomistic approaches.

4.6. The Stillinger-Weber potential

In this work, interactions between the atoms in the system were described by means of the well-known Stillinger-Weber (SW) potential. This model has been used to describe the crystalline and liquid phases of bulk Si [43], and more recently to investigate the structures, nanomechanics, phonon spectra and thermal conductivities of thin Si nanowires (see, *e.g.*, Refs. 41, 139 and those cited therein). It is a potential with two- and three-body contributions in the general form of Eq. (2.3) and with the following functional choices [43]:

Table 4.1 Parameters of the SW potential for Si, from Ref. 43.

$\sigma = 0.2091$ nm	$\epsilon = 2.1678$ eV	$A = 7.049556277$
$B = 0.6022245584$	$a = 1.80$	$\lambda = 21.0$
$p = 4$	$q = 0$	$\gamma = 1.20$

$$V_{ij}^{(2)}(r) = \epsilon f^{(2)}\left(\frac{r}{\sigma}\right) \tag{4.37a}$$

$$V_{ijk}^{(3)}\left(\vec{r}_i, \vec{r}_j, \vec{r}_k\right) = \epsilon f^{(3)}\left(\frac{\vec{r}_i}{\sigma}, \frac{\vec{r}_j}{\sigma}, \frac{\vec{r}_k}{\sigma}\right) \tag{4.37b}$$

$$f^{(2)}(r) = \begin{cases} A\left(Br^{-p} - r^{-q}\right) exp\left\{(r-a)^{-1}\right\}, & r < a \\ 0, & r > a \end{cases} \tag{4.37c}$$

$$f^{(3)}\left(\vec{r}_i, \vec{r}_j, \vec{r}_k\right) = h\left(r_{ij}, r_{ik}, \theta_{ijk}\right) + h\left(r_{ji}, r_{jk}, \theta_{jik}\right) + h\left(r_{ki}, r_{kj}, \theta_{kij}\right) \tag{4.37d}$$

$$h\left(r_{ij}, r_{ik}, \theta_{ijk}\right) = \begin{cases} \lambda\, exp\left\{\gamma\left(r_{ij} - a\right)^{-1} + \gamma\left(r_{ik} - a\right)^{-1}\right\}\left(cos\,\theta_{ijk} + \frac{1}{3}\right)^2, & r_{ij}, r_{ik} < a \\ 0, & \text{otherwise.} \end{cases} \tag{4.37e}$$

The optimal parameters for Si were also taken from Stillinger and Weber's original paper [43], and are included in Table 4.1

4.7. Computational details

According to Sections 4.3 and 4.4, the theoretical approach for obtaining the thermal conductivity of a nanowire can be summarised as follows: compute the Green's function of a perfect nanowire, use it in conjunction with $\boldsymbol{V}$ to calculate the scattering cross section of any defect of interest for all possible frequencies and modes employing Eqs. (4.28) and (4.11), convert this set of values to MFPs and substitute them in Eq. (4.35) in order to obtain the thermal conductivity. Therefore, the crucial missing object is the submatrix $g^+(0,0)$: a block from the diagonal of the real-space representation of the Green's function of an infinite, perfect nanowire. This can, obviously, be approximated to an arbitrary degree by a block in the central part of the diagonal (*i.e.*, far from the edges) of the real-space representation of the Green's function of a finite

but very long nanowire. For this work an extremely efficient method to obtain such block was used, decimation [140–142], an iterative renormalisation-group approach which operates with the two non-zero blocks of the interatomic force constant matrix for the perfect nanowire yielding, at its j-th iteration, $\boldsymbol{g}^{+}\,(0,0)$ for a nanowire with 2^j copies of the original unit cell, thereby quickly reaching macroscopic dimensions (since $log_2\, 6.022{\cdot}10^{23} \simeq 79$). With 36 decimation steps, this calculation was fully converged with respect to the number of steps and was insensitive to the precise value of the imaginary part of ω^2 — the variable denoted as η in Eq. (4.17) — which was taken as $\left(10^{-5}\ \mathrm{THz}\right)\omega$.

All the systems for which force constant matrices were calculated were relaxed to their minimum-energy configurations, but the degree of surface reconstruction afforded by the SW potential is rather limited due to its being optimised for bulk silicon. It must be noted that, in contrast to the MD models of previous chapters, no rigid boundary conditions are needed for the Green's function calculations undertaken here.

Perfect [111] nanowires of hexagonal cross-section have D_3 symmetry (like an equilateral triangle): they are invariant under the identity operation 1, under inversions about three axes separated by $2\pi/3$ (operations A, B and C), and under $2\pi/3$ and $4\pi/3$ rotations around OZ (operations D and E). D_3 has three irreducible representations (irreps) denoted as Γ_1, Γ_2 and Γ_3, and a character table like the one in Table 4.2. As a consequence, representations of linear operators such as the interatomic force matrix and the Green's function of the nanowire can be reduced to a block-diagonal form in a symmetry-adapted basis. Such basis was constructed in two steps. First, the incomplete projection operators [143] associated to the three irreps were found, in the canonical basis formed by the displacements along OX, OY and OZ of all the atoms in a unit cell. Then, an orthonormal basis was extracted from each of these rank-deficient matrices. The union of the three bases is precisely the symmetry-adapted basis. Harnessing symmetries was essential in order to make the whole calculation process feasible, since the complexity of matrix inversion and other related operations is proportional to the cube of the matrix dimensions. Symmetries were used in the calculation of normal modes — the three blocks of the dynamical matrix can be diagonalised separately, and for instance vibrational modes that transform like translation under the action of D_3 come from the Γ_3-adapted part of $\boldsymbol{D}$ — and in the decimation process. However, symmetry is broken by the introduction of defects, and thus the sparse LU decomposition [144] employed to calculate the matrix elements of $\boldsymbol{t}^{+}$ used in Eq.

Table 4.2 Character table for group D_3.

	1	A,B,C	D,E
Γ_1	1	1	1
Γ_2	1	−1	1
Γ_3	2	0	−1

(4.28) is, by a large margin, the most time-consuming part of the calculation.

The SW potential, its analytical derivatives and the numerical calculation of its Hessian according to Eq. (3.9) where implemented in C using LAPACK built on the highly optimised Goto version of BLAS [145]. The code for the decimation process was ported to C from a Mathematica® notebook kindly provided by Dr. Natalio Mingo. The rest of the code was implemented in Python and run in parallel on 16 processors. Each CPU ran the calculations for a set of frequencies; in the harmonic approximation, different frequencies can be treated independently, thereby allowing a linear scaling of performance with number of processors.

4.8. Results and discussion

A nanowire with a diameter $d = 2.22$ nm was considered — four atomic layers in the radial direction, 182 atoms in the unit cell — as the starting perfect system. As in previous chapters, thin nanowires were deemed the most interesting because of their lower similarity to the bulk. Moreover, real-space Green's function methods are even more limited than MD-based models with regard to the number of atoms that can be treated, because of their different computational complexities (cubic *vs.* linear scaling with the number of atoms).

In order to simulate the effect of surface roughness, two scenarios were investigated: shallow roughness, where only atoms from the outermost layer were removed at random, with 50% probability; and deep roughness, where, on top of the existing shallow roughness, deep semi-spherical cavities were dug along the wire surface. An example of each case, along with an image of the perfect nanowire, is shown in Fig. 4.3. The associated scattering cross sections were then computed using Eq. (4.28), and the MFPs and relaxation times were derived from them.

Figure 4.3 $d = 2.22$ nm Si nanowire: perfect (left), with shallow surface roughness (centre) and with deeper surface cavities (right)

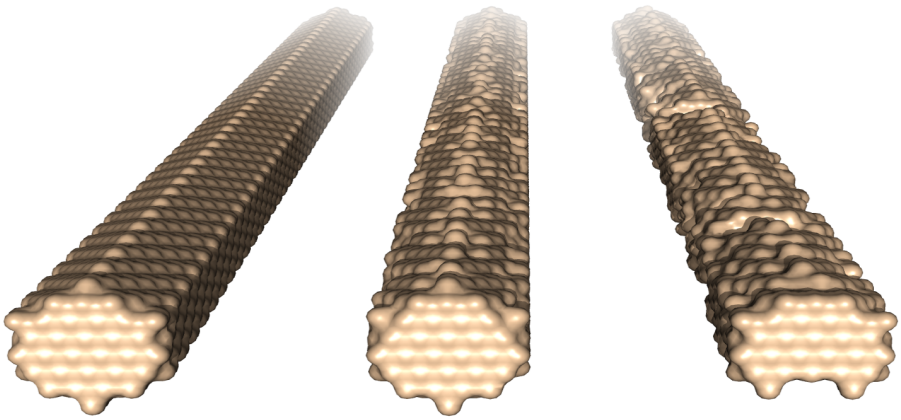

Figure 4.4 (top) shows the spectrum of the nanowire as obtained from the diagonal form of the dynamical matrix for each value of $k^{(z)}$. For comparison, the bottom panel of the same figure shows the same calculation performed with other of the most used potentials for Si, the Tersoff potential [116]. This potential was also implemented in C and a subset of the calculations presented here repeated with it, as well as with a parameterisation of the SW potential for germanium [146], with comparable conclusions. Comparing both panels of Fig. 4.4, it can be seen that the SW potential overestimates the upper edge of the vibrational spectrum, a suspicion confirmed by *ab initio* and experimental results for bulk Si [147]. Fortunately, the high-frequency part of the spectrum has a very small influence on thermal conductivity. The Tersoff potential also has its shortcomings, such as not predicting the diamond structure as the ground state of bulk silicon and inaccuracies in the prediction of bulk elastic constants [148]; this goes to show that, in general, there is no "perfect" semiempirical potential. On the other hand, the fact that the results presented here are robust with respect to the change of potential lends them greater weight.

The average relaxation times for each frequency are shown in Fig. 4.5. Both the exact results and those obtained using the Born approximation diverge at low frequencies, indicating quasi-ballistic transmission. At higher frequencies, the exact relaxation times suggest that the Casimir approximation is adequate. There is, however, a striking difference of $1 - 2$ orders of magnitude between the red and green curves, with the Born approximation resulting in an unreal-

Figure 4.4 Vibrational spectrum of a $d = 2.22$ nm nanowire obtained using the SW (top) and Tersoff (bottom) potentials. Line styles correspond to irreps: full⇒ Γ_1, dotted⇒ Γ_2, dashed⇒ Γ_3.

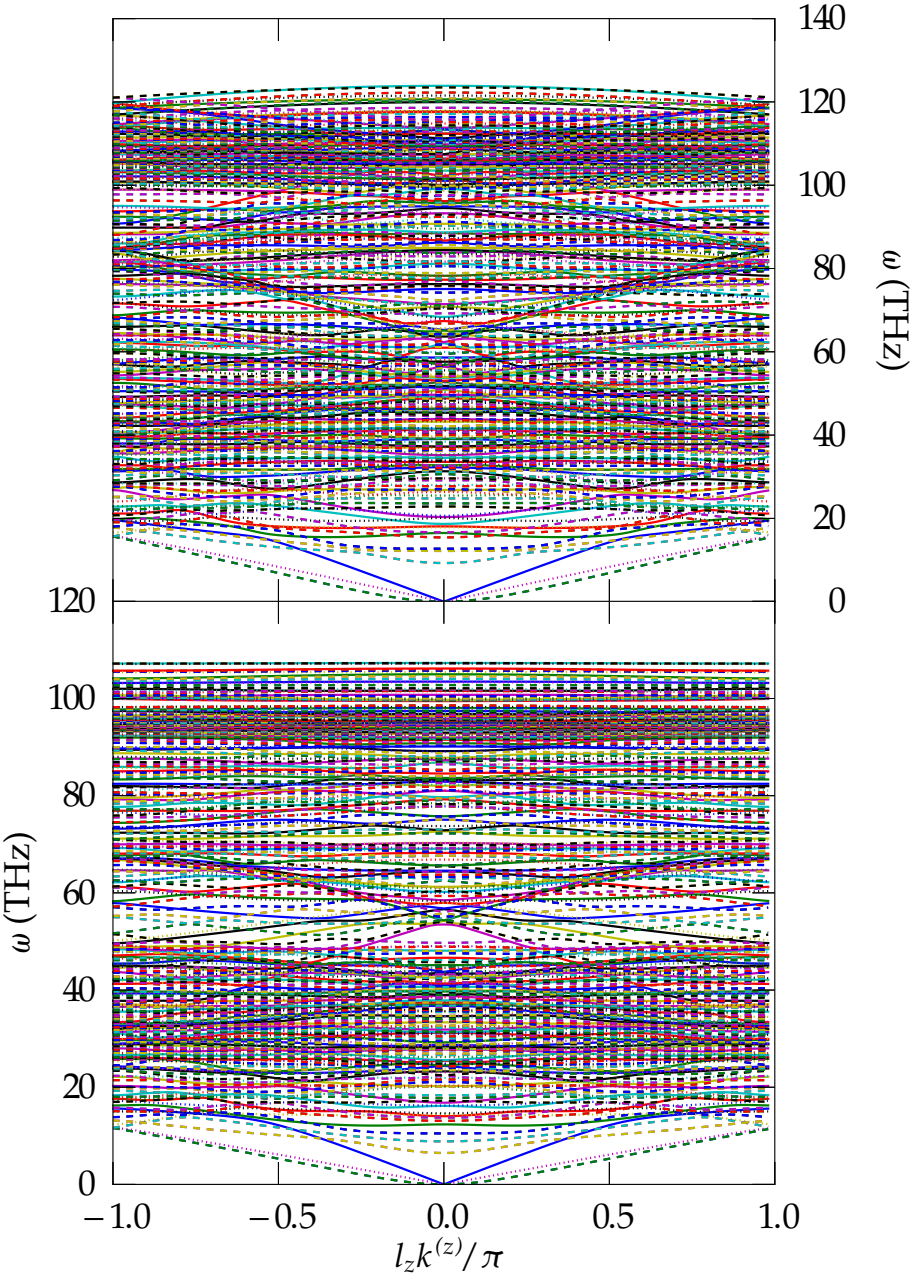

Figure 4.5 Relaxation times, averaged over all the available modes for each frequency, in a $d = 2.22$ nm wire with half of its outermost atoms removed, calculated using the exact $\boldsymbol{t}^+$ matrix and the Born approximation. The Casimir limit is also plotted for comparison. The shadowed area corresponds to the part of the spectrum for which the resistance of the contacts would be the dominating factor, as explained in the text.

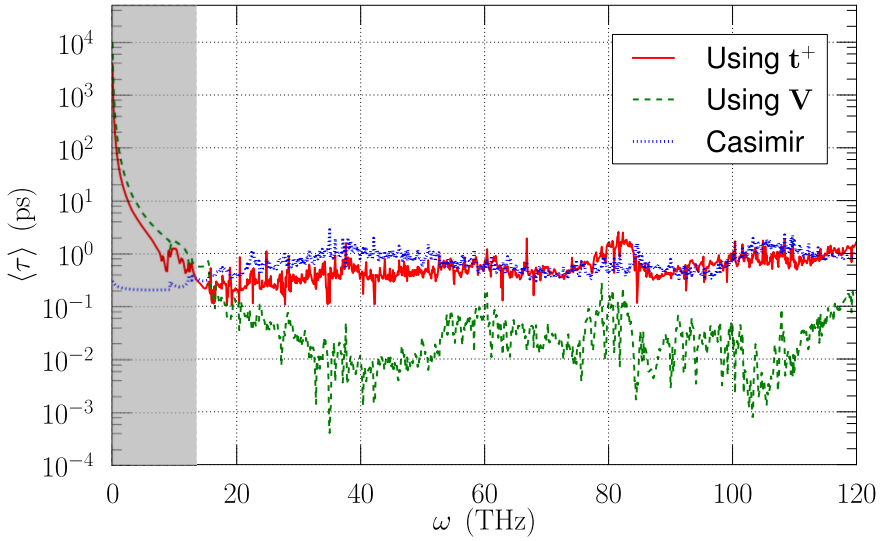

istically high estimate of the scattering cross section. This is a general feature of the approximation in this context and becomes even worse when larger defects are introduced.

Further evidence of this failure is the fact that, if the total reflectance of a single defective segment is calculated using Eq. (4.25) and summing over one of the subscripts, and again introducing the perturbative approximation $\boldsymbol{t}^+ \simeq \boldsymbol{V}$, for most frequencies this reflectance is much larger than the transmission of the perfect system. This is a clearly absurd result which, if substituted into Eq. (4.5) and integrated, would yield a negative value for the thermal conductivity.

Surface roughness with a characteristic size larger than the size of the simulation cell (1.9 nm) is not included in the simulation and thus the scattering of longer-wavelength/lower-frequency phonons is Rayleigh-like, nearly ballistic. The contribution of this part of the spectrum to the thermal conductivity is, however, negligible if the frequency dependence of the transmission probability between the contacts used for measuring the thermal conductance and the

nanowire itself is taken into account. As shown in Ref. 149, it is proportional to ω^2. This probability was included in the thermal conductivity calculation by using a composition rule for the transmission of the wire plus contact system [150]. The region where contact scattering dominates the composition, causing the results from t-matrix calculations alone to be insufficient, is shown shadowed in Fig. 4.5.

Figure 4.6 compares the thermal conductivities calculated from Eq. (4.35) using MFPs predicted by Eq. (4.28) —in red—, the Born approximation — dashed green— and the Casimir formula with the appropriate form factor — dotted blue— for the system discussed in the foregoing paragraph. The exact MFPs afford a thermal conductivity in reasonable agreement with the Casimir approximation, whereas the perturbative result is qualitatively and quantitatively different, reaching saturation at much lower temperature and conductivity. The values shown here agree in order of magnitude with those obtained in Ref. 151 for rough Si nanowires using MD simulations. As mentioned before, there could be some overestimation of the conductivities due to the fact that the SW potential yields phonon frequencies above their true values, but this would affect the three curves in Fig. 4.6 and thus not undermine this conclusion. Since very thin nanowires are those furthest removed from the context of the derivation of the Casimir formula (which is known to be valid for thick ones), these results suggest that such formula should be a good approximation also for all larger thicknesses. The role of the contact-nanowire transmission (less important for thick wires) in suppressing the divergence at low frequencies would be played in that case by the vanishing, bulk-like number of available states for each frequency [36].

It is possible to go well below the Casimir value by blocking the phonons using defects which penetrate deeper into the nanowire. Figure 4.7 shows the effect on the conductivity (computed at $T = 1000$ K) of removing an almost semi-spherical cluster of up to 100 atoms from each 1.9 nm-long segment of the wire. The conductivity is normalised to the value obtained by the Casimir formula. As before, the Born approximation overestimates the thermal resistance by an order of magnitude. From the t-matrix results it can be concluded that the reduction in conductivity resulting from further removal of atoms is rather slow once about a quarter of the cross-sectional area of the wire has been removed. Thus, it is difficult to achieve a reduction in conductivity of more than one order of magnitude with respect to the Casimir limit without compromising other desirable properties or even the structural stability of the

Figure 4.6 Thermal conductivity of a $d = 2.22$ nm nanowire with half of its outermost atoms removed, as a function of temperature, calculated using Eq. (4.35) either with the exact t-matrix, the Born approximation or the Casimir MFP.

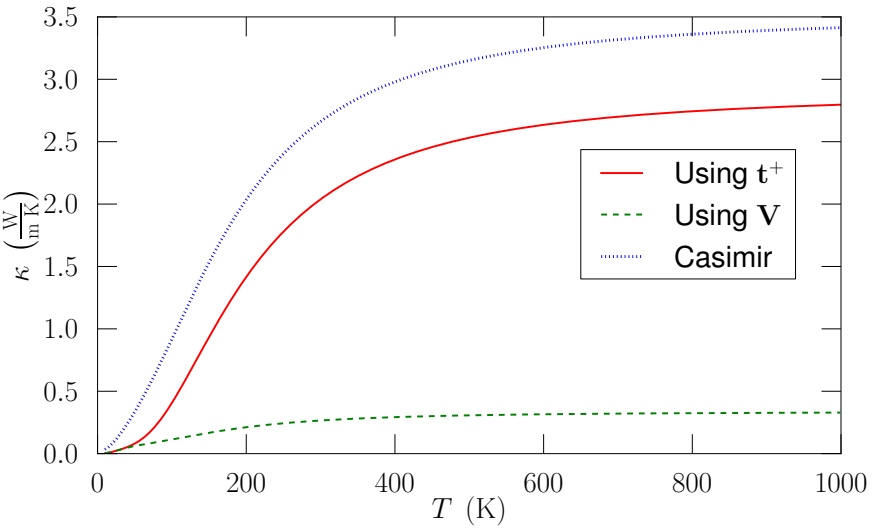

system.

The progressively smaller efficiency of further removal of atoms is to be expected if the situation is compared, qualitatively, to the scattering of phonons by spherical nanoparticles studied by Kim and Majumdar [152], who suggest the interpolation formula $\sigma^{-1} = \sigma^{-1}_{\text{Rayleigh}} + \sigma^{-1}_{\text{near -gometrical}}$, resulting in a scattering efficiency that increases quickly with the radius of the sphere when it is small, but simply oscillates around the geometrical limit for larger radii.

The possibility of reducing wire conductivity below the Casimir limit had been investigated in the past using non-atomistic approaches. The Montecarlo work by Moore *et al.* [153] introduced deep boundary roughness in the form of sawtooth boundaries. They found that phonon backscattering can cause the coefficients of specularity to become negative, indicating MFPs below the Casimir limit. However, neither their predictions nor the ones reported in this work match the extremely low experimental conductivities found in Ref. 130. This is especially surprising since the depth of the disordered layers in the experimental nanowires is smaller (relative to their diameter) than in the simulations. All of this and the difference in order of magnitude between the exact

Figure 4.7 Bottom: Thermal conductivity at $T = 1000$ K, relative to the Casimir value, of a $d = 2.22$ nm nanowire with half of its outermost atoms and an additional cluster of atoms removed, calculated using Eq. (4.35) with the exact t-matrix (solid line) or the Born approximation (dashed line). Top: minimum cross-sectional area of each nanowire, relative to the perfect system.

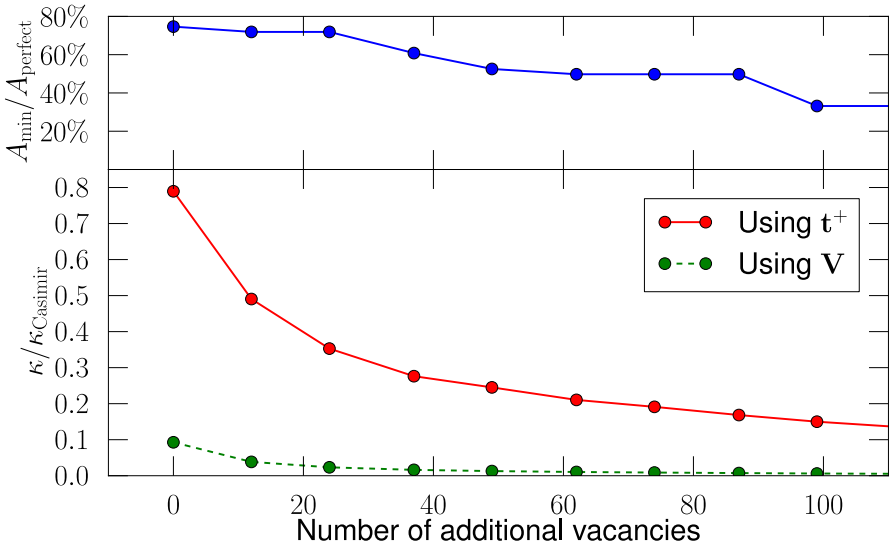

and approximate curves in Fig. 4.7 suggest that the interpretation of experimental data in Ref. 131 may be just an artifact caused by the Born approximation.

The Casimir limit can be overcome, but in most feasible situations the Casimir formula still constitutes a good approximation to the effect of boundary scattering on phonon transport in thin semiconductor nanowires with surface disorder and, as a result, achieving a reduction in conductivity of more than one order of magnitude below the Casimir limit might involve such a strong surface distortion so as to compromise the structural stability of the nanowire. Surface roughness cannot be the only cause for the extremely low thermal conductivity that has been experimentally reported for Si nanowires [130]. A full theoretical understanding of such data is therefore still lacking; however, the results about deep surface cavities just presented suggest the existence of clusters of defects inside the measured nanowires as a very plausible hypothesis. Experimental support for this possibility has been provided very recently by measurements on silicon nanowire arrays with controlled

roughness performed by Cahill and coworkers [154], who found that it can be used to explain not only values of κ below the Casimir limit — their results still being significantly higher, however, than those by Hochbaum *et al.* [130] — but also some features found in the Raman spectra of their arrays.

References

16. Economou, E. N. *Green's Functions in Quantum Physics* (Springer-Verlag, New York, 1990).

36. Mingo, N. *Phys. Rev. B* **68,** 113308 (2003).

41. Ponomareva, I., Srivastava, D. & Menon, M. *Nano Lett.* **7,** 1155 (2007).

43. Stillinger, F. H. & Weber, T. A. *Phys. Rev. B* **31,** 5262 (1985).

116. Tersoff, J. *Phys. Rev. B* **38,** 9902 (1988).

128. Casimir, H. B. G. *Physica* **5,** 495 (1938).

129. Zhu, Y. F., Lian, J. S. & Jiang, Q. *Appl. Phys. Lett.* **92,** 113101 (2008).

130. Hochbaum, A. I., Chen, R., Delgado, R. D., Liang, W., Garnett, E. C., Najarian, M., Majumdar, A. & Yang, P. *Nature (London)* **451,** 163 (2008).

131. Martin, P., Aksamija, Z., Pop, E. & Ravaioli, U. *Phys. Rev. Lett.* **102,** 125503 (2009).

132. Goodnick, S. M., Gann, R. G., Sites, J. R., Wilmsen, C. W., Fathy, D. & Krivanek, O. L. *J. Vac. Sci. Technol.* **1,** 582696 (1983).

133. Holland, M. G. *Phys. Rev.* **132,** 2461 (1963).

134. Glassbrenner, C. J. & Slack, G. A. *Phys. Rev.* **134,** A1058 (1964).

135. Mingo, N., Esfarjani, K., Broido, D. A. & Stewart, D. A. *Phys. Rev. B* **81,** 045408 (2010).

136. Dirac, P. A. M. *Proc. Roy. Soc. (London)* **114,** 243 (1927).

137. Ziman, J. M. *Electrons and Phonons* (Oxford University, New York, 1960).

138. Dingle, R. B. *Proc. Roy. Soc. (London)* **A201,** 545 (1950).

139. Thonhauser, T. & Mahan, G. D. *Phys. Rev. B* **71,** 081307(R) (2005).

140. Guinea, F., Tejedor, C., Flores, F. & Louis, E. *Phys. Rev. B* **28,** 4397 (1983).

141. M. P. López-Sancho, J. M. L.-S. & Rubio, J. *J. Phys. F: Met. Phys.* **15,** 851 (1985).

142. Zhang, W., Mingo, N. & Fisher, T. *Numer. Heat Transfer, Part B* **51,** 333 (2007).

143. Cotton, F. A. *Chemical Applications of Group Theory* third (John Wiley & Sons, Ney York, 1990).

144. Golub, G. H. & van Loan, F. *Matrix Computations* 3rd ed. (JHU Press, 1996).

145. Goto, K. & van de Geijn, R. *ACM T. Math. Software* **35,** 4 (2008).

146. Jian, Z., Kaiming, Z. & Xide, X. *Phys. Rev. B* **41,** 12915 (1990).

147. Wei, S. & Chou, M. Y. *Phys. Rev. B* **50,** 2221 (1994).

148. *Trends in Computational Nanomechanics: Transcending Length and Time Scales* 1st ed. (ed Dumitrica, T.) (Springer, New York, 2009).

149. Chang, C. & Geller, M. R. *Phys. Rev. B* **71,** 125304 (2005).

150. Heron, J.-S., Bera, C., Fournier, T., Mingo, N. & Bourgeois, O. *Phys. Rev. B* **82,** 155458 (2010).

151. Donadio, D. & Galli, G. *Nano Lett.* **10,** 847 (2010).

152. Kim, W. & Majumdar, A. *J. Appl. Phys.* **99,** 084306 (2006).

153. Moore, A. L., Saha, S. K., Prasher, R. S. & Shi, L. *Appl. Phys. Lett.* **93,** 083112 (2008).

154. Feser, J. P., Sadhu, J. S., Azeredo, B. P., Hsu, K. H., Ma, J., Kim, J., Seong, M., Fang, N. X., Li, X., Ferreira, P. M., Sinha, S. & Cahill, D. G. *Thermal Conductivity of Silicon Nanowire Arrays with Controlled Roughnes* Preprint available online at `http://users.mrl.uiuc.edu/cahill/SiNW_TDTR.pdf`. Retrieved on 2012-04-06. 2012.

5 Thermoelectric properties of hybrid organic-inorganic superlattices

> For in the blended wine there are both water and wine in potentiality, but not potentiality in the first sense, I mean in the sense of suitableness as water is in potential to mist; but neither simply in the second sense, I mean the one according to the state only, as it is with the sleeping geometer. But rather it is in the manner of the drunken geometer, trying to do geometry, acting according to his state but not uncorruptedly, that also the water and wine remain in the blend. For each acts in the mixture in a limited way. So, on the one hand, both are preserved in potentiality, but neither is in actuality such as it was at the beginning.
>
> *Commentary on Aristotle's "On Generation and Corruption"*
> John Philoponous

5.1. Introduction

The rational control of thermoelectric transport has been the subject of growing interest in recent years. One of the driving forces behind this phenomenon is the pursuit of a device able to take advantage of temperature

gradients and provide electric power without employing any moving parts and delivering an efficiency at least comparable to more conventional systems like steam turbines. Waste heat is omnipresent in our industrial society, and if such a device existed that could make use of it, it could be used everywhere from solar cells to hot water pipes. The same thermodynamic cycle, when run in reverse, moves heat against a temperature gradient at the expense of electric power which, if done efficiently, would provide a basis for cooling devices of different scales, from microelectronics to solid state air conditioning.

The efficiency η of a thermoelectric generator operating cyclically between two thermal baths at temperatures $T_\pm = T \pm \Delta T/2$ is defined as the ratio between the power transferred to its electric load and the thermal energy absorbed per unit time. Conservation of energy guarantees that $0 \leq \eta \leq 1$ in a cyclic stationary process, and the second law of thermodynamics translates into an upper bound $\eta_C = 1 - \frac{T_-}{T_+}$, the Carnot efficiency [155]. It can be shown [156] that, for a given thermoelectric material,

$$\left(\frac{\eta}{\eta_C}\right)_{\max} = \frac{\sqrt{1+ZT}-1}{\sqrt{1+ZT}-\eta_C+1} \tag{5.1}$$

is the maximum relative efficiency attainable with a single thermoelectric element in a steady state. Here, Z is the thermoelectric figure of merit — defined in the next section, Eq (5.5). Since $Z \propto \sigma/\kappa$, metals are poor candidates for thermoelectric materials as this ratio is approximately universal at a given temperature according to the Wiedemann-Franz law (2.2). But even for semiconductors, where heat and charge carriers are different (phonons and electrons+holes, respectively), the inability to independently manipulate the thermal and electric properties remains a major obstacle to viable thermoelectric conversion. In traditional inorganic thermoelectrics the density and mobility of charge carriers is interlinked with thermal transport, as any scattering mechanism introduced in these systems tends to affect both electrons and phonons. Several values of ZT have been proposed as the threshold for practical viability of thermoelectric devices beyond niche markets. For instance, an efficiency $\eta/\eta_C \sim 30\%$ — comparable to home refrigeration — could be achieved with $ZT = 4$ [157]. Unfortunately, the best room-temperature thermoelectric semiconductor alloys available (*e.g.*, highly doped Bi_2Te_2) have $ZT \sim 1$. Higher values, around 2.4, have been measured in Bi_2Te_3/Sb_2Te_3 superlattices [158]. On the organic side, conducting polymers have also been explored for thermoelectric applications owing to their relatively low thermal conductivity (typic-

Figure 5.1 Schematic representation of three periods of a HOI superlattice.

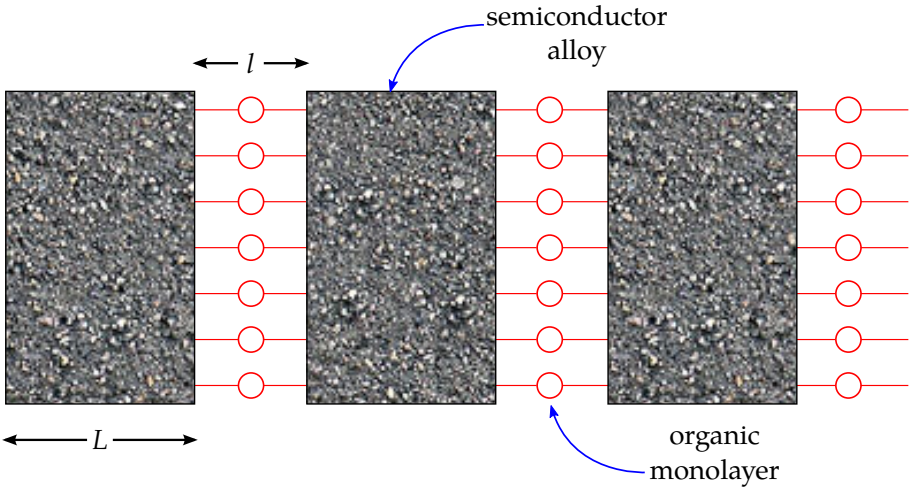

ally an order of magnitude less than inorganic materials). Nonetheless, the Seebeck coefficient values so obtained also tend to be an order of magnitude lower than for inorganic materials and maintaining high electric conductivities through robust doping schemes can be challenging [159, 160].

An emerging class of materials that has not been investigated for thermoelectric applications is that of hybrid organic/inorganic structures (HOI) [161]. An HOI is a bulk material, typically a superlattice or a nanocomposite, composed of alternating organic and inorganic layers or domains of nanometer size. A particular case of this is a superlattice where inorganic layers of the same thickness are separated by self-assembled monolayers of organic molecules (Fig. 5.1). Such materials have been synthesised in several instances [162–167], and their application as semiconducting channels in thin-film field-effect transistors [168, 169], photoconductive devices [170], and diodes [171] has been envisaged. However, research on thermoelectric properties of hybrid systems has so far been limited to one single molecular interface [172–175], so the properties of a hypothetical bulk HOI superlattice are not known, either theoretically or experimentally. Intuitively, the thermal conductivity of the HOI superlattice could be expected to be extremely low, because phonons will be strongly backscattered by the soft organic interfaces. In addition, organic chemistry techniques might allow to tailor the electronic properties of the interface so as to achieve a high enough overall ZT for the bulk HOI. This

Figure 5.2 Left: a tri-thiophene molecule, with (top) or without (bottom) a lateral phenyl group, connected to a pair of hydrogen-passivated semiconductor atoms. Right: fragment of a SiGe+tri-thiophene superlattice, showing a monolayer of tri-thiophene molecules inserted between two blocks of a random $Si_{0.5}Ge_{0.5}$ alloy.

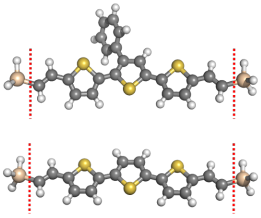

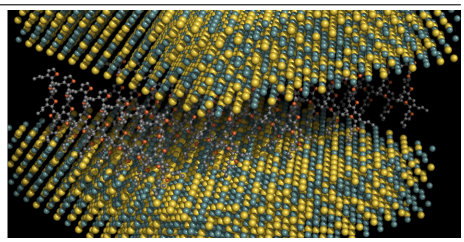

question is investigated in this chapter; it is concluded that HOI materials can indeed display very low thermal conductivities and enhanced ZT, and that they can be fine tuned by organic chemistry techniques. It is also found that using a semiconductor alloy as the inorganic component is crucial to obtain a high ZT in the HOI structures.

The particular systems investigated here are made of periodically repeated layers of monocrystalline Si, or of a SiGe alloy, separated by self-assembled monolayers (SAM) of tri-thiophene (see Fig. 5.2). It may not be easy to synthesise a HOI superlattice containing SiGe, since the high temperatures typically required to grow the semiconductor may destroy the organic part. Ref. 162 presents various alternative synthesis approaches already used in other systems. For example, it would be possible to roll up an epitaxial layer of SiGe coated with the organic SAM, in the way already demonstrated for other hybrid HOIs in Refs. 165–167. Substrate transfer techniques may also be an option to circumvent this problem. SAMs of related molecules, such as ω-thiophene-functionalised n-alkyltrichlorosilane, allyl phenyl thiophene ether and thiophene-terminated alkyl chains, have been experimentally grown on Si substrates [176–178]. The choice of SiGe for the present work is based on ease of calculation, but the physical phenomena identified by this study are likely to take place in any generic HOI superlattice that uses a thermoelectric alloy as the inorganic component. From an experimental point of view, it may be simpler to employ other alloys such as BiSbTeSe, which are compatible with low temperature growth and wet chemistry techniques.

5.2. Thermoelectric coefficients

If an electric field $E^{(z)}$ and a temperature gradient $\partial T/\partial z$ are applied to a system such as the one in Fig. 5.1 along the OZ direction (horizontal axis in the figure) charge and energy currents will appear. Provided that $\left|E^{(z)}\right|$ and $\left|\partial T/\partial z\right|$ are small enough, those thermal and electric currents will be linearly related to these thermodynamic forces. Although an HOI superlattice is clearly anisotropic, when only forces along the OZ direction are considered the resulting currents ($j^{(z)}$ and $j_Q^{(z)}$) will be parallel to them because of inversion symmetries with respect to any plane containing the OZ axis. Therefore, the linear transport regime can be described in terms of the following two scalar phenomenological relations:

$$j^{(z)} = l_{EE}E^{(z)} + l_{ET}\left(-\frac{\partial T}{\partial z}\right) \tag{5.2a}$$

$$\frac{j_Q^{(z)}}{T} = l_{TE}E^{(z)} + l_{TT}\left(-\frac{\partial T}{\partial z}\right). \tag{5.2b}$$

The left-hand sides have been chosen [179] so as to ensure that the sum of their products by the corresponding thermodynamic forces, $j^{(z)}E^{(z)}+T^{-1}j_Q^{(z)}\left(-\partial T/\partial z\right)$, is proportional to a valid entropy source term, thereby allowing Onsager's reciprocity relations [180] to be used, which in this case means that $l_{ET} = l_{TE}$. It must be noted, however, that Onsager's results were originally developed for macroscopic systems and that they cannot be simply assumed to be valid in the nanoscale. In the sixties, T. L. Hill solved a related problem, namely the *a priori* non-applicability of conventional equilibrium thermodynamics to small systems. His approach began by considering a large ensemble of such elements, well in the thermodynamic limit, and using it to develop equations for the average nanosystem. The resulting formalism, known as nanothermodynamics, has been successfully applied to several kinds of systems, including micelles [181] and nanosolids [182]. More importantly for the present chapter, it has recently been extended to non-equilibrium situations [183]. The most important consequence drawn from that theoretical development is that, even though the theoretical reasoning leading to Onsager's reciprocity relations has to be modified to take into account the non-extensive character of nanothermodynamics, those relations can still be expected to hold. Thus, there is a solid theoretical basis for relying on Onsager's reciprocity in the context of, *e.g.*, a self-assembled molecular monolayer of the kind treated in this chapter.

By considering some particular cases, the four phenomenological coefficients in Eqs. (5.2) can be identified with combinations of more usual physical parameters. As regards the diagonal coefficients, when $\partial T/\partial z = 0$, Eq. (5.2a) is recognisable as a microscopic version of Ohm's law; thus, $l_{EE} = \sigma$. On the other hand, κ, as used in Fourier's law (2.1), is defined for $j^{(z)} = 0$ (as opposed to $E^{(z)} = 0$) so, according to Eqs. (5.2), $\kappa = T\left(l_{TT} - l_{TE}^2/\sigma\right)$. At this point, only one coefficient remains in its original form, precisely the one coupling electric and thermal transport. The earliest known manifestation of thermoelectric phenomena, first observed in 1821 and published in 1823 [184], is known as the Seebeck effect. In its simplest form, it consists of the fact that if a temperature difference ΔT is applied between the ends of a bar built from a metal or a semiconductor, an open-circuit voltage difference ΔV can be measured between them. The Seebeck coefficient is then defined as

$$S = -\left(\frac{\Delta V}{\Delta T}\right)_{j^{(z)}=0} = \left(\frac{E^{(z)}}{\partial T/\partial z}\right)_{j^{(z)}=0} = \frac{l_{ET}}{\sigma}. \tag{5.3}$$

As a consequence, Eqs. (5.2) may be rewritten in terms of more experimentally meaningful coefficients as

$$j^{(z)} = \quad \sigma E^{(z)} \qquad\qquad + \sigma S\left(-\frac{\partial T}{\partial z}\right) \tag{5.4a}$$

$$j_Q^{(z)} = \sigma S T E^{(z)} + \left(\kappa + \sigma S^2 T\right)\left(-\frac{\partial T}{\partial z}\right). \tag{5.4b}$$

It is these coefficients that enter the definition of the thermoelectric figure of merit Z, introduced in the previous section:

$$Z = \frac{\sigma S^2}{\kappa}. \tag{5.5}$$

The numerator of this expression is known as the power factor of the material, P. Disregarding electron-phonon interactions, P depends mainly on the electronic band structure of the material under study. On the other hand, it has already been mentioned that in semiconductors κ has two contributions, κ_l due to phonons and κ_e associated to electrons, and that the first dominates. Therefore, an ideal thermoelectric material would behave like a crystal (with high conductivity) for electrons but like a glass (with very low conductivity) for phonons [185].

Even though the superlattices under consideration do not possess complete translational symmetry in the OX and OY directions, with regard to heat and charge carrier distributions, mesoscopic volume elements may be considered that contain a large enough number of molecules that their properties only depend on z when $\vec{E}$ and ∇T are parallel to OZ. In this way, the three-dimensional problem is reduced to a quasi-one-dimensional one, with an infinite set of identical elements of area A conducting heat in parallel, and Eq. (4.5) remains valid for obtaining κ_l if an appropriate transmission per unit area is defined.

A process similar to the one leading to Eq. (4.35) can be followed to yield expressions for σ, S and κ_e. At equilibrium, electrons are distributed among the available states according to the Fermi-Dirac distribution

$$f_{FD}(\epsilon) = \frac{1}{e^{\frac{\epsilon-\mu}{k_B T}} + 1}, \tag{5.6}$$

where ϵ denotes the energy of each state and μ the chemical potential. The measured electric field [137] is given by the gradient of the electrochemical potential, *i.e.*, $E^{(z)} = -\partial\left(\phi - \mu/e\right)/\partial z$, where the electrostatic potential is represented by ϕ and the elementary charge by e.

In a linear non-equilibrium regime, at each z the steady-state distribution can be decomposed in a sum of f_{FD} evaluated at the local temperature $T(z)$ and electrostatic potential $\phi(z)$ and a small perturbation. For electrons in band $\Diamond$ with a momentum $\hbar\vec{k}$ and a velocity $\vec{v}_\Diamond = \left(\partial\epsilon_\Diamond/\partial\vec{k}\right)/\hbar$,

$$f\left(z;\vec{k},\Diamond\right) = f_{FD}\left(T(z), \phi(z); \vec{k}, \Diamond\right) + g_1\left(z;\vec{k},\Diamond\right), \text{ with } \left|g_1\right| \ll \left|f_{FD}\right|, \tag{5.7}$$

and the Boltzmann transport equation adopts the form

$$v_\Diamond^{(z)}\left[\frac{\partial f_{FD}\left(T,\phi;\vec{k},\Diamond\right)}{\partial T}\frac{\partial T}{\partial z} + \frac{\partial f_{FD}\left(T,\phi;\vec{k},\Diamond\right)}{\partial \epsilon} e E^{(z)}\right] = -\frac{g_1\left(z;\vec{k},\Diamond\right)}{\tau_\Diamond} \tag{5.8}$$

in the relaxation time approximation, by arguments analogous to those preceding Eq. (4.33), but taking the electric field into account. Due to the form of f_{FD}, $\partial f_{FD}/\partial T$ is proportional to $\partial f_{FD}/\partial\epsilon$ through a factor $\left(\mu - \epsilon\right)/(k_B T)$, so

$$g_1\left(z;\vec{k},\Diamond\right) = -\tau_\Diamond v_\Diamond^{(z)} \frac{\partial f_{FD}\left(T,\phi;\vec{k},\Diamond\right)}{\partial\epsilon}\left(e E^{(z)} - \frac{\epsilon_\Diamond - \mu}{k_B T}\frac{\partial T}{\partial z}\right). \tag{5.9}$$

Just as in the case of phonons, only this perturbation with respect to equilibrium has to be considered when computing the net currents. The contribution of each electron to $j^{(z)}$ is simply $-ev^{(z)}$, while its share of $j_Q^{(z)}$ can be obtained by subtracting its chemical potential (which cannot be identified as heat, being associated to a deformation coordinate, namely the number of particles) from the total energy it carries and multiplying by its velocity, with the result $\left(\epsilon-\mu\right)v^{(z)}$. Summing over all available k-points per unit volume (*i.e.*, integrating these contributions over the Brillouin zone and dividing by $8\pi^3$) and over bands, the following expressions for the net currents are found

$$j^{(z)} = \sum_{\lozenge}\int_{BZ} -ev_{\lozenge}^{(z)}\left(\vec{k}\right)g_1\left(\vec{k},\lozenge\right)\frac{d^3\vec{k}}{8\pi^3} = E^{(z)}\left\{\sum_{\lozenge}\int_{BZ} e^2v_{\lozenge}^{(z)}\left(\vec{k}\right)\Lambda_{\lozenge}\left(\vec{k}\right)\frac{\partial f_{FD}}{\partial\epsilon}\frac{d^3\vec{k}}{8\pi^3}\right\} + \\ + \frac{\partial T}{\partial z}\left\{-\sum_{\lozenge}\int_{BZ} e\frac{\epsilon_{\lozenge}\left(\vec{k}\right)-\mu}{k_BT}\frac{\partial f_{FD}}{\partial\epsilon}\frac{d^3\vec{k}}{8\pi^3}\right\} \tag{5.10a}$$

$$j_Q^{(z)} = \sum_{\lozenge}\int_{BZ}\left[\epsilon_{\lozenge}\left(\vec{k}\right)-\mu\right]v_{\lozenge}^{(z)}\left(\vec{k}\right)g_1\left(\vec{k},\lozenge\right)\frac{d^3\vec{k}}{8\pi^3} = \\ = E^{(z)}\left\{-\sum_{\lozenge}\int_{BZ} e\left[\epsilon_{\lozenge}\left(\vec{k}\right)-\mu\right]v_{\lozenge}^{(z)}\left(\vec{k}\right)\Lambda_{\lozenge}\left(\vec{k}\right)\frac{\partial f_{FD}}{\partial\epsilon}\frac{d^3\vec{k}}{8\pi^3}\right\} \\ + \frac{\partial T}{\partial z}\left\{\sum_{\lozenge}\int_{BZ}\frac{\left[\epsilon_{\lozenge}\left(\vec{k}\right)-\mu\right]^2}{k_BT}\frac{\partial f_{FD}}{\partial\epsilon}\frac{d^3\vec{k}}{8\pi^3}\right\}. \tag{5.10b}$$

Clearly, expressions for σ, S and κ_e can be extracted from these equations by comparison with Eqs. (5.4). Defining $r \coloneqq \left(k_BT\right)^{-1}\left(\epsilon-\mu\right)$ and performing some simple algebraic transformations, they can be cast in the following convenient forms [186]

$$\sigma = e^2\int \mathscr{S}\left(k_BTr+\mu\right)\left(-\frac{df_{FD}}{dr}\right)dr \tag{5.11a}$$

$$T\sigma S = k_BTe\int r\mathscr{S}\left(k_BTr+\mu\right)\left(-\frac{df_{FD}}{dr}\right)dr \tag{5.11b}$$

$$\kappa_e + T\sigma S^2 = k_B^2T\int r^2\mathscr{S}\left(k_BTr+\mu\right)\left(-\frac{df_{FD}}{dr}\right)dr, \tag{5.11c}$$

with

$$\mathscr{S}(\epsilon) \coloneqq \sum_{\lozenge} \int_{BZ} v_{\lozenge}^{(z)}\left(\vec{k}\right) \Lambda_{\lozenge}\left(\vec{k}\right) \delta\left[\epsilon - \epsilon_{\lozenge}\left(\vec{k}\right)\right] \frac{d^3\vec{k}}{8\pi^3}. \tag{5.11d}$$

In the next section some simplifications will be assumed in order to arrive at even more tractable expressions. It must be noted that, although in this deduction the charge carriers have been assumed to be electrons, all the results are readily applicable to holes if the appropriate signs are changed.

5.3. Transmission calculations

Three steps are needed in order to be able to perform the electric and thermal calculations: model the semiconducting part, characterise the molecule, and combine the two parts in a sensible fashion.

SiGe is a well-known material, so good parameterisations are readily available for it in the scientific literature. As regards charge carrier behaviour, the model employed for SiGe alloys comprised a single parabolic valence band and two conduction bands (L, with six equivalent parabolic minima, and X, with four). The required band parameters where taken from Refs. 187 and 188. For each band, an energy-independent relaxation time was assumed [188] with two contributions, bulk and alloy scattering, compounded using Matthiessen's rule:

$$\tau_{\lozenge} = \frac{m_{c,\lozenge}}{e} \frac{1}{\mu_{\text{bulk}}^{-1} + \mu_{\text{alloy}}^{-1}} \tag{5.12a}$$

$$\mu_{\text{bulk}} = \left(8.6 \cdot 10^{-3}\ \frac{\text{m}^2}{\text{V s}}\right)(1-x) + \left(4.07 \cdot 10^{-3}\ \frac{\text{m}^2}{\text{V s}}\right)x \tag{5.12b}$$

$$\mu_{\text{alloy}} = \frac{1.6 \cdot 10^{-2}\ \frac{\text{m}^2}{\text{V s}}}{4x\,(1-x)\sqrt{\frac{T}{300\ \text{K}}}}, \tag{5.12c}$$

where m_c denotes the conduction effective mass of each band and x is the fraction of silicon in the alloy.

Under these hypotheses, the electric conductivity of SiGe, its Seebeck coefficient and the contribution of charge carriers to its thermal conductivity can be calculated as:

$$\sigma = \frac{2e^2}{h} \int \left(-\frac{df_{FD}}{dr} \right) \Pi(r)\, dr \tag{5.13a}$$

$$S = k_B \frac{\int \left(-\frac{df_{FD}}{dr} \right) r\Pi(r)\, dr}{\int \left(-\frac{df_{FD}}{dr} \right) \Pi(r)\, dr} \tag{5.13b}$$

$$\kappa_e = \frac{2k_B^2 T}{\hbar} \int \left(-\frac{df_{FD}}{dr} \right) r^2 \Pi(r)\, dr - T\sigma S^2 \tag{5.13c}$$

with

$$\Pi(r) = \frac{\sqrt{8}}{3\pi\hbar} \left[\sum_{\substack{\lozenge \in \\ \text{conduction} \\ \text{bands}}} N_\lozenge \tau_\lozenge \Theta\left(k_B T r + \mu - \epsilon_{0,\lozenge}\right) \sqrt{m^*_\lozenge \left(k_B T r + \mu - \epsilon_{0,\lozenge}\right)^3} + \right.$$
$$\left. + \tau_{\text{val}} \Theta\left(\epsilon_{0,\text{val}} - k_B T r - \mu\right) \sqrt{m^*_0 \left(\epsilon_{0,\text{val}} - k_B T r - \mu\right)^3} \right], \tag{5.13d}$$

simplified versions of Eqs. (5.11) with the integration around each parabolic minimum solved analytically. Here, N is the number of equivalent minima in each band, m^* the corresponding density-of-states effective mass, ϵ_0 the energy of the band edge and Θ a step function. Band parameters are listed in Table 5.1. By comparing these equations to the one-dimensional result for the thermal conductivity (4.5) or, more generally, to the Landauer-Buttiker formalism for electrons [17], built upon similar premises, it can be seen that they are also applicable to a bidimensional array of quasi-one-dimensional conducting elements such as a molecular monolayer if Π is replaced with $\rho_S L \mathscr{T}_e$, *i.e.*, the product of the electronic transmission of each element ($\mathscr{T}_e$), the surface density of elements (ρ_S) and the width of the layer (L). Thus, Π can be thought of as a bulk analogue of the transmission; knowledge of Π for a given material is sufficient to calculate its thermoelectric power factor $P = \sigma S^2$ and, if the phononic contribution to its thermal conductivity can be estimated, also its thermoelectric figure of merit.

With respect to the thermal transmission of SiGe, it was provided by Dr. Natalio Mingo, who calculated it in a simplified way by the use of an approximate linear phonon dispersion — a Debye model with a carefully selected cutoff frequency — and parameterised relaxation times [189] that take into account anharmonic and alloy scattering.

Table 5.1 Parameters for each band in SiGe, from Refs. 187 and 188. Here, m_0 is the electron mass; for non-rotationally-symmetric paraboloids, m_l and m_t are the longitudinal and transverse effective masses, respectively.

$\Diamond$ (Band)	$m_{l,\Diamond}/m_0$	$m_{t,\Diamond}/m_0$	$m_{c,\Diamond}/m_0$	$m^*_\Diamond/m_0$
X	0.97	0.19	$3\left(m_0/m_{l,X} + 2m_0/m_{t,X}\right)$	$\sqrt[3]{m_{l,X}m^2_{t,X}}/m_0$
L	1.64	0.082	$3\left(m_0/m_{l,L} + 2m_0/m_{t,L}\right)$	$\sqrt[3]{m_{l,L}m^2_{t,L}}/m_0$
Valence	1	1	1	1

$$\text{Gap widths (eV):} \begin{cases} \epsilon_{g,X} = 0.8941 + x\,(0.0421 + 0.1691x) \\ \epsilon_{g,L} = 0.7596 + x\,(1.0860 + 0.3306x) \end{cases}.$$

The percentage of germanium in the Si_xGe_{1-x} alloy plays a crucial role in the modulation of the thermoelectric properties of the superlattice. Compared to pure silicon, an alloy with significant disorder scatters both electrons and phonons more efficiently. In order to evaluate the net effect of this parameter, calculations were run for the two most extreme cases: $x = 1$ (no germanium) and $x = 0.5$ (maximum disorder). The position of the Fermi level (ϵ_F) was chosen so as to maximise the power factor $P = \sigma S^2$, which happens close to the edge of the conduction band and yields carrier densities $n \sim 10^{20}$ cm^{-3}. A superlattice whose semiconducting part is made of pure silicon proved a poor choice for thermoelectric applications. Therefore, the discussion in the next section will concentrate on the maximally-disordered, optimally-doped SiGe:SAM HOI.

The organic molecules were modelled atomistically by Prof. Hans Ågren and coworkers. They used density functional theory (DFT) calculations at the B3LYP level [190] with the 6-31G basis set in order to get the optimised geometries and electronic structures of SiH_3-tri-thiophene-SiH_3, GeH_3-tri-thiophene-GeH_3, SiH_3-phenyl-tri-thiophene-SiH_3 and GeH_3-phenyl-tri-thiophene-GeH_3 molecules. All of the quantum chemical calculations were performed with GAUSSIAN 09 [191]. In DFT [192], electrons are described not in terms of their wave functions, but of their total charge density which, according to the Hohenberg-Kohn theorems [193], contains all the physics of the system. This charge density is, in turn, calculated by solving the Kohn-Sham equations

[194], formally identical to the time-independent Schrödinger equation

$$\boldsymbol{H}\left|\psi\right\rangle = \epsilon\left|\psi\right\rangle \tag{5.14}$$

but describing a set of fictitious, non-interacting electrons. This difference is reflected in the form of the hamiltonian ($\boldsymbol{H}$), which contains exchange and correlation contributions to the potential energy to account for the collective effect of all the other electrons. Nuclear coordinates are typically decoupled from electronic degrees of freedom and treated in the Born-Oppenheimer approximation [195]. The force associated to atomic coordinate $x_j^{(\mu)}$ is defined, as usual, by $f_j^{(\mu)} = -\partial\epsilon/\partial x_j^{(\mu)}$, but advantage can be taken of the Hermitian nature of $\boldsymbol{H}$, through a process analogous to the one leading to Eq. (3.8) for group velocities, to obtain a more convenient expression,

$$f_j^{(\mu)} = -\left\langle\psi\left|\frac{\partial\boldsymbol{H}}{\partial x_j^{(\mu)}}\right|\psi\right\rangle, \tag{5.15}$$

known as the Hellman-Feynman theorem [196]. For this work, the numerical derivative of these forces was computed using Eq. (3.9); however, it should be mentioned that an alternative algorithm exists [197, 198] to solve the problem directly in terms of the hamiltonian in the framework of density functional perturbation theory (DFPT), of which Eq. (5.15) can be considered a particular application.

Since force constants obtained by DFT methods do not come from a short-range potential, they are seldom directly usable in phononic calculations. For instance, conservation of momentum (or, equivalently, translational symmetry) demands that all the components of the total harmonic force on the whole system, $\sum_{\mu,\mu',j,j'} \tilde{K}_{j,j'}^{(\mu,\mu')} u_{j'}^{(\mu')}$, be zero, which is only possible if $\sum_{\mu',j'} \tilde{K}_{j,j'}^{(\mu,\mu')} = 0$ for every atom j along every direction μ. Similar linear constraints on the elements of $\tilde{\boldsymbol{K}}$ can be derived from the conservation of angular momentum. Force constants derived from DFT can deviate from these constraints quite significantly; if used to calculate the vibrational frequencies of a molecule, they would fail to predict the $\omega = 0$ modes associated to translations and rotations, while if used to calculate its transmission along the OZ axis when attached to two leads, they would yield a value smaller than the theoretical $\mathscr{T}(0) = 4$ due to such modes. When it is not feasible to use a larger simulation box in order to avoid this effect, $\tilde{\boldsymbol{K}}$ may be corrected using a method devised by Mingo

Table 5.2 Parameters of the SW potential for Ge, from Ref. 146.

$\sigma = 0.2181$ nm	$\epsilon = 1.93$ eV	$A = 7.049556277$
$B = 0.6022245584$	$a = 1.80$	$\lambda = 31.0$
$p = 4$	$q = 0$	$\gamma = 1.20$

and Broido [199], which enforces the symmetries while keeping the relative correction to the force constants minimal, through a Lagrange-multiplier approach. In practical terms, this translates into the problem of finding the solution of a relatively large linear system, which can be accomplished more efficiently than a larger DFT calculation. Thus, it was the method chosen for the present work.

The phononic transmission of the molecular layer was computed considering a single molecule between pure Si or pure Ge leads with the same methods from Chapter 4. The force constant matrix of the defective system (semiconductor leads+molecule) was built by parts: the corrected force constants from DFT were used for the molecule and for the force between the molecule and the leads, whereas semiconductor-semiconductor interactions were again modelled using the SW potential [43, 146], with the parameters for Si of Table 4.1 and those listed in Table 5.2 for Ge. An added advantage of this was that Green's functions obtained by decimation [140] for the previous chapter were reused. The cross-sectional area of the nanowire studied there was deemed enough to yield a transmission per unit area representative of a molecule attached to the bulk.

The electronic transmission probabilities across the molecular interface were calculated with the QCME (Quantum Chemistry for Molecular Electronics) program [200], which is based on the general Green's function formalism [201, 202]. QCME has been successfully applied to describe the electronic transport properties of various molecular junction systems [203–205]. In their calculations, Ågren and coworkers divided the molecular junction into three parts: source, extended molecule, and drain. The source and drain electrodes were described by an effective mass approximation, while the electronic structure of the extended molecule was calculated with DFT. With such a setup, they were able to accurately describe both the bulk electrodes and the extended molecule. In the framework of elastic-scattering theory, the

transition probability can be calculated as $\mathscr{T} = \sum_r |T(\varepsilon_r)|^2$. Here $T(\varepsilon_r)$ is the energy-dependent transition matrix element, which is defined as [201]

$$T(\varepsilon_r) = \sum_{j,j'} V_{jS} V_{Dj'} \sum_{\eta} \frac{\langle j | \eta \rangle \langle \eta | j' \rangle}{\zeta_r - \epsilon_\eta}, \tag{5.16}$$

where j and j' run over all atomic sites, and V_{jS} ($V_{Dj'}$) denotes the coupling energy between the atomic site j (j') and the left (right) electrode. The coupling energies, which are the key parameters in computing the transition matrix elements, can be calculated analytically with the electronic structure obtained from quantum chemical calculations [202]. The product of the two overlap matrix elements $\langle j | \eta \rangle \langle \eta | j' \rangle$ represents the delocalisation of the molecular orbital $|\eta\rangle$. ϵ_η is the eigenvalue of orbital $|\eta\rangle$. The overlap elements and the molecular orbitals can also be obtained from DFT calculations. The complex variable ζ is defined as $\zeta_r = \varepsilon_r + i\Gamma_r$, ε_r being the energy at which the scattering process is observed. h/Γ_r is the escape rate, which is determined by Fermi's golden rule [202].

Finally, in order to compute the transport properties of a $Si_{0.5}Ge_{0.5}$/trithiophene superlattice, these data must be used in conjunction with the approximations to the phononic and electronic behaviours of SiGe alloys described above. While the width $l = 2$ nm of a molecular monolayer is fixed, the superlattice period $l + L$ can be adjusted by a suitable choice of the width of the semiconductor part (L), subject only to technological constraints. Therefore, different transport regimes can be achieved. The long MFP of the aforementioned long-wavelength phonons in SiGe [206] provides adequate ground for treating phonon transport as quasi-ballistic, *i.e.*, for combining the scattering probabilities of the semiconductor and the molecular monolayer into a joint transmission and using the latter in the calculations of the phenomenological coefficients. A phonon can transverse two segments of the system, a and b, with (normalised) transmission probabilities $\mathscr{T}_a$ and $\mathscr{T}_b$ either without suffering any scattering or after experiencing any even number of reflections. The probabilities of all those incompatible events have to be summed to obtain the

joint transmission probability of a and b [207]:

$$\begin{aligned}\mathscr{T}_{a+b} &= \mathscr{T}_a\mathscr{T}_b + \mathscr{T}_a\left(1-\mathscr{T}_b\right)\left(1-\mathscr{T}_a\right)\mathscr{T}_b + \mathscr{T}_a\left[\left(1-\mathscr{T}_b\right)\left(1-\mathscr{T}_a\right)\right]^2\mathscr{T}_b + \ldots = \\ &= \mathscr{T}_a\mathscr{T}_b\sum_{j=0}^{\infty}\left[\left(1-\mathscr{T}_b\right)\left(1-\mathscr{T}_a\right)\right]^j = \frac{1}{\mathscr{T}_a^{-1}+\mathscr{T}_b^{-1}-1}.\end{aligned} \tag{5.17}$$

On the other hand, an equivalent combination rule cannot be expected to hold for electrons in superlattices with a period beyond 5 nm, approximately, since this is the order of the electronic MFP [188]. Thus, for longer periods a hypothesis of ohmic transport is more appropriate, whereby the transport coefficients derived from the transmission probabilities of the charge carriers (electric conductivity, electronic contribution to the thermal conductivity and Seebeck coefficient) are calculated separately for each kind of layer in the superlattice and then combined using rules analogous to those from ordinary concentrated-parameter circuit theory. In order to derive those, let us first consider a homogeneous, translationally-symmetric thermoelectric element of cross-sectional area A, length L and parameters (σ, S, κ), oriented along the OZ axis and placed between two reservoirs at temperatures and electric potentials T_+, V_+ (on its left) and T_-, V_- (on its right). Integrating Eqs. (5.2) over a plane perpendicular to OZ, the following macroscopic phenomenological equations are obtained:

$$I = G\Delta\phi + GS\Delta T \tag{5.18a}$$

$$\frac{I_Q}{T} = GS\Delta\phi + \frac{G_T}{T}\Delta T, \tag{5.18b}$$

with $\Delta V = V_+ - V_- = E^{(z)}L$ and $\Delta T = T_+ - T- = -\left(\partial T/\partial z\right)L$. Here, $G \coloneqq \sigma A/L$ and $G_T \coloneqq \left(\kappa + \sigma S^2 T\right)A/L$ are the electric conductance of the element and its thermal conductance at zero electric field, respectively. I and I_Q are the total electric and thermal fluxes along OZ, area integrals of $j^{(z)}$ and $j_Q^{(z)}$. Eqs. (5.18) can also be expressed in the matrix form $\vec{I} = \boldsymbol{L}\left(\vec{F}_+ - \vec{F}_-\right)$ through the following definitions:

$$\boldsymbol{L} \coloneqq \begin{pmatrix} G & GS \\ GS & G_T/T \end{pmatrix};\ \vec{I} \coloneqq \begin{pmatrix} I \\ \frac{I_Q}{T} \end{pmatrix};\ \vec{F}_j \coloneqq \begin{pmatrix} \phi_j \\ T_j \end{pmatrix},\ j \in \{+,-\}. \tag{5.19}$$

Now let us consider two of these elements, a and b, with phenomenological matrices $\boldsymbol{L}_a$ and $\boldsymbol{L}_b$, connected in series and in a steady state. The value of the vector $\vec{F}$ on the left (right) of both will again be by denoted $\vec{F}_+$ ($\vec{F}_-$), and its value between both elements by $\vec{F}_m$. Since in a steady state there cannot be an accumulation of charge or energy at any point, $\vec{I}$ must be the same through both elements. Therefore, the equivalent $\boldsymbol{L}$ of the whole system can be obtained from the equations

$$\vec{I} = \boldsymbol{L}\left(\vec{F}_+ - \vec{F}_-\right) = \boldsymbol{L}_a\left(\vec{F}_+ - \vec{F}_m\right) = \boldsymbol{L}_b\left(\vec{F}_m - \vec{F}_-\right). \tag{5.20}$$

Solving one of them for $\vec{F}_m$ and substituting in the other,

$$\boldsymbol{L} = \boldsymbol{L}_a\left(\boldsymbol{L}_a + \boldsymbol{L}_b\right)^{-1}\boldsymbol{L}_b \tag{5.21}$$

is obtained, from which the composition rules for each coefficient can be extracted:

$$G_{a+b} = \left(G_a^{-1} + G_b^{-1}\right)^{-1} \tag{5.22a}$$

$$S_{a+b} = \frac{G_{T,a}^{-1}S_a + G_{T,b}^{-1}S_b}{G_{T,a}^{-1} + G_{T,b}^{-1}} \tag{5.22b}$$

$$G_{T,a+b} = \left(G_{T,a}^{-1} + G_{T,b}^{-1}\right)^{-1}, \tag{5.22c}$$

of which the first and third equations are merely the well-known rule for electric resistors in series and its thermal equivalent, respectively.

In either case, ballistic or ohmic, coherency between neighbouring semiconductor layers is broken by the organic molecules inserted between them; therefore, different periods of the superlattice behave incoherently, a phenomenon known to lead to low thermal conductivities in similar systems [208].

5.4. Results and discussion

The process of finding the optimal doping is illustrated in Fig. 5.3, which shows the power factor of a $Si_{0.5}Ge_{0.5}$/tri-thiophene superlattice as a function of the position of the Fermi level with respect to its intrinsic value ϵ_i, in the ballistic regime, for $L = 10$ nm. Apart from the peak near the border of the conduction band, already mentioned and which can in principle be attained

Figure 5.3 Power factor of a $Si_{0.5}Ge_{0.5}$/tri-thiophene superlattice as a function of the position of the Fermi level with respect to its intrinsic value ϵ_i, in the ballistic regime, for L = 10 nm.

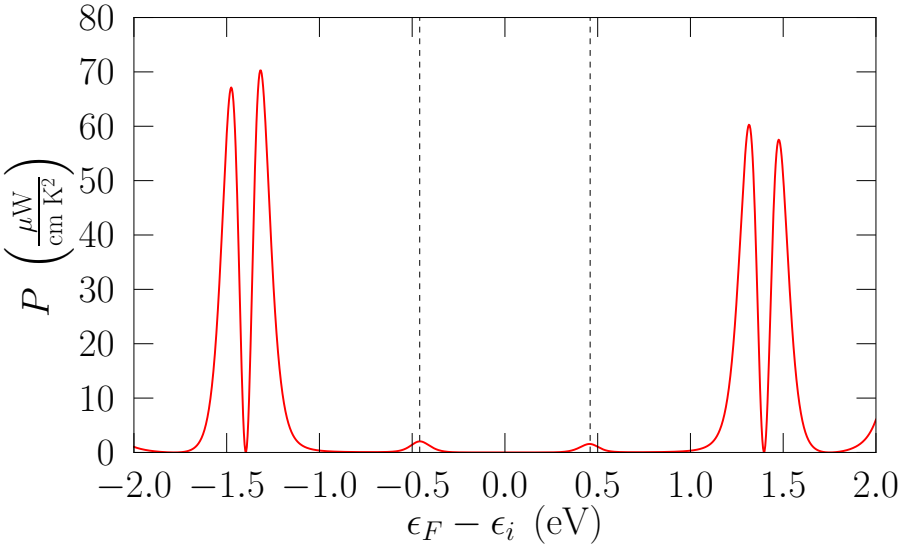

experimentally using high doping levels, there are two other much higher maxima about 1 eV into the conduction band. However, such Fermi energies correspond to unrealistic doping levels with carrier concentrations around 10^{22} cm^{-3}, and furthermore are so far away from the bottom of the lowest conduction band as to render the three-band, parabolic approximation absurd.

The left panels of Fig. 5.4 show the electronic transmission of a tri-thiophene molecule, with or without a lateral phenyl group, placed between $Si_{0.5}Ge_{0.5}$ leads, for an energy range around the Fermi level. Those transmissions were obtained by averaging *ab initio* results for pure Si and pure Ge. As expected, the transmission profile consists of narrow peaks centred around the electronic states of the tiophene oligomer, and the modifications introduced by the side phenyl ring are relatively minor. In the same figure, the right panels show the phononic transmissions of the same systems. In the frequency range most relevant for thermal transport ($\omega \lesssim 40$ THz) the side ring introduces several vibrational modes which change the transmission profile in a comparatively more significant fashion.

Figure 5.5 (bottom) shows the total thermal conductivity of a $Si_{0.5}Ge_{0.5}$/tri-

Figure 5.4 Electronic (left) and phononic (right) transmissions for a tri-thiophene molecule (top, in red) and a phenyl-tri-thiophene molecule (bottom, in green) between SiGe leads. In all cases, transmissions were calculated for pure Si and pure Ge leads and averaged in order to yield these results.

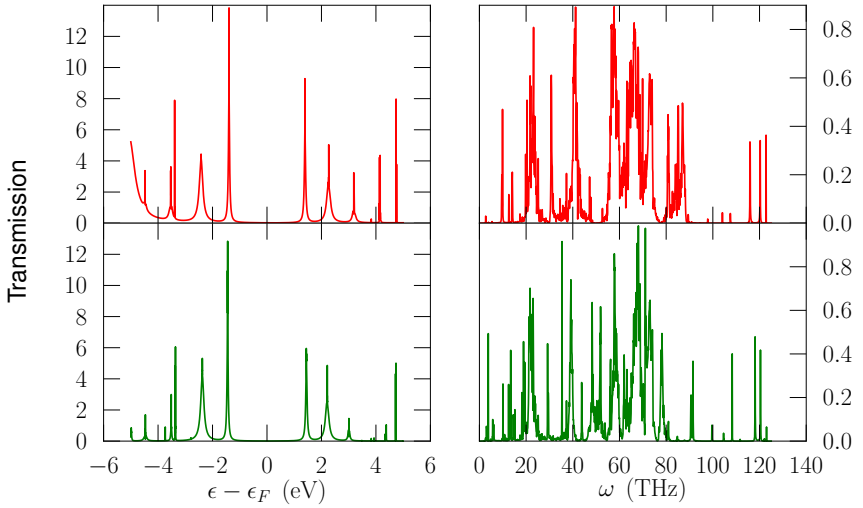

thiophene superlattice for optimal doping, which includes the contributions from phonons and charge carriers, as a function of its period. There is very little difference between the results obtained under an assumption of quasi-ballistic electron transport (which have been omitted for clarity) and those afforded by ohmic combination rules, due to the predominance of the phononic contribution. It can be seen, accordingly, that a phenyl ring bonded to the oligomer can make a significant difference through the addition of conduction channels for phonons. In any case, the computed total thermal conductivity is extremely small: by way of comparison, it is two orders of magnitude lower that the value for bulk silicon, about one half of the thermal conductivity experimentally reported for some of the most promising thermoelectric Si nanostructures [130] and one tenth of the value for bulk $Si_{0.5}Ge_{0.5}$ [209]. The molecular layers play a crucial role in scattering low-frequency phonons, which are relatively unaffected by alloy scattering due to their being in the Rayleigh limit when compared to the characteristic length of alloy disorder. The importance of alloy scattering is clearly shown in the top panel of Fig. 5.5, which contains a comparison between $Si_{0.5}Ge_{0.5}$/tri-thiophene

Figure 5.5 Top: comparison between the thermal conductivities of $Si_{0.5}Ge_{0.5}$ /tri-thiophene and Si/tri-thiophene superlattices, using ohmic composition rules, as a function of their period length. Bottom: results for $Si_{0.5}Ge_{0.5}$/tri-thiophene, with κ in linear scale to highlight the effect a phenyl side group.

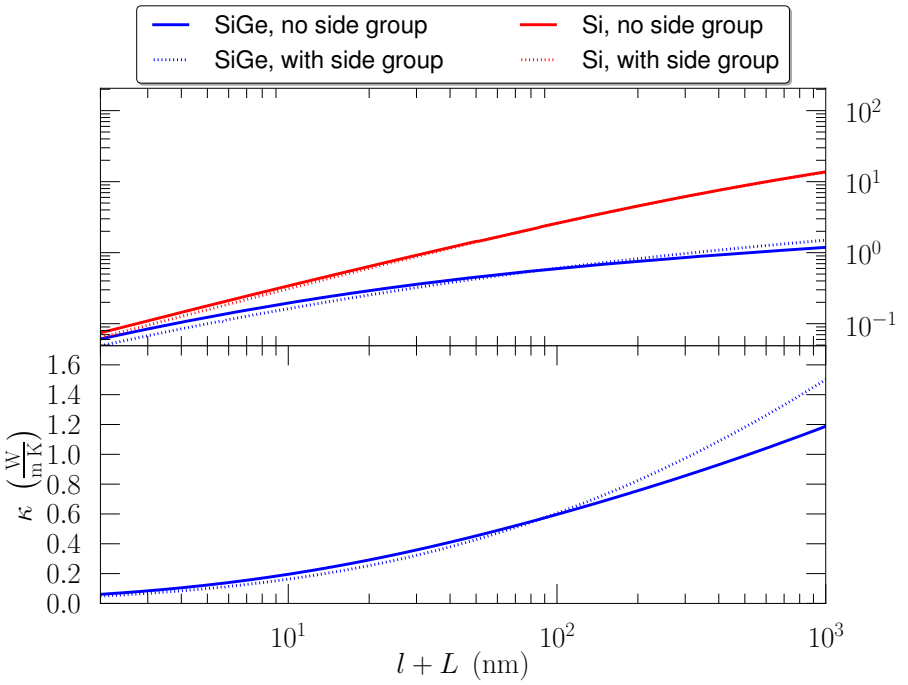

and Si/tri-thiophene superlattices with the same period length, and shows differences of up to one order of magnitude.

Electronic transport is also somewhat hindered by the thiophene molecules, as reflected in Fig. 5.6, which shows the power factor of the superlattice under study for optimal doping. The presence or absence of the phenyl group has little effect, as expected from the similarity of the electronic transmission profiles in both cases. The attainable values of P are rather modest, 5 – 10 times lower than those of bulk SiGe [206]. Fortunately, the reduction in P is not enough to compensate for the extremely low thermal conductivity of the superlattice, so the dimensionless thermoelectric figure of merit, $ZT = PT/\kappa$ (Fig. 5.7) still improves by about a factor of two upon the optimal theoretical value for SiGe [206]. Figure 5.7 further shows that practically useful values of ZT can be achieved in both the ballistic and ohmic

Figure 5.6 Room-temperature power factor of a $Si_{0.5}Ge_{0.5}$/tri-thiophene superlattice as a function of its period length, using ohmic and ballistic composition rules for the electronic calculations, with or without a side phenyl group.

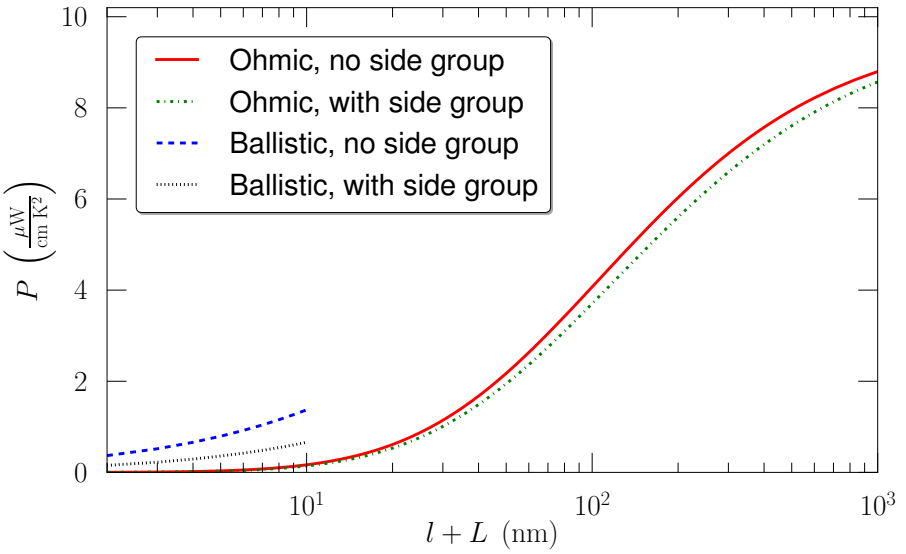

coupling regimes. Although it seems unlikely that the ballistic picture affords good results for $l + L$ as large as 10 nm, even if it only held up to a fifth of that value it would still yield $ZT \simeq 0.23$. At the other extreme, a very long period ($\sim 0.2 - 0.3$ μm) maximises the figure of merit in the ohmic regime, with a similar optimum value.

A third interesting conclusion which can be drawn from Fig. 5.7 is that thermoelectric properties are easily tunable by chemical methods. The phenyl group marks a significant 20% difference in the optimum ZT in the ohmic regime, and a huge departure of almost 100% for ballistic coupling, by virtue of affecting the phononic and electronic transmission profiles to very different degrees. The almost infinite flexibility offered by organic molecules for substitution with different residues, different choices of the length of the oligomer, etc., therefore appears as a promising avenue for improving ZT even further. At the current stage of technological development, these methods are possibly more economical and easily scalable to industrial sizes than other alternative routes dependent on nanoscale material engineering [130].

Therefore, these calculations reveal that, whereas when the inorganic part

Figure 5.7 Room-temperature figure of merit of a $Si_{0.5}Ge_{0.5}$/tri-thiophene superlattice as a function of its period length, using ohmic (left) and ballistic (right) composition rules for the electronic calculations.

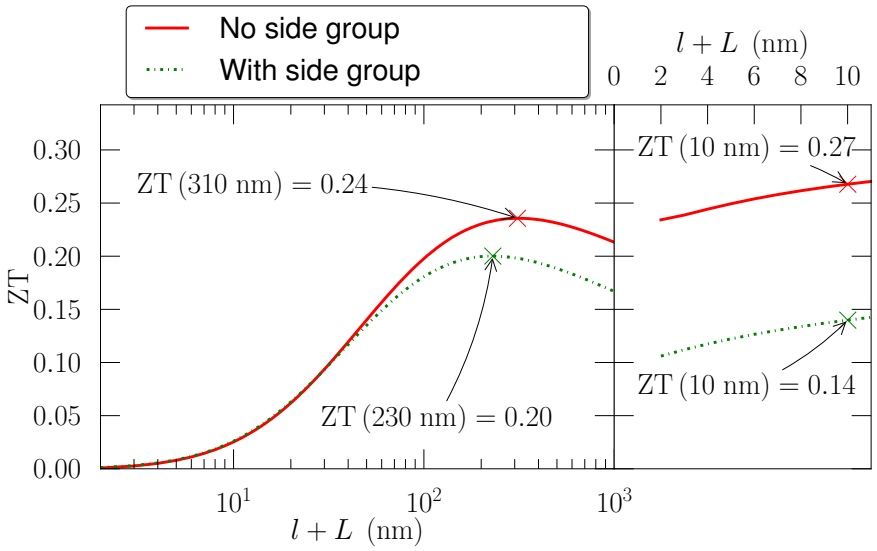

consists of pure silicon the thermoelectric behaviour of the resulting structure is rather poor, an alloy with a percentage of Si around 50%, leading to a maximal configurational entropy, offers promising results. In particular, as regards electric transport, it is found that the organic layers significantly reduce the conductivity with respect to that of bulk SiGe. Nevertheless, since it was also detected that thermal conductivity is reduced by a much larger factor [resulting in values in the order of magnitude from 0.1 to 1 W/(m K)], the thermoelectric figure of merit (ZT) of this kind of hybrid structure can improve upon that of SiGe alone by a factor of more than two. Optimal values of ZT around 0.25 were achieved at room temperature ($\sim$ 2.5 times larger than for bulk SiGe), which could make this kind of material competitive for practical thermoelectric applications if, as expected, they are easier to engineer and manufacture than other, more sophisticated, nanostructures. Moreover, the addition of a phenyl ring to each polymer alters the value of ZT by about 20%, which suggests that the thermoelectric properties of these systems can be easily tailored and improved by chemical methods.

References

17. Datta, S. *Quantum Transport: Atom to Transistor* second (Cambridge University, New York, 2005).

43. Stillinger, F. H. & Weber, T. A. *Phys. Rev. B* **31,** 5262 (1985).

130. Hochbaum, A. I., Chen, R., Delgado, R. D., Liang, W., Garnett, E. C., Najarian, M., Majumdar, A. & Yang, P. *Nature (London)* **451,** 163 (2008).

137. Ziman, J. M. *Electrons and Phonons* (Oxford University, New York, 1960).

140. Guinea, F., Tejedor, C., Flores, F. & Louis, E. *Phys. Rev. B* **28,** 4397 (1983).

146. Jian, Z., Kaiming, Z. & Xide, X. *Phys. Rev. B* **41,** 12915 (1990).

155. Carnot, S. *Réflexions sur la Puissance Motrice du Feu* (Bachelier, Paris, 1824).

156. Snyder, G. J. & Ursell, T. S. *Phys. Rev. Lett.* **91,** 148301 (2003).

157. DiSalvo, F. J. *Science* **30,** 703 (1999).

158. Venkatasubramanian, R., Siivola, E., Colpitts, T. & O'Quinn, B. *Nature* **413,** 597 (2001).

159. Leclerc, M. & Najari, A. *Nat. Mater.* **10,** 409 (2011).

160. Dubey, N. & Leclerc, M. *J. Polym. Sci., Part B: Polym. Phys.* **49,** 467 (2011).

161. Sanchez, C. *J. Mater. Chem.* **15,** 3557 (2005).

162. Mitzi, D. B. *Chem. Mater.* **13,** 3283 (2001).

163. Xing, L.-L., Li, D.-P., Hu, S.-X., Jing, H.-Y., Fu, H., Mai, Z.-H. & Li, M. *J. Am. Chem. Soc.* **128,** 1749 (2006).

164. Yoon, K.-H., Han, K.-S. & Sung, M.-M. *Nanoscale Res. Lett.* **7,** 71 (2012).

165. Deneke, C., Zschieschang, U., Klauk, H. & Schmidt, O. G. *Appl. Phys. Lett.* **89,** 263110 (2006).

166. Deneke, C., Schumann, J., Engelhard, R., Thomas, J., Sigle, W., Zschieschang, U., Klauk, H., Chuvilin, A. & Schmidt, O. G. *Phys. Status Solidi C* **5,** 2704 (2008).

167. Bufon, C. C. B., Espinoza, J. D. A., Thurmer, D. J., Bauer, M., Deneke, C., Zschieschang, U., Klauk, H. & Schmidt, O. G. *Nano Lett.* **11,** 3727 (2011).

168. Mitzi, D. B., Chondroudis, K. & Kagan, C. R. *IBM Res. Dev.* **45,** 29 (2001).

169. Kagan, C. R., Mitzi, D. B. & Dimitrakopoulos, C. D. *Science* **286,** 945 (1999).

170. Carrasco-Orozco, M. A., Stirner, T., O'Neill, M., Ellis, C., Dong, D., Kelly, R., Piepenbrock, M. O. & Kelly, S. M. *Phys. Rev. B* **75,** 035207 (2007).

171. Park, Y., Han, K. S., Lee, B. H., Cho, S., Lee, K. H., Im, S. & Sung, M. M. *Org. Electron.* **12,** 348 (2010).

172. See, K. C., Feser, J. P., Chen, C. E., Majumdar, A., Urban, J. J. & Segalman, R. A. *Nano Lett.* **10,** 4664 (2010).

173. Malen, J. A., Doak, P., Baheti, K., Tilley, T. D., Majumdar, A. & Segalman, R. A. *Nano Lett.* **9,** 3406 (2009).

174. Ke, S.-H., Yang, W., Curtarolo, S. & Baranger, H. U. *Nano Lett.* **9,** 1011 (2009).

175. Yan, L., Shao, M., Wang, H., Dudis, D., Urbas, A. & Hu, B. *Adv. Mater.* **23,** 4120 (2011).

176. D. Appelhansa, a. D. F., Adlera, H., Pliethb, W., Fikusb, A., Grundkec, K., Schmittc, F., Bayerc, T. & Adolphid, B. *Colloids Surf., A* **161,** 203 (2000).

177. Sathyapalan, A., Ng, S. C., Lohani, A., Ong, T. T., Chen, H., Zhang, S., Lam, Y. M. & Mhaisalkar, S. G. *Thin Solid Films* **516,** 5645 (2008).

178. Fabre, B., Lopinski, G. P. & Wayner, D. D. M. *Chem. Commun.* **2002,** 2904 (2002).

179. de Groot, S. R. & Mazur, P. *Non-Equilibrium Thermodynamics* (Dover, New York, 1984).

180. Onsager, L. *Phys. Rev.* **37,** 405 (1931).

181. Hill, T. L. *Thermodynamics of Small Systems* (Benjamin, New York, 1963).

182. Letellier, P., Mayaffre, A. & Turmine, M. *Phys. Rev. B* **76,** 045428 (2007).

183. Carrete, J., Varela, L. M. & Gallego, L. J. *Phys. Rev. E* **77,** 022102 (2008).

184. Seebeck, T. J. *Abh. K. Akad. Wiss.* **2,** 265 (1823).

185. *CRC Handbook of Thermoelectrics* 1st ed. (ed Rowe, D. M.) (CRC Press, Boca Raton, 1995).

186. Mahan, G. D. & Sofo, J. O. *Proc. Natl. Acad. Sci. USA* **93,** 7436 (1996).

187. Krishnamurthy, S., Sher, A. & Chen, A. *Appl. Phys. Lett.* **47,** 160 (1985).

188. Slack, G. A. & Hussain, M. A. *J. Appl. Phys.* **47,** 2694 (1991).

189. Mingo, N., Hauser, D., Kobayashi, N. P., Plissonnier, M. & Shakouri, A. *Nano Lett.* **9,** 711 (2009).

190. Kim, K. & Jordan, K. D. *J. Phys. Chem.* **98,** 10089 (1994).

191. Frisch, M. J. *et al. Gaussian 09 Revision A.02* Gaussian Inc. Wallingford CT 2009.

192. Parr, R. G. & Yang, W. *Density Functional Theory of Atoms and Molecules* (Oxford University Press, New York, 1989).

193. Hohenberg, P. & Kohn, W. *Phys. Rev.* **136,** B864 (1964).

194. Kohn, W. & Sham, L. J. *Phys. Rev.* **140,** A1133 (1965).

195. Born, M. & Oppenheimer, R. *Ann. Phys.* **84,** 459 (1927).

196. Feynman, R. P. *Phys. Rev.* **56,** 340 (1939).

197. Gonze, X., Allan, D. C. & Teter, M. P. *Phys. Rev. Lett* **68,** 3603 (1992).

198. Gonze, X. *Phys. Rev. A* **52,** 1086 (1995).

199. Mingo, N., Stewart, D. A., Broido, D. A. & Srivastava, D. *Phys. Rev. B* **77,** 033418 (2008).

200. Jiang, J. & Luo, Y. *QCME-V1.0 (Quantum Chemistry for Molecular Electronics)* Royal Institute of Technology, Sweden, 2005.

201. Wang, C.-K., Fu, Y. & Luo, Y. *Phys. Chem. Chem. Phys.* **3,** 5017 (2001).

202. Jiang, J., Kula, M. & Luo, Y. *J. Chem. Phys.* **124,** 034708 (2006).

203. Hu, W., Jiang, J., Nakashima, H., Luo, Y., Kashimura, Y., Chen, K.-Q., Shuai, Z., Furukawa, K., Lu, W., Liu, Y., Zhu, D. & Torimitsu, K. *Phys. Rev. Lett.* **96,** 027801 (2006).

204. Su, W. Y., Jiang, J., Lu, W. & Luo, Y. *Nano Lett.* **6,** 2091 (2006).

205. Cao, H., Jiang, J., Ma, J. & Luo, Y. *J. Am. Chem. Soc.* **130,** 6674 (2008).

206. Vining, C. B. *J. Appl. Phys.* **69,** 331 (1991).

207. Savić, I., Mingo, N. & Stewart, D. A. *Phys. Rev. Lett.* **101,** 165502 (2008).

208. Chiritescu, C., David G. Cahill and, N. N., Johnson, D., Bodapati, A., Keblinski, P. & Zschack, P. *Science* **315,** 351 (2007).

209. Schaffler, F. in. *Properties of Advanced Semiconductor Materials GaN, AlN, InN, BN, SiC, SiGe* (eds Levinshtein, M. E., Rumyantsev, S. L. & Shur, M. S.) 149 (Wiley, New York, 2001).

Part II

Ionic liquids

6 Nanostructure of imidazolium-based ionic liquids

And yet it is hard to believe that anything
in nature could stand revealed as solid matter.
The lightning of heaven goes through the walls of houses,
like shouts and speech; iron glows white in fire;
red-hot rocks are shattered by savage steam;
hard gold is softened and melted down by heat;
chilly brass, defeated by heat, turns liquid;
heat seeps through silver, so does piercing cold;
by custom raising the cup, we feel them both
as water is poured in, drop by drop, above.

De Rerum Natura
LUCRETIUS

6.1. Introduction

Ionic liquids (ILs) are substances present in the liquid state and formed exclusively by ions at room temperature. In practice, a substance is usually considered an IL if it is fully dissociated and its melting temperature lies below 100 °C. If the latter requirement were lifted, ordinary molten salts, like liquid

NaCl, would also enter the category. This second kind of substances, corrosive and very viscous, share certain characteristics with ILs, but their much higher melting point clearly separates their domain of usefulness from that of the latter, which is the main reason behind their separate treatment.

An IL is formed by an organic cation, whose complexity can vary, and an anion which can range from a single halogen atom to another complex organic structure. The first documented synthesis of an IL, ethylammonium nitrate, was reported in 1914 [210, 211], and the first systematic experimental description of one of these systems dates from 1948 [212], although interest in ILs for use as solvents emerged in the 80s [213, 214]. Another key moment was the synthesis by Wilkes, in the 90s, of ILs based on weakly coordinating ions, more economical than those available up to that point [215].

ILs are singular in their structure and dynamics, which confers them an important theoretical appeal, but without a doubt their popularity is due to their great practical usefulness as solvents, reaction media and catalysts of multiple chemical reactions [12–14]. The main properties that make them especially suitable for such purposes are:

- Their low vapour pressure: as a matter of fact, this pressure is so low as to be undetectable in most measurements. A liquid which essentially does not evaporate is easy to manipulate without losses to the environment, and to separate from certain solutes using energetically inexpensive procedures. Thus, sometimes ILs are referred to as "green solvents", even though this point has to be qualified, since their syntheses can be environmentally wasteful and some of them are toxic [216].

- Their wide range of work temperatures: an intelligent choice of ions can result in ILs with a melting temperature anywhere between −90 °C and 200 °C. The other extreme of the temperature range is defined by the compound's thermal decomposition temperature, which can be as high as 400 °C [217]. As a consequence, these liquids are ideal media for many chemical processes at different temperatures.

A particular group of ILs with the added property of a great chemical stability is that formed by those whose cation is based on an imidazole — or 1, 3-diazacyclopenta-2, 4-diene — ring. As can be deduced from its systematic name, this is a pentagonal carbon ring with two of its atoms, in non-adjacent sites, substituted by nitrogen atoms. In imidazole, those bonds not responsible

Figure 6.1 From left to right: imidazolium, $[BMIM]^+$, $[PF_6]^-$ and $[BF_4]^-$.

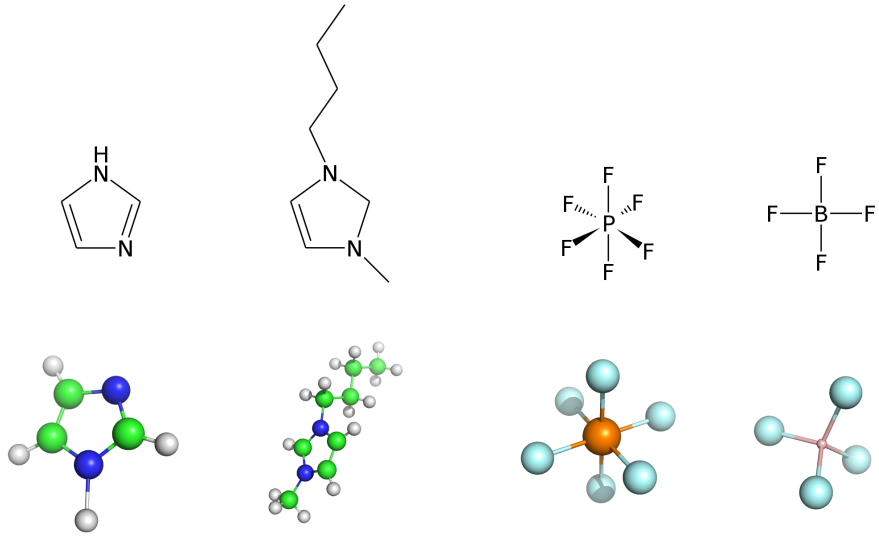

for the pentagonal structure are saturated by hydrogen, yielding the formula $C_3H_4N_2$. If a methyl group and a generic alkyl chain are bound to the nitrogen atoms instead, the family of 1-alkyl-3-methylimidazoles is obtained. In order to avoid the repetition of such a verbose notation, the most common members of this family are referred to as DMIM (1, 3-dimethylimidazole), EMIM (1-ethyl-3-methylimidazole), BMIM (1-buthyl-3-methylimidazole), HMIM (1-hexyl-3-methylimidazole), MOIM (1-methyl-3-octylimidazole), etc. A less often seen but still common notation is based on specifying the number of carbons in the alkyl chain: C_6MIM instead of HMIM, for instance. Following the first of these conventions, $[BMIM]^+$ is 1-buthyl-3-methylimidazolium, the monovalent cation resulting from ionisation of BMIM. Some of the most frequent counterions are hexafluorophosphate ($[PF_6]^-$), tetrachloroborate ($[BF_4]^-$) and halogens such as chloride (Cl^-). Although the theoretical aspects in Part II of this thesis will try to be as general as possible, whenever specific examples are needed, most often they will be imidazolium-based ILs, since they are widely used in industry and there are force fields parameterised specifically for them and tested in MD simulations [218, 219]. An imidazolium ring, along with the $[BMIM]^+$, $[PF_6]^-$ and $[BF_4]^-$ ions, is represented in Fig. 6.1.

During the last years, a huge amount of research has been devoted to the synthesis and characterisation of new ILs, to the point that measurements on thousands of them have been reported in the literature. Nevertheless, the total number of possible binary ILs is on the order of magnitude of 10^6 and this estimation rises to 10^{18} if ternary liquids are also included [220], which leaves almost unlimited room for further growth of the accumulated experimental knowledge in the field. Unfortunately, this explosion in the spectrum of available ILs has not yet been followed by the development of a comprehensive theoretical framework. Therefore, at this point it is relatively easy to create new ILs but extremely difficult to predict their properties in advance. Instead, it is usually necessary to review a vast amount of bibliography or to perform new measurements. In this way, the breadth of this family of liquids and the absence of a predictive theoretical model collude to make the process of finding the optimal IL for a given application notoriously challenging.

The very first works about ionic liquids, almost a century ago, already concerned themselves with their electric conductivity [211]. Today, members of this family of "designer solvents" are being considered as candidates for multiple electrochemical applications, ranging from solar cells to mechanical actuator devices [221]. There is thus little doubt that their transport properties are of great practical importance. The final two chapters in this thesis are devoted to the elements of a new theory of electric and thermal transport in ILs based upon ideas which have already been proven fruitful for equilibrium studies. This chapter, however, deals with an MD investigation into the nanostructure of this kind of systems and their mixtures. Such study was considered necessary because, as it will be seen in later sections, the structure at this level has a great impact on transport properties. This comes as no surprise since it is already known to play an important role in equilibrium variables [222–224]. In fact, ILs not only are undoubtedly nanostructured media, but can also serve as nanostructuring agents, for instance for the *in situ* synthesis of nanoparticles of Ru and Co [225].

It is known that in ILs the choice of cation and anion can affect the miscibility with other solvents such as water or alcohols; for example, the solubility of imidazolium-based ILs in water decreases with an increase in the length of the alkyl side chain [226], while the behaviour in mixtures with an alcohol is exactly the opposite [226, 227]. The relation of the miscibility behaviour with a variation of the anion is more complex but, in general, solubility is higher for smaller anions [228]. The presence of these solvents can completely change

several physical and chemical properties of ILs such as polarity, viscosity and electric conductivity [229–231]. Therefore, an insight at the molecular level into the properties of mixtures of ILs with solvents such as water or alcohols is of primary importance from both theoretical and industrial perspectives.

The presence of water in ILs is very common since all of them are hygroscopic (even hydrophobic ILs can absorb a significant amount of water from the atmosphere [14, 232–234]). Because of this reason, a large number of both experimental [235–238] and computational [239–244] studies of the nanostructural organisation of ILs when mixed with water and of the interactions between them can be found in the literature. However, studies concerned with mixtures of ILs with alcohols have been scarcer and, in the bibliographic search performed for this work, only one [223] was found that deals, albeit through indirect inferences, with the evolution of cluster formation with alcohol concentration.

Among the experimental studies reported up to now, Fazio *et al.* [236] investigated in 2008, by using Raman and infrared spectroscopy, the local organisation of water in mixtures with 1-buthyl-3-methylimidazolium tetrafluoroborate ([BMIM][BF_4]). They indicated that at very high concentrations of IL water molecules tend to be isolated from each other or exist as small independent clusters embedded in the polar network. They proposed a picture where, as water concentration increases, a continuous water network appears and coexists with the IL. That same year, Zhang *et al.* [238] applied two-dimensional vibrational spectroscopy to investigate the dilution process of 1-ethyl-3-methylimidazolium tetrafluoroborate ([EMIM][BF_4]) in water. They found that the network formed by cations and anions in pure ILs is gradually split into huge ionic clusters, and then those are further dissociated into ionic pairs surrounded by water.

Regarding computational studies, the first molecular description of water structuring within an IL was provided by Hanke and Lynden-Bell [239]. They performed MD simulations of mixtures of 1, 3-dialkylimidazolium ILs and water in order to investigate their microscopic physical properties as a function of composition. They reported that water molecules tend to be isolated from each other in mixtures with fewer water molecules than ions, while at high solvent concentrations a percolating network of water coexists with some isolated water molecules and small clusters of this solvent. Last year, Bernardes *et al.* [240] performed MD simulations of the structure of aqueous solutions of 1-ethyl-3-methylimidazolium ethylsulfate ([EMIM][$EtSO_4$]) in the entire con-

centration range. They described the size and connectivity of different water and ion aggregates as a function of the solvent concentration, identifying four concentration ranges with distinct structural regimes and two different percolation thresholds. Another useful way of gathering information about the microscopic structure of these mixtures is the study of the angular distribution of the molecules. Spickermann *et al.* [244] presented results from a first principles MD simulation of a single 1-ethyl-3-methylimidazolium chloride ([EMIM][Cl]) ion pair dissolved in 60 water molecules. They studied the orientation of water molecules within the solvation shells and they found evidence for a linear hydrogen bond arrangement from chloride to water, in contrast to a tangential orientation of water around the hydrophobic subgroups.

In spite of these experimental and computational studies on mixtures, knowledge of the interaction between the IL and the solvent, as well as of the aggregation process in the mixture, remains somewhat empirical. This chapter reports the conclusions of simulations of [BMIM][BF_4] with three different solvents, water, methanol and ethanol, at several concentrations over the whole miscibility range. The choice of $[BF_4]^-$ for the anion responds to its displaying an intermediate hydrophobicity between that of halogens and $[PF_6]^-$, in addition to being one of the most popular choices in practical applications. This work focused on the study of the formation of ionic and solvent clusters in all the systems, as well as on the structural changes brought about by variations in the solvent mole fraction. Moreover, the angular distribution of the solvent around the cation and the anion was analysed in order to gain insight into the relative orientation of the molecules.

6.2. Simulation details

In contrast to the MD simulations in Part I, a custom piece of software was not developed for the simulation of ILs; instead, an open-source package was used, version 4.5.4 of GROMACS (GROningen MAchine for Chemical Simulations) [245–248]. GROMACS can be considered a standard for the classical simulation of organic molecules — for instance, the four references just mentioned have been cited around 7000 times, in applications that range from protein folding to viral capsid assembly. This software package offers carefully optimised algorithms, excellent parallel performance and good integration with post-processing tools. Among the force fields implemented in GROMACS, OPLS-AA (Optimised Potential for Liquid Simulations

– All Atom) was chosen [249] due to the availability of a recent parameterisation [219] for 1-alkyl-3-methylimidazoliums that affords results close to experiments for a range of temperatures and alkyl chain lengths.

OPLS-AA, like most of the potentials used for simulations of organic molecules (sometimes called molecular mechanics) depends on a relatively high number of parameters, which traditionally were fitted to thermodynamic properties of the substances of interest, but more recently are calculated using *ab initio* simulations. On the other hand, the functional forms of its terms are quite simple and determined *a priori* so as to capture the essential features of each kind of interaction. These are classified as bonded or non-bonded depending on whether they act only between atoms in the same molecule or between any set of atoms, respectively. Here it must be noted that in all-atom force fields, such as OPLS-AA, the notion of atom is the physical one, whereas in the so-called united-atom force fields a single atom can comprise a whole functional group (*e.g.* CH_3). In particular, OPLS-AA consists of:

- Non-bonded van der Waals and Coulomb interactions, in their usual forms. For two molecules a and b,

$$V_{\text{non-bonded}}(a,b) = \sum_{\substack{i\in a \\ j\in b}} f_{ij} \left\{ 4\epsilon_{ij} \left[\left(\frac{\sigma_{ij}}{r_{ij}} \right)^{12} - \left(\frac{\sigma_{ij}}{r_{ij}} \right)^{6} \right] + \frac{1}{4\pi\varepsilon_0} \frac{q_i q_j}{r_{ij}} \right\}, \tag{6.1}$$

  where q_i is the partial charge of atom i and σ_{ij} and ϵ_{ij} are van der Waals parameters (Lennard-Jones — LJ — radii and well depths, respectively) for atom pair (i,j) calculated using the combination rules $\epsilon_{ij} = \sqrt{\epsilon_i \epsilon_j}$ and $\sigma_{ij} = \sqrt{\sigma_i \sigma_j}$. To avoid interactions between first, second and third neighbours in a molecule being counted twice (once as bonded interactions and once as non-bonded) a factor f_{ij} is introduced which depends on the number of bonds, $n_b(i,j)$ between two atoms:

$$f_{ij} = \begin{cases} 1, & a \neq b \\ 1, & a = b \text{ and } n_b(i,j) > 4 \\ \frac{1}{2}, & a = b \text{ and } n_b(i,j) = 4 \\ 0, & a = b \text{ and } n_b(i,j) < 4. \end{cases} \tag{6.2}$$

Because of its role in reducing the energy ascribed to interactions between first-to-fourth neighbours, f_{ij} is known as the $1-4$ scaling factor.

- Bonded interactions that account for the contributions to energy due to bond and angle stretching and to changes in dihedrals with respect to their equilibrium values. These three contributions have the following forms, based on series expansions:

$$V_{\text{bonded}} = V_{\text{stretch}} + V_{\text{angle}} + V_{\text{dihedrals}} \tag{6.3a}$$

$$V_{\text{stretch}} = \sum_{(i,j)\text{ are bonded}} K_r\left(i,j\right)\left[r_{ij} - r_{0,ij}\right]^2 \tag{6.3b}$$

$$V_{\text{angle}} = \sum_{\substack{(i,j,k)\text{ form} \\ \text{an angle}}} K_\theta\left(i,j,k\right)\left[\theta_{ijk} - \theta_{0,ijk}\right]^2 \tag{6.3c}$$

$$V_{\text{dihedrals}} = \sum_{\text{dihedrals } \Phi_s} \left\{ \frac{V_1(s)}{2}\left[1 + cos\,\Phi_s\right] + \frac{V_2(s)}{2}\left[1 - cos\left(2\Phi_s\right)\right] + \right.$$
$$\left. + \frac{V_3(s)}{2}\left[1 + cos\left(3\Phi_s\right)\right] + \frac{V_4(s)}{2}\left[1 - cos\left(4\Phi_s\right)\right] \right\}. \tag{6.3d}$$

The cation was modelled using the all-atom representation of the CH_2 and CH_3 groups in the alkyl chain, as well as that of the methyl group attached to the imidazolium ring. As for the anion, $[BF_4]^-$ was modelled as a set of 5 sites with partial charges of 1.176 for the boron atom and −0.544 for the fluorine atoms [250]. These partial charges, obtained from the literature, were computed using MP2/6-31g(d) by means the ChelpG methodology [251] as implemented in the GAUSSIAN [191] package. On the other hand, water molecules were represented using the TIP5P water model [252], which consists of a LJ centre placed on the oxygen, two positive +0.241 charges located at the hydrogen atoms and two partial −0.241 charges representing the lone pairs of the oxygen atoms. For ethanol and methanol the molecular model proposed by Jorgensen [219] was employed. Long-range electrostatic interactions were computed using the Particle-Mesh Ewald (PME) [253] method with a grid spacing of 0.12 nm and cubic interpolation. A cut-off distance of 1.1 nm was used for LJ interactions, a neighbour search was carried out up to this same distance from the central ion, and its results updated every five simulation steps. The Linear Constraint Solver (LINCS) algorithm [254, 255] with a fourth-order

expansion of the coupling matrix was used to constrain the bonds, and long range dispersion corrections were applied to energy and pressure. As regards the integration method, instead of the velocity Verlet algorithm [Eqs. (2.6)], GROMACS by default uses the following equations, known as the leapfrog integration scheme [256]:

$$\vec{r}_i(t+\Delta t) = \vec{r}_i(t) + \vec{v}_i\left(t+\frac{\Delta t}{2}\right)\Delta t \tag{6.4a}$$

$$\vec{v}_i\left(t+\frac{\Delta t}{2}\right) = \vec{v}_i\left(t-\frac{\Delta t}{2}\right) + \vec{a}_i(t)\,\Delta t. \tag{6.4b}$$

The leapfrog integrator is somewhat more efficient than the velocity Verlet algorithm but, since its positions and velocities are not evaluated at the same time steps, it may afford less accurate results in some situations.

Initial configurations for the molecules in the simulation boxes were generated at random using PACKMOL [257] to ensure that no two of them lied beneath a minimum distance of 3 Å from each other, and the sides of the box chosen so as to yield a density slightly below the experimental value. Periodic boundary conditions were applied in all directions. These configurations were then energy-minimised for 10^6 steps using a conjugated gradients algorithm in order to remove bad contacts resulting from the initial random placement of ions. The maximum step size and the tolerance were set to 0.01 nm and 0.1 kJ/(nm mol), respectively. The equilibration phase was performed in the isothermal-isobaric $\left(N,p,T\right)$ ensemble for a length of 100 ps, which is usually considered to be enough for imidazolium-based ILs [258]. The results of an additional 2000 ps-long simulation in the isothermal-isobaric ensemble were used for analysis. The temperature control was implemented using a V-rescale thermostat [259]. Cations and anions (and water or alcohols in those cases where a solvent is included) were separated in two (three) baths with temperature coupling constants of 0.1 ps. Pressure was controlled using the Parrinello-Rahman barostat [260] with a reference pressure of 1 atm, an isothermal compressibility of $4.5 \cdot 10^{-5}$ bar^{-1}, and a relaxation time of 0.1 ps.

6.3. Results and discussion

In order to investigate cluster formation when a solvent is added to [BMIM][BF_4], the size of both ionic clusters and clusters of solvent molecules

Figure 6.2 Top: cation-anion, cation-cation and anion-anion RDFs in pure [BMIM][BF_4]. The dashed line marks the cut-off distance taken for considering two ions as connected. Bottom: oxygen-oxygen RDFs in pure water, ethanol and methanol.

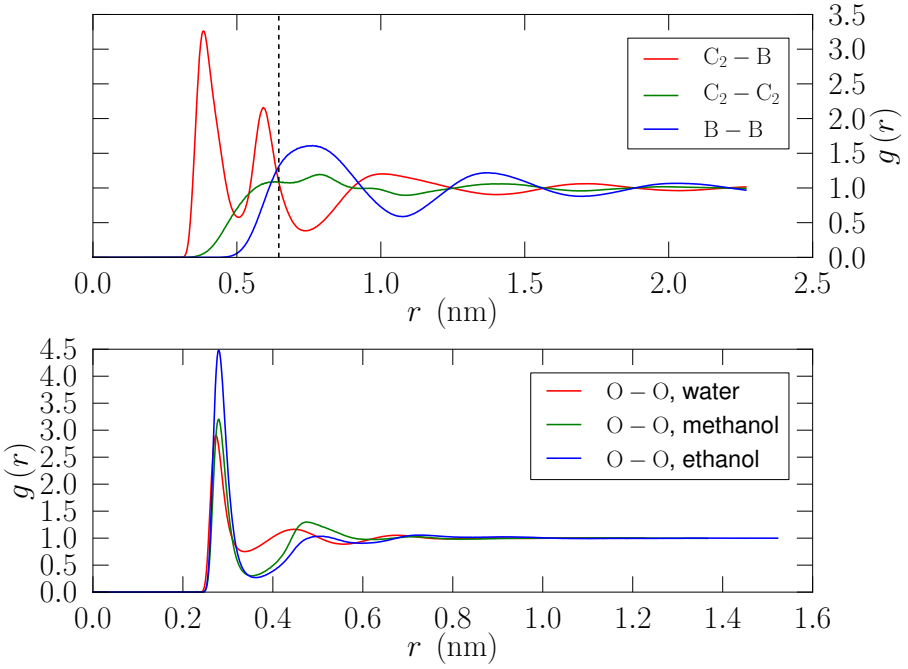

were analysed. Following the criterion defined by Hanke and Lynden-Bell [239] and later employed by Bernardes *et al.* [240], it was considered that two molecules of water or alcohol are connected to each other and thus belong to the same cluster if the distance between their oxygen atoms is smaller than the radius corresponding to the first minimum in the oxygen-oxygen radial distribution function [RDF, $g(r)$] in the pure liquids (Fig. 6.2, bottom). This is the limit of the first solvation layer, and corresponds approximately to the distance used to define a hydrogen bond in the geometrical criterion commonly employed in MD (hydrogen-acceptor distance smaller than 3.5 Å, and donor-hydrogen-acceptor angle less than 30° [261]).

The criterion used to define ionic clusters is slightly different. Heterocoordination between cations and anions is the norm in ILs due to its energetic advantages; therefore, the distance considered as the cut-off was 0.65 nm, which is the distance where the cation-anion and cation-cation RDFs of pure

Figure 6.3 Solvent concentration dependence of the percentage of ions (left panels) and solvent molecules (right panels) forming clusters and big clusters in mixtures of [BMIM][BF_4] with water (top), methanol (centre) and ethanol (bottom). Solid circles mark the simulated concentrations; lines are provided only as guides to the eye.

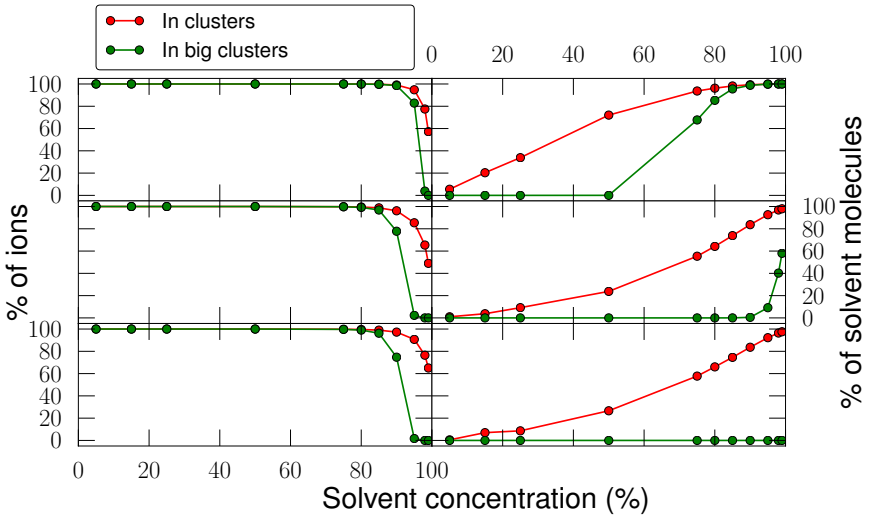

[BMIM][BF_4] intersect (Fig. 6.2, top), and accordingly the minimum distance at which it is more likely to find a second cation after a cation-anion pair. These RDFs were calculated using the boron atom (B), at the centre of mass of $[BF_4]^-$, as representative of the anion, and the carbon atom between the two nitrogens (C_2) as representative of the imidazolium ring. It should be noted that these cut-off distances remain unaffected when the solvent concentration is varied.

For each frame along the MD trajectory, a search was performed to build the connectivity matrix of an undirected network representing the neighbourhood relations of solvent molecules or ions in the mixture at that particular time step, according to the cut-off radii previously chosen. Clusters were then defined as the connected components of that undirected graph. The cluster distribution of each mixture was obtained by taking into account the clusters formed at all time steps in the simulation. Big clusters were arbitrarily defined, for the purposes of the present work, as those that comprise more than 50% of the particles belonging to the class under study (either solvent molecules or ionic pairs) in the simulation box.

Figure 6.3 shows the evolution of the percentage of water, methanol and

ethanol molecules, respectively, that belong to a cluster (*i.e.*, which are not isolated) and to a big cluster. As Fig. 6.3 (top left) shows, all the ions belong to big clusters up to a water molar percentage of 90%; after this concentration, the number of cations and anions forming clusters decreases when the amount of water is increased. However, in mixtures with methanol and ethanol (Fig. 6.3, centre left and bottom left, respectively) the percentage of ions in big clusters starts to decrease at an alcohol concentration of 80%. In regard to solvent clusters, the percentage of water molecules that belong to a cluster increases rapidly with the amount of water (Fig. 6.3, top right): indeed, at a molar percentage of approximately 35% half of the water molecules belong to a cluster, and when 80% of water is reached more than 80% of the water molecules are forming big clusters. The behaviour of alcohol molecules is markedly different: firstly, the increase with alcohol concentration of the number of solvent molecules belonging to a cluster (Fig. 6.3, centre right and bottom right) is much slower than in the case of water. Even at 70% alcohol, half of the alcohol molecules still do not belong to any cluster. Methanol molecules start to form big clusters in a significant number at very high alcohol concentrations (99% and above) but those clusters are conspicuously absent from [BMIM][BF_4] + ethanol mixtures.

Further insight into the modifications introduced by a solvent in the clustering process of [BMIM][BF_4] is given by the size distribution histograms of ionic and solvent clusters for each of the systems. Figure 6.4 shows the probability of finding an ion or a molecule of water in an aggregate comprising a given percentage of the particles in the simulation box for three different water concentrations. Solid dots show the actual cluster sizes n in order $n = 1$, $n = 2$… The same quantities are shown for mixtures with methanol and ethanol in Figs. 6.5 and 6.6. The broken horizontal axes in these figures serve the purposes of highlighting the lower and higher percentages and hiding the intermediate values, which were found to have negligible probability.

As Fig. 6.4 (top) shows, the size of ionic clusters decreases when the amount of water in the mixture is increased, which is in good agreement with the results reported by Bernardes *et al.* [240]. Up to a water concentration around 90%, all the ions tend to be part of the same large cluster, which can in fact be identified as a polar IL network; after this percentage the probability of finding small ionic clusters starts to increase, and at over 98% of water most of the ions are isolated within bulk water. As expected, the behaviour of water molecules is exactly the opposite. As depicted in Fig. 6.4 (bottom), at

Figure 6.4 Probability of finding an ion (top) or a water molecule (bottom) in a cluster comprising a given percentage of the particles of that same type in the simulation box, for three different water concentrations. Solid circles mark the possible sizes: $n = 1$, $n = 2$… starting from the left. The inset shows the probabilities for low concentrations in greater detail.

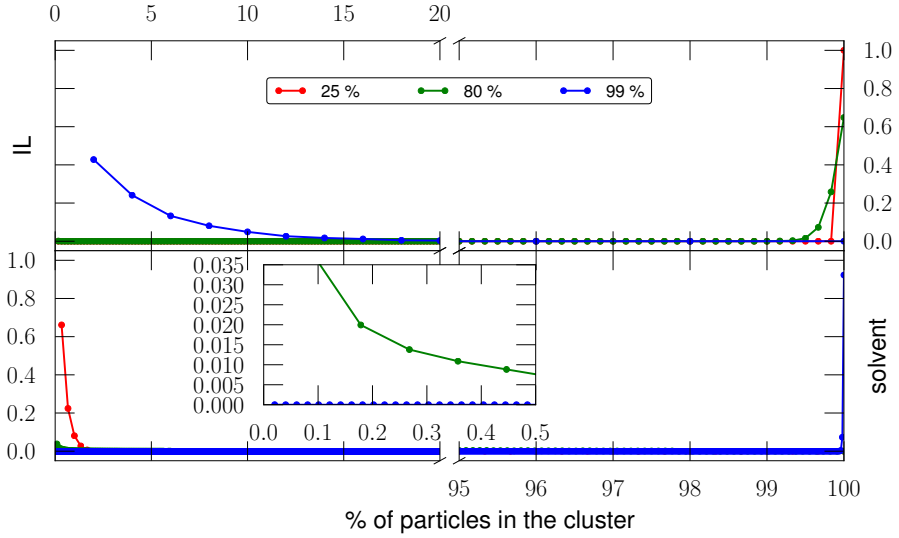

Figure 6.5 As in Fig. 6.4, but for methanol instead of water.

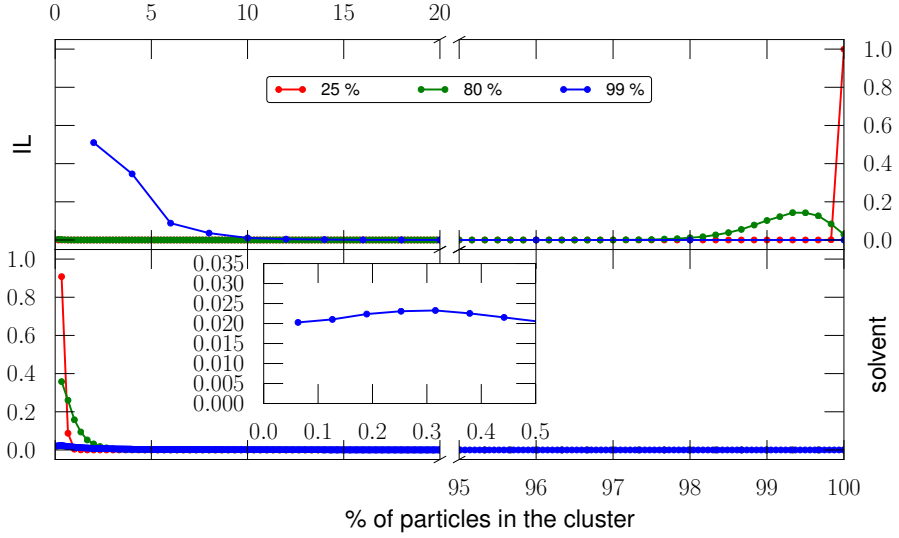

Figure 6.6 As in Fig. 6.4, but for ethanol instead of water.

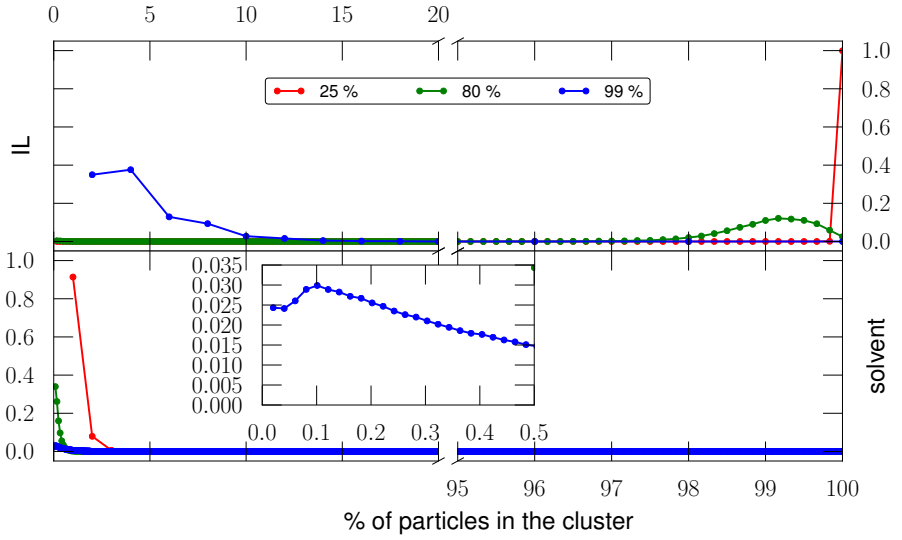

low water concentrations isolated water molecules or those belonging to very small clusters (no more than 4 or 5 molecules) dominate the mixture. As the amount of water increases, the probability of finding water aggregates with larger sizes starts to rise, and over a water concentration of 85% many water molecules belong to a cluster whose size is very close to the total number of water molecules in the mixture, with only a few isolated or forming small independent water clusters. The fact that most water molecules are isolated at low water concentrations is consistent with conclusions previously reported in the literature [236, 239], and it has been attributed to the strong interaction between water molecules and anions [237, 243]. It must be noted that there is no particular tendency to the formation of ion pairs or larger uncharged clusters in preference to single ions or charged clusters. This may be attributed to the high dielectric constant of water, $\varepsilon_{\text{water}} = 78.5\varepsilon_0$.

As suggested by some previous results [222], the behaviour of clusters in IL + alcohol mixtures is markedly different. For IL + ethanol mixtures with 25% ethanol, Fig. 6.6 (top) shows that the size distribution of ionic clusters shares its main features with the case of IL+water mixtures. However, as more alcohol is added (for example, at 80%) the mode of the distribution is shifted from 100% to somewhat smaller percentages, which implies that the IL network has

been broken into large ionic clusters. This intermediate regime is not observed in mixtures with water at any concentration, since in that case ions predominantly appear either isolated or forming a single IL network. Figure 6.6 (top) also provides evidence of the tendency of ions to appear in pairs even at very high solvent concentrations, such as 99% ethanol. This is reflected in the fact that the mode of the distribution is not $n = 1$, but $n = 2$. Histograms for the most dilute IL + methanol mixtures (included as Fig. 6.5) reveal that, in contrast to this, within these systems isolated ions are more likely than ionic pairs. In regard to alcohol clusters, Figure 6.6 (bottom) shows that, although it is true that when more alcohol is present clusters somewhat larger than a dimer become possible, an alcohol network is never formed (even in pure alcohol), in stark contrast to what happens in water. This behaviour, now directly observed in the simulations, is probably at the root of the differences in equilibrium and dynamical properties of IL + water *vs.* IL + alcohol mixtures [222, 262].

Arguably, expressing concentrations in terms of mole fractions may not be the most informative choice as regards the spatial organisation of a liquid mixture. The ability of solvent molecules to interact among themselves depends not only on their number but also on the space available to them, related, in turn, to their molar volume. This is especially important when molecules of quite different sizes are being compared, as is the case in this work. Further insight can be gained by studying aggregation as a function of the volume fraction of solvent, Φ_s. By way of example, volume fraction is also considered the relevant magnitude for spatial occupation in the Flory-Huggins polymer solution theory [263] and the statistical lattice theory of mixtures [264], and will also be used in this role in Chapter 7. Figure 6.7 shows the same information as Fig. 6.3 but now presented as a function of Φ_s. A set of equivalences between mole fractions and volume fractions are shown in Table 6.1. The densities used to build this table were also taken from GROMACS simulations, already proven capable of yielding reliable values of this variable [223].

The behaviour of ionic clusters is approximately universal when studied as a fraction of solvent volume fraction, due to the fact that, water molecules being smaller than alcohol molecules, $\Phi_{\text{water}}(x)$ is the slowest-growing function in Table 6.1, which neutralises the relatively small differences apparent in the left panels of Fig. 6.3. On the other hand, the greater tendency of water to form clusters is even more patent in Fig. 6.7: big clusters are clearly dominant in water from volume fractions as low as 20%, whereas for alcohols they are either totally absent (in ethanol) or present only at very high solvent volume fractions

Table 6.1 Volume fraction *vs.* mole fraction for the three solvents studied.

x (%)	Φ_{water} (%)	Φ_{methanol} (%)	Φ_{ethanol} (%)
5	0.50	1.12	1.57
15	1.66	3.67	5.07
25	3.09	6.73	9.18
50	8.75	17.92	23.44
75	22.38	40.05	48.20
80	27.77	47.28	55.45
85	35.27	56.22	63.94
90	46.44	67.43	73.96
95	64.77	81.77	85.83
98	82.64	92.24	94.04
99	90.61	96.05	96.98

(in methanol). Even small solvent clusters, known from the detailed analysis of sizes performed above to be mainly aggregates of less than 10 molecules, appear only very gradually when alcohol is added to the mixtures, while in water they contain nearly four out of ten solvent molecules at a solvent volume fraction just over 3%.

Thus, from the analysis of cluster formation in mixtures of [BMIM][BF_4] with water, ethanol and methanol it can be concluded that when a low amount of solvent is present in the mixture both water and alcohol molecules tend to be isolated from each other or forming clusters smaller than 4 or 5 molecules. When more solvent is added to the mixture, the probability of finding larger solvent clusters increases while at the same time the probability of finding all the ions in a single large cluster forming a polar network of IL decreases, which is a sign that solvent clusters are starting to break the ionic network. Finally, at very high water concentrations water molecules tend to belong to a single large cluster whose size is approximately the same as the number of water molecules present in the mixture, pointing to the formation of a water network that completely breaks the ionic network, since ions tend to be isolated or forming very small clusters at this water concentration. Figure 6.8 illustrates this by showing the ionic clusters at a particular time step for three water concentrations. Regarding alcohols, at very high concentrations ions tend to form pairs in mixtures with ethanol and to be isolated if the added solvent is methanol. This difference can be attributed to the lower dielectric constant of ethanol compared with water and methanol ($\varepsilon_{\text{methanol}} = 33.0\varepsilon_0$, $\varepsilon_{\text{ethanol}} = 24.2\varepsilon_0$). Contrary to what happens in mixtures with water, far fewer, if any, very large clusters

Figure 6.7 As Fig. 6.3, but with the volume fraction as the independent variable. From top to bottom: water, methanol and ethanol.

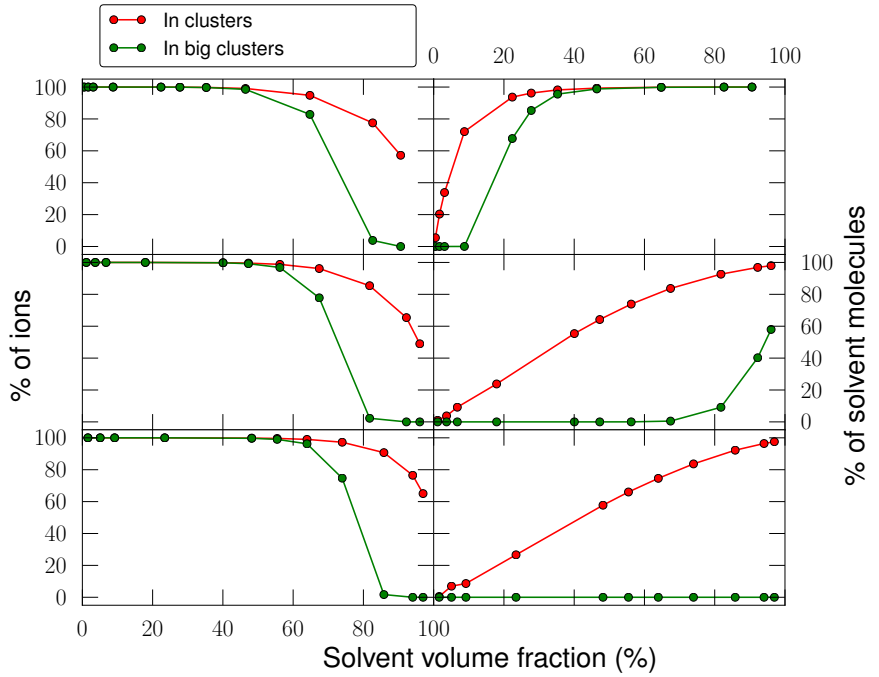

of alcohol molecules are found at any amount of either ethanol or methanol, which suggests that alcohol molecules are homogeneously distributed in the structure of the imidazolium-based IL. This explains their reduced ability to break the IL network, reflected in the fact that an intermediate regime with large ionic clusters appears in mixtures with alcohol, but not in those with water.

Another way to study the structure of mixtures of [BMIM][BF_4] with water and alcohols is the analysis of the angular distribution of the solvent around the cation and the anion in the systems. To this end, a coordinate system centred on C_2 (the carbon atom between the nitrogen atoms in the ring) for the cation or B (the central boron atom) for the anion was taken, and the angle θ_1 between two vectors computed: the first is the position vector of the oxygen atom of the solvent; the second goes from the oxygen atom to the middle point of the two hydrogens (in water) or to middle point between the *H* and *C* atoms bonded to the oxygen (in alcohols). This definition is shown schematically in

Figure 6.8 Ionic clusters in a [BMIM][BF_4] + water mixture with 25% (top), 95% (centre) and 99% (bottom) water. The different colours of the surfaces enclosing the clusters are intended to help differentiate them. The progressive breakdown of the ionic network can be observed.

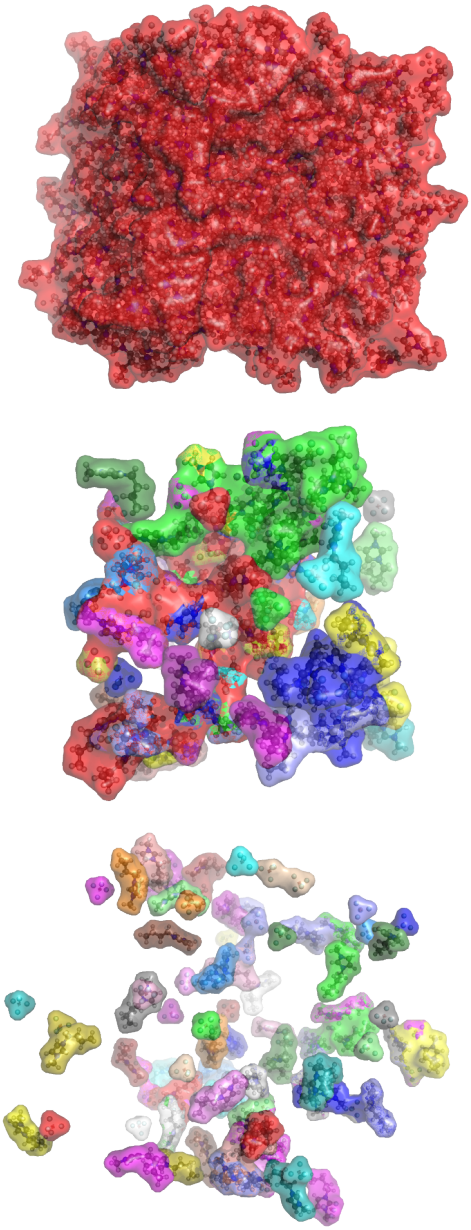

Figure 6.9 Graphical scheme of the definition of θ_1 for two molecules, water and ethanol, around a $[BMIM]^+$ ion. The criterion for methanol is identical to that for ethanol.

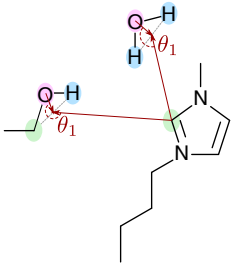

Fig. 6.9 for water and ethanol; the definition for the latter of is also valid for methanol. Therefore, this second vector is parallel to the dipole moment of water, but forms an angle of 27.8° with the dipole moment of ethanol and a 47.4° angle with the dipole moment of methanol. The conditional probability density $f\,(cos\ \theta_1|r)$, *i.e.*, the probability density that a solvent molecule known to be placed at a distance r from a central ion is oriented in such a way that it yields a value of $cos\,\theta_1$ in a particular interval, was then studied. This density provides a detailed picture of the structure of each solvation layer of both cations and anions.

Figures 6.10 and 6.11 illustrate the probability density of $cos\,\theta_1$ in $[BMIM][BF_4]$ + water mixtures for different distances and two water concentrations (25% and 95%, respectively) in order to analyse the orientation of the solvent around the cation (left) and the anion (right) and its evolution with the addition of solvent to the mixtures. Taking into account the definitions given above, in Figs. 6.10 and 6.11 it can be seen that those water molecules placed immediately beyond the van der Waals excluded volume of the ions are closely aligned with the monopole term of the cation and anion fields, since $cos\,\theta_1 = +1$ and $cos\,\theta_1 = -1$, respectively. As expected from their charges, the cation prefers the region near the oxygen atom of water and far from the two hydrogen atoms, while the anion gets close to the oxygen atom approaching from between the two hydrogen atoms. Moreover, in the first solvation layer of water molecules around both the cation and the anion an exclusion area can be observed, antiparallel to the field, where no water molecules can be found. In the case of the solvation of the anion, at low water concentrations there is another exclusion area at around 0.5 nm in which there are no water

Figure 6.10 Conditional probability density of $cos\,\theta_1$ for water molecules at different distances in mixtures of [BMIM][BF_4] with a water concentration of 25%. Cation-cation or anion-anion (red), cation-anion (green) and ion-solvent (blue) RDFs are also included for easy comparison.

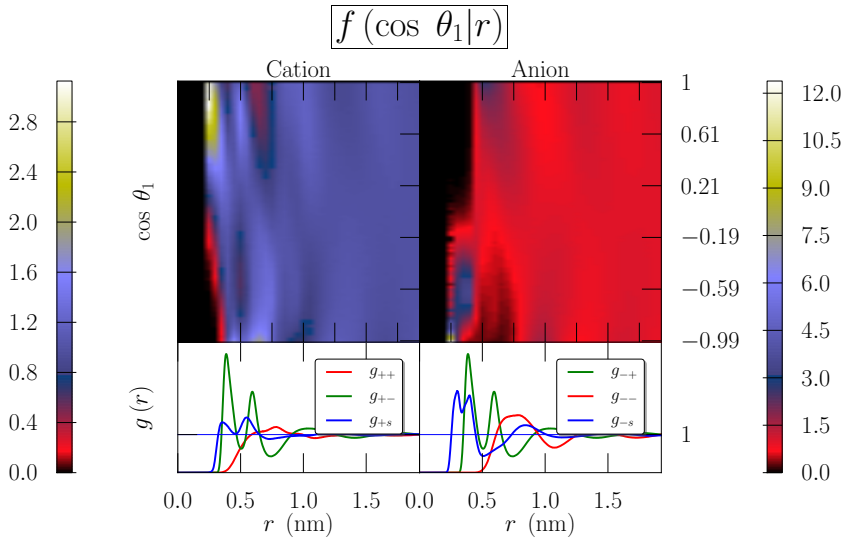

Figure 6.11 As in Fig. 6.10, but for a water concentration of 95%.

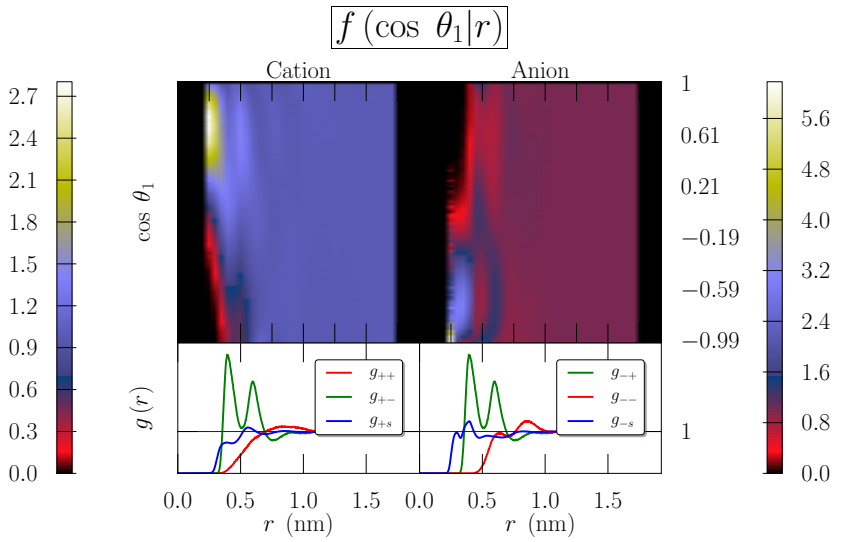

Figure 6.12 As in Fig. 6.10, but for ethanol molecules in a [BMIM][BF_4] + ethanol mixture with 25% ethanol.

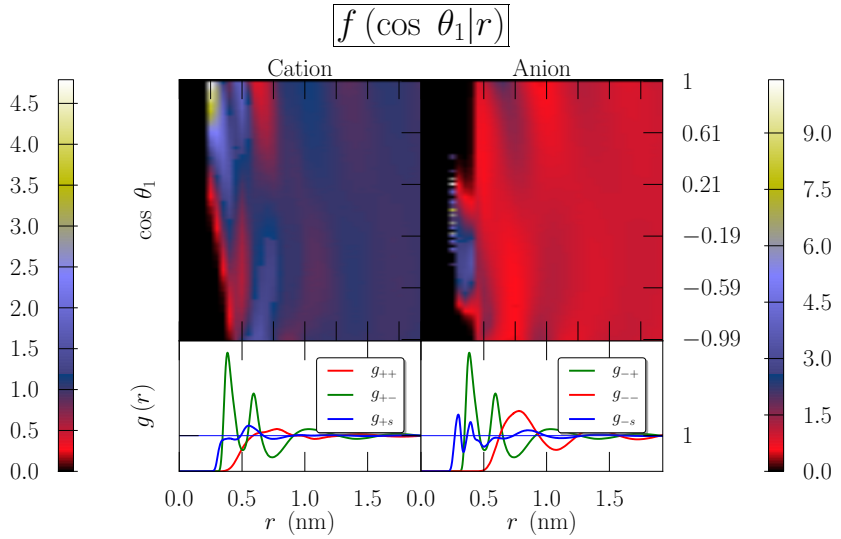

Figure 6.13 As in Fig. 6.10, but for ethanol molecules in a [BMIM][BF_4] + ethanol mixture with 95% ethanol.

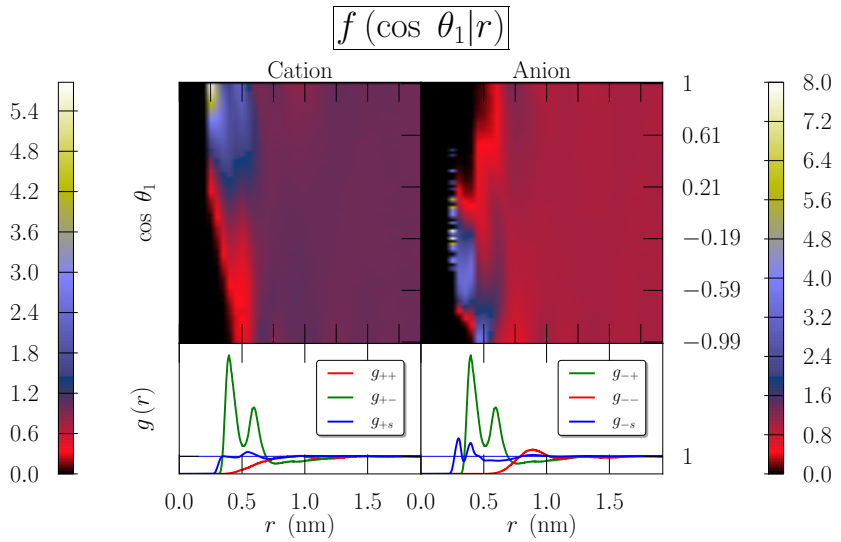

Figure 6.14 As in Fig. 6.10, but for methanol molecules in a [BMIM][BF_4] + methanol mixture with 25% methanol.

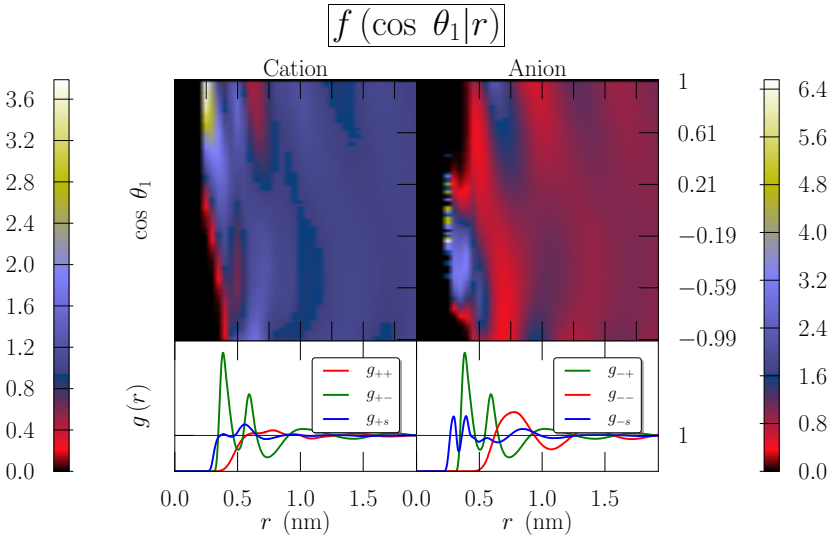

Figure 6.15 As in Fig. 6.10, but for methanol molecules in a [BMIM][BF_4] + methanol mixture with 95% methanol.

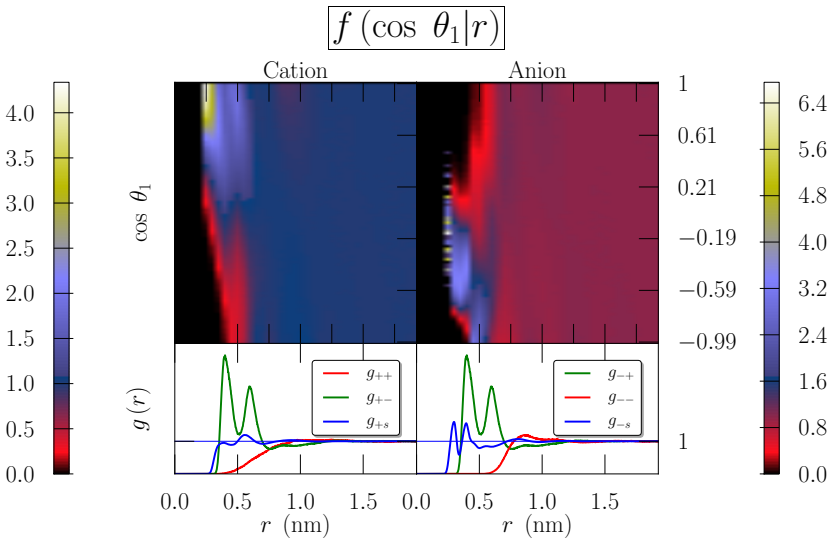

molecules, parallel to the field. However, this exclusion area disappears with the addition of water to the mixture and it cannot be detected over a water concentration of 50%. This indicates that the interaction of water molecules with the anion is very strong at low water concentrations, as reported in the analysis of cluster formation. Furthermore, it can be seen that as water is added to the mixture it gradually becomes less oriented around the ions (the maximum of the probability density is more diffuse and not so clearly placed at $cos\,\theta_1 = \pm 1$) since water molecules tend to interact more strongly with each other than with the charged ions. This is another sign of the formation of water clusters in mixtures of [BMIM][BF_4] and water.

In Figs. 6.12 and 6.13 it can be seen that the behaviour of ethanol molecules is completely different from that of water. Firstly, while in the solvation layer of the cation there is also an area without alcohol molecules parallel to the field, the orientation of alcohol molecules around the anion shows two exclusion zones, one of them corresponding to alcohol molecules parallel to the field and the other to antiparallel orientations. Additionally, looking at the orientation of alcohol molecules around the anion, it can be seen that in the first solvation shell (presumably with the anion near the oxygen atom) several discrete orientations are possible, probably due to the presence of cations in the neighbourhood, whose chains interact with the alcohol molecules, favoring only a certain number of angles. Moreover, the second layer seems to be more oriented than the first one. The orientation of alcohol molecules around both ions experiences almost no changes with the addition of alcohol to the mixture, which shows that alcohol distribution in bulk mixtures depends only slightly on the concentration, in agreement with the previous statement that alcohol molecules do not form large aggregates in the mixture. The results for methanol are similar, albeit with a narrower distribution of orientations around the anion. They are presented as Figs. 6.14 and 6.15.

Since the limited ability of ethanol and methanol to form hydrogen bonds impedes cluster formation, it is convenient to look for subtler clues about the structure of these alcohols in mixtures with ILs. One such clue is provided by the atomistic RDFs shown in Fig. 6.16, where the first group considered comprises the carbon atoms in the alkyl side chain of $[BMIM]^+$ and the second group is formed by the carbon atom (both carbon atoms) of methanol (ethanol). Therefore, Fig. 6.16 contains information about the distribution of distances between the apolar parts of both the IL and the solvent in [BMIM][BF_4]+alcohol mixtures. Not unexpectedly, there is a tendency for

Figure 6.16 Atomistic RDFs of the carbon atoms in the alcohols with respect to the carbons in the alkyl chain of $[BMIM]^+$, for six different mole fractions of methanol (top) and ethanol (bottom).

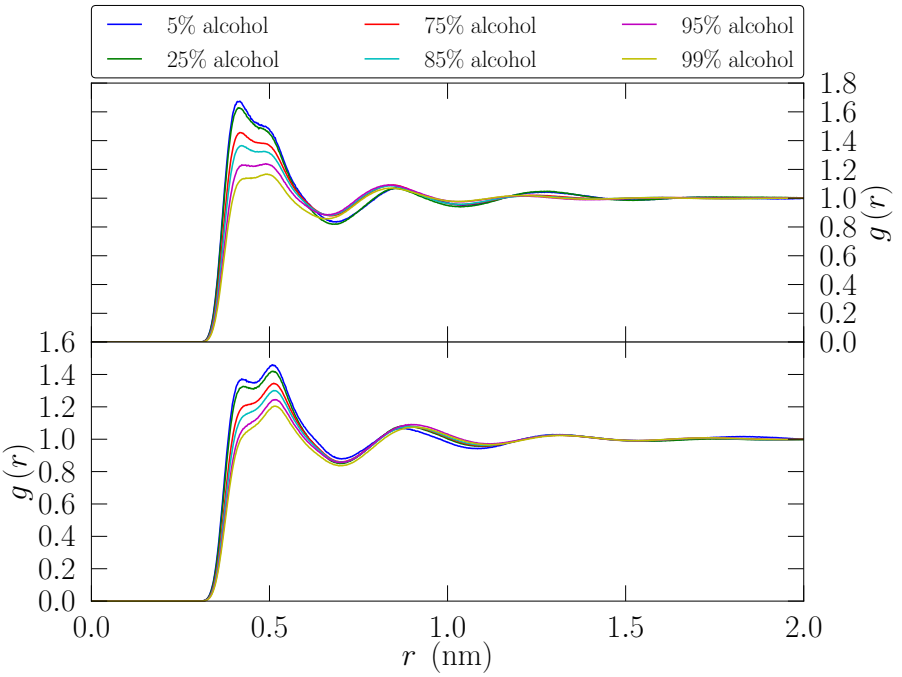

apolar chains to stick together, manifested in the sheer rise of these RDFs right after the excluded region: the preferred distance is not much larger than the parameter σ for alkane carbons in OPLS-AA (0.35 nm). The broad width of the peaks in Fig. 6.16 is explained by the fact that carbons in the alcohol can be close to any of the four carbons in the alkyl chain of the IL, the most extreme of which are separated by 0.38 nm. This small degree of structure is gradually lost as more alcohol is added and alcohol-alcohol interactions become more relevant in detriment of alcohol-IL interactions.

Finally, some order could be expected to exist in alcohols due to dipole interactions, which should result in the formation of structures consisting of predominantly parallel alcohol molecules, rather than clusters. In a mixture with N_a molecules of alcohol, each with a dipole moment of modulus μ, a standard variable used to study the degree to which a molecular dipole $\vec{\mu}_j$ inside a sphere of radius r with its centre on another dipole $\vec{\mu}_i$ is (on average) oriented

at random or aligned parallel to $\vec{\mu}_i$ is the Kirkwood G factor [265],

$$G_K(r) = \frac{1}{N_a \mu^2} \sum_{i,j} \vec{\mu}_i \cdot \vec{\mu}_j \quad \Big| \quad r_{ij} < r. \tag{6.5}$$

G_K can also be calculated as an integral [265]:

$$G_K(r) = 1 + \frac{4\pi}{3V} N_a \int_0^r h_\Delta(s)\, s^2 ds \tag{6.6a}$$

with

$$h_\Delta(r) = 3 g_{OO}(r) \langle \cos\theta \rangle_r . \tag{6.6b}$$

Here, $g_{OO}(r)$ is the RDF for alcohol oxygen atoms and $\langle \cos\theta \rangle_r$ the average cosine of the angle between two dipoles at distance r. Thus, $h_\Delta(r)$ is an indicator of the tendency to parallelism of alcohol molecules at a particular distance. Figure 6.17 shows both $g_{OO}(r)$ and $h_\Delta(r)$ for pure ethanol (top) and for its mixtures with [BMIM][BF_4] at two different mole fractions of ethanol: 99% (centre) and 98% (bottom). The contrast between the behaviour of both variables is noteworthy, since while the oxygen-oxygen RDF is essentially identical for any of the three concentrations, h_Δ falls by three orders of magnitude even when just a tiny amount of IL is added to pure ethanol. In physical terms, this means that the angular correlation that is detected in pure ethanol, induced by dipole interactions, is almost completely destroyed by the monopole field of ions. Furthermore, at 98% ethanol it can be seen that $g_{OO}(r)$ and h_Δ have opposite signs around the first peak of the former, a sign that even neighbouring ethanol molecules are more influenced by whatever ion they are solvating than by each other. This trend continues at lower concentrations not shown in Fig. 6.17. Equivalent conclusions can be drawn from the corresponding plots for methanol, included as Fig. 6.18, except that h_Δ does not change sign even at lower alcohol concentrations. This is probably due to a combination of the greater relative importance of the polar part in methanol with respect to ethanol and of the tendency of ions to form pairs in ethanol, which makes it more likely that two neighbouring methanol molecules, solvating the same ion, are parallel.

Therefore, even though an analysis of the RDFs of the apolar part of the alcohols with respect to the apolar part of $[BMIM]^+$ shows some signs of structure due to hydrophobic interactions, very few traces of order can be said to

Figure 6.17 Oxygen-oxygen RDF and h_Δ (see definition in the text) for ethanol molecules in pure ethanol (top) and in mixtures with [BMIM][BF_4] at two different mole fractions of ethanol: 99% (centre) and 98% (bottom).

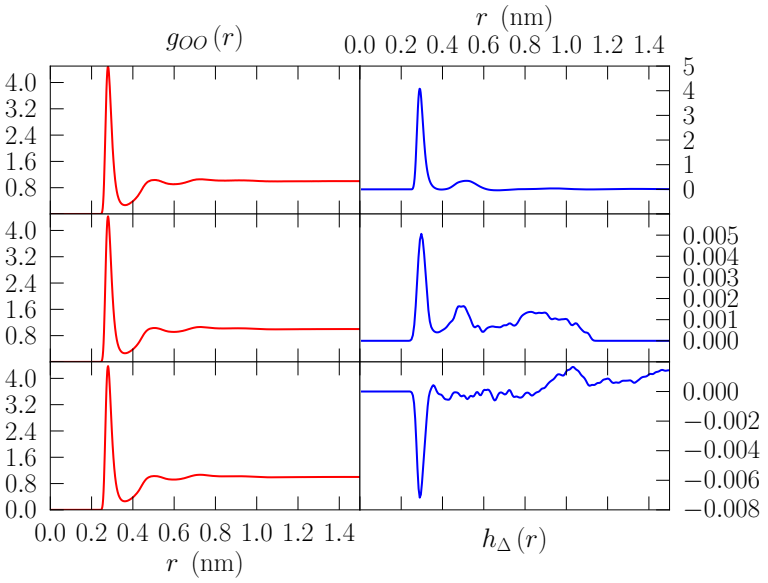

exist in the solvent in [BMIM][BF_4]+alcohol mixtures, as the influence of ions on methanol or ethanol molecules clearly outweighs their natural tendency to parallel alignment. This reinforces the conclusions drawn, earlier in this chapter, from comparison of cluster formation statistics and orientation diagrams with those obtained for [BMIM][BF_4]+water mixtures.

Figure 6.18 As Fig. 6.17, but for methanol instead of ethanol.

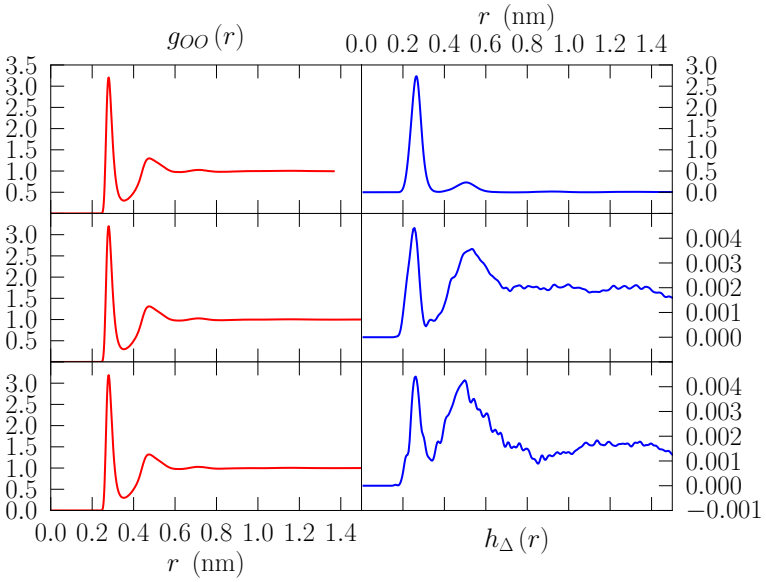

References

12. Rogers, R. D. & Seddon, K. R. *Ionic Liquids: Industrial Applications for Green Chemistry* (American Chemical Society, Washington, DC, 2002).

13. Rogers, R. D. & Seddon, K. R. *Ionic Liquids as Green Solvents: Progress and Prospects* (American Chemical Society, Washington, DC, 2003).

14. Wasserscheid, P. & Welton, T. *Ionic Liquids in Synthesis* 2nd (Wiley-VCH, New York, 2008).

191. Frisch, M. J. *et al. Gaussian 09 Revision A.02* Gaussian Inc. Wallingford CT 2009.

210. Walden, P. *Chem. Zentralbl.* **85,** 1800 (1914).

211. Walden, P. *Bull. Acad. Imper. Sci. St. Pétersbourg.* **8,** 405 (1914).

212. Hurley, F. H. & Wier, T. P. *J. Electrochem. Soc.* **98,** 207 (1951).

213. Scheffler, T. B., Hussey, C. L., Seddon, K. R., Kear, C. M. & Armitage, P. D. *Inorg. Chem.* **22,** 2099 (1983).

214. Laher, T. M. & Hussey, C. L. *Inorg. Chem.* **22,** 3247 (1983).

215. Wilkes, J. S. & Zaworotko, M. J. *Chem. Comm,* 965 (1992).

216. Swatloski, R. P., Holbrey, J. D. & Rogers, R. D. *Green Chem.* **5,** 361 (2003).

217. Yan, F., Xia, S., Wang, Q., & Ma, P. *J. Chem. Eng. Data* **57,** 805 (2012).

218. Méndez-Morales, T. *Trabajo fin de máster: Estudio Teórico-Computacional de Líquidos Iónicos basados en el Catión Imidazolio* Universidade de Santiago de Compostela, 2010.

219. Sambasivarao, S. . V. & Acevedo, O. *J. Chem. Theory Comput.* **5,** 1038 (2009).

220. Seddon, K. R. in *The International George Papatheodorou Symposium: Proceedings* (eds Boghosian, S. *et al.*) (Institute of Chemical Engineering and High Temperature Chemical Processes, Patras, Greece, 1999), 131.

221. Tsuda, T. & Hussey, C. L. *Electrochem. Soc. Interface* **Spring 2007,** 44 (2007).

222. Méndez-Morales, T., Carrete, J., Cabeza, O., Gallego, L. J. & Varela, L. M. *J. Phys. Chem. B* **115,** 6995 (2011).

223. Méndez-Morales, T., Carrete, J., Cabeza, O., Gallego, L. J. & Varela, L. M. *J. Phys. Chem. B* **115,** 11170 (2011).

224. Méndez-Morales, T., Carrete, J., García, M., Cabeza, O., Gallego, L. J. & Varela, L. M. *J. Phys. Chem. B* **115,** 15313 (2011).

225. Salas, G., Podgoršek, A., Campbell, P. S., Santini, C. C., Pádua, A. A. H., Costa Gomes, M. F., Philippot, K., Chaudret, B. & Turmine, M. *Physical Chemistry Chemical Physics* **13,** 13527 (2011).

226. Zhao, Y., Chen, Z., Wang, J. & Zhuo, K. *Z. Phys. Chem.* **223,** 857 (2009).

227. Pereiro, A. B. & Rodríguez, A. *J. Chem. Thermodyn.* **39,** 978 (2007).

228. Seddon, K. R., Stark, A. & Torres, M. J. *Pure Appl. Chem.* **72,** 2275 (2000).

229. Rebelo, L. P. N., Najdanovic-Visak, V., Visak, Z. P., da Ponte, M. N., Szydlowskia, J., Cerdeiriña, C. A., Troncoso, J., Romaní, L., Esperança, J. M. S. S., Guedes, H. J. R. & de Sousa, H. C. *Green Chem.* **6,** 369 (2004).

230. Najdanovic-Visak, V., Esperança, J. M. S. S., Rebelo, L. P. N., da Ponte, M. N., Guedes, H. J. R., Seddon, K. R., de Sousa, H. C. & Szydlowski, J. *J. Phys. Chem. B* **107,** 12797 (2003).

231. Kelkar, M. S. & Maginn, E. J. *J. Phys. Chem. B* **111,** 4867 (2007).

232. Huddleston, J. G., Visser, A. E., Reichert, W. M., Willauer, H. D., Broker, G. A. & Rogers, R. D. *Green Chem.* **3,** 156 (2001).

233. Carrete, J., García, M., Rodríguez, J., Cabeza, O. & Varela, L. M. *Fluid Phase Equilib.* **301,** 118 (2011).

234. Cuadrado-Prado, S., Domínguez-Pérez, M., Rilo, E., García-Garabal, S., Segade, L. & C. Franjo, O. C. *Fluid Phase Equilib.* **278,** 36 (2009).

235. Cammarata, L., Kazarian, S. G., Salter, P. A. & Welton, T. *Phys. Chem. Chem. Phys.* **3,** 5192 (2001).

236. Fazio, B., Triolo, A. & Marco, G. D. *J. Raman Spectroscopy* **39,** 233 (2008).

237. Takamuku, T., Kyoshoin, Y., Shimomura, T., Kittaka, S. & Yamaguchi, T. *J. Phys. Chem. B* **113,** 10817 (2009).

238. Zhang, L., Xu, Z., Wang, Y. & Li, H. *J. Phys. Chem. B* **112,** 6411 (2008).

239. Hanke, C. G. & Lynden-Bell, R. M. *J. Phys. Chem. B* **107,** 10873 (2003).

240. Bernardes, C. E. S., da Piedade, M. E. M. & Canongia-Lopes, J. N. *J. Phys. Chem. B* **115,** 2067 (2011).

241. Feng, S. & Voth, G. A. *Fluid Phase Equilib.* **294,** 148 (2010).

242. Jiang, W., Wang, Y. & Voth, G. A. *J. Phys. Chem. B* **111,** 4812 (2007).

243. Moreno, M., Castiglione, F., Mele, A., Pasqui, C. & Raos, G. *J. Phys. Chem. B* **112,** 7826 (2008).

244. Spickermann, C., Thar, J., Lehmann, S. B. C., Zahn, S., Hunger, J., Buchner, R., Hunt, P. A., Welton, T., & Kirchner, B. *J. Chem. Phys.* **129,** 104505 (2008).

245. Berendsen, H. J. C., van der Spoel, D. & van Drunen, R. *Comp. Phys. Comm* **91,** 43 (1995).

246. Lindahl, E., Hess, B. & van der Spoel, D. *J. Mol. Model.* **7,** 306 (2001).

247. Van der Spoel, D., Lindahl, E., Hess, B., Groenhof, G., Mark, A. E. & Berendsen, H. J. C. *J. Comput. Chem.* **26,** 1701 (2005).

248. Hess, B., Kutzner, C., der Spoel, D. V. & Lindahl, E. *J. Chem. Theory Comput.* **4,** 435 (2008).

249. Jorgensen, W. L., Maxwell, D. S. & Tirado-Rives, J. *J. Am. Chem. Soc.* **118,** 11225 (1996).

250. Prado, C. E. R. & Freitas, L. C. G. *J. Mol. Struct. (Theochem.)* **847,** 93 (2007).

251. Brenneman, C. M. & Wiberg, K. B. *J. Comp. Chem.* **11,** 361 (1990).

252. Mahoney, M. W. & Jorgensen, W. L. *J. Chem. Phys.* **112,** 8910 (2000).

253. Darden, T., York, D. & Pedersen, L. *J. Chem. Phys.* **98,** 10089 (1993).

254. Hess, B., Bekker, H., Berendsen, H. J. C. & Fraaije, J. G. E. M. *J. Comp. Chem.* **18,** 1463 (1997).

255. Hess, B. *J. Chem. Theory Comp.* **4,** 116 (2007).

256. Hockney, R., Goel, S. P. & Eastwood, J. *J. Comp. Phys.* **14,** 148 (1974).

257. Martínez, L., Andrade, R., Birgin, E. G. & Martínez, J. M. *J. Comput. Chem.* **30,** 2157 (2009).

258. Micaelo, N. M., Baptista, A. M. & Soares, C. M. *J. Phys. Chem. B* **110,** 14444 (2006).

259. Bussi, G., Donadio, D. & Parrinello, M. *J. Chem. Phys.* **126,** 014101 (2007).

260. Parrinello, M. & Rahman, A. *J. Appl. Phys.* **52,** 7182 (1981).

261. Haughney, M., Ferrario, M. & McDonald, I. R. *J. Phys. Chem.* **91,** 4934 (1987).

262. Méndez-Morales, T., Carrete, J., García, M., Cabeza, O., Gallego, L. J. & Varela, L. M. *J. Phys. Chem. B* **115,** 15322 (2011).

263. Flory, P. J. *Principles of Polymer Chemistry* (Cornell University Press, Ithaca, New York, 1953).

264. Lacombe, R. H. & Sanchez, I. *J. Phys. Chem.* **80,** 2568 (1976).

265. Nymand, T. M. & Linse, P. *J. Chem. Phys* **112,** 6386 (2000).

7 Pseudolattice theory of electric conductivity

> To explain all nature is too difficult a task for any one man or even for any one age. 'Tis much better to do a little with certainty, & leave the rest for others that come after you, than to explain all things by conjecture without making sure of any thing.
>
> Isaac Newton

7.1. Introduction

As mentioned in the previous chapter, electric conduction was among the first properties studied in ILs [211]. Likewise, research about the electric conductivity of ionic solutions has a long tradition in the scientific community and remains a major problem in chemical physics. In contrast with the solid-state systems studied in Part I of this work, in ILs and electrolyte solutions charge transport due to electrons is severely hindered by the difficulty of "jumping" from one molecule to another, even though it can be easy for electrons to move within the limits of one particular molecule. Thus, electric conduction is mainly due to the physical movement of ions. Beyond this fact,

the current theoretical understanding of the mechanism of charge transport in these systems is almost completely constrained to dilute ionic solutions, for which the so-called Debye-Hückel-Onsager (DHO) or Onsager-Fuoss theory was originally developed [266–271]. As it is well known, the existence of an inhomogeneity in the charge distribution around each ion, commonly known as the ionic atmosphere, is the basic structural assumption of this theoretical formalism [266]. The perturbation of this structure by the external electric field, as well as ion-solvent interactions, are responsible for the concentration dependence of transport coefficients through the so-called relaxation field and electrophoretic effect.

However, it has long been known that the preservation of this continuous structure at concentrations beyond 0.01 M is doubtful since, as pointed out by Bockris and Reddy [272], at this concentration "only one ion produces 50% of the effect of the ionic atmosphere on the central ion", but in the DHO formalism the effect of this single ion is smeared out over a sphere with a radius of about 0.25 Å. Thus, in practice a discrete charge distribution, instead of an average and continuous cloud of charge, is expected to be present around the central ion. Moreover, the exponential behaviour of the charge density in the neighbourhood of each ion is known to become oscillatory at intermediate concentrations (around 1 M for 1 : 1 electrolytes) in a phenomenon known as the Kirkwood crossover [273], reflecting a structural transition in the bulk ionic distribution incompatible with the existence of ionic atmospheres.

As a consequence, the thermodynamic properties of ionic solutions must be interpreted in terms of a cube-root dependence with concentration, a kind of law which has been shown to be compatible with the existence of a "loose" lattice structure (hereafter referred to as a pseudolattice) for concentrations beyond 0.01 M. Of course, this structural arrangement is maintained, and even gradually reinforced, up to the highest possible concentrations of ions or, in the case of ILs, up to the limit of pure IL. The pseudolattice goes beyond an useful metaphor, as it stems from the observation in electrolyte solutions of X-ray diffraction patterns similar to those registered in experiments involving crystalline solids [274–278]. In fact, concrete lattice structures — such as face-centred cubic for 1 : 1 electrolytes — can be identified from these results, a sign of the existence of medium-range order. These observations led Bahe [276] to propose a theory for ionic solutions in which this pseudo-reticular order was explained in terms of Coulomb interactions between ions, and the solvent was introduced through its dielectric constant. Bahe's theory was completed by

Varela *et al.* [18] through the addition of excluded volume interactions among molecules — which become more relevant at high concentrations — as well as attractive van der Waals forces. The resulting Bahe-Varela theory affords a satisfactory explanation of a wide range of bulk and surface thermodynamic properties of electrolyte solutions not only in the high-concentration region — where traces of the lattice present in the solid salt could be expected to remain present — but essentially all the way through to the DHO regime. ILs were *a priori* perfect candidates to be described using this theory, and indeed Turmine *et al.*'s works in 2007 and 2008 [279–281] showed that the Bahe-Varela formalism could explain the behaviour of partial molar magnitudes in mixtures of [BMIM][BF_4] with water, among other systems. Since then, it has also been applied to sorption processes [282]. A more in-depth revision of the history, conceptual roots and applications of the Bahe-Varela theory can be found in Ref. 283.

Despite its being, by now, quite a successful framework, the adaptation of the charge transport formalism to this pseudolattice structural scheme has registered very limited activity. Two main approaches have been followed in the field, combinations of either a pseudolattice structural model and the DHO formalism or a pseudolattice model and hopping mechanisms. As regards the first approach, the works by Murphy [284] and by Lemordant and coworkers [285–288] are the only significant reported results found in the bibliographic search done prior to this work. The latter authors combined the pseudolattice theory with the DHO formalism by assuming that ions are placed at the nodes of a pseudolattice but that the classical Debye-Hückel random picture of ionic solutions can be preserved even at moderate-to-high concentrations if Debye's length is replaced with the average distance between ions of opposite charge. The conductance of dilute electrolyte solutions thus follows a $\propto c^{1/3}$ law, instead of the $c^{1/2}$ proportionality predicted by DHO, from concentrations as low as 0.01 M, a manifestation of the underlying pseudolattice structure. This behaviour can be theoretically understood if the ionic cloud is replaced by statistical cells and the relaxation field and electrophoretic effect are recalculated. Besides, a lot of similarities have been reported to exist between the transport behaviour of a crystalline matrix with defects and a liquid electrolyte containing dissolved ions [289].

Regarding the second approach, the number of contributions reported to date seems to be rather limited. Woodward and Harris [290] introduced a lattice-hole model with ionic hopping between cells as the mechanism

responsible for charge transport and decreasing mobility in the mixture associated to the concept of site availability. However, as the authors themselves admit [290], they adopt a phenomenological approach in order to provide a qualitative description of the conductivity of IL+solvent mixtures. In particular, they do not provide a microscopic explanation for the values of the fitting parameters they employ in the analysis of experimental data. Villullas and González [291] also analysed the behaviour of the electric conductivity of both aqueous and non-aqueous electrolytes, although on different theoretical grounds. They treated electric transport as being governed by dissipation and feedback mechanisms, and analysed — in the context of dynamical systems — the existence of maxima in the curves of conductivity as a function of concentration in ionic solutions. Using the normalised logistic equation, the authors obtained a law for the conductivity of an ionic mixture identical to the one presented in later sections of this chapter [Eq. (7.9)]. They did not, however, connect this result to any structural arrangement in the liquid system, or to hopping processes in the pseudolattice. Consequently, their phenomenological contribution lacks an associated microscopically-based interpretation. Moreover, the effects on conductivity of ion-ion and ion-solvent interactions are not explicitly treated by the authors.

In the present chapter, a statistical-mechanical pseudolattice model of charge transport in ionic fluid+solvent mixtures is introduced, and its predictions compared with literature data on the electric conductivity of aqueous electrolyte solutions and IL+water mixtures. Moreover, in order to analyse the effect of the dielectric constant of the molecular liquid in the mixture, measurements of the conductivity of binary mixtures of [BMIM][BF_4], [HMIM][BF_4] and [MOIM][BF_4] with ethanol were performed specifically for this purpose and kindly provided by Prof. Óscar Cabeza's group; their results are also included here. In the model developed for this work, ions are assumed to move randomly between the cells of a statistical lattice representing the cooperative rearrangement regions in the liquids. Each of these was defined by Adam and Gibbs [292] as "the smallest region that can undergo a transition to a new configuration without a requisite simultaneous configurational change on and outside its boundary". Charge carriers are assumed to jump over energy barriers between adjacent cells by classical hopping mechanisms. For non-correlated ion transport, conductivity maxima are predicted in terms of the probability of a jump between different kinds of cells, and the behaviour of conductivity as a function of concentration, when both variables are nor-

malised to their values at the maximum, is seen to approximately follow a universal corresponding-states law. Deviations from this law are attributable to ion-ion an ion-solvent interactions, which are analysed in the framework of the Bragg-Williams (BW) mean-field approximation.

7.2. Experimental details

ILs were purchased from Solvent Innovation and the purities of the [BMIM][BF_4], [HMIM][BF_4] and [MOIM][BF_4] employed were better than 99%. Ethanol was supplied by Panreac and its purity was higher than 99.5%. Due to the hygroscopic character of the ILs, all chemicals were extracted from their original tins and mixed with ethanol in a dry chamber with a relative humidity degree lower than 10%. This humidity degree, and the speed of the mixing process, ensured that the original ILs were not contaminated with water from moisture. Mixtures were bottled and sealed before taking them out of the chamber. The mass fraction of water in the three pure ILs was lower than 10^{-3} as certified by the dealer, and they were not purified further.

The electric conductivity of IL+ethanol mixtures was measured using a Crison conductivimeter GLP31+, which has a repeatability of 0.1% and an uncertainty better than 0.5%. Samples were thermostated in an external bath with an uncertainty of 0.1 °C. The conductivimeter was calibrated before each measurement session with three certified KCl solutions (0.001, 0.01 and 0.1 M) supplied by Crison.

7.3. Theoretical section

Let us consider a binary IL+solvent mixture comprising $N = N_+ + N_-$ ions (N_+ cations and N_- anions) and N_0 neutral solvent molecules, defining $M = N + N_0$ cells in a 3D pseudolattice of coordination number s and lattice constant a. This spatial arrangement defines a sublattice on which the ions are embedded and move by means of hops between adjacent cells under the action of an external electric field $\vec{E}$. For simplicity, a $1:1$ binary symmetric electrolyte will be considered, with charges $q_+ = -q_- = q$. Moreover, consecutive hops of an ion will be considered statistically independent. Cells can be seen as potential wells associated to rearrangement regions in the bulk, forming a pseudolattice in which two adjacent cells are separated by an energy barrier whose height is a random variable. The description of ionic trans-

Figure 7.1 Left: schematic representation of the k-clusters defining an α-cell for a 2D simple square lattice (s=4). Right: schematic representation of the energy barriers in the pseudolattice model defined in the text.

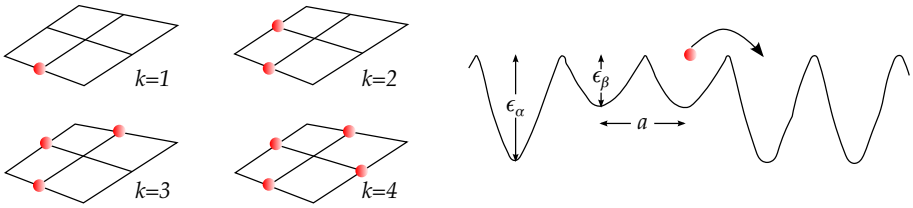

port in this medium is the subject of the well-known random-energy model, suggested some decades ago [293] and considered a very plausible model for ionic movement in glasses. However, the ergodic nature associated to the short characteristic times of molecular motion in liquids leads to much simpler energy landscapes and homogeneous molecular environments in the bulk, which make it sensible to assume that the heights of energy barriers are averaged because of particle movement. In fact, it will be assumed that, on average, only two different types of ionic environment occur: β-cells with no ions in their s first-neighbour cells, and α-cells with neighbouring ions. The average energy barriers experienced by ions in each of these types of cells will be denoted by ϵ_β and ϵ_α, respectively. β-cells are mainly associated to solvent molecules in the lattice or to hole-like low-density regions in the bulk. Thus, in this model solvent molecules are explicitly taken into account but, for simplicity, treated on equal footing with empty sites, as far as ion hopping is concerned. On the other hand, α-cells arise as the average of s different types of cells, as shown in Fig. 7.1 (left). The energy barrier associated to the latter type of cells will thus, in fact, be given by an average $\epsilon_\alpha = \sum_{k=1}^{s} f_k \epsilon_{\alpha,k}$, where f_k represents the relative frequency of cells with configuration k among α-cells, and $\epsilon_{\alpha,k}$ is the average depth of the potential energy minimum in the centre of a cell of type k.

As pointed out by Böttger and Bryksin [294], barriers cause the motion of an ion to be characterised by two different times, namely the residence time τ_0, *i.e.*, the time it spends in a cell or potential well, and the time of free flight between cells τ_1. The hopping regime of conduction in liquids is associated to $0 < \tau_1/\tau_0 < 1$ and the extreme values correspond to solid-like (0) and gas-like (1) motion, respectively. In concentrated mixtures or pure ILs, an ion moves more like a diffusing oscillator rather than a diffusing ion; however, as the con-

centration of ions is diminished, the empty or solvent-occupied cells become dominant in the bulk, and the diffusive motion associated to the DHO theory is expected to be gradually recovered.

Let us assume that the external electric field $\vec{E}$ is applied along the z direction and therefore neglect charge transport in the other two independent directions. It will also be assumed that there is no net thermal or concentration gradient which could act as another force behind charge transfer. Thus, the problem becomes essentially one-dimensional. Figure 7.1 (right) shows a very schematic picture of the hopping process along one direction of the BW-like energy landscape built from these hypotheses. Even though this approximation might seem rather crude given the long-ranged nature of interionic interactions, it must be borne in mind that, in general, mean-field treatments improve in precision as the number of interactions is increased [295], one of the reasons why the Debye-Hückel formalism has been extended to concentrations were its underlying assumptions are completely wrong. In fact, BW treatments of ionic space charge have been reported that satisfactorily compare to simulation results [296] and these treatments are able to reproduce the surface properties of IL+water mixtures [282]. Besides, the Flory-Huggins mean-field theory has been proven to afford a successful interpretation of the solvent power of ILs [297].

In this framework, the probability of a cell being of type α or β is $x_\alpha = N/M$ and $x_\beta = (M-N)/M$, respectively. However, to account for the different sizes of the particles in the mixture — an important factor in ILs, typically formed by very assymmetric ions — volume fractions Φ, instead of molar fractions, will be considered the relevant variable as far as cell occupation is concerned, very much in the spirit of the Flory-Huggins polymer solution theory [263] and the statistical lattice theory of mixtures [264].

In the absence of an electric field, the probability per unit time that an ion jumps a barrier of height ϵ_i ($i \in \{\alpha, \beta\}$) is proportional to the Boltzmann factor $exp\{-\epsilon_i/(k_B T)\}$; more precisely, it is given by [298]

$$\bar{\nu}_i = \frac{1}{6\pi} \frac{(k_B T)^3}{\hbar^3 \omega_{s,i}^2} e^{-\frac{\epsilon_i}{k_B T}}, \tag{7.1}$$

where $\omega_{s,i}$ is the vibrational frequency associated to the curvature of the saddle point in the two directions perpendicular to the direction of flow in an average cell of type i. Obviously, both ϵ_i and $\omega_{s,i}$ are affected by interionic and ion-

solvent interactions, and may be dependent on concentration in a fashion that will be considered later.

An electric field $E^{(z)}\hat{z}$ lowers the energy barrier by an amount $aqE^{(z)}/2$ in its direction and raises it by the same amount in the opposite direction; as a consequence, the excess probability that an ion hops in the direction of the field is

$$\bar{\nu}_{p,i} = \frac{1}{6\pi}\frac{(k_B T)^3}{\hbar^3 \omega_{s,i}^2}\left[e^{-\frac{\epsilon_i + aqE^{(z)}/2}{k_B T}} - e^{-\frac{\epsilon_i - aqE^{(z)}/2}{k_B T}}\right] = 2\bar{\nu}_i \, sinh\left(\frac{aqE^{(z)}}{2k_B T}\right). \tag{7.2}$$

Since an ion crosses a fraction Φ_α of α cells in its motion, the weighted average excess probability per unit time of hopping a barrier in the direction of the field can be written as

$$\begin{aligned}\bar{\nu}_p &= \sum_{i\in\{\alpha,\beta\}} \Phi_i \bar{\nu}_{p,i} = \frac{1}{6\pi}\frac{(k_B T)^3}{\hbar^3}\left(\Phi_\alpha \frac{e^{-\frac{\epsilon_\alpha}{k_B T}}}{\omega_{s,\alpha}^2} + \Phi_\beta \frac{e^{-\frac{\epsilon_\beta}{k_B T}}}{\omega_{s,\beta}^2}\right)\frac{aqE^{(z)}}{k_B T} \\ &= \frac{qa}{k_B T}\left(\Phi_\alpha \bar{\nu}_\alpha + \Phi_\beta \bar{\nu}_\beta\right) E^{(z)},\end{aligned} \tag{7.3}$$

for electric fields small enough that the *sinh* function in Eq. (7.2) can be linearised. The density of mobile ions in the pseudolattice, n_α, can be assumed to be $\simeq \Phi_\alpha / V_\alpha$, where V_α is the ionic volume, as long as the excess volume is low; this is usually true for ionic liquids. Hence, the electric conductivity of the mixture is finally given by

$$\sigma = \frac{q^2 a^2}{V_\alpha k_B T}\left[\Phi_\alpha^2 \bar{\nu}_\alpha + (1 - \Phi_\alpha)\,\Phi_\alpha \bar{\nu}_\beta\right]. \tag{7.4}$$

As previously mentioned, similar results are reported in Refs. 290 and 291, although here the coefficients of the second-order polynomial in Eq. (7.4) have a physical meaning instead of being treated as mere fitting parameters from the start.

In this model, at high ionic concentrations conductivity is dominated by hopping between α-cells, with a probability per unit time $\bar{\nu}_\alpha$ dependent on ionic concentrations. At the other end of the concentration range, ion-solvent interactions are the main cause behind the behaviour of electric conductivity. The residence time of β-cells can be reasonably considered as the physical origin of ionic friction in the solvent. Average residence times in β-cells are

shorter than in α-cells so, as concentration is decreased, conventional diffusive transport is recovered as expected.

It must be noted that the movement of an ion is influenced by its surroundings through interactions due to charge, polarisation of the solvent, induced strain, etc. Correlations in the ionic distributions are introduced by these interactions that confer a markedly cooperative character to the diffusion process. Due to this phenomenon, the coefficients $\{\bar{\nu}_i\}$ in the right-hand side of Eq. (7.4), which contain all the relevant features of ion-ion and ion-solvent interactions, are expected to be functions of concentration. A detailed calculation of the exact form of such dependence can be expected to be rather involved due to the intricacy of ion-ion and ion-solvent interaction potentials, but the effect of interactions on charge transport in solid electrolytes has been addressed by Kikuchi and Sato by means of the path probability method [299, 300]. In the notation employed here, their result is

$$\sigma = \frac{q^2 a^2}{V_\alpha k_B T} \frac{e^{-\frac{u}{k_B T}}}{\nu} \frac{2\Phi_\alpha (1-\Phi_\alpha)}{1+R} \left[\frac{2(1-\Phi_\alpha)}{R+1-2\Phi_\alpha} \right]^2, \tag{7.5}$$

where u is the energy barrier between cells, assumed to be unique in Refs. 299 and 300, $R = \sqrt{1 - 4\Phi_\alpha (1-\Phi_\alpha)\left(1 - e^{\frac{\epsilon}{k_B T}}\right)}$, and $-\epsilon$ is the average nearest neighbour interaction between charge carriers. A BW-like approximation will be used to adapt this expression to the situation treated in this work, where not only two types of charge carriers are considered (instead of only one, as Kikuchi and Sato assume) but also a neutral (polar or apolar) solvent is included in order to get a realistic picture of the movement of charges in the solution. One of the ionic species will be taken as averaged over the whole volume of the mixture, relegated to the role of preserving both local and global neutrality, in the same way done in the well-known case of the one-component plasma. Thus, one is left with a statistical lattice of cells associated to ions in an ionic environment (α-cells) or to a rearrangement region mainly defined by solvent molecules (β-cells) that interact between them by means of a mean-field nearest-neighbour interaction $\epsilon_{i,j}$ ($i, j \in \{\alpha, \beta\}$). The energy of a configuration of the mixture is then given by a simple linear combination weighted using the number of each kind of pair of neighbouring cells ($\bar{N}_{\alpha,\alpha}$, $\bar{N}_{\beta,\beta}$ and $\bar{N}_{\alpha,\beta}$); in a

Figure 7.2 Concentration dependence of the conductivity of several aqueous solutions of alkali halides. Data taken from Ref. 301.

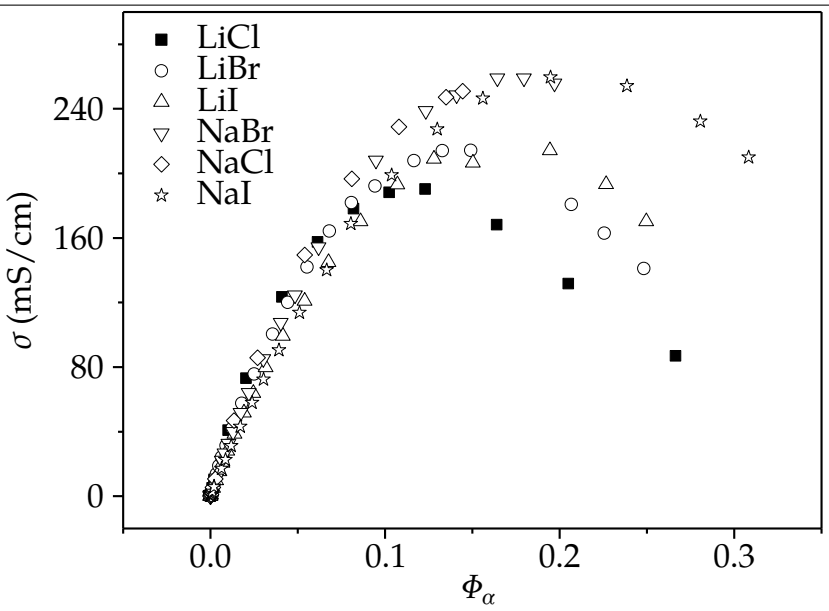

BW model this translates into:

$$E = \bar{N}_{\alpha,\alpha}\epsilon_{\alpha,\alpha} + \bar{N}_{\beta,\beta}\epsilon_{\beta,\beta} + \bar{N}_{\alpha,\beta}\epsilon_{\alpha,\beta} = -\frac{N_{\alpha,\beta}}{2}\left(\epsilon_{\alpha,\alpha} - 2\epsilon_{\alpha,\beta}\right) + \frac{N_\alpha}{2}\epsilon_{\alpha,\alpha}, \qquad (7.6)$$

where $\epsilon_{\beta,\beta}$ has been taken as the origin of energies in order to simplify the notation. This equation can be compared to those in Refs. 299 and 291; from that comparison, an effective mean-field interaction among charge carriers $\epsilon = \epsilon_{\alpha,\alpha} - 2\epsilon_{\alpha,\beta}$ may be defined that includes the interaction between ions in different environments as well as — at least in an indirect fashion — the effects of ion-solvent interactions.

7.4. Results and discussion

Figures 7.2 to 7.4 show the electric conductivity as a function of concentration for several alkali halides with solubilities large enough to show a maximum (data from Ref. 301), of IL + water mixtures (data from Ref. 302) and of IL + ethanol mixtures (measured for this work by Prof. Óscar Cabeza's group). The existence of conductivity maxima in electrolyte solutions and in IL mix-

Figure 7.3 Concentration dependence of the conductivity of IL + water mixtures. Data taken from Ref. 302.

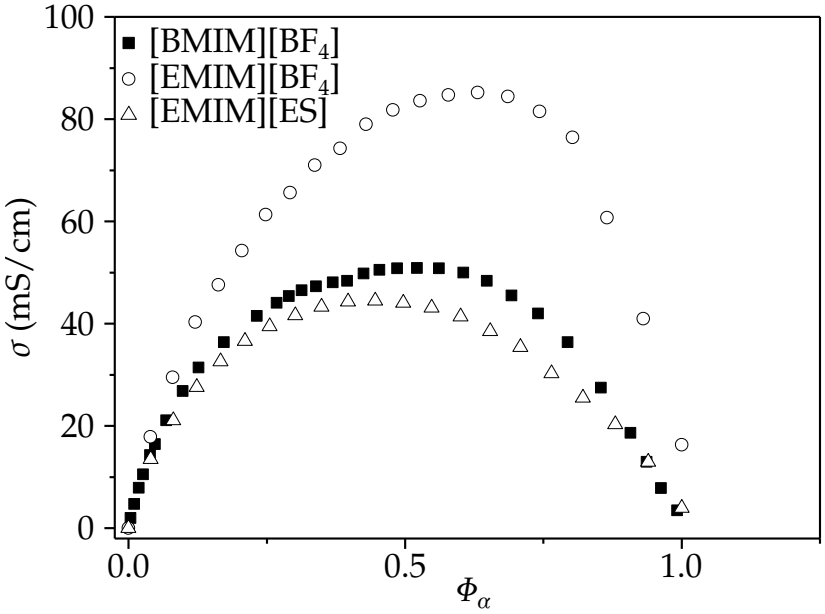

Figure 7.4 Experimental results for the concentration dependence of the conductivity of IL + ethanol mixtures.

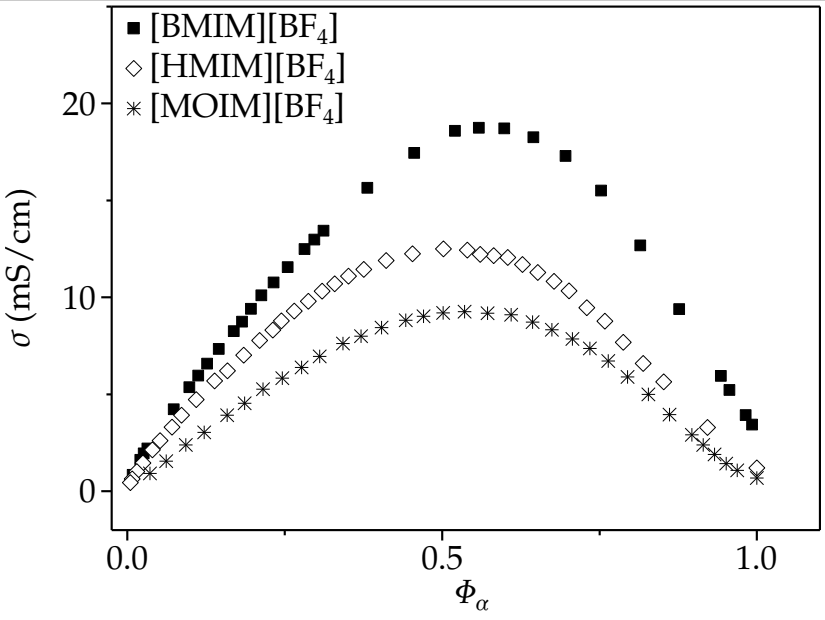

Figure 7.5 Normalised conductivity *vs.* scaled concentration for the alkali halides in Fig. 7.2. The solid curve represents the predictions of Eq. (7.9).

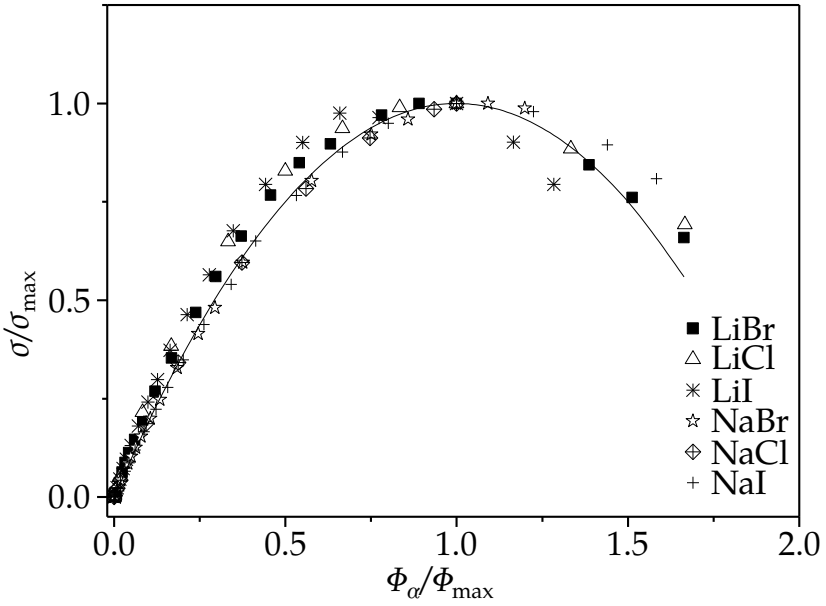

tures has been attributed to two opposing effects: an increase in the number of charge carriers and a decrease in their mobility as the concentration is increased [290, 303–306]. Both effects are described by Eq. (7.4). In this theoretical model, the reduction in mobility is associated to a progressive increment in the fraction of long-residence-time α-cells in detriment of vacant environments or other β-cells.

It is clearly visible in Figs. 7.2 to 7.4 that the concentration at which the maximum is reached varies with the electrolyte (see also Table 7.1). In alkali halide solutions, these maxima are ordered according to their hydrophobicity, following the Hoffmeister series, so the structure of the solvent seems to be behind this behaviour. The greater the ability of cations and anions to change the structure of water, the lower the concentration at which the maximum is reached, and also the value of this maximum conductivity. As regards the behaviour of ILs, Figs. 7.3 and 7.4 show that the length of the alkyl chain is determinant: as it increases, the maximum value of the conductivity decreases sharply, reflecting an increase of the residence times of ions in the cells of the pseudolattice. The effect of the anion can also be discerned by comparing the

Table 7.1 Molar volumes calculated from the density of the pure substances, ionic volume fractions at the conductivity maxima, and maximum values of the conductivity for the solutions analysed in the text.

System	$V_\alpha \left(\frac{\mathrm{cm}^3}{\mathrm{mol}}\right)$	$\Phi_{\max}$	$\sigma_{\max} \left(\frac{\mathrm{mS}}{\mathrm{cm}}\right)$
LiCl	20.50	0.123	190.20
LiBr	25.07	0.143	214.20
LiI	32.84	0.194	214.30
NaCl	26.99	0.145	250.89
NaBr	32.05	0.164	259.07
NaI	40.84	0.195	259.49
[EMIM][BF_4]+water	154.69	0.578	85.20
[EMIM][ES]+water	192.42	0.446	44.50
[BMIM][BF_4]+water	186.80	0.522	50.90
[BMIM][BF_4]+ethanol	186.80	0.559	18.74
[HMIM][BF_4]+ethanol	225.00	0.509	12.50
[MOIM][BF_4]+ethanol	262.94	0.551	9.26

results for [EMIM][BF_4] with those for [EMIM][ES]. The greater hydrophobicity of the anion in the latter IL is responsible for a decrease of the conductivity at the maximum by about 52%. At the same time, the effect of the solvent on charge transport in ILs is also clear from a comparison between Figs. 7.3 and 7.4: the maximum conductivity of [BMIM][BF_4] in water, $\sigma_{\max} = 50.9$ mS cm^{-1}, is reduced in ethanol to a value of merely 18.7 mS cm^{-1}. Ion-solvent interactions are probably the main reason for this behaviour, since the much lower dielectric constant of ethanol induces different solvation structures around the ions and a much weakened screening of interionic interactions.

The reduced conductivities $\sigma/\sigma_{\max}$ are shown in Figs. 7.5 to 7.7 as functions of the reduced concentrations $\xi_\alpha := \Phi_\alpha/\Phi_{\max}$ for the systems introduced above. It can be seen that in these representations the scaled conductivities approximately collapse into one master curve, indicating that the opposing tendencies acting on the ionic system at the concentration corresponding to the conductivity maximum are virtually the same regardless of the solvent and the nature of the electrolyte, a fact first pointed out by Casteel and Amis [306] without any theoretical consideration. The deviations from the master curve are registered mainly at high concentrations, as expected, since it is in this regime where the peculiarities of ions (morphological asymmetries, ion-ion interactions, etc.) are most influential. These deviations are also larger in water than

Figure 7.6 Normalised conductivity *vs.* scaled concentration for the IL + water mixtures in Fig. 7.3. The solid curve represents the predictions of Eq. (7.9).

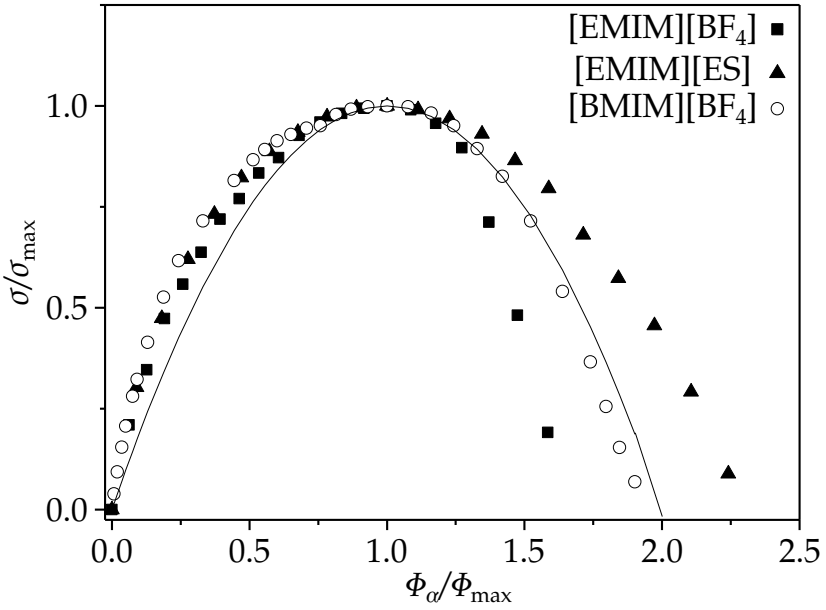

in alcohol, in keeping with the results presented in Chapter 6: as water is added to the pure IL, it quickly forms clusters; thus, the efficiency of water as a scatterer of moving ions (related to the cross section of these clusters) is expected to increase less rapidly than that of ethanol, whose molecules remain essentially isolated up to very high concentrations, making the behaviour of aqueous mixtures more dependent on the ions. Likewise, for low concentrations of IL water causes a larger deviation from the master curve than ethanol; this can be interpreted as a manifestation of the fact that there is a continuous water network percolating the IL, which renders the pseudolattice formalism less applicable.

In order to gain further insight about the physics behind this universal behaviour in the framework of a pseudolattice model, and in spite of the arguments in the previous section with regard to the concentration dependence of the coefficients of the polynomial in Φ_α in Eq. (7.4), as a first approximation $\{\bar{\nu}_i\}_{i\in\{\alpha,\beta\}}$ in that equation will be considered concentration-independent. Such

Figure 7.7 Normalised conductivity *vs.* scaled concentration for the IL + ethanol mixtures in Fig. 7.4. The solid curve represents the predictions of Eq. (7.9).

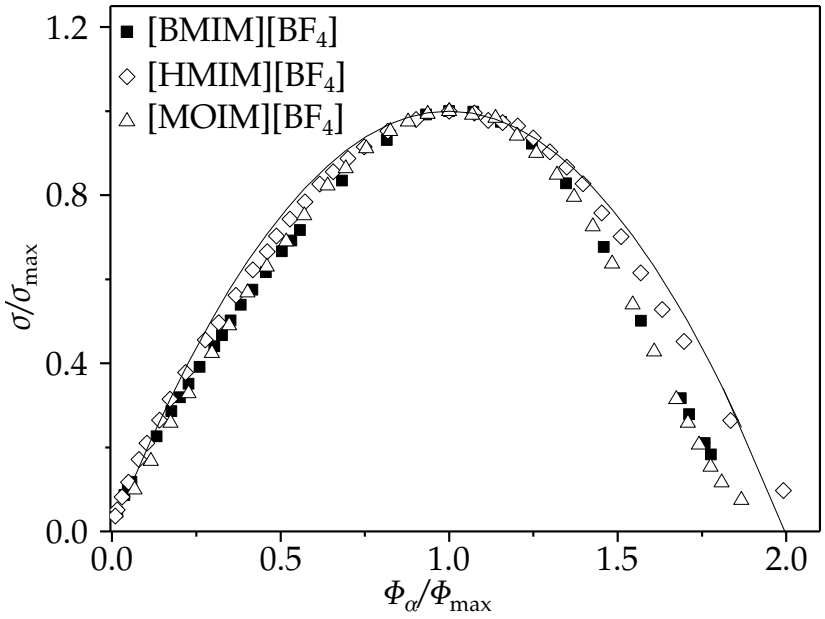

hypothesis makes the calculation of $\Phi_{\max}$ completely straightforward:

$$\Phi_{\max} = \frac{\bar{\nu}_\beta}{2\left(\bar{\nu}_\beta - \bar{\nu}_\alpha\right)}, \tag{7.7}$$

which yields a maximum conductivity

$$\sigma_{\max} = \frac{q^2 a^2}{4 V_\alpha k_B T} \frac{\bar{\nu}_\beta^2}{\bar{\nu}_\beta - \bar{\nu}_\alpha}. \tag{7.8}$$

The measured values of $\sigma_{\max}$ are also listed in Table 7.1. Applying somewhat lengthy but trivial algebra, Eq. (7.4) can be rewritten in the universal form

$$\frac{\sigma}{\sigma_{\max}} = 2\xi_\alpha \left(1 - \frac{\xi_\alpha}{2}\right) \tag{7.9}$$

in terms of the reduced conductivity and concentration. It is immediate to check that the above equation is also recovered from Kikuchy and Sato's result [Eq. (7.5)] when $\epsilon = 0$. Thus, a pseudolattice theory with concentration-independent hopping probabilities is capable of predicting the existence of a

maximum in the electric conductivity and, even more interestingly, of a universal behaviour of σ/σ_{max} *vs.* ξ_α. The predictions of the parameter-free Eq. (7.9) are represented in Figs. 7.5 to 7.7, and an excellent agreement with experimental results is found for all the analyzed systems. Thus, a corresponding-states law can be said to exist (in concentration space) for charge transport in ionic solutions, and this universal behaviour can be understood on the basis of three main hypotheses:

- The pseudolattice model itself, with charge transport driven by hopping mechanisms throughout the concentration range.
- The statistical independence of equal-sized ions and of different hops.
- The invariance of the probability per unit time of a jump over a barrier between cells.

Considering these restrictions, the simplicity of the analytical form of the universal corresponding-states law for ionic transport in ionic solutions represented by Eq. (7.9) and its agreement with experimental data cannot be but surprising. A compensation of otherwise highly complicated interactions seems to take place in these media.

However, as expected, deviations from the universal curve can be seen in the figures, both in the low-concentration regime and at high concentrations, which have already been discussed qualitatively and related to the results in the previous chapter. Moreover, as it can be seen in Table 7.1, for ILs the maximum of the conductivity is always reached around or above $\Phi_\alpha = 0.5$, while for conventional electrolyte solutions $\Phi_{max} < 0.5$. Equation (7.7) yields in the latter case a negative value of $\bar{v}_\alpha$, which does not make sense in physical terms. This facts shows the limitations of the non-correlated model in the strongly-correlated, low-concentration region of ionic solutions, but does not seem to invalidate the main features of the structural model, as the non-correlated hopping hypothesis is just an added approximation. Another serious limitation of the present model may come from the hypothesis of constant size of the cells, which must be relaxed as ionic concentration is modified.

Some conclusions about the deviations from universality can be straightforwardly derived from Eq. (7.5). If that equation is expanded to second order around $\Phi_\alpha = 0.5$ and the position of the vertex of resulting parabola is taken as a second-order approximation to the maximum of that equation — a procedure equivalent to analytically approximating the solution of $d\sigma/d\Phi_\alpha = 0$ using

a single iteration of the Newton-Raphson method —- the fact that the reduced curves do not cross the horizontal axis at $\xi_\alpha = 2$ can be easily understood: the deviation from this value is proportional to $e^{\frac{\epsilon}{k_B T}} - 1$, and therefore its sign is that of ϵ. From Figs. 7.4 to 7.7 it can be concluded that this sign depends not only on the solute but also on the solvent, in agreement with the discussion following Eq. (7.6).

References

18. Varela, L. M., García, M., Sarmiento, F., Attwood, D. & Mosquera, V. *J. Chem. Phys.* **107,** 6415 (1997).

211. Walden, P. *Bull. Acad. Imper. Sci. St. Pétersbourg.* **8,** 405 (1914).

263. Flory, P. J. *Principles of Polymer Chemistry* (Cornell University Press, Ithaca, New York, 1953).

264. Lacombe, R. H. & Sanchez, I. *J. Phys. Chem.* **80,** 2568 (1976).

266. Debye, P. & Hückel, E. *Phys. Z.* **24,** 185 (1923).

267. Onsager, L. *Phys. Z.* **27,** 388 (1926).

268. Onsager, L. & Fuoss, R. M. *J. Phys. Chem.* **36,** 2689 (1932).

269. Onsager, L. & Fuoss, R. M. *Proc. Natl. Acad. Sci. U.S.A.* **41,** 274 (1955).

270. Onsager, L. & Fuoss, R. M. *J. Phys. Chem.* **61,** 668 (1957).

271. Fuoss, R. M. *J. Am. Chem. Soc.* **80,** 3163 (1958).

272. Bockris, J. O. & Reddy, A. K. N. *Modern Electrochemistry 1: Ionics.* 2nd ed. (Plenum Press, New York, 2000).

273. Kirkwood, J. G. *Chem. Rev. (Washington, D.C.)* **19,** 275 (1936).

274. Robinson, R. A. & Stokes, R. H. *Electrolyte solutions* (Butterworths, 1959).

275. Hyman, A. & Vaughn, V. in *Proceedings of the conference held at Syracuse University, June, 1966* (Gordon and Breach, 1967).

276. Bahe, L. W. *J. Phys. Chem* **76,** 1062 (1972).

277. Bahe, L. W. & Parker, D. J. *J. Am. Chem. Soc.* **97,** 5664 (1975).

278. Alves Marques, M., de Barros Marques, M. I., Cabaço, M. I., Gaspar, A. M., Marques, M. P. M., Amado, A. M. & Amorim da Costa, A. M. *J. Mol. Liq.* **134,** 142 (2007).

279. Bou Malham, I., Letellier, P. & Turmine, M. *Talanta* **72,** 155 (2007).

280. Bou Malham, I., Letellier, P., Mayaffre, A. & Turmine, M. *J. Chem. Thermodyn.* **39,** 1132 (2007).

281. Bouguerra, S., Bou Malham, I., Letellier, P., Mayaffre, A. & Turmine, M. *J. Chem. Thermodyn.* **40,** 146 (2008).

282. Varela, L. M., Carrete, J., Turmine, M., Rilo, E. & Cabeza, O. *J. Phys. Chem. B* **113,** 12500 (2009).

283. Varela, L. M., Carrete, J., García, M., Rodríguez, J. R., Gallego, L. J., Turmine, M. & Cabeza, O. in. *Ionic Liquids: Theory, Properties, New Approaches* (ed Kokorin, A.) (InTech, 2011).

284. Murphy, G. *J. Chem. Soc. Faraday Trans. 2* **79,** 1607 (1983).

285. Chagnes, A., Carré, B., Willmann, P. & Lemordant, D. *Electrochimica Acta* **46,** 1783 (2001).

286. Claude-Montigny, B., Rioteau, E., Lemordant, D., Topart, P. & Bosser, G. *Electrochimica Acta* **47,** 533 (2001).

287. Chagnes, A., Carré, B., Willmann, P. & Lemordant, D. *J. Power Sources* **109,** 203 (2002).

288. Chagnes, A., Nicolis, S., Carré, B., Willmann, P. & Lemordant, D. *Chem. Phys. Chem.* **4,** 559 (2003).

289. Janek, J., Martin, M. & Yoo, H.-I. *Ber. Bunsenges Phys. Chem.* **98,** 655 (1994).

290. Woodward, C. E. & Harris, K. R. *Phys. Chem. Chem. Phys.* **12,** 1172 (2010).

291. Villullas, H. M. & González, E. R. *J. Phys. Chem. B* **109,** 9166 (2005).

292. Adams, G. & Gibbs, J. H. *J. Chem. Phys.* **43,** 139 (1965).

293. Baranovskii, S. D & Cordes, H. *J. Chem. Phys.* **111,** 7546 (1999).

294. Böttger, H. & Bryksin, V. V. *Hopping Conduction in Solids* (VCH, Berlin, 1985).

295. Varela, L. M., García, M. & Mosquera, V. *Phys. Rep.* **382,** 1 (2003).

296. McDonald, J. R., Lehnen, A. P. & Franceschetti, D. R. *J. Phys. Chem. Solids* **43,** 39 (1982).

297. Lou, P., Kang, S, Ko, K. & Lee, J. *J Phys. Chem. B* **111,** 13047 (2007).

298. Seitz, F. *The Modern Theory of Solids* (Dover, New York, 1987).

299. Kikuchi, H. & Sato, R. *J. Chem. Phys.* **55,** 677 (1971).

300. Kikuchi, H. & Sato, R. *J. Chem. Phys.* **55,** 702 (1971).

301. Lobo, V. M. M. *Handbook of Electrolyte Solutions* (Elsevier, Amsterdam, 1990).

302. Rilo, E., Vila, J., Pico, J., García-Garabal, S., Segade, L., Varela, L. M. & Cabeza, O. *J. Chem. Eng. Data* **55,** 639 (2010).

303. Molenat, J. *J. Chim. Phys. Phys. Chim. Biol.* **66,** 825 (1969).

304. Vila, J., Rilo, E., Segade, L., Cabeza, O. & Varela, L. M. *Phys. Rev. E* **71,** 312011 (2005).

305. Vila, J., Ginés, P., Rilo, E., Cabeza, O. & Varela, L. M. *Fluid Phase Equilib.* **247,** 32 (2006).

306. Casteel, J. F. & Amis, E. S. *J. Chem. Eng. Data* **17,** 55 (1972).

8 Heat transport in a pseudolattice

— […] Dígoche eu que por moito que saques de ti unha historia, i aínda canto máis a saques de ti, sempre pos catro ou cinco fíos de verdade, que quizabes sen decatarte lévalos na túa memoria.

Merlín e Familia
Álvaro Cunqueiro

8.1. Introduction

Given that one of the main uses of ILs is as reaction media, the control of their global and local temperatures can be of great importance in industrial processes. This means that thermal transport must generally be taken into account during the design phase of any reactor. The calculation of temperature profiles and heat currents at such a scale is best done through finite element solutions of the coupled differential equations governing energy and mass transfer. Thermal conductivity is merely taken as an input parameter to those calculations. Thus, it is desirable to have a microscopic theoretical framework able to afford useful predictions of its values, or at least of its qualitative

trends as a function of relevant parameters such as concentration, choice of anion and cation, or chain length. In this chapter, a model for the thermal conductivity of ILs and their mixtures with solvents is presented. It is again based on the Bahe-Varela pseudolattice framework, chosen, as in chapter 7, because of its transferability.

The main objective of this study is to arrive at a reliable expression for the thermal conductivity of a pure IL and its mixtures with a solvent, reusing as much as possible from the well-developed theory of the thermal conductivity of crystalline solids used extensively in Part I. An important point to note is that in a liquid system energy can flow from one point to another through physical displacement of its supporting medium, *i.e.*, through advection. This mechanism can even be dominant in a variety of situations characterised by diffusion or macroscopic flows, but it is not included in this description, as it can be treated through conventional hydrodynamic methods. Here, thermal conduction refers exclusively to heat transport not associated to advection, as measured using experimental methodologies such as the transient hot wire method [307, 308] in which advection is minimised.

The idea that the behaviour of a liquid can be explained in terms of its movement around a potential well in phase-space was proposed speculatively already in the sixties by Eyring *et al.* [309], who in their significant structure method consider, somewhat imprecisely, that the system "remembers" its configuration as a solid. A more stringent test of this hypothesis came, however, in the eighties, when Stillinger and Weber developed their celebrated potential for solid and liquid silicon [43] that allowed them to study the phase-space trajectory of this system in greater detail than previously possible and to reach the conclusion that atoms in liquid silicon spend most of the time oscillating around the closest potential energy minimum, and only occasionally jump to a different attraction basin. Subsequent work by different authors has developed these observations into harmonic theories of liquids, some of them of great breadth and complexity, such as that reported by Gaeta *et al.* in Ref. 310, where a number of non-equilibrium thermodynamic relations are rederived on the basis that a liquid can be described as a system of material particles interacting with a gas of phonons through forces analogous to radiation pressure. Most harmonic studies of liquids, however, limit themselves to the prediction of the velocity autocorrelation function (see Ref. 311 and references cited therein) following the line of work initiated by Zwanzig [312] almost immediately after Stillinger and Weber's study.

Extensions of the idea of normal modes — solutions to Eqs. (3.6) — to liquids can be found in the literature that follow two very different approaches. The first, known as instantaneous normal modes (INM) theory [313–317], performs a second-order expansion of the potential energy at any arbitrary point in phase space to determine a set of normal modes. In general, the resulting dynamical matrix is non-Hermitian and yields a mixture of real and imaginary normal mode frequencies. Proponents of INM theories have suggested an interpretation of those imaginary values as describing barriers between minima, but several problems such as anharmonicities and the existence of "fake barriers" [318] cast doubt on such an explanation. The second possibility, known as quenched normal modes (QNM), is to associate to a given point in configuration space the set of normal modes corresponding to the potential energy minimum to whose attraction basin it belongs. This idea, closer to the original work by Stillinger and Weber and with more solid physical foundations, will be the one adopted in this chapter.

Two problems inherent to the harmonic study of any system not strictly confined to the neighbourhood of a particular potential energy minimum are the complexity of its energy landscape and the interaction between vibration and translation. Since the number of minima in the energy landscape of a system with N particles increases at least exponentially [319, 320] with N, the study of clusters of even a modest number of particles, whose minima have very different properties from one another, is an extremely challenging task [321]. Fortunately, as deduced by Wallace [322] for monoatomic liquids based on experimental entropy data and confirmed using MD and density functional theory simulations [323–325], only a few of those minima belong to the class of crystalline minima, high-symmetry configurations that impose a global order and can have very different properties among them (like the different phases of a crystalline solid), with the rest of the estimated $e^{0.8N}$ local potential wells being random minima, similar among them because they depend only on local order. These random minima dominate the statistical behaviour of the liquid system. Therefore, it is possible to sample the configuration space of the system in order to characterise a reasonable number of minima and study a simplified version of the energy landscape in which each of the virtually infinite random minima has been replaced by an average minimum calculated from the sample. Wallace's mean atom trajectory model [311] works from this idea and integrates translation as a series of jumps between these identical minima, happening at random with a stationary probability τ^{-1}, the only adjustable

parameter in the model. The velocity autocorrelation function obtained from the mean atom model is in good agreement with MD data. Furthermore, this theory decouples vibration and diffusion almost completely, hence also solving the second of the aforementioned problems in the simplest and most elegant way possible. But its main feature from the point of view of this work is the unambiguous definition of a single set of normal modes for a liquid system: those computed by diagonalising its dynamical matrix evaluated at the average potential energy minimum. The accuracy of this approximation for a particular liquid can be judged *a posteriori* by the convergence of the algorithm with respect to further sampling of configuration space.

The next section contains computational results for the vibrational density of states of [HMIM][PF_6] and [HMIM][BF_4] in the framework just introduced. Next, an expression for the thermal conductivity of an IL is developed by considering that heat conduction takes place through phonon hopping, which has already been used by several authors for describing amorphous solids and other systems with medium-range order [326–330]. Likewise, an interpolation formula for mixtures of ILs with solvents is deduced. These results are then qualitatively compared with experimental measurements of the thermal conductivity of pure [BMIM][BF_4] as a function of temperature, and quantitatively with those of the room-temperature thermal conductivity of [BMIM][BF_4]+water and [HMIM][PF_6]+ethanol mixtures. Those measurements were kindly provided by Prof. Óscar Cabeza's group. Their experimental methods are also briefly summarised for completeness. Imidazolium-based ionic liquids were chosen as examples because of their chemical stability and practical importance, with these particular counterions considered because of the complete miscibility of the resulting ILs with water or ethanol.

8.2. Vibrational spectrum of an IL

As in Chapter 6, all computational work was performed using version 4.5.4 of GROMACS [245–248], one of the packages for MD simulations in most widespread use, and the OPLS-AA [249] potential [Eqs. (6.1) to (6.3)] with Sambasivarao and Acevedo's parameters [219].

In order to obtain a statistically significant sample of the minima in the energy landscape of our system, the starting points for the quenching were taken from room-temperature simulation trajectories long enough to yield stable values of all the relevant thermodynamic properties. Some of these thermody-

namic results have been reported and favourably compared to experiment in a separate study [223]. In particular, ten 20 ns-long MD trajectories were generated at 298.15 K and 1 atm for simulation cells with 50, 100, 150, 200, 250 and 300 [HMIM][PF_6] or [HMIM][BF_4] ionic pairs and periodic boundary conditions in all directions. The number or atoms in each ion is 31 for $[HMIM]^+$, 7 for $[PF_6]^-$ and 5 for $[BF_4]^-$. After this, 100 points were taken at equally spaced time steps along each of those trajectories and an energy minimisation was performed so as to find the potential energy minimum to whose attraction basin each one belonged. The energy minimisation was carried out using 10^6 iterations of a conjugated gradients method [331] followed by the application of the L-BFGS (Low-memory Broyden-Fletcher-Goldfarb-Shanno) algorithm [332, 333] until convergence to a maximum force of 10^{-3} kJ/(mol nm). Next, the dynamical matrix was computed at each of the resulting minima through numerical differentiation of the forces with respect to all the cartesian coordinates [Eq. (3.9)] and diagonalised in order to obtain a set of quenched normal mode frequencies associated to each of the 6000 starting configurations of each IL. Iterative methods were needed for this minimisation because of the much larger number of atoms compared, for example, with the calculations in Chapter 4. Finally, the discrete set of frequencies was transformed into a continuous vibrational density of states (DOS) by means of Gaussian kernel density estimation. Strictly speaking, the dynamical matrix was calculated only for a wavevector $\vec{k} = 0$. Nevertheless, since the simulation cell employed is assumed to be significantly larger than the pseudolattice unit cell, the associated reciprocal-space unit cell is small enough that the vibrational DOS at $\vec{k} = 0$ is representative of the total DOS.

These calculations took about 20 days on a machine with 16 processors and yielded 6000 sets of normal modes for [HMIM][PF_6] and the same quantity for [HMIM][BF_4]. In no case did the calculations yield any imaginary frequency, which shows that the minimisation procedure was strict enough to reach the local minimum in each case.

The inverse participation ratio (IPR) of each vibrational mode was also calculated as a means to quantify its spatial extent. The IPR of a mode $\lozenge$ in which

each atom i has a displacement amplitude $\vec{u}_{\Diamond,i}$ is defined [334] as

$$\mathrm{IPR}_{\Diamond} = \frac{\sum_i \left[\left| \vec{u}_{\Diamond,i} \right|^2 \right]^2}{\left[\sum_i \left| \vec{u}_{\Diamond,i} \right|^2 \right]^2}. \tag{8.1}$$

The upper bound for an IPR is 1, which is attained when a vibrational mode involves only one atom. Likewise, and more generally, a large IPR suggests a localised vibration. For instance, in the framework of the anharmonic Allen-Feldman model, Shenogin *et al.* [334] detected a clear correlation between localised modes and IPRs greater than 0.25 – 0.35. Conversely, the more atoms that take part in a collective oscillation, the lower the IPR of that vibrational mode. Thus, an IPR close to zero corresponds to a very extended vibration. In order to make sure that all values under consideration for the IPRs in each IL were directly comparable in terms of numbers of particles, this calculation was performed only for the largest box size. In this case, a sample of 250 starting configurations was taken from the MD room-temperature trajectories of each IL.

Figure 8.1 shows the average DOS for each system. The relative standard deviations were always lower than 1% for this sample. The small variance found in the DOS among different configurations lends support to the hypotheses behind the mean atom trajectory model. Moreover, the fact that no significant difference is observed between results obtained with different cell sizes is compatible with the notion of a pseudolattice, since in a periodic arrangement of atoms taking a larger amount of unit cells merely amounts to "folding" the original unit cell in reciprocal space into a smaller one, without any change in the net vibrational DOS.

Also patent in Fig. 8.1 is the fact that the vibrational spectrum of these imidazolium-based ILs is dominated by the cation. In particular, the first wide band, which extends from 0 to about 7 THz, is almost identical for both liquids, and the same can be said about the part of the spectrum above 60 THz. In spite of this, the influence of the anion can be readily identified by comparing Figs. 8.1 and 8.2, the latter of which shows the normal modes of each isolated ion. The vibrational modes of each anion manifest themselves as narrow peaks in the DOS, an example of which is the peak at about 52 THz visible in the spectrum for [HMIM][PF_6] but absent from the DOS for [HMIM][BF_4]. On the whole, for anions with frequency distributions similar to these the cation

Figure 8.1 Vibrational DOS for two ILs: [HMIM][BF_4] (top) and [HMIM][PF_6] (bottom).

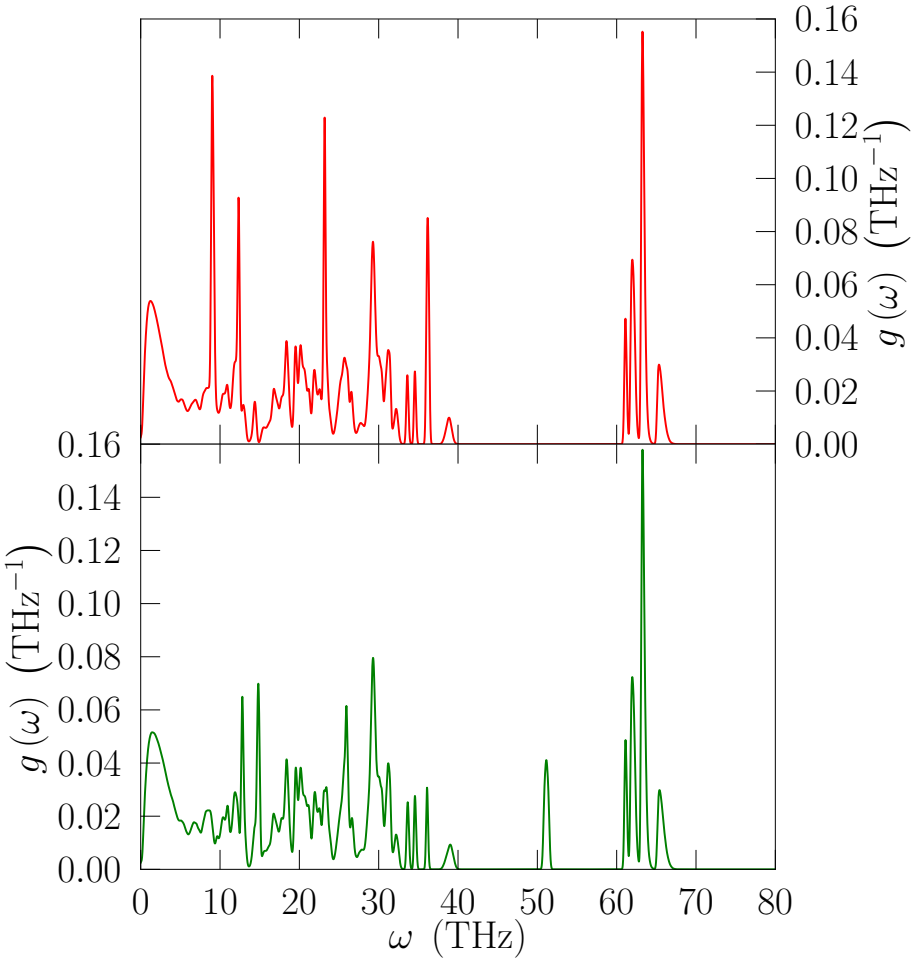

Figure 8.2 Normal modes of a single $[HMIM]^+$, $[BF_4]^-$ and $[PF_6]^-$ ion (from top to bottom).

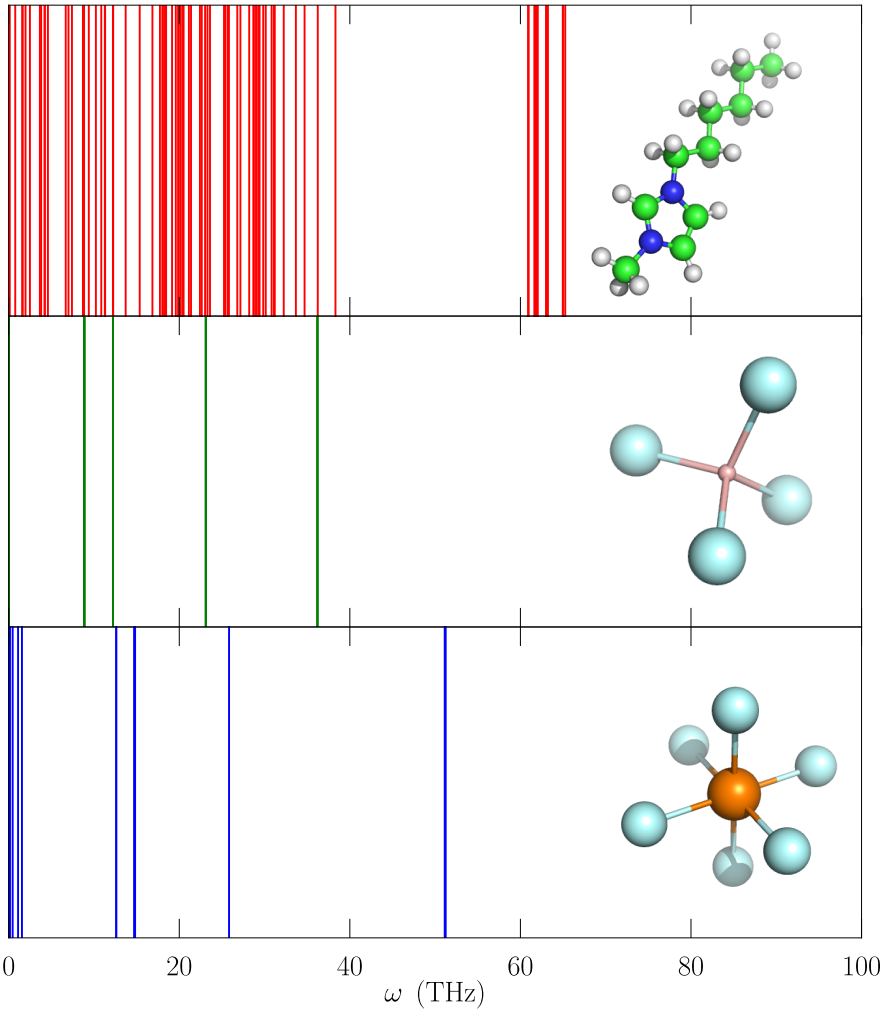

Figure 8.3 Hexagonal-bin histogram of the joint density of vibrational modes of [HMIM][BF_4] (top) and [HMIM][PF_6] (bottom) over frequencies and IPRs. The colour of each hexagon is associated to the fraction of normal modes with the corresponding frequency and inverse participation ratio. The sum of all bins in each histogram is equal to unity.

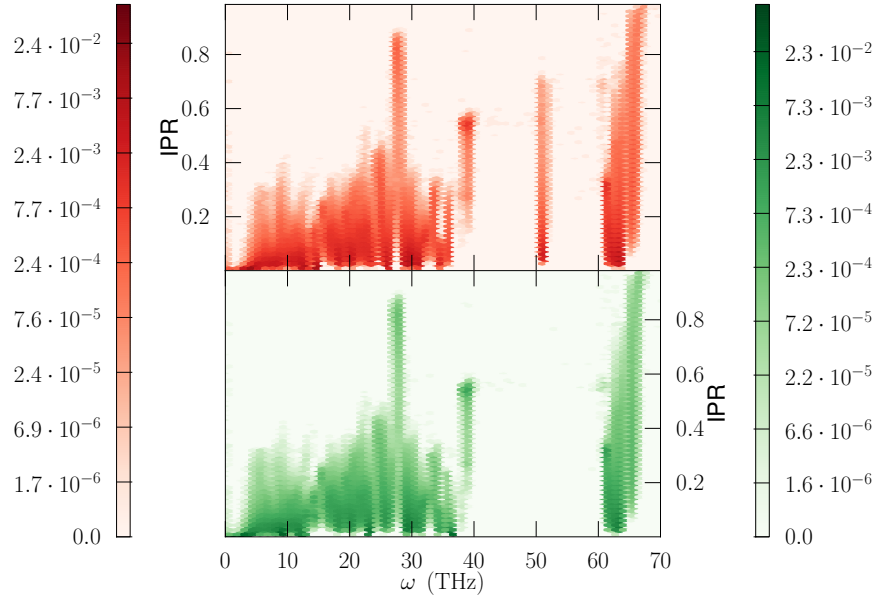

can be expected to have a greater influence on the thermal conductivity since lower-frequency vibrational levels are both more populated and less efficiently scattered.

Figure 8.3 presents a more detailed picture of the distribution of vibrational modes, not only over frequencies but also over IPRs. In addition to corroborating the similitude between [HMIM][BF_4] and [HMIM][PF_6], this figure points to the existence of very extended modes. In particular, at frequencies below 15 THz the dominant modes have almost vanishing IPRs, and even up to 35 THz many vibrational modes with IPRs well below 0.05 can be found. In contrast, there seems to be a lower bound for the IPRs of those vibrational modes in the frequency band between 60 and 70 THz. This can be understood as resulting from the absence of any normal mode of the anions in that range with which the vibrations of the cation can hybridise. Thus, in order to estab-

lish a collective oscillation with such a frequency the cation depends on interaction with other cations. This is less likely on average, due to the preference for heterocoordination in these systems, as manifested in the radial distribution functions [223] of [HMIM][BF_4] and [HMIM][PF_6]. The same reasoning holds for the $[PF_6]^-$ modes around 52 THz. The greater localisation of very-high-frequency modes makes them even less relevant for thermal conduction.

8.3. Thermal conduction mechanism

The identification of a well-defined vibrational spectrum in ILs and the presence of spatially extended vibrational modes suggests the possibility of considering them as heat carriers. Clearly, however, the absence of long-range order in the pseudolattice rules out quasi-ballistic phonon propagation as a reasonable conduction mechanism. Fortunately, the same kind of problem arose and was solved by previous authors in other kinds of systems with medium-range order, such as polycrystalline or amorphous solids and quantum dot superlattices. The proposed propagation mechanism is called phonon hopping and has been formulated several times in the literature in slightly different terms depending on the context [326–330]. The adaptation to liquids introduced here in based on the quantum dot superlattice model published by Shamsa *et al.* in 2005 [330].

The starting point in this theory is an image of the liquid as formed by a set of ordered domains of a certain size, separated by barriers. It must be emphasised that in liquids it is not possible to identify more ordered *vs.* less ordered regions (as opposed to the situation in polycrystalline solids, for instance), but it is still true that in order to travel from one point whose neighbourhood is ordered to another which also has an ordered environment a phonon must travel through an effective barrier, *i.e.*, a region whose structure is uncorrelated to those of the initial or final areas. In such a medium, the behaviour of vibrational modes depends on the ratio between their spatial extent and the characteristic size of the ordered domains: high-frequency modes will be essentially confined to one ordered domain, whereas more extended ones will have a probability of hopping between domains, giving them a phonon-like character (in the pseudolattice model, a wavelength can be assigned to these modes using standard spectral analysis techniques, since they extend over a number of periods of the pseudolattice). This behaviour can be illustrated with the trivial one-dimensional example of an infinite chain of harmonic oscillators

with a faulty link, whose Green's function can be calculated analytically [335] in order to obtain the phononic transmission for its single mode. The precise shape of this transmission depends on the elastic constant of the faulty link, but in any case low-frequency phonons pass through it almost unscattered. A more general example of the same behaviour of waves is Rayleigh scattering in optics [336].

The hamiltonian of a system composed of ordered domains with known normal modes, coupled through barriers, can be written as

$$\boldsymbol{H} = \underbrace{\sum_{i,\lozenge} \hbar\omega_{i,\lozenge} \left(\boldsymbol{a}^{\dagger}_{i,\lozenge} \boldsymbol{a}_{i,\lozenge} + \frac{1}{2} \right)}_{\boldsymbol{H_0}} + \underbrace{\sum_{\substack{i,j \\ \lozenge,\clubsuit}} t_{\substack{i,j \\ \lozenge,\clubsuit}} \boldsymbol{a}^{\dagger}_{i,\lozenge} \boldsymbol{a}_{j,\clubsuit}}_{\boldsymbol{H_1}}, \tag{8.2}$$

where i and j run over the domains and $\lozenge$ and $\clubsuit$ run over the vibrational modes of each of them. The first term — compare with Eq. (4.1) — is a sum of contributions from a set of independent harmonic oscillators or, in the second quantisation formalism, from the creation and annihilation of quasiparticles inside each domain (in which case $\boldsymbol{a}^{\dagger}_{i,\lozenge}$ and $\boldsymbol{a}_{i,\lozenge}$ are creation and annihilation operators, respectively). In contrast, $\boldsymbol{H_1}$ is precisely the hopping term, which describes the interaction between domains or the change in energy resulting from an annihilation in one domain and the creation of a quasiparticle in a different one.

The rate of hopping per unit time from a vibrational state $\clubsuit$ in domain j to a state $\lozenge$ in domain i can be calculated using standard time-dependent perturbation theory, of the same kind developed at length in Section 4.3. If the coupling between ordered regions is weak enough, the causal t-matrix connecting a (hypothetical) system of non-interacting ordered domains with the real situation can be approximated by $\boldsymbol{H_1}$ and the rate of hopping is given by Fermi's golden rule:

$$w_{\substack{i,j \\ \lozenge,\clubsuit}} = \frac{2\pi}{\hbar^2} \left| \langle i, \lozenge \,|\, \boldsymbol{H_1} \,|\, \clubsuit, s \rangle \right|^2 \delta\left(\omega_{i,\lozenge} - \omega_{j,\clubsuit}\right) = \frac{2\pi}{\hbar^2} \left| t_{\substack{i,j \\ \lozenge,\clubsuit}} \right|^2 \delta\left(\omega_{i,\lozenge} - \omega_{j,\clubsuit}\right). \tag{8.3}$$

The net energy flux $J_{Q,i,j}$ between two adjacent domains i and j can be calculated straightforwardly with the help of this set of hopping rates by taking

into account the total energy carried per unit time from j to i minus the energy flux in the opposite direction:

$$\begin{aligned} J_{Q,i,j} &= \underbrace{\sum_{\diamondsuit,\clubsuit} w_{\substack{i,j \\ \diamondsuit,\clubsuit}} \hbar\omega_{j,\clubsuit} f_{BE}\left(T_j, \omega_{j,\clubsuit}\right)}_{j \text{ to } i} - \underbrace{\sum_{\diamondsuit,\clubsuit} w_{\substack{j,i \\ \clubsuit,\diamondsuit}} \hbar\omega_{i,\diamondsuit} f_{BE}\left(T_i, \omega_{i,\diamondsuit}\right)}_{i \text{ to } j} = \\ &= \Delta T_{i,j} \left\{ \frac{2\pi}{\hbar} \sum_{\diamondsuit,\clubsuit} \left| t_{\substack{i,j \\ \diamondsuit,\clubsuit}} \right|^2 \left. \frac{df_{BE}}{dT} \right|_{T_{i,j},\omega_{i,\diamondsuit}} \omega_{j,\clubsuit} \delta\left(\omega_{i,\diamondsuit} - \omega_{j,\clubsuit}\right) \right\}, \end{aligned} \tag{8.4}$$

where T_i is the temperature of domain i, and the difference in temperature between two neighbouring domains, $\Delta T_{i,j} = T_j - T_i$, is small enough to justify the first-order series approximation in the right-hand side, which is reasonable even for large macroscopic temperature gradients. Note, moreover, that only harmonic processes are considered and that the interaction between any two non-adjacent domains is neglected. It should also be noted here that, when mass fluxes are considered, the experimentally relevant heat flux may not be equal to this energy flux. The corrections needed, however, are not free from ambiguity, so since advection has been excluded from the physical picture, it will be assumed that the relevant thermal flux is $J_{Q,i,j}$. This is another manifestation of the ambiguities in the definition of heat in a context so far removed from simple hydrostatic systems, already encountered in Chapter 2. An extended discussion of this topic can be found in Ref. 337 and references cited therein.

Equation (8.4) shows that, under these assumptions, the behaviour of a barrier between two ordered regions is resistive. The coefficient of proportionality between the temperature difference and the thermal flux it induces is the barrier conductance, $G_{i,j}$. If the first derivative of the Bose-Einstein distribution [Eq. (4.2)] is explicitly introduced and the sum over discrete states is replaced by an integration over a continuous DOS, its expression becomes

$$G_{i,j} = \frac{18\pi k_B}{\hbar^2} N_i N_j \int |t|^2 g^2(\omega) \left[\frac{\frac{\hbar\omega}{2k_B T}}{sinh\left(\frac{\hbar\omega}{2k_B T}\right)} \right]^2 d\omega, \tag{8.5}$$

where T is the average temperature of the two domains separated by the barrier, N_i is the number of particles in domain i and $|t|$ is an appropriate average of $\left| t_{\substack{i,j \\ r,s}} \right|$ over all the modes with frequency ω. As illustrated in the previous

section, it is possible to calculate the vibrational DOS of an IL. In principle, $|t|$ is also computable using Green's functions if the precise structure of a barrier between domains is known, which makes this formula directly applicable. However, in order to be able to proceed with an analytic discussion, some further simplifications will be introduced: a Debye model with a normalised DOS $g(\omega) = \frac{3}{\omega_D^3}\omega^2$ for frequencies between 0 and ω_D in each domain (a crude approximation which does not match the MD DOS, but gives the right speed of sound and number of states) and a extreme version of the phonon hopping mechanism,

$$|t|^2(\omega) = \begin{cases} \alpha \in (0,1), & \omega \leq \omega_C \\ 0, & \omega > \omega_C \end{cases}, \tag{8.6}$$

according to which modes above a certain cutoff frequency $\omega_C < \omega_D$, determined by the spatial width and other characteristics of the barrier, are completely confined to one ordered region, whereas all longer-wavelength phonon-like vibrations can hop across the barrier with the same probability per unit time. This finite probability can be considered a combination of the reflection caused by the barrier itself with the effect of any scattering mechanism operating inside the (imperfectly) ordered domains. Introducing these hypotheses into Eq. (8.5), it is transformed into

$$G_{i,j} = \frac{5148\pi k_B}{\hbar^2} N_i N_j \frac{\alpha \omega_T^5}{\omega_D^6} \Xi\left(\frac{\omega_C}{2\omega_T}\right), \tag{8.7a}$$

with

$$\omega_T := \frac{k_B T}{\hbar}, \tag{8.7b}$$

$$\Xi(x) := \int_0^x \frac{y^6}{sinh^2 y} dy. \tag{8.7c}$$

The monotonically increasing function $\Xi(x)$ thus defined grows proportionally to x^5 for small values of its argument and reaches a horizontal asymptote with value $\pi^6/42$ for all practical purposes before $x \simeq 8$.

Once the conductance of an individual barrier is known, the final step is to think of a macroscopic sample of liquid placed between a hot and a cold bath as a network of barriers that behave as thermal resistors. Strictly speaking,

Figure 8.4 2D analog of the assumed topology for the set of resistive barriers inside a macroscopic sample of liquid between two thermal baths.

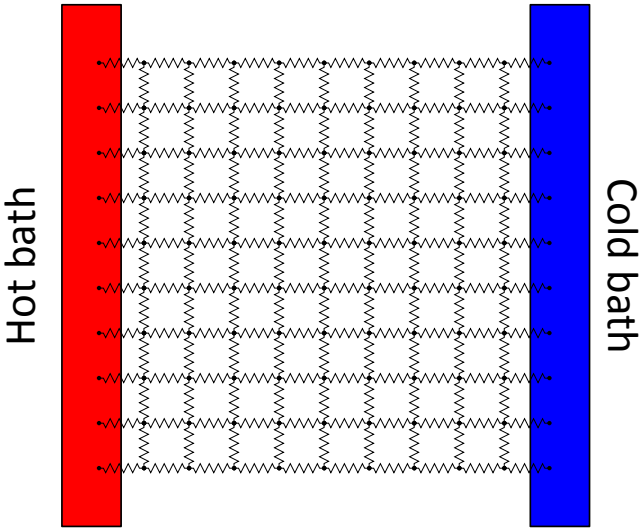

the values of these resistors must be considered to follow a probability distribution, which in fact increases the value of the thermal conductivity by offering the thermal current lower-resistance routes [329]. Additionally, the precise result depends on the topology of this network. Nevertheless, the presence of several adjustable parameters in this model (which can compensate for this simplifications) makes it acceptable to assume a simple cubic network of equal resistors, $G_{i,j} = G$, *i.e.*, the 3D analog of Fig. 8.4. With this assumption and taking the direction between the baths as the OZ axis, if ΔT is the temperature difference across the whole sample, l the characteristic length of each ordered domain and $\mathcal{N}_z$ the number of resistances along the OZ axis, the thermal conductivity of the sample is simply

$$\kappa = \frac{J}{\Delta T}\frac{\mathcal{N}_x}{\mathcal{N}_y\mathcal{N}_z l} = \frac{G}{l}. \tag{8.8}$$

8.4. Experimental procedure

All ILs used for the measurements were supplied by Iolitec. Samples of [HMIM][PF_6] and [BMIM][BF_4] had purities > 99%. The water employed was

milli-Q grade and ethanol was supplied by Panreac with purity better than 99.5%.

The original IL bottles were opened inside a sealed cabin under an inert atmosphere and with a humidity degree lower than 15% in order to avoid possible water adsorption. All the binary mixtures were built by weight with a balance whose accuracy is ±0.0001 g

Thermal conductivities were measured in a F5 LAMBDA instrument that uses the well known transient hot wire technique [307, 308]; it has a reproducibility of ±1%.

To regulate the sample temperature, two thermostats were used, a Julabo and a Haake F3. The temperature of the sample was measured by an internal thermometer calibrated with an ANTON PAAR model DT 100-30. The final resolution is better than 0.1 °C for the range of temperatures measured. For the different temperature ranges different substances had to be used in order to stabilise the sample temperature: from 353 to 423 K the sample was immersed in a paraffin wax bath while from 253 to 353 K a mixture of ethylene glycol and water was employed.

8.5. Discussion for pure ILs

When the number of particles in each ordered domain is N_0, Eqs. (8.7) and (8.8) can be combined into

$$\kappa = \frac{G_0}{l}\left(\frac{\omega_T}{\omega_D}\right)^5 \chi\left(\frac{\omega_C}{2\omega_T}\right) \tag{8.9a}$$

with

$$G_0 := \frac{858 N_0^2 \pi^7 \alpha k_B}{7\hbar^2 \omega_D}, \tag{8.9b}$$

$$\chi(x) := \frac{42}{\pi^6}\Xi(x). \tag{8.9c}$$

Note that, in the definition of χ, Ξ has been normalised to its asymptotic value; hence, $0 \leq \chi < 1$. Neglecting, as a first approximation, the small dependence on temperature which could result from thermal expansion and contraction of the domains, κ depends on T through the dimensionless factor $\left(\frac{\omega_T}{\omega_D}\right)^5 \chi\left(\frac{\omega_C}{2\omega_T}\right)$. Thus, this thermal conductivity depends on the ratios between three frequencies: the Debye frequency ω_D, the cutoff frequency imposed by the barriers,

ω_C, and the thermal frequency $\omega_T \propto T$, which determines which modes are significantly populated. At a temperature $T = 300$ K, $\omega_T \simeq 40$ THz. It was determined in the second section of this chapter that the vibrational spectrum of the studied ILs has an upper bound between 60 and 80 THz, which can be identified with ω_D. A rather crude estimation of ω_C in the framework of the Debye model, assuming that only those vibrations with a wavelength longer than the typical width a of a barrier can hop between domains, is $\omega_C \sim 2\pi c_s/a$, where c_s denotes the speed of sound. For imidazolium-based ILs, experimental measurements of the speed of sound yield [338] $c_s \sim 1500$ m/s, and if an *fcc* structure with the interatomic distances reported in Ref. 222 is assumed, $a \sim 0.6$ nm, so $\omega_C \sim 15$ THz.

All three frequencies are therefore of the same order of magnitude, with ω_C being the lowest. $\omega_C/(2\omega_T)$, the argument to χ, has a value of about 0.18, well within the range of validity of $\chi\left(\frac{\omega_C}{2\omega_T}\right) \simeq \frac{21}{16\pi^6}\left(\omega_C/\omega_T\right)^5$, so Eq. (8.9a) predicts a thermal conductivity plateau at room temperature. As a matter of fact, a small downwards slope is to be expected due to anharmonic effects not taken into account in this model. This prediction is confirmed by experimental data from the bibliography [307, 339], as well as by Prof. Óscar Cabeza's group's experimental measurements on [BMIM][BF_4], which are presented in Fig. 8.5.

8.6. Mixtures with a solvent

Let us now consider a binary mixture of an IL with some other miscible liquid, which will be called the solvent regardless of its relative concentration. In such a situation, three kinds of interactions must be considered, namely IL-IL, solvent-solvent and IL-solvent. The first kind gives rise to the pseudolattice arrangement and has already been dealt with, whereas solvent-solvent interactions cannot be treated in general without some hypothesis about the nature of this substance. The third kind of interactions will be discussed now in the framework of the Bahe-Varela theory [18]. The subscript s will be used to refer to magnitudes of the solvent, and a (0) superscript to allude to the value of a variable for a component considered as a pure substance.

The maximum contribution to the thermal current in a mixture coming from one of its constituents, i, is proportional to its number of degrees of freedom, which in turn is proportional to its molar concentration c_i. Thus, the total thermal conductivity can be expressed as a weighted average $\kappa = \frac{c_{\mathrm{IL}}}{c_{\mathrm{IL}}^{(0)}}\kappa_{\mathrm{IL}} + \frac{c_s}{c_s^{(0)}}\kappa_s$.

Figure 8.5 Thermal conductivity of pure [BMIM][BF_4] at room temperature and higher, together with its slope obtained from a linear fit.

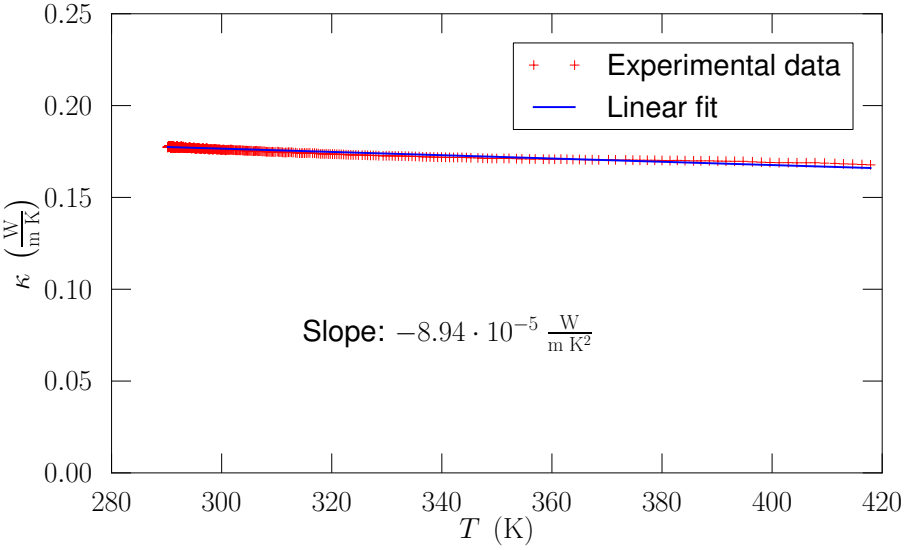

It must be noted, however, that the thermal conductivities per degree of freedom appearing in this formula are not necessarily those of the pure components, as their structure and dynamics in the mixture are affected by the presence of each other. As regards κ_{IL}, in the light of Eq. (8.9a) it can be seen that, if the range of the ordering, l, is taken as a constant, κ_{IL} is proportional to the number of particles in an ordered domain squared, N_0^2. The Bahe-Varela theory [283] predicts that the mean interatomic distance and the pseudolattice parameter in an IL are proportional to $c_{\mathrm{IL}}^{-\frac{1}{3}}$. Therefore, ionic density is proportional to c_{IL}, as is the number of ions that fit in a fixed volume. Thus, $\kappa_{\mathrm{IL}} \propto N_0^2 \propto c_{\mathrm{IL}}^2$ and

$$\kappa = \left(\frac{c_{\mathrm{IL}}}{c_{\mathrm{IL}}^{(0)}} \right)^3 \kappa_{\mathrm{IL}}^{(0)} + \frac{c_s}{c_s^{(0)}} \kappa_s. \tag{8.10}$$

The precise behaviour predicted by this formula depends on the model adopted for the conductivity of the solvent, which in turn depends on its nature. The crudest approximation possible is $\kappa_s = \kappa_s^{(0)}$ for all concentrations, which turns Eq. (8.10) into a parameter-free interpolation formula. In order to explore its prediction for two illustrative cases, it can be com-

Figure 8.6 Thermal conductivity of [BMIM][BF_4] + water and [HMIM][PF_6] + ethanol mixtures as a function of IL molarity. For [BMIM][BF_4] + water, the first series of data presented was measured at equal intervals of IL molarity, while the second was measured at equal intervals of IL mole fraction.

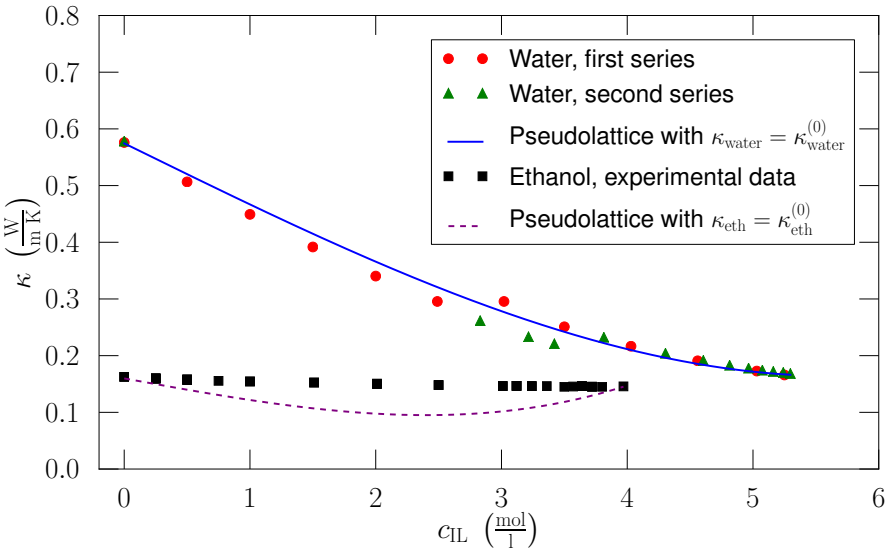

pared to measurements of the thermal conductivities of two IL+solvent mixtures: [BMIM][BF_4]+water and [HMIM][PF_6]+ethanol. These systems were chosen as examples because of their miscibility in the whole range of concentrations, as opposed for instance to the case of [HMIM][BF_4]+ethanol and [HMIM][PF_6]+water mixtures. Both the experimental data and the results from this interpolation are shown in Fig. 8.6. The agreement between this crude prediction and experimental data is excellent in the case of [BMIM][BF_4]+water mixtures, but poor for [HMIM][PF_6]+ethanol. This shows that the behaviour of both solvents in the bulk mixtures is very different.

A closer look into these differences in behaviour can be gained by calculating the value of κ_s for each case using Eq. (8.10) and the measured values of the total thermal conductivities. Figure 8.7 shows the results, normalised to their values for the respective pure solvents. In the case of water, deviations from unity are small but there is a clear change of trend at intermediate concentrations — the precise concentration at which this happens is different in the two series of measurements, which was later found to be due to an imperfect relaxation of some of the mixtures — which could be explained by some

Figure 8.7 Measured contribution of the solvent to the thermal conductivity of [BMIM][BF_4]+water and [HMIM][PF_6]+ethanol mixtures as a function of solvent molarity.

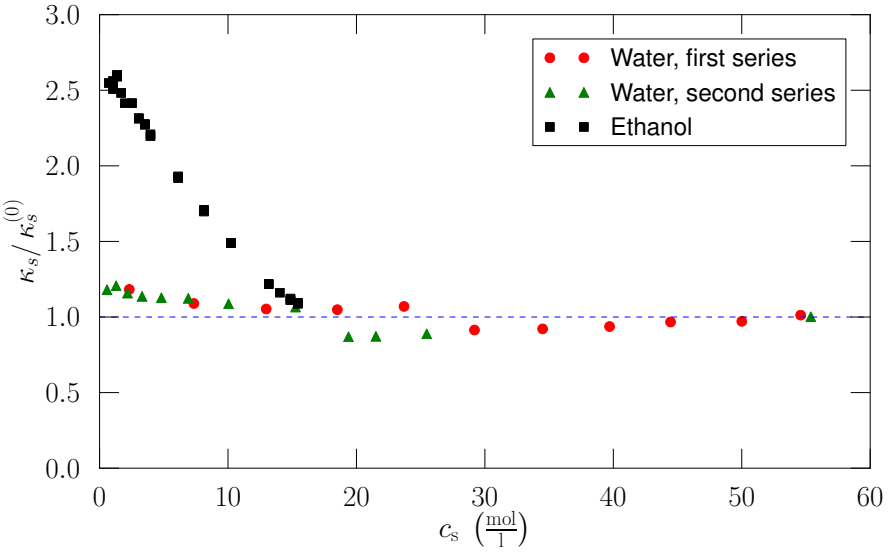

kind of percolation threshold: adding a few ions to water creates scattering centres that hinder the propagation of heat, but above this threshold the water network seems to become more and more structured with increasing IL concentration. In stark contrast to this, the behaviour with ethanol presents large deviations from its conductivity as a pure substance and a monotonically decreasing trend with increasing ethanol molarity. This can be explained by the different clustering behaviour of ethanol and water in their mixtures with ILs, as discussed in Chapter 6 and, indirectly, in Refs. 222 and 223. Water forms large clusters in the mixture, inside of which water molecules experience an environment similar to that of the bulk solvent. On the other hand, ethanol is almost homogeneously distributed inside the IL, so the interactions between an ethanol molecule and the ions are expected to be more important and concentration-dependent. Figure 8.7 suggests that this dependence can be reasonably well fitted to a straight line when describing the contribution of ethanol to the thermal conductivity of its mixtures with [HMIM][PF_6]; in any case, this contribution clearly cannot be considered constant.

The examples presented in this work are only the first steps in exploring the

possibilities of this theory. More experiments are needed in order to assess its transferability to different settings and to determine those characteristics of an IL which have a predominant influence on its thermal conductivity. Further simulation work can be done so as to calculate the vibrational spectra of other ILs and, most crucially, to look for ways to evaluate the parameters involved in the equations of this model. The ultimate aim of such effort must be to reach a point where a reasonable *a priori* estimate of the thermal conductivity of an IL can be provided, so as to help researchers and engineers to find the most convenient liquid for any particular application involving heat management. Only when this end is sufficiently approached will the often-used designation of "designer solvents" be truly appropriate for ILs as far as such applications are concerned.

References

18. Varela, L. M., García, M., Sarmiento, F., Attwood, D. & Mosquera, V. *J. Chem. Phys.* **107,** 6415 (1997).

43. Stillinger, F. H. & Weber, T. A. *Phys. Rev. B* **31,** 5262 (1985).

219. Sambasivarao, S. . V. & Acevedo, O. *J. Chem. Theory Comput.* **5,** 1038 (2009).

222. Méndez-Morales, T., Carrete, J., Cabeza, O., Gallego, L. J. & Varela, L. M. *J. Phys. Chem. B* **115,** 6995 (2011).

223. Méndez-Morales, T., Carrete, J., Cabeza, O., Gallego, L. J. & Varela, L. M. *J. Phys. Chem. B* **115,** 11170 (2011).

245. Berendsen, H. J. C., van der Spoel, D. & van Drunen, R. *Comp. Phys. Comm* **91,** 43 (1995).

246. Lindahl, E., Hess, B. & van der Spoel, D. *J. Mol. Model.* **7,** 306 (2001).

247. Van der Spoel, D., Lindahl, E., Hess, B., Groenhof, G., Mark, A. E. & Berendsen, H. J. C. *J. Comput. Chem.* **26,** 1701 (2005).

248. Hess, B., Kutzner, C., der Spoel, D. V. & Lindahl, E. *J. Chem. Theory Comput.* **4,** 435 (2008).

249. Jorgensen, W. L., Maxwell, D. S. & Tirado-Rives, J. *J. Am. Chem. Soc.* **118,** 11225 (1996).

283. Varela, L. M., Carrete, J., García, M., Rodríguez, J. R., Gallego, L. J., Turmine, M. & Cabeza, O. in. *Ionic Liquids: Theory, Properties, New Approaches* (ed Kokorin, A.) (InTech, 2011).

307. De Castro, C. A. N., Lourenço, M. J. V., Ribeiro, A. P. C., Langa, E., Vieira, S. I. C., Goodrich, P. & Hardacre, C. *J. Chem. Eng. Data* **55,** 653 (2010).

308. Assael, M. J., Antoniadis, K. D. & Wakeham, W. A. *Int. J. Thermophys.* **31,** 1051 (2010).

309. Lin, S. H., Eyring, H. & Davis, W. J. *J. Phys. Chem.* **10,** 3017 (1964).

310. Gaeta, F. S., Albanese, C., Mita, D. G. & Peluso, F. *Phys. Rev. E* **49,** 433 (1994).

311. Chisolm, E. D., Clements, B. E. & Wallace, D. C. *Phys. Rev. E* **63,** 031204 (2001).

312. Zwanzig, R. *J. Chem. Phys.* **79,** 4507 (1983).

313. Madan, B., Keyes, T. & Seeley, G. *J. Chem. Phys.* **92,** 7565 (1990).

314. Madan, B., Keyes, T. & Seeley, G. *J. Chem. Phys.* **94,** 6762 (1991).

315. Moore, P. & Keyes, T. *J. Chem. Phys.* **100,** 6709 (1994).

316. Keyes, T. *J. Chem. Phys.* **103,** 9810 (1996).

317. Bembenek, S. D. & Laird, B. B. *J. Chem. Phys.* **104,** 5199 (1996).

318. Gezelter, J. D., Rabani, E. & Berne, B. J. *J. Chem. Phys.* **107,** 4618 (1997).

319. Wales, D. J. *Energy Landscapes* (Cambridge University Press, 2004).

320. Majumdar, S. N. & Martin, O. C. *Phys. Rev. E* **74,** 061112 (2006).

321. Wales, D. J. & Doye, J. P. K. *J. Phys.Chem. A* **101,** 5111 (1997).

322. Wallace, D. C. *Phys. Rev. E* **56,** 4179 (1997).

323. Wallace, D. C. & Clements, B. E. *Phys. Rev. E* **59,** 2942 (1999).

324. Clements, B. E. & Wallace, D. C. *Phys. Rev. E* **59,** 2955 (1999).

325. Holmström, E., Bock, N., Peery, T. B., Lizárraga, R., Lorenzi-Venneri, G. D., Chisolm, E. D. & Wallace, D. C. *Phys. Rev. E* **80,** 051111 (2009).

326. Böttger, H. & Damker, T. *Phys. Rev. B* **50,** 12509 (1994).

327. Böttger, H. & Damker, T. *Phys. Rev. B* **52,** 12481 (1995).

328. Damker, T., Bryskin, V. V. & Böttger, H. *Physica B* **263–264,** 133 (1999).

329. Braginsky, L., Lukzen, N., Shklover, V. & Hofmann, H. *Phys. Rev. B* **66,** 134203 (2002).

330. Shamsa, M., Liu, W., Balandin, A. A. & Liu, J. *Appl. Phys. Lett.* **87,** 202105 (2005).

331. Press, W. H., Teukolsky, S. A., Vetterling, W. T. & Flannery, B. P. *Numerical Recipes in C — The Art of Scientific Computing* 2nd (Cambridge University Press, 1992).

332. Byrd, R. H., Lu, P. & Nocedal, J. A. *SIAM J. Scientif. Statistic. Comput.* **16,** 1190 (1995).

333. Zhu, C., Byrd, R. H. & Nocedal, J. *ACM Trans. Math. Softw.* **23,** 550 (1997).

334. Shenogin, S., Bodapati, A., Keblinski, P., & McGaughey, A. J. H. *J. Appl. Phys.* **105,** 034906 (2009).

335. Mingo, N. in *Thermal Nanosystems and Nanomaterials* (ed Volz, S.) 63 (Springer Berlin / Heidelberg, 2009).

336. Bohren, C. F. & Huffman, D. *Absorption and scattering of light by small particles* (Wiley, 1983).

337. Perronace, A., Ciccotti, G., Leroy, F., Fuchs, A. H. & Rousseau, B. *Phys. Rev. E* **66,** 031201 (2002).

338. Gardas, R. L., Dagade, D. H., Terdale, S. S., Coutinho, J. A. P. & Patil, K. J. *J. Chem. Thermodynamics* **40,** 695 (2008).

339. Tomida, D., Kenmochi, S., Tsukada, T., Qiao, K. & Yokoyama, C. *Int. J. Thermophys.* **28,** 1147 (2007).

9 Conclusions

— Al fin y al cabo aquí no hacía nada.
— ¡Cuánta pérdida de tiempo, Don Pedro! Se lo digo yo que he visto tanta juventud gastada en esta casa… ¿Y para qué, dígame Don Pedro, y para qué? ¿Quién se lo iba a agradecer? Son ilusiones bobas. Lo único que vi que valiera la pena es sacarse la tesis, eso sí. Luego van ya a cátedras. ¿Pero, otra cosa? ¡Pamplinas! ¡Váyase! ¡Váyase y gane dinero!

Tiempo de Silencio
Luis Martín-Santos

1. The thermal conductivity (κ) of hexagonal [111] InP nanowires has been studied using a direct molecular dynamics method. Its order of magnitude has been shown to be lower than that of bulk InP, and its dependence on the diameter of the wire to have a maximum, suggesting a small enhancement in κ when the diameter is reduced below a certain point. Such enhancement has been interpreted in terms of the phonon density of states (DOS) of the nanowires.

2. The same molecular dynamics method has been used to calculate the thermal conductivity of [111] InP, InAs and GaAs nanowires using two

very different potentials, a simple (Harrison) and a complex (Branício-Rino for InP, Hammerschmidt for InAs and GaAs) potential in each case. The Harrison potential has been shown to yield conductivities an order of magnitude below the others, highlighting the importance of an appropriate choice of potential. The phonon DOS calculated using each of the interaction models confirmed the differences.

3. Nevertheless, some of the theoretical results derived in the literature using the Harrison potential in conjunction with the Boltzmann transport equation are corroborated by the more complex models.

4. A non-equilibrium Green's functions method has been applied to the problem of thermal conduction by phonons in an atomistically-described [111] silicon nanowire with a rough boundary. It has been concluded that the Casimir formula yields a good approximation to the mean free path even in very thin wires; it is possible to go beneath this limit, but at the cost of introducing very deep defects in the wire.

5. Experimental reports about very low conductivities in silicon nanowires, previously thought to be attributable to boundary scattering, have been shown, in this work, to be well below the limit of its effects. A previous theoretical explanation based on perturbation theory seems very likely to be invalid due to methodological errors.

6. A new theoretical method was developed that allows the detailed energy transmission probabilities between any two vibrational modes at both sides of a defect in a quasi-one-dimensional system to be calculated.

7. The thermal, electric and thermoelectric properties of an organic-inorganic superlattice made of alternating layers of tri-tiophene molecules and blocks of a random SiGe alloy have been characterised. The results point to this class of materials as very promising for thermoelectric applications, since the dimensionless figure of merit of the superlattice improves upon that of SiGe alone by a factor of 2.5. This has been proved to be due to the fact that the organic layers block phonons to a much larger degree than that to which they block electrons.

8. The thermoelectric properties of the superlattice studied have been shown to be changed by about 20% by the simple addition of a phenyl

ring to each tri-tiophene, suggesting a great potential for optimisation of this kind of structures through chemical methods.

9. As a necessary prelude to the study of transport processes in a second kind of nanostructured materials, ionic liquids (ILs), the clustering behaviour of water, methanol and ethanol in their mixtures with imidazolium-based ILs has been characterised. Water has been found to form big clusters inside the mixtures, while even at high concentrations alcohol molecules only form small clusters. Ions tend to be parts of a polar network inside these systems, which breaks down into isolated ions or ion pairs at high solvent concentrations. An intermediate regime exists in the case of IL+alcohol mixtures in which big ionic clusters are present.

10. The orientation of water, methanol and ethanol molecules around ions in their mixtures with ILs has been investigated, showing big differences between water and alcohols which contribute to the understanding of their clustering behaviour.

11. The tendency of nearby alcohol molecules to be parallel in pure alcohol has been found to be broken by the addition of even a minute amount of ionic liquid.

12. A model for the electric conductivity of ILs and their mixtures with solvents, as well as for traditional electrolyte solutions, has been developed in the framework of the Bahe-Varela pseudolattice theory. This model predicts the existence of a conductivity maximum with respect to concentration, which is detected in experimental results. Likewise, data from experiments shows excellent agreement with the corresponding-states law derived from the model. Deviations from it can be explained in terms of clustering.

13. A precise notion of normal mode in the context of liquids has been adopted from the literature; the vibrational density of states of two pure ILs has been characterised and extended phonon-like normal modes have been shown to exist.

14. The same pseudolattice theory has been used to develop a general model for the thermal conductivity of ILs and their mixtures based on phonon

hopping, a heat transfer mechanism adapted from studies of other media with medium-range order. After introducing some simplifications to make an analytic treatment possible, a room-temperature plateau has been predicted, which is confirmed by experimental data.

15. Finally, a parameter-free interpolation formula for the thermal conductivity of mixtures of an IL with a solvent has been deduced based on the model, which agrees with experimental results for mixtures with water under a hypothesis of bulk-like behaviour of the solvent at any concentration. However, this hypothesis has been shown to be unwarranted for alcohols, as expected given the different clustering behaviour of these substances.

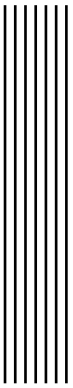

List of Tables

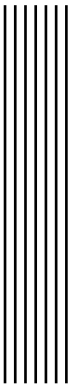

List of Figures

List of publications related to this thesis

- **Nonequilibrium nanothermodynamics**, Carrete, J., Varela, L. M., and & Gallego, L. J. *Phys. Rev. E* **77**, 022102 (2008).
- **Pseudolattice theory of the surface tension of ionic liquid-water mixtures**, Varela, L. M., Carrete, J., Turmine, M., Rilo, E. & Cabeza, O. *J. Phys. Chem. B* **113**, 12500 (2009).
- **Molecular-dynamics prediction of the thermal conductivity of thin InP nanowires: Similarities to Si**, Carrete, J., Longo, R. C., Varela, L. M., Rino, J. P. & Gallego, L. J. *Phys. Rev. B* **80**, 155408 (2009).
- **Pseudolattice theory of charge transport in ionic solutions: Corresponding states law for the electric conductivity**, Varela, L. M., Carrete, J., García, M., Gallego, L. J., Turmine, M., Rilo, E. & Cabeza, O. *Fluid Phase Equilib.* **298**, 280 (2010).
- **Theoretical model for moisture adsorption on ionic liquids: A modified Brunauer–Emmet–Teller isotherm approach**, Carrete, J. , García, M., Rodríguez, L. M., Cabeza, O. & Varela, L. M. *Fluid Phase Equilib.* **301**, 118 (2011).
- **Prediction of phonon thermal transport in thin GaAs, InAs and InP nanowires by molecular dynamics simulations: Influence of the in-**

teratomic potential, Carrete, J., Longo, R. C. & Gallego, L. J. *Nanotechnology* **22**, 185704 (2011).

- **Molecular dynamics simulation of the structure and dynamics of water-1-alkyl-3-methylimidazolium ionic liquid mixtures** Méndez-Morales, T., Carrete, J., Cabeza, O., Gallego, L. J. & Varela, L. M. *J. Phys. Chem. B* **115**, 6995 (2011).

- **Surface roughness and thermal conductivity of semiconductor nanowires: Going below the Casimir limit**, Carrete, J., Gallego, L. J., Varela, L. M. & Mingo, N. *Phys. Rev. B* **84**, 075403 (2011).

- **Molecular dynamics simulations of the structural and thermodynamic properties of imidazolium-based ionic liquid mxtures**, Méndez-Morales, T., Carrete, J., Cabeza, O., Gallego, L. J. & Varela, L. M. *J. Phys. Chem. B* **115**, 1170 (2011).

- **Surfactant self-assembly structures in protic ionic liquids**, Fernández-Castro, B., Méndez-Morales, T., Carrete, J., Fazer, E., Cabeza, O., Rodríguez, J. R, Turmine, M. & Varela, L. M., *J. Phys. Chem. B* **115**, 8145 (2011).

- **Dynamical properties of alcohol + 1-hexyl-3-methylimidazolium ionic liquid mixtures: A computer simulation study**, Méndez-Morales, T., Carrete, J., García, M., Cabeza, O., Gallego, L. J. & Varela, L. M. *J. Phys. Chem. B* **115**, 15313 (2011).

- **Thermal conductivity of ionic liquids: A pseudolattice approach**, Carrete, J., Méndez-Morales, T., García, M., Vila, J., Cabeza, O., Gallego, L. J. & Varela, L. M. *J. Phys. Chem. C* **116**, 1265 (2012).

- **Liquid–solid–liquid phase transition hysteresis loops in the ionic conductivity of ten imidazolium-based ionic liquids**, Vila, J., Fernández-Castro, B., Rilo, E., Carrete, J., Domínguez-Pérez, M., Rodríguez, J. R., García, M., Varela, L. M. & Cabeza, O. *Fluid Phase Equilib.* **320**, 1 (2012).

- **Investigation of the local structure of mixtures of an ionic liquid with polar solvents through molecular dynamics: Cluster formation and angular distributions**, Carrete, J., Méndez-Morales, T., Cabeza, O., Lynden-Bell, R. M., Gallego, L. J. & Varela, L. M. *submitted to J. Phys. Chem. B*.

- **Thermoelectric properties of hybrid organic-inorganic superlattices**, Carrete, J., Mingo, N., Tian, G., Ågren, H., Baev, A. & Prasad, P. N. *submitted to J. Phys. Chem. C*.

- **Pseudolattice theory of ionic liquids**, Varela, L. M., Carrete, J., García, M., Rodríguez, J. R., Gallego, L. J., Turmine, M. & Cabeza, O. in. *Ionic Liquids: Theory, Properties, New Approaches* (ed Kokorin, A.) (InTech, 2011). ISBN 978-953-307-349-1.

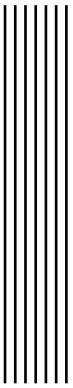

Complete references

1. Feynman, R. *Eng. Sci. Mag.* **23,** 22 (1960).
2. Eric Drexler, K. *Engines of Creation: The Coming Era of Nanotechnology* (Anchor Books, New York, 1986).
3. Knight, W. D., Clemenger, K., de Heer, W. A. & Saunders, W. A. *Phys. Rev. Lett.* **52,** 2141 (1984).
4. Kroto, H. W., Heath, J. R., O'Brien, S. C., Curl, R. F. & Smalley, R. E. *Nature* **318,** 162 (1985).
5. Zhang, Q. L., O'Brien, S. C., Heath, J. R., Liu, Y., Curl, R. F., Kroto, H. W. & Smalley, R. E. *J. Phys. Chem.* **90,** 525 (1986).
6. Novoselov, K. S., Geim, A. K., Morozov, S. V., Jiang, D., Zhang, Y., Dubonos, S. V., Grigorieva, I. V. & Firsov, A. A. *Science* **306,** 666 (2004).
7. Hullman, A. *The Economic Development of Nanotechnology — An Indicators Based Analysis* tech. rep. (DG Research and European Commision, 2006).
8. Ratchev, S. & Turitto, M. *Vision for Micro- and Nano-Manufacturing* tech. rep. (European Technology Platform for Micro- and Nano Manufacturing (MINAM), 2008).
9. Despotuli, A. & Andreeva, A. *Int. J. Nanosci.* **8,** 389 (2009).
10. Balandin, A. A. *IEEE Potentials* **21,** 11 (2002).

11. Nolas, G. S., Sharp, J. & Goldsmid, H. J. *Thermoelectrics* (Springer, New York, 2001).
12. Rogers, R. D. & Seddon, K. R. *Ionic Liquids: Industrial Applications for Green Chemistry* (American Chemical Society, Washington, DC, 2002).
13. Rogers, R. D. & Seddon, K. R. *Ionic Liquids as Green Solvents: Progress and Prospects* (American Chemical Society, Washington, DC, 2003).
14. Wasserscheid, P. & Welton, T. *Ionic Liquids in Synthesis* 2nd (Wiley-VCH, New York, 2008).
15. Griebel, M., Knapek, S. & Zumbusch, G. *Numerical Simulation in Molecular Dynamics: Numerics, Algorithms, Parallelization, Applications* (Springer, New York, 2007).
16. Economou, E. N. *Green's Functions in Quantum Physics* (Springer-Verlag, New York, 1990).
17. Datta, S. *Quantum Transport: Atom to Transistor* second (Cambridge University, New York, 2005).
18. Varela, L. M., García, M., Sarmiento, F., Attwood, D. & Mosquera, V. *J. Chem. Phys.* **107,** 6415 (1997).
19. Shi, J. & Li, J. C. M. *Nano Lett.* **9,** 1307 (2009).
20. Xia, Y., Yang, P., Sun, Y., Wu, Y., Mayers, B., Gates, B., Yin, Y., Kim, F. & Yan, H. *Adv. Mater.* **15,** 353 (2003).
21. Law, M., Goldberger, J. & Yang, P. *Annu. Rev. Mater. Res.* **34,** 83 (2004).
22. Kim, W., Wang, R. & Majumdar, A. *Nanotoday* **2,** 40 (2007).
23. Wang, G. & Li, X. *J. Appl. Phys.* **104,** 113517 (2008).
24. Kim, D. R., Lee, C. H. & Zheng, X. *Nano Lett.* **10,** 1050 (2010).
25. Zou, J. & Balandin, A. *Proc. Electrochem. Soc.* **2001-19,** 70 (2001).
26. Schelling, P. K., Shi, L. & Goodson, K. E. *Mater. Today* **8,** 30 (2005).
27. Hicks, L. D. & Dresselhaus, M. S. *Phys. Rev. B* **47,** 12727 (1993).
28. Mahan, G., Sales, B. & Sharp, J. *Phys. Today* **50,** 42 (1997).
29. Majumdar, A. *Science* **303,** 777 (2004).
30. Li, D., Wu, Y., Kim, P., Shi, L., Yang, P. & Majumdar, A. *Appl. Phys. Lett.* **83,** 2934 (2003).

31. Li, D., Wu, Y., Fan, R., Yang, P. & Majumdar, A. *Appl. Phys. Lett.* **83,** 3186 (2003).

32. Zhou, J., Jin, C., Seol, J. H., Li, X. & Shi, L. *Appl. Phys. Lett.* **87,** 133109 (2005).

33. Shi, L., Hao, Q., Yu, C., Mingo, N., Kong, X. & Wang, Z. L. *Appl. Phys. Lett.* **84,** 2638 (2004).

34. Bourgeois, O., Fournier, T. & Chaussy, J. *J. Appl. Phys.* **101,** 016104 (2007).

35. Chen, R., Hochbaum, A. I., Murphy, P., Moore, J., Yang, P. & Majumdar, A. *Phys. Rev. Lett.* **101,** 105501 (2008).

36. Mingo, N. *Phys. Rev. B* **68,** 113308 (2003).

37. Mingo, N., Yang, L., Li, D. & Majumdar, A. *Nano Lett.* **3,** 1713 (2003).

38. Chantrenne, P., Barrat, J. L., Blase, X. & Gale, J. D. *J. Appl. Phys.* **97,** 104318 (2005).

39. Volz, S. G. & Chen, G. *Appl. Phys. Lett.* **75,** 2056 (1999).

40. Chen, Y., Li, D., Lukes, J. & Majumdar, A. *J. Heat Transfer.* **127,** 1129 (1999).

41. Ponomareva, I., Srivastava, D. & Menon, M. *Nano Lett.* **7,** 1155 (2007).

42. Schelling, P. K., Phillpot, S. R. & Keblinski, P. *Phys. Rev. B* **65,** 144306 (2002).

43. Stillinger, F. H. & Weber, T. A. *Phys. Rev. B* **31,** 5262 (1985).

44. Stillinger, F. H. & Weber, T. A. *Phys. Rev. B* **33,** 1451 (1986).

45. Zhang, Y., Cao, J. X., Xiao, Y. & Yan, X. H. *J. Appl. Phys.* **102,** 104303 (2007).

46. Boukai, A. I., Bunimovich, Y., Tahir-Kheli, J., Yu, J.-K., III, W. A. G. & Heath, J. R. *Nature (London)* **451,** 168 (2008).

47. Trentler, T. J., Hickman, K. M., Goel, S. C., Viano, A. M., Gibbons, P. C. & Buhro, W. E. *Science* **270,** 1791 (1995).

48. Trentler, T. J., Goel, S. C., Hickman, K. M., Viano, A. M., Chiang, M. Y., Beatty, A. M., Gibbons, P. C. & Buhro, W. E. *J. Am. Chem. Soc.* **119,** 419 (1997).

49. Duan, X. F. & Lieber, C. M. *Adv. Mater.* **12,** 298 (2000).

50. Gudiksen, M. S. & Lieber, C. M. *J. Am. Chem. Soc.* **122,** 8801 (2000).

51. Gudiksen, M. S., Wang, J. F. & Lieber, C. M. *J. Phys. Chem. B* **105,** 4062 (2001).

52. Tang, C., Bando, Y., Liu, Z. & Golberg, D. *Chem. Phys. Lett.* **376,** 676 (2003).

53. Yu, H., Li, J., Loomis, R. A., Wang, L.-W. & Buhro, W. E. *Nature Mater.* **2,** 517 (2003).

54. Gudiksen, M. S., Wang, J. & Lieber, C. M. *J. Phys. Chem. B* **106,** 4036 (2002).

55. Huang, Y. & Lieber, C. M. *Pure Appl. Chem.* **76,** 2051 (2004).

56. Duan, X. F., Huang, Y., Cui, Y., Wang, J. & Lieber, C. M. *Nature (London)* **409,** 66 (2001).

57. Alemany, M. M. G., Huang, X., Tiago, M. L., Gallego, L. J. & Chelikowsky, J. R. *Nano Lett.* **7,** 1878 (2007).

58. Alemany, M. M. G., Jain, M., Kronik, L. & Chelikowsky, J. R. *Phys. Rev. B* **69,** 075101 (2004).

59. Alemany, M. M. G., Jain, M., Tiago, M. L., Zhou, Y., Saad, Y. & Chelikowsky, J. R. *Comput. Phys. Commun.* **177,** 339 (2007).

60. Harrison, W. A. *Electronic Structure and the Properties of Solids* (Dover, New York, 1989).

61. Mingo, N. & Broido, D. A. *Phys. Rev. Lett.* **93,** 246106 (2004).

62. Mingo, N. *Appl. Phys. Lett.* **84,** 2652 (2004).

63. Branício, P. S. & Rino, J. P. *Phys. Stat. Sol. (b)* **244,** 331 (2007).

64. Vashishta, P., Kalia, R. K., Rino, J. P. & Ebbsjö, I. *Phys. Rev. B* **41,** 12197 (1990).

65. Shimojo, F., Ebbsjö, I., Kalia, R. K., Nakano, A., Rino, J. P. & Vashishta, P. *Phys. Rev. Lett.* **84,** 3338 (2000).

66. Rino, J. P., Chatterjee, A., Ebbsjö, I., Kalia, R. K., Nakano, A., Shimojo, F. & Vashishta, P. *Phys. Rev. B* **65,** 195206 (2002).

67. Branício, P. S., Kalia, R. K., Nakano, A., Rino, J. P., Shimojo, F. & Vashishta, P. *Appl. Phys. Lett.* **82,** 1057 (2003).

68. Rino, J. P. & Branício, P. S. *Phys. Stat. Sol. (b)* **244,** 239 (2007).

69. Lieb, E. H. & Yngvason, J. *Phys. Rep.* **310,** 1 (1996).

70. Carathéodory, C. *Math. Ann* **67,** 355 (1909).

71. Buchdahl, H. A. *The Concepts of Classical Thermodynamics* (Cambridge University Press, Cambridge, 1966).

72. Boyling, J. B. *Proc. Roy. Soc. London A* **329,** 35 (1972).

73. Grandy, W. T. Jr. *Found. Phys.* **34,** 21 (2004).

74. Kittel, C. *Introduction to Solid State Physics* 8th Edition (Wiley, 2004).

75. Vavilov, M. G. & Stone, A. D. *Phys. Rev. B* **72,** 205107 (2005).

76. Tanatar, M. A., Paglione, J., Petrovic, C. & Taillefer, L. *Science* **316,** 1320 (2007).

77. Shanks, H. R., Maycock, P. D., Sidles, P. & Danielson, G. C. *Phys. Rev.* **130,** 1743 (1963).

78. Kudman, I. & Steigmeier, E. F. *Phys. Rev.* **133,** 1665 (1964).

79. Ju, Y. S. *Appl. Phys. Lett.* **87,** 153106 (2005).

80. Van Duin, A. C. T., Dasgupta, S., Lorant, F. & Goddard III, W. A. *J. Phys. Chem. A* **105,** 9396 (2001).

81. Rey, C., Gallego, L. J., García-Rodeja, J., Alonso, J. A. & Iñiguez, M. P. *Phys. Rev. B* **48,** 8253 (1993).

82. García-Rodeja, J., Rey, C., Gallego, L. J. & Alonso, J. A. *Phys. Rev. B* **49,** 8495 (1994).

83. Xiao-Kun, G. & Bing-Yang, C. *Chin. Phys.* **16,** 3777 (2007).

84. N. Yang, G. Z. & Li, B. *Nano Lett.* **8,** 276 (2007).

85. Gomes, C. J., Madrid, M., Goicochea, J. V. & Amon, C. H. *J. Heat Transfer* **128,** 1114 (2006).

86. Chen, G. Y., Stolojan, V., Cox, D. C., Giusca, C. & Silva, S. R. P. in *IEEE Conference on Emerging Technologies - Nanoelectronics* (2006), 376.

87. Yang, W., Araki, H., Kohyama, A., Thaveethavorn, S., Suzuki, H. & Noda, T. *Mater. Lett.* **58,** 3145 (2004).

88. Wang, S., Liang, X. & Ohara, T. *J. Appl. Phys.* **105,** 014316 (2009).

89. Swope, W. C., Andersen, H. C. & amd K. R. Wilson, P. H. B. *J. Chem. Phys.* **76,** 637 (1982).

90. Van Zon, R. *CHM1464: Foundations of Molecular Dynamics, course notes* Booklet avaliable online at the University of Toronto web site `http://www.chem.utoronto.ca/~rzon/simcourse/notes.html`. Retrieved on 2012-04-06. 2005.

91. Carrete, J., Varela, L. M. & Gallego, L. J. *Physica A* **27,** 6752 (2008).

92. Guajardo-Cuéllar, A., Go, D. B. & Sen, M. *J. Chem. Phys.* **132,** 104111 (2010).

93. Evans, D. J. & Morriss, G. P. *Statistical Mechanics of NonEquilibrium Liquids* 1st ed. (Academic Press, London, 1990).

94. G, G. P., Ely, J. F., McCabe, C. & Isbister, D. J. *J. Chem. Phys.* **122,** 094114 (2005).

95. Mandadapu, K. K., Jones, R. E. & Papadopoulos, P. *J. Chem. Phys.* **133,** 034122 (2010).

96. Mandadapu, K. K., Jones, R. E. & Papadopoulos, P. *J. Chem. Phys.* **130,** 204106 (2009).

97. Huang, X., Huai, X., Liang, S. & Wang, X. *J. Phys. B* **42,** 095416 (2009).

98. Turney, J. E., McGaughey, A. J. H. & Amon, C. H. *Phys. Rev. B* **79,** 224305 (2009).

99. Zhou, X. W., Aubry, S., Jones, R. E., Greenstein, A. & Schelling, P. K. *Phys. Rev. B* **79,** 115201 (2009).

100. Jund, P. & Jullien, R. *Phys. Rev. B* **59,** 13707 (1999).

101. Berendsen, H. J. C., Postma, J. P. M., van Gunsteren, W. F., Dinola, A. & Haak, J. R. *J. Chem. Phys.* **81,** 3684 (1984).

102. Papanicolaou, N. I., Lagaris, I. E. & Evangelakis, G. A. *Surf. Sci.* **337,** L819 (1995).

103. Heino, P. *Eur. Phys. J. B* **60,** 171 (2007).

104. Yoo, Y.-G., Car, R., Srolovitz, D. J. & Scandolo, S. *Phys. Rev. B* **70,** 012302 (2004).

105. Aliev, S. A., Nashelskii, A. Y. & Shalyt, S. S. *Sov. Phys. Solid State* **7,** 1287 (1965).

106. Balandin, A. & Wang, K. L. *Phys. Rev. B* **58,** 1544 (1998).

107. Adu, K. W., Gutiérrez, H. R., Kim, U. J., Sumanasekera, G. U., & Eklund, P. C. *Nano Lett.* **5,** 409 (2005).

108. Mingo, N. *Appl. Phys. Lett.* **88,** 149902 (2006).

109. Mingo, N. *Appl. Phys. Lett.* **85,** 5986 (2004).

110. Hammerschmidt, T., Kratzer, P. & Scheffler, M. *Phys. Rev. B* **77,** 235303 (2008).

111. Thomas, J. A., Intzi, R. M. & McGaughey, A. J. H. *Phys. Rev. B* **81,** 045413 (2010).

112. Sellan, D. P., Landry, E. S., Turney, J. E., McGaughey, A. J. H. & Amon, C. H. *Phys. Rev. B* **81,** 214305 (2010).

113. Yang, X., To, A. C. & Tian, R. *Nanotechnology* **21,** 155704 (2010).

114. Tersoff, J. *Phys. Rev. Lett.* **56,** 632 (1986).

115. Tersoff, J. *Phys. Rev. B* **37,** 6991 (1988).

116. Tersoff, J. *Phys. Rev. B* **38,** 9902 (1988).

117. Tersoff, J. *Phys. Rev. B* **39,** 5566 (1989).

118. Both, W., Gottschalch, V. & Wagner, G. *Crysr. Res. Technol.* **21,** K85 (1986).

119. *Properties of Gallium Arsenide* 3rd (eds Brozel, M. R. & Stillman, G. E.) (INSPEC, London, 1996).

120. Steigmeier, E. F. & Kudman, I. *Phys. Rev.* **132,** 508 (1963).

121. Fritsch, J., Pavone, P. & Schröder, U. *Phys. Rev. B* **52,** 11326 (1995).

122. Borcherds, P. H., Alfrey, G. F., Saunderson, D. H. & Woods, A. D. B. *J. Phys. C* **8,** 2022 (1975).

123. Mooradian, A. & Wright, G. B. *Solid State Commun.* **4,** 431 (1966).

124. *Semiconductors: Physics of Group IV and III-IV Compounds* (ed Madelung, O.) (Springer-Verlag, Berlin, 1982).

125. *Semiconductors: Intrinsic Properties of Group IV Elements and III-V, II-VI, and I-VII Compounds* (ed Madelung, O.) (Springer-Verlag, Berlin, 1987).

126. Persson, A. I., Koh, Y. K., Cahill, D. G., Samuelson, L. & Linke, H. *Nano Lett.* **9,** 4484 (2009).

127. Mavrokefalos, A., Pettes, M. T., Saha, S., Zhou, F. & Shi, L. *25th International Conference on Thermoelectrics,* 234 (2006).

128. Casimir, H. B. G. *Physica* **5,** 495 (1938).

129. Zhu, Y. F., Lian, J. S. & Jiang, Q. *Appl. Phys. Lett.* **92,** 113101 (2008).

130. Hochbaum, A. I., Chen, R., Delgado, R. D., Liang, W., Garnett, E. C., Najarian, M., Majumdar, A. & Yang, P. *Nature (London)* **451,** 163 (2008).

131. Martin, P., Aksamija, Z., Pop, E. & Ravaioli, U. *Phys. Rev. Lett.* **102,** 125503 (2009).

132. Goodnick, S. M., Gann, R. G., Sites, J. R., Wilmsen, C. W., Fathy, D. & Krivanek, O. L. *J. Vac. Sci. Technol.* **1,** 582696 (1983).

133. Holland, M. G. *Phys. Rev.* **132,** 2461 (1963).

134. Glassbrenner, C. J. & Slack, G. A. *Phys. Rev.* **134,** A1058 (1964).

135. Mingo, N., Esfarjani, K., Broido, D. A. & Stewart, D. A. *Phys. Rev. B* **81,** 045408 (2010).

136. Dirac, P. A. M. *Proc. Roy. Soc. (London)* **114,** 243 (1927).

137. Ziman, J. M. *Electrons and Phonons* (Oxford University, New York, 1960).

138. Dingle, R. B. *Proc. Roy. Soc. (London)* **A201,** 545 (1950).

139. Thonhauser, T. & Mahan, G. D. *Phys. Rev. B* **71,** 081307(R) (2005).

140. Guinea, F., Tejedor, C., Flores, F. & Louis, E. *Phys. Rev. B* **28,** 4397 (1983).

141. M. P. López-Sancho, J. M. L.-S. & Rubio, J. *J. Phys. F: Met. Phys.* **15,** 851 (1985).

142. Zhang, W., Mingo, N. & Fisher, T. *Numer. Heat Transfer, Part B* **51,** 333 (2007).

143. Cotton, F. A. *Chemical Applications of Group Theory* third (John Wiley & Sons, Ney York, 1990).

144. Golub, G. H. & van Loan, F. *Matrix Computations* 3rd ed. (JHU Press, 1996).

145. Goto, K. & van de Geijn, R. *ACM T. Math. Software* **35,** 4 (2008).

146. Jian, Z., Kaiming, Z. & Xide, X. *Phys. Rev. B* **41,** 12915 (1990).

147. Wei, S. & Chou, M. Y. *Phys. Rev. B* **50,** 2221 (1994).

148. *Trends in Computational Nanomechanics: Transcending Length and Time Scales* 1st ed. (ed Dumitrica, T.) (Springer, New York, 2009).

149. Chang, C. & Geller, M. R. *Phys. Rev. B* **71,** 125304 (2005).

150. Heron, J.-S., Bera, C., Fournier, T., Mingo, N. & Bourgeois, O. *Phys. Rev. B* **82,** 155458 (2010).

151. Donadio, D. & Galli, G. *Nano Lett.* **10,** 847 (2010).

152. Kim, W. & Majumdar, A. *J. Appl. Phys.* **99,** 084306 (2006).

153. Moore, A. L., Saha, S. K., Prasher, R. S. & Shi, L. *Appl. Phys. Lett.* **93,** 083112 (2008).

154. Feser, J. P., Sadhu, J. S., Azeredo, B. P., Hsu, K. H., Ma, J., Kim, J., Seong, M., Fang, N. X., Li, X., Ferreira, P. M., Sinha, S. & Cahill, D. G. *Thermal Conductivity of Silicon Nanowire Arrays with Controlled Roughnes* Preprint available online at `http://users.mrl.uiuc.edu/cahill/SiNW_TDTR.pdf`. Retrieved on 2012-04-06. 2012.

155. Carnot, S. *Réflexions sur la Puissance Motrice du Feu* (Bachelier, Paris, 1824).

156. Snyder, G. J. & Ursell, T. S. *Phys. Rev. Lett.* **91,** 148301 (2003).

157. DiSalvo, F. J. *Science* **30,** 703 (1999).

158. Venkatasubramanian, R., Siivola, E., Colpitts, T. & O'Quinn, B. *Nature* **413,** 597 (2001).

159. Leclerc, M. & Najari, A. *Nat. Mater.* **10,** 409 (2011).

160. Dubey, N. & Leclerc, M. *J. Polym. Sci., Part B: Polym. Phys.* **49,** 467 (2011).

161. Sanchez, C. *J. Mater. Chem.* **15,** 3557 (2005).

162. Mitzi, D. B. *Chem. Mater.* **13,** 3283 (2001).

163. Xing, L.-L., Li, D.-P., Hu, S.-X., Jing, H.-Y., Fu, H., Mai, Z.-H. & Li, M. *J. Am. Chem. Soc.* **128,** 1749 (2006).

164. Yoon, K.-H., Han, K.-S. & Sung, M.-M. *Nanoscale Res. Lett.* **7,** 71 (2012).

165. Deneke, C., Zschieschang, U., Klauk, H. & Schmidt, O. G. *Appl. Phys. Lett.* **89,** 263110 (2006).

166. Deneke, C., Schumann, J., Engelhard, R., Thomas, J., Sigle, W., Zschieschang, U., Klauk, H., Chuvilin, A. & Schmidt, O. G. *Phys. Status Solidi C* **5,** 2704 (2008).

167. Bufon, C. C. B., Espinoza, J. D. A., Thurmer, D. J., Bauer, M., Deneke, C., Zschieschang, U., Klauk, H. & Schmidt, O. G. *Nano Lett.* **11,** 3727 (2011).

168. Mitzi, D. B., Chondroudis, K. & Kagan, C. R. *IBM Res. Dev.* **45,** 29 (2001).

169. Kagan, C. R., Mitzi, D. B. & Dimitrakopoulos, C. D. *Science* **286,** 945 (1999).

170. Carrasco-Orozco, M. A., Stirner, T., O'Neill, M., Ellis, C., Dong, D., Kelly, R., Piepenbrock, M. O. & Kelly, S. M. *Phys. Rev. B* **75,** 035207 (2007).

171. Park, Y., Han, K. S., Lee, B. H., Cho, S., Lee, K. H., Im, S. & Sung, M. M. *Org. Electron.* **12,** 348 (2010).

172. See, K. C., Feser, J. P., Chen, C. E., Majumdar, A., Urban, J. J. & Segalman, R. A. *Nano Lett.* **10,** 4664 (2010).

173. Malen, J. A., Doak, P., Baheti, K., Tilley, T. D., Majumdar, A. & Segalman, R. A. *Nano Lett.* **9,** 3406 (2009).

174. Ke, S.-H., Yang, W., Curtarolo, S. & Baranger, H. U. *Nano Lett.* **9,** 1011 (2009).

175. Yan, L., Shao, M., Wang, H., Dudis, D., Urbas, A. & Hu, B. *Adv. Mater.* **23,** 4120 (2011).

176. D. Appelhansa, a. D. F., Adlera, H., Pliethb, W., Fikusb, A., Grundkec, K., Schmittc, F., Bayerc, T. & Adolphid, B. *Colloids Surf., A* **161,** 203 (2000).

177. Sathyapalan, A., Ng, S. C., Lohani, A., Ong, T. T., Chen, H., Zhang, S., Lam, Y. M. & Mhaisalkar, S. G. *Thin Solid Films* **516,** 5645 (2008).

178. Fabre, B., Lopinski, G. P. & Wayner, D. D. M. *Chem. Commun.* **2002,** 2904 (2002).

179. de Groot, S. R. & Mazur, P. *Non-Equilibrium Thermodynamics* (Dover, New York, 1984).

180. Onsager, L. *Phys. Rev.* **37,** 405 (1931).

181. Hill, T. L. *Thermodynamics of Small Systems* (Benjamin, New York, 1963).

182. Letellier, P., Mayaffre, A. & Turmine, M. *Phys. Rev. B* **76,** 045428 (2007).

183. Carrete, J., Varela, L. M. & Gallego, L. J. *Phys. Rev. E* **77,** 022102 (2008).

184. Seebeck, T. J. *Abh. K. Akad. Wiss.* **2,** 265 (1823).

185. *CRC Handbook of Thermoelectrics* 1st ed. (ed Rowe, D. M.) (CRC Press, Boca Raton, 1995).

186. Mahan, G. D. & Sofo, J. O. *Proc. Natl. Acad. Sci. USA* **93,** 7436 (1996).

187. Krishnamurthy, S., Sher, A. & Chen, A. *Appl. Phys. Lett.* **47,** 160 (1985).

188. Slack, G. A. & Hussain, M. A. *J. Appl. Phys.* **47,** 2694 (1991).

189. Mingo, N., Hauser, D., Kobayashi, N. P., Plissonnier, M. & Shakouri, A. *Nano Lett.* **9,** 711 (2009).

190. Kim, K. & Jordan, K. D. *J. Phys. Chem.* **98,** 10089 (1994).

191. Frisch, M. J. *et al. Gaussian 09 Revision A.02* Gaussian Inc. Wallingford CT 2009.

192. Parr, R. G. & Yang, W. *Density Functional Theory of Atoms and Molecules* (Oxford University Press, New York, 1989).

193. Hohenberg, P. & Kohn, W. *Phys. Rev.* **136,** B864 (1964).

194. Kohn, W. & Sham, L. J. *Phys. Rev.* **140,** A1133 (1965).

195. Born, M. & Oppenheimer, R. *Ann. Phys.* **84,** 459 (1927).

196. Feynman, R. P. *Phys. Rev.* **56,** 340 (1939).

197. Gonze, X., Allan, D. C. & Teter, M. P. *Phys. Rev. Lett* **68,** 3603 (1992).

198. Gonze, X. *Phys. Rev. A* **52,** 1086 (1995).

199. Mingo, N., Stewart, D. A., Broido, D. A. & Srivastava, D. *Phys. Rev. B* **77,** 033418 (2008).

200. Jiang, J. & Luo, Y. *QCME-V1.0 (Quantum Chemistry for Molecular Electronics)* Royal Institute of Technology, Sweden, 2005.

201. Wang, C.-K., Fu, Y. & Luo, Y. *Phys. Chem. Chem. Phys.* **3,** 5017 (2001).

202. Jiang, J., Kula, M. & Luo, Y. *J. Chem. Phys.* **124,** 034708 (2006).

203. Hu, W., Jiang, J., Nakashima, H., Luo, Y., Kashimura, Y., Chen, K.-Q., Shuai, Z., Furukawa, K., Lu, W., Liu, Y., Zhu, D. & Torimitsu, K. *Phys. Rev. Lett.* **96,** 027801 (2006).

204. Su, W. Y., Jiang, J., Lu, W. & Luo, Y. *Nano Lett.* **6,** 2091 (2006).

205. Cao, H., Jiang, J., Ma, J. & Luo, Y. *J. Am. Chem. Soc.* **130,** 6674 (2008).

206. Vining, C. B. *J. Appl. Phys.* **69,** 331 (1991).

207. Savić, I., Mingo, N. & Stewart, D. A. *Phys. Rev. Lett.* **101,** 165502 (2008).

208. Chiritescu, C., David G. Cahill and, N. N., Johnson, D., Bodapati, A., Keblinski, P. & Zschack, P. *Science* **315,** 351 (2007).

209. Schaffler, F. in. *Properties of Advanced Semiconductor Materials GaN, AlN, InN, BN, SiC, SiGe* (eds Levinshtein, M. E., Rumyantsev, S. L. & Shur, M. S.) 149 (Wiley, New York, 2001).

210. Walden, P. *Chem. Zentralbl.* **85,** 1800 (1914).

211. Walden, P. *Bull. Acad. Imper. Sci. St. Pétersbourg.* **8,** 405 (1914).

212. Hurley, F. H. & Wier, T. P. *J. Electrochem. Soc.* **98,** 207 (1951).

213. Scheffler, T. B., Hussey, C. L., Seddon, K. R., Kear, C. M. & Armitage, P. D. *Inorg. Chem.* **22,** 2099 (1983).

214. Laher, T. M. & Hussey, C. L. *Inorg. Chem.* **22,** 3247 (1983).

215. Wilkes, J. S. & Zaworotko, M. J. *Chem. Comm,* 965 (1992).

216. Swatloski, R. P., Holbrey, J. D. & Rogers, R. D. *Green Chem.* **5,** 361 (2003).

217. Yan, F., Xia, S., Wang, Q., & Ma, P. *J. Chem. Eng. Data* **57,** 805 (2012).

218. Méndez-Morales, T. *Trabajo fin de máster: Estudio Teórico-Computacional de Líquidos Iónicos basados en el Catión Imidazolio* Universidade de Santiago de Compostela, 2010.

219. Sambasivarao, S. . V. & Acevedo, O. *J. Chem. Theory Comput.* **5,** 1038 (2009).

220. Seddon, K. R. in *The International George Papatheodorou Symposium: Proceedings* (eds Boghosian, S. *et al.*) (Institute of Chemical Engineering and High Temperature Chemical Processes, Patras, Greece, 1999), 131.

221. Tsuda, T. & Hussey, C. L. *Electrochem. Soc. Interface* **Spring 2007,** 44 (2007).

222. Méndez-Morales, T., Carrete, J., Cabeza, O., Gallego, L. J. & Varela, L. M. *J. Phys. Chem. B* **115,** 6995 (2011).

223. Méndez-Morales, T., Carrete, J., Cabeza, O., Gallego, L. J. & Varela, L. M. *J. Phys. Chem. B* **115,** 11170 (2011).

224. Méndez-Morales, T., Carrete, J., García, M., Cabeza, O., Gallego, L. J. & Varela, L. M. *J. Phys. Chem. B* **115,** 15313 (2011).

225. Salas, G., Podgoršek, A., Campbell, P. S., Santini, C. C., Pádua, A. A. H., Costa Gomes, M. F., Philippot, K., Chaudret, B. & Turmine, M. *Physical Chemistry Chemical Physics* **13,** 13527 (2011).

226. Zhao, Y., Chen, Z., Wang, J. & Zhuo, K. *Z. Phys. Chem.* **223,** 857 (2009).

227. Pereiro, A. B. & Rodríguez, A. *J. Chem. Thermodyn.* **39,** 978 (2007).

228. Seddon, K. R., Stark, A. & Torres, M. J. *Pure Appl. Chem.* **72,** 2275 (2000).

229. Rebelo, L. P. N., Najdanovic-Visak, V., Visak, Z. P., da Ponte, M. N., Szydlowskia, J., Cerdeiriña, C. A., Troncoso, J., Romaní, L., Esperança, J. M. S. S., Guedes, H. J. R. & de Sousa, H. C. *Green Chem.* **6,** 369 (2004).

230. Najdanovic-Visak, V., Esperança, J. M. S. S., Rebelo, L. P. N., da Ponte, M. N., Guedes, H. J. R., Seddon, K. R., de Sousa, H. C. & Szydlowski, J. *J. Phys. Chem. B* **107,** 12797 (2003).

231. Kelkar, M. S. & Maginn, E. J. *J. Phys. Chem. B* **111,** 4867 (2007).

232. Huddleston, J. G., Visser, A. E., Reichert, W. M., Willauer, H. D., Broker, G. A. & Rogers, R. D. *Green Chem.* **3,** 156 (2001).

233. Carrete, J., García, M., Rodríguez, J., Cabeza, O. & Varela, L. M. *Fluid Phase Equilib.* **301,** 118 (2011).

234. Cuadrado-Prado, S., Domínguez-Pérez, M., Rilo, E., García-Garabal, S., Segade, L. & C. Franjo, O. C. *Fluid Phase Equilib.* **278,** 36 (2009).

235. Cammarata, L., Kazarian, S. G., Salter, P. A. & Welton, T. *Phys. Chem. Chem. Phys.* **3,** 5192 (2001).

236. Fazio, B., Triolo, A. & Marco, G. D. *J. Raman Spectroscopy* **39,** 233 (2008).

237. Takamuku, T., Kyoshoin, Y., Shimomura, T., Kittaka, S. & Yamaguchi, T. *J. Phys. Chem. B* **113,** 10817 (2009).

238. Zhang, L., Xu, Z., Wang, Y. & Li, H. *J. Phys. Chem. B* **112,** 6411 (2008).

239. Hanke, C. G. & Lynden-Bell, R. M. *J. Phys. Chem. B* **107,** 10873 (2003).

240. Bernardes, C. E. S., da Piedade, M. E. M. & Canongia-Lopes, J. N. *J. Phys. Chem. B* **115,** 2067 (2011).

241. Feng, S. & Voth, G. A. *Fluid Phase Equilib.* **294,** 148 (2010).

242. Jiang, W., Wang, Y. & Voth, G. A. *J. Phys. Chem. B* **111,** 4812 (2007).

243. Moreno, M., Castiglione, F., Mele, A., Pasqui, C. & Raos, G. *J. Phys. Chem. B* **112,** 7826 (2008).

244. Spickermann, C., Thar, J., Lehmann, S. B. C., Zahn, S., Hunger, J., Buchner, R., Hunt, P. A., Welton, T., & Kirchner, B. *J. Chem. Phys.* **129,** 104505 (2008).

245. Berendsen, H. J. C., van der Spoel, D. & van Drunen, R. *Comp. Phys. Comm* **91,** 43 (1995).

246. Lindahl, E., Hess, B. & van der Spoel, D. *J. Mol. Model.* **7,** 306 (2001).

247. Van der Spoel, D., Lindahl, E., Hess, B., Groenhof, G., Mark, A. E. & Berendsen, H. J. C. *J. Comput. Chem.* **26,** 1701 (2005).

248. Hess, B., Kutzner, C., der Spoel, D. V. & Lindahl, E. *J. Chem. Theory Comput.* **4,** 435 (2008).

249. Jorgensen, W. L., Maxwell, D. S. & Tirado-Rives, J. *J. Am. Chem. Soc.* **118,** 11225 (1996).

250. Prado, C. E. R. & Freitas, L. C. G. *J. Mol. Struct. (Theochem.)* **847,** 93 (2007).

251. Brenneman, C. M. & Wiberg, K. B. *J. Comp. Chem.* **11,** 361 (1990).

252. Mahoney, M. W. & Jorgensen, W. L. *J. Chem. Phys.* **112,** 8910 (2000).

253. Darden, T., York, D. & Pedersen, L. *J. Chem. Phys.* **98,** 10089 (1993).

254. Hess, B., Bekker, H., Berendsen, H. J. C. & Fraaije, J. G. E. M. *J. Comp. Chem.* **18,** 1463 (1997).

255. Hess, B. *J. Chem. Theory Comp.* **4,** 116 (2007).

256. Hockney, R., Goel, S. P. & Eastwood, J. *J. Comp. Phys.* **14,** 148 (1974).

257. Martínez, L., Andrade, R., Birgin, E. G. & Martínez, J. M. *J. Comput. Chem.* **30,** 2157 (2009).

258. Micaelo, N. M., Baptista, A. M. & Soares, C. M. *J. Phys. Chem. B* **110,** 14444 (2006).

259. Bussi, G., Donadio, D. & Parrinello, M. *J. Chem. Phys.* **126,** 014101 (2007).

260. Parrinello, M. & Rahman, A. *J. Appl. Phys.* **52,** 7182 (1981).

261. Haughney, M., Ferrario, M. & McDonald, I. R. *J. Phys. Chem.* **91,** 4934 (1987).

262. Méndez-Morales, T., Carrete, J., García, M., Cabeza, O., Gallego, L. J. & Varela, L. M. *J. Phys. Chem. B* **115,** 15322 (2011).

263. Flory, P. J. *Principles of Polymer Chemistry* (Cornell University Press, Ithaca, New York, 1953).

264. Lacombe, R. H. & Sanchez, I. *J. Phys. Chem.* **80,** 2568 (1976).

265. Nymand, T. M. & Linse, P. *J. Chem. Phys* **112,** 6386 (2000).

266. Debye, P. & Hückel, E. *Phys. Z.* **24,** 185 (1923).

267. Onsager, L. *Phys. Z.* **27,** 388 (1926).

268. Onsager, L. & Fuoss, R. M. *J. Phys. Chem.* **36,** 2689 (1932).

269. Onsager, L. & Fuoss, R. M. *Proc. Natl. Acad. Sci. U.S.A.* **41,** 274 (1955).

270. Onsager, L. & Fuoss, R. M. *J. Phys. Chem.* **61,** 668 (1957).

271. Fuoss, R. M. *J. Am. Chem. Soc.* **80,** 3163 (1958).

272. Bockris, J. O. & Reddy, A. K. N. *Modern Electrochemistry 1: Ionics.* 2nd ed. (Plenum Press, New York, 2000).

273. Kirkwood, J. G. *Chem. Rev. (Washington, D.C.)* **19,** 275 (1936).

274. Robinson, R. A. & Stokes, R. H. *Electrolyte solutions* (Butterworths, 1959).

275. Hyman, A. & Vaughn, V. in *Proceedings of the conference held at Syracuse University, June, 1966* (Gordon and Breach, 1967).

276. Bahe, L. W. *J. Phys. Chem* **76,** 1062 (1972).

277. Bahe, L. W. & Parker, D. J. *J. Am. Chem. Soc.* **97,** 5664 (1975).

278. Alves Marques, M., de Barros Marques, M. I., Cabaço, M. I., Gaspar, A. M., Marques, M. P. M., Amado, A. M. & Amorim da Costa, A. M. *J. Mol. Liq.* **134,** 142 (2007).

279. Bou Malham, I., Letellier, P. & Turmine, M. *Talanta* **72,** 155 (2007).

280. Bou Malham, I., Letellier, P., Mayaffre, A. & Turmine, M. *J. Chem. Thermodyn.* **39,** 1132 (2007).

281. Bouguerra, S., Bou Malham, I., Letellier, P., Mayaffre, A. & Turmine, M. *J. Chem. Thermodyn.* **40,** 146 (2008).

282. Varela, L. M., Carrete, J., Turmine, M., Rilo, E. & Cabeza, O. *J. Phys. Chem. B* **113,** 12500 (2009).

283. Varela, L. M., Carrete, J., García, M., Rodríguez, J. R., Gallego, L. J., Turmine, M. & Cabeza, O. in. *Ionic Liquids: Theory, Properties, New Approaches* (ed Kokorin, A.) (InTech, 2011).

284. Murphy, G. *J. Chem. Soc. Faraday Trans. 2* **79,** 1607 (1983).

285. Chagnes, A., Carré, B., Willmann, P. & Lemordant, D. *Electrochimica Acta* **46,** 1783 (2001).

286. Claude-Montigny, B., Rioteau, E., Lemordant, D., Topart, P. & Bosser, G. *Electrochimica Acta* **47,** 533 (2001).

287. Chagnes, A., Carré, B., Willmann, P. & Lemordant, D. *J. Power Sources* **109,** 203 (2002).

288. Chagnes, A., Nicolis, S., Carré, B., Willmann, P. & Lemordant, D. *Chem. Phys. Chem.* **4,** 559 (2003).

289. Janek, J., Martin, M. & Yoo, H.-I. *Ber. Bunsenges Phys. Chem.* **98,** 655 (1994).

290. Woodward, C. E. & Harris, K. R. *Phys. Chem. Chem. Phys.* **12,** 1172 (2010).

291. Villullas, H. M. & González, E. R. *J. Phys. Chem. B* **109,** 9166 (2005).

292. Adams, G. & Gibbs, J. H. *J. Chem. Phys.* **43,** 139 (1965).

293. Baranovskii, S. D & Cordes, H. *J. Chem. Phys.* **111,** 7546 (1999).

294. Böttger, H. & Bryksin, V. V. *Hopping Conduction in Solids* (VCH, Berlin, 1985).

295. Varela, L. M., García, M. & Mosquera, V. *Phys. Rep.* **382,** 1 (2003).

296. McDonald, J. R., Lehnen, A. P. & Franceschetti, D. R. *J. Phys. Chem. Solids* **43,** 39 (1982).

297. Lou, P., Kang, S, Ko, K. & Lee, J. *J Phys. Chem. B* **111,** 13047 (2007).

298. Seitz, F. *The Modern Theory of Solids* (Dover, New York, 1987).

299. Kikuchi, H. & Sato, R. *J. Chem. Phys.* **55,** 677 (1971).

300. Kikuchi, H. & Sato, R. *J. Chem. Phys.* **55,** 702 (1971).

301. Lobo, V. M. M. *Handbook of Electrolyte Solutions* (Elsevier, Amsterdam, 1990).

302. Rilo, E., Vila, J., Pico, J., García-Garabal, S., Segade, L., Varela, L. M. & Cabeza, O. *J. Chem. Eng. Data* **55,** 639 (2010).

303. Molenat, J. *J. Chim. Phys. Phys. Chim. Biol.* **66,** 825 (1969).

304. Vila, J., Rilo, E., Segade, L., Cabeza, O. & Varela, L. M. *Phys. Rev. E* **71,** 312011 (2005).

305. Vila, J., Ginés, P., Rilo, E., Cabeza, O. & Varela, L. M. *Fluid Phase Equilib.* **247,** 32 (2006).

306. Casteel, J. F. & Amis, E. S. *J. Chem. Eng. Data* **17,** 55 (1972).

307. De Castro, C. A. N., Lourenço, M. J. V., Ribeiro, A. P. C., Langa, E., Vieira, S. I. C., Goodrich, P. & Hardacre, C. *J. Chem. Eng. Data* **55,** 653 (2010).

308. Assael, M. J., Antoniadis, K. D. & Wakeham, W. A. *Int. J. Thermophys.* **31,** 1051 (2010).

309. Lin, S. H., Eyring, H. & Davis, W. J. *J. Phys. Chem.* **10,** 3017 (1964).

310. Gaeta, F. S., Albanese, C., Mita, D. G. & Peluso, F. *Phys. Rev. E* **49,** 433 (1994).

311. Chisolm, E. D., Clements, B. E. & Wallace, D. C. *Phys. Rev. E* **63,** 031204 (2001).

312. Zwanzig, R. *J. Chem. Phys.* **79,** 4507 (1983).

313. Madan, B., Keyes, T. & Seeley, G. *J. Chem. Phys.* **92,** 7565 (1990).

314. Madan, B., Keyes, T. & Seeley, G. *J. Chem. Phys.* **94,** 6762 (1991).

315. Moore, P. & Keyes, T. *J. Chem. Phys.* **100,** 6709 (1994).

316. Keyes, T. *J. Chem. Phys.* **103,** 9810 (1996).

317. Bembenek, S. D. & Laird, B. B. *J. Chem. Phys.* **104,** 5199 (1996).

318. Gezelter, J. D., Rabani, E. & Berne, B. J. *J. Chem. Phys.* **107,** 4618 (1997).

319. Wales, D. J. *Energy Landscapes* (Cambridge University Press, 2004).

320. Majumdar, S. N. & Martin, O. C. *Phys. Rev. E* **74,** 061112 (2006).

321. Wales, D. J. & Doye, J. P. K. *J. Phys.Chem. A* **101,** 5111 (1997).

322. Wallace, D. C. *Phys. Rev. E* **56,** 4179 (1997).

323. Wallace, D. C. & Clements, B. E. *Phys. Rev. E* **59,** 2942 (1999).

324. Clements, B. E. & Wallace, D. C. *Phys. Rev. E* **59,** 2955 (1999).

325. Holmström, E., Bock, N., Peery, T. B., Lizárraga, R., Lorenzi-Venneri, G. D., Chisolm, E. D. & Wallace, D. C. *Phys. Rev. E* **80,** 051111 (2009).

326. Böttger, H. & Damker, T. *Phys. Rev. B* **50,** 12509 (1994).

327. Böttger, H. & Damker, T. *Phys. Rev. B* **52,** 12481 (1995).

328. Damker, T., Bryskin, V. V. & Böttger, H. *Physica B* **263–264,** 133 (1999).

329. Braginsky, L., Lukzen, N., Shklover, V. & Hofmann, H. *Phys. Rev. B* **66,** 134203 (2002).

330. Shamsa, M., Liu, W., Balandin, A. A. & Liu, J. *Appl. Phys. Lett.* **87,** 202105 (2005).

331. Press, W. H., Teukolsky, S. A., Vetterling, W. T. & Flannery, B. P. *Numerical Recipes in C — The Art of Scientific Computing* 2nd (Cambridge University Press, 1992).

332. Byrd, R. H., Lu, P. & Nocedal, J. A. *SIAM J. Scientif. Statistic. Comput.* **16,** 1190 (1995).

333. Zhu, C., Byrd, R. H. & Nocedal, J. *ACM Trans. Math. Softw.* **23,** 550 (1997).

334. Shenogin, S., Bodapati, A., Keblinski, P., & McGaughey, A. J. H. *J. Appl. Phys.* **105,** 034906 (2009).

335. Mingo, N. in *Thermal Nanosystems and Nanomaterials* (ed Volz, S.) 63 (Springer Berlin / Heidelberg, 2009).

336. Bohren, C. F. & Huffman, D. *Absorption and scattering of light by small particles* (Wiley, 1983).

337. Perronace, A., Ciccotti, G., Leroy, F., Fuchs, A. H. & Rousseau, B. *Phys. Rev. E* **66,** 031201 (2002).

338. Gardas, R. L., Dagade, D. H., Terdale, S. S., Coutinho, J. A. P. & Patil, K. J. *J. Chem. Thermodynamics* **40,** 695 (2008).

339. Tomida, D., Kenmochi, S., Tsukada, T., Qiao, K. & Yokoyama, C. *Int. J. Thermophys.* **28,** 1147 (2007).